Physik-Department
Technische Universität München
und
Technische Universität Wien

TUM

Energy Dependence of the Beta Asymmetry in Neutron Beta Decay

Heiko Saul

Vollständiger Abdruck der von der Fakultät für Physik der Technischen Universität München zur Erlangung des akademischen Grades eines

Doktors der Naturwissenschaften (Dr. rer. nat.)

genehmigten Dissertation.

Vorsitzender: Priv.-Doz. Dr. Herbert Balasin

Prüfende der Dissertation:
1. Prof. Dr. Bastian Märkisch
2. Prof. Dr. Lothar Oberauer
3. Prof. Dr. Hartmut Abele
4. Prof. Dr. Jochen Schieck
5. Prof. Dr. Werner Heil

Die Dissertation wurde am 23.10.2018 bei der Technischen Universität München eingereicht und durch die Fakultät für Physik am 20.11.2018 angenommen.

Abstract

Neutron beta decay provides an excellent toolkit for the investigation of the structure of the weak interaction and potential deviations from the predictions of the standard model of particle physics.

Measuring the experimental beta asymmetry provides the most precise way to determine the ratio of axialvector- and vector-coupling, λ, and is also sensitive to non-zero scalar and tensor couplings via the Fierz interference term, b.

In this thesis the analysis of the experimental beta asymmetry measured with PERKEO III at the Institut Laue-Langebin, Grenoble, in 2009 is presented. This includes the data reduction process, as well as the analyis of the measured spectra including detector and background systematics as energy-dependent effects. Major refinements to the detector model are presented with regards to the non-linearity and energy resolution of the detectors.

The result of this analysis is a new results for the beta asymmetry $A = -0.11985(21)$ which is two times more precise than previous measurements. A correlated analysis of λ and b is performed. With $b = 0.017(21)$ this analysis provides the currently most precise limit from a single measurement in neutron decay.

Zusammenfassung

Die Untersuchung des Zerfalls des freien Neutrons ist ein exzellentes Werkzeug zur Untersuchung der Struktur der schwachen Wechselwirkung und erlaubt die Beobachtung potentieller Abweichungen von den Vorhersagen des Standardmodells der Teilchenphysik. Die präsziseste Methode zur Bestimmung des Verhältnisses von Axial- und Vektorkopplungskonstanten, λ, ist die Messung der Beta Asymmetrie im Neutronenzerfall. Diese beschreibt die Korrelation von Elektronenimpuls und Neutronenspin. Durch ihre Abhängigkeit vom Fierz Interferenz Term, b, ist diese ebenfalls sensitiv auf Skalar- und Tensorkopplungen abweichend von 0.

Im Rahmen dieser Arbeit wird die Analyse der experimentellen Beta Asymmetry, gemessen mit dem Zerfallsspektrometer PERKEO III, durchgeführt und beschrieben. Dies beinhaltet die Reduktion der Rohdaten und die Analyse der gemessenen Spektren inklusive Detektor- und Untergrundsystematiken. Wesentliche Erweiterungen des verwendeten Detektormodells in Bezug auf die Nichtlinearität und Energieauflösung wurden implementiert und erlauben eine unabhängige Kalibrierung mit Elektronenquellen.

Das Ergebnis dieser Analyse ist ein neues Resultat für die Beta Asymmetry $A = -0.11985(21)$ und $\lambda = -1.27641(56)$. Dies ist um einen Faktor zwei präziser als vorige Messungen und ist die derzeit präziseste Messung von λ.

Alle Systematiken sind als energieabhängige Korrekturen implementiert. Dies erlaubt die Extraktion des Fierz Interferenz Terms aus einer simultenen Analyse von λ und b. Das Ergebnis dieser Analyse ist $b = 0.017(21)$ und das derzeit beste Limit auf den Fierz Interferenz Term aus einer einzelnen Messung im Neutronenzerfall.

Contents

Introduction

The free neutron decays into a proton, electron and electron antineutrino:

$$n \rightarrow p^+ + e^- + \bar{\nu}_e \tag{0.1}$$

Within the Standard Model of particle physics the decay of the neutron is described using only two free parameters, the first element of the CKM-matrix V_{ud} and the ratio of axialvector to vector coupling $\lambda = g_A/g_V$.

Due to the abscence of nuclear structure neutron beta decay requires only small theoretical corrections. This makes investigations of neutron decay one of the most important probes to test the structure of the weak interaction.

Neutron decay observables may be seperated into two types, the neutron lifetime, which is sensitive to V_{ud} and λ, and the correlations between the kinematic properties of the neutron and its decay products. Within the Standard Model these correlations only depend on λ. The most precise measurements of λ are measurements of the partiy-violating beta asymmetry in neutron decay.

Neutron decay observables are sensitive to other couplings not described in the Standard Model. Combining measurements of several correlation coefficients allows to derive competitive limits on some of these couplings, as their dependence on the coupling parameters is different. The Fierz interference b in particular, is a direct probe for scalar and tensor interactions. It may be measured directly via the electron spectrum, but also enters the measured spectra which are used to extract some of the correlation coefficients in an energy-dependent fashion. Usually a combination of several correlation parameters is used to extract b, since the direct measurement of the Fierz interference term is experimentally challenging. However, to a certain extent this neglects experimental details such as energy range, detector resolution and background effects of the individual measurements. This can be solved by performing a correlated λ-b analysis. For the beta asymmetry such an analysis requires the knowledge of all major systematics effects and their energy dependent contribution to the measured spectra.

The spectrometer PERKEO III has been developed in order to measure several correlation coefficients in neutron decay. Within this thesis the analysis of a new measurement of the beta asymmetry is presented which has been performed by PERKEO III in 2009. This includes the selection and reduction of the recorded data, as well as the analysis of detector and background systematics in an energy-dependent fashion. To blind the analysis of the beta asymmetry, the neutron beam polarisation and systematic effects related to the magnetic field have been analysed seperately.

The work presented in this thesis is partly based on a first analysis performed after the beamtime [Mes11]. Several additions to this initial analysis are made, including refinements to the theoretical description of the measured data as well as an analysis of

background induced by the neutron beam. Major additions to the detector response model address the description of the detector non-linearity and energy resolution. These are supported by off-line measurements to understand the origin of the detector non-linearity. This finally allows to use independent measurements for the detector calibration.

The result presented for the beta asymmetry is the most precise measurement of the beta asymmetry and includes the contribution of all systematic effects in an energy-dependent fashion. This allows for correlated λ-b analysis which provides the most precise limits on the Fierz interfernece term from a single measurement in neutron decay.

Chapter 1

Theoretical Background

1.1 Beta Decay of the free Neutron

A free neutron decays into a proton, electron and electron anti-neutrino with a measured lifetime of $\tau = 880.2\,(1.0)$ s [PDG18]

$$n \rightarrow p + e + \bar{\nu}_e. \tag{1.1}$$

The total energy release is given by the mass difference of the neutron and the decay products

$$E_{tot} = m_n - m_p - m_e = 782.33324\,(42) \text{ keV}, \tag{1.2}$$

neglecting the neutrino mass. This energy is distributed among the kinetic energies of the decay products fulfilling energy and momentum conservation.

This weak semi-leptonic decay is mediated by a W-Boson as illustrated in the Feynman Graph figure 1.1. The propagator of the W-Boson can be written as

$$W\left(q^2\right) = -i\frac{g_{\mu\nu} - \frac{q_\mu q_\nu}{m_W^2}}{q^2 - m_W^2}, \tag{1.3}$$

where $g_{\mu\nu}$ is the metric tensor, q the momentum transfer and $m_W = 80.385\,(15)$ GeV the mass of the W-Boson. Using $m_W \gg E_0$ the propagator term can be approximated as

$$W\left(q^2\right) \overset{m_W \gg q}{\approx} i\frac{g_{\mu\nu}}{m_W^2} \tag{1.4}$$

Fig. 1.1: Feynman Graph of Neutron Decay.

which is equal to a point like interaction where the hadronic and leptonic currents couple directly [CB83].

1.2 Neutron Beta Decay within the Standard Model

The most general Lorentz-invariant Hamiltonian that describes the semileptonic charge current can be written as [LY56]

$$
\begin{aligned}
H_W = {} & \left(\bar{\psi}_p \psi_n\right) \left(C_S \bar{\psi}_e \psi_\nu + C_S' \bar{\psi}_e \gamma_5 \psi_\nu\right) \\
& + \left(\bar{\psi}_p \gamma_\mu \psi_n\right) \left(C_V \bar{\psi}_e \gamma_\mu \psi_\nu + C_V' \bar{\psi}_e \gamma_\mu \gamma_5 \psi_\nu\right) \\
& + \frac{1}{2} \left(\bar{\psi}_p \sigma_{\lambda\mu} \psi_n\right) \left(C_T \bar{\psi}_e \sigma_{\lambda\mu} \psi_\nu + C_T' \bar{\psi}_e \sigma_{\lambda\mu} \gamma_5 \psi_\nu\right) \\
& - \left(\bar{\psi}_p \gamma_\mu \gamma_5 \psi_n\right) \left(C_A \bar{\psi}_e \gamma_\mu \gamma_5 \psi_\nu + C_A' \bar{\psi}_e \gamma_\mu \psi_\nu\right) \\
& + \left(\bar{\psi}_p \gamma_5 \psi_n\right) \left(C_P \bar{\psi}_e \gamma_5 \psi_\nu + C_P' \bar{\psi}_e \psi_\nu\right).
\end{aligned}
\tag{1.5}
$$

Where ψ_p, ψ_n, ψ_e and ψ_ν denote the wave functions of the proton, neutron, electron and electron antineutrino. The indices V, A, S, T, P indicate vector, axialvector, scalar, tensor and pseudoscalar couplings respectively. The coefficients C_i, C_i' are necessary to introduce parity non-conservation into the theory and are allowed to be complex only in the case that time reversal invariance is not fulfilled. Accounting for the fact that only left-handed neutrinos are observed (maximum parity violation) the relation between the coefficients is fixed by $C_i = -C_i'$ [CB83],

$$
C_i \bar{\psi}_e O_i \psi_\nu + C_i' \bar{\psi}_e O_i \gamma_5 \psi_\nu \to C_i \bar{\psi}_e O_i (1 - \gamma_5) \psi_\nu.
\tag{1.6}
$$

Based on experimental observations [Wu+57; GGS58] this general Hamiltonian is restricted by the V-A theorem to contain vector and axialvector couplings with opposite signs [LY56; FG58]. The resulting Hamiltonian is given by

$$
\begin{aligned}
H_W\left(x\right) &= \frac{1}{\sqrt{2}} \left(J_\mu^{V,\mathrm{hadr}} + J_\mu^{A,\mathrm{hadr}}\right) J^{\mathrm{lept},\mu}, \\
\text{with } J_\mu^{V,\mathrm{hadr}}\left(x\right) &= C_V \bar{\psi}_p\left(x\right) \gamma_\mu \psi_n\left(x\right), \\
J_\mu^{A,\mathrm{hadr}}\left(x\right) &= C_A \bar{\psi}_p\left(x\right) \gamma_\mu \gamma^5 \psi_n\left(x\right), \\
J^{\mathrm{lept},\mu}\left(x\right) &= \left[\bar{\psi}_e \gamma^\mu \left(1 - \gamma^5\right) \psi_\nu\left(x\right)\right],
\end{aligned}
\tag{1.7}
$$

The vector coupling C_V is given in terms of the Fermi coupling constant G_F as measured in muon decay [PDG16]

$$
C_V = G_\mathrm{F}\ V_\mathrm{ud}\ g_V, \text{ with } G_\mathrm{F} = 1.1663787\,(6) \cdot 10^{-5}\ \mathrm{GeV}^{-2}
\tag{1.8}
$$

where $g_V = 1$ and V_ud the first element of the CKM-matrix, that accounts for the rotation of weak and mass eigenstates of quarks [Cab63; KM73]. The axialvector coupling C_A on the other hand is given by

$$
C_A = G_\mathrm{F}\ V_\mathrm{ud}\ g_A = G_F\ V_\mathrm{ud}\ \lambda, \text{ with } \lambda = \frac{C_A}{C_V} = \frac{g_A}{g_V}.
\tag{1.9}
$$

The couplings g_A and g_V are the couplings on nucleon level as relevant in β-decay and implicitly contain QCD corrections for the nucleon structure and radiative corrections [Sha71]. These couplings must not be confused with the weak coupling constants at quark level where the ratio of vector and axialvector couplings is defined to be unity by the V-A theorem giving rise to the universality of the weak interaction as it is described by the single parameter G_F.

1.2.1 Electron Spectrum and Neutron Lifetime

The decay width $\mathrm{d}\Gamma$ of an unpolarised neutron depending on the kinetic energy of the decay electron can be derived by using Fermi's Golden Rule

$$\mathrm{d}^5\Gamma = \frac{2\pi}{\hbar} \left|M_{fi}\right|^2 \rho\left(E_e\right) \mathrm{d}E_e \mathrm{d}\Omega_e \mathrm{d}\Omega_\nu, \tag{1.10}$$

where M_{fi} denotes the transition matrix element, E_e the electrons kinetic energy and $\rho\left(E_e\right)$ the phase space density. The decay rate can be calculated with the approximation of an infinitely massive nucleus and without consideration of electromagnetic interaction between the decay products,

$$\mathrm{d}\Gamma_n = \frac{G_F^2 \left|V_{ud}\right|^2}{32\pi^5} \left(1 + 3\lambda^2\right) \left(E_0 - E_e\right)^2 E_e p_e \mathrm{d}E_e \tag{1.11}$$

where the integration over the solid angles of electron and anti-neutrino as well as the anti-neutrino energy has been carried out. These assumptions are equivalent to a setup where antineutrino momenta and electron momentum directions remain undetected. The phase space density has become [Wil82]

$$\rho_0\left(E_e\right) = \left(E_0 - E\right)^2 E_e p_e, \tag{1.12}$$

where the endpoint energy of the electron spectrum E_0 contains a correction for the finite mass of the proton that leads to

$$E_0 = \frac{m_n^2 - m_p^2 + m_e^2}{2m_n}. \tag{1.13}$$

For precision analysis some theoretical corrections for the phase space volume are required which are discussed in detail in section 2.1.

After integration over the electron phase space the total decay probability for the neutron is given by [MS06]

$$\frac{1}{\tau} = \left|V_{ud}\right|^2 \frac{1 + 3\left|\lambda\right|^2}{4908.7(1.9)s}. \tag{1.14}$$

This illustrates that within the Standard Model neutron decay can be calculated requiring two parameters λ and $\left|V_{ud}\right|$ to be determined by experiment. The uncertainty in the numerator accounts for the theoretical uncertainties of the radiative corrections.

1.2.2 Decay Parameters for Polarized Neutrons

A formulation for the differential β-decay rate for oriented spin-1/2-nuclei depending on the electron and neutron momentum directions and the electron energy has been derived by Jackson, Treimann and Wyld [JTW57]:

$$\mathrm{d}\Gamma_n\left(E_e, \Omega_e, \Omega_\nu, \langle\boldsymbol{\sigma}_n\rangle\right)\mathrm{d}E_e\mathrm{d}\Omega_e\mathrm{d}\Omega_\nu =$$
$$\frac{1}{32\pi^5}\rho\left(E_e\right)\xi\left\{1 + a\frac{\boldsymbol{p}_e\cdot\boldsymbol{p}_\nu}{E_eE_\nu} + b\frac{m_e}{E_e} + \langle\boldsymbol{\sigma}_n\rangle\left[A\frac{\boldsymbol{p}_e}{E_e} + B\frac{\boldsymbol{p}_\nu}{E_\nu} + D\frac{\boldsymbol{p}_e\times\boldsymbol{p}_\nu}{E_eE_\nu}\right]\right\}. \quad (1.15)$$

Here $\langle\boldsymbol{\sigma}_n\rangle = \langle\boldsymbol{J}\rangle/J$ is the average spin orientation of the neutron and $\rho\left(E_e\right)$ is the phase space density including corrections as shown in section 1.2.1. The decay parameters ξ, a, b, A, B, D describe the amplitude of dependences of or correlations between different particle momenta. The values of these decay parameters are a function of the considered (in general complex) coupling constants without necessarily being restricted to V-A couplings only. However, within the Standard Model all the correlation coefficients are a function of λ or predicted to be 0.

The first parameter ξ just contains the influence of coupling constants on the decay rate

Coefficient		λ-dependence		Value	
X	Name	$X\left(\lambda\right)$	$\left\lvert\frac{\partial X}{\partial\lambda}\left(\lambda_0\right)\right\rvert$	Recent	World Average
a	Electron Neutrino Angular Correlation	$\frac{1-\lvert\lambda\rvert^2}{1+3\lvert\lambda\rvert^2}$	0.30	$-0.1090(41)$[1]	$-0.1059(28)$
b	Fierz Interference Term	0	0	$0.067\left(^{+0.090}_{-0.061}\right)$[2]	*none*
A	Beta Asymmetry	$-2\frac{\lvert\lambda\rvert^2+Re(\lambda)}{1+3\lvert\lambda\rvert^2}$	0.37	$-0.12015(71)$[3]	$-0.11840(10)$
B	Neutrino Asymmetry	$2\frac{\lvert\lambda\rvert^2-Re(\lambda)}{1+3\lvert\lambda\rvert^2}$	0.08	$0.9802(50)$[4]	$0.9807(30)$
C	Proton Asymmetry	$4x_C\frac{Re(\lambda)}{1+3\lvert\lambda\rvert^2}$	0.12	$-0.2377(26)$[4]	$-0.2377(26)$
D	Triple Correlation	$2\frac{Im(\lambda)}{1+3\lvert\lambda\rvert^2}$	0	$-0.9(2.1)\cdot10^{-4}$[5]	$-1.2(2.0)\cdot10^{-4}$
τ	Neutron Lifetime	$\propto\frac{1}{1+3\lvert\lambda\rvert^2}$	0	$877.7(0.7)$[6]	$880.2(1.0)$ s

1: [Dar+17], 2: [Hic+17], 3: [Bro+18], 4: [Sch+07] and [Sch+08], 5: [Chu+12], 6: [Pat+18]

Tbl. 1.1: Correlation coefficients and their dependence on $\lambda = g_A/g_V$ within the Standard Model. For the comparison on the λ sensitivity a value of $\lambda_0 = -1.2748$ has been used. The most recent published results and the world averages according to [PDG18] are listed.

and is identified with the factor $\left(1+3\lambda^2\right)$ within the standard model. The correlation coefficients a and b are observed for unpolarised neutrons and fulfil C, P and T symmetries, whereas A, B, D correlate particle momenta with the neutron spin and are either P or T violating. Table 1.1 summarizes the correlation coefficients with their λ-dependence and the most recent experimental results. The neutron lifetime plays a special role in this compilation as it is the only parameter that is not only dependent on λ but also on $\lvert V_{ud}\rvert$.

The CKM-matrix element $|V_{ud}|$ can be determined from neutron decay, by combining results from measurements of λ and the neutron lifetime. The correlation coefficient C describes the preferred recoil direction of the proton with respect to the neutron polarisation which effectively is a combination of the Beta and Neutrino Asymmetries

$$C = -x_C \left(A + B\right) \tag{1.16}$$

with a kinematic factor of $x_C = 0.27484$.

In addition to the correlation coefficients mentioned above there are plenty more observables when considering other kinematic observables such as the electron polarisation, providing about a dozen decay parameters in total. This over-determined system of observables is an excellent probe to test the consistency of the Standard Model and the underlying assumptions about the nature of the weak interaction.

1.2.3 The Beta Asymmetry

The most sensitive parameter to determine λ is the beta asymmetry A. This parameter is measured in terms of the asymmetry between the number of decay electrons emitted parallel and antiparallel to the neutron spin, which is called the experimental asymmetry.

$$A_{\text{exp}}\left(E_e\right) = \frac{N^{\uparrow}\left(E_e\right) - N^{\downarrow}\left(E_e\right)}{N^{\uparrow}\left(E_e\right) + N^{\downarrow}\left(E_e\right)}. \tag{1.17}$$

Where $N^{\uparrow}$ and $N^{\downarrow}$ denote the electron count rates measured with emission direction parallel and antiparallel to the neutron spin, respectively. Using equation 1.15 the emission probability with respect to the electron emission direction relative to the neutron spin can be written as

$$\mathrm{d}\Gamma_n\left(E_e\right)\mathrm{d}E_e = \frac{1}{8\pi^3}\rho\left(E_e\right)\xi\left\{1 \mp A\left\langle\sigma\right\rangle\frac{p_e}{E_e}\cos\left(\theta\right)\right\}, \tag{1.18}$$

where integration over the complete solid angle of neutrino emission has been carried out and the electron emission angle θ is defined relative to the neutron spin axis. In analalogy to the experimental setup to measure the beta asymmetry described in chapter 3 the integration over electron emission angles of the half-spaces finally leads to

$$A_{\text{exp}}\left(E_e\right) = \frac{1}{2}AP_n\beta\left(E_e\right). \tag{1.19}$$

Where the average neutron beam polarisation P_n is introduced, $\beta\left(E_e\right) = p_e/E_e$ and A is the beta asymmetry as defined in table 1.1.

The most precise measurement of the beta asymmetry has been performed with PERKEO II. The combined results of three measurements performed yields [Mun+13; Abe+02; Abe+97]

$$A_{\text{PERKEO II}} = -0.11926(^{+47}_{-53}). \tag{1.20}$$

The combined value from the UCNA collaboration is recently updated including a new

measurement [Bro+18]

$$A_{\mathrm{UCNA}} = -0.12054(34)_{\mathrm{stat}}(63)_{\mathrm{sys}}. \tag{1.21}$$

1.2.4 Experimental Status of λ and τ from Neutron Decay

Current experimental limits for both the neutron lifetime as well as the ratio of coupling constants $\lambda = g_A/g_V$ are shown in figures 1.2 and 1.3. Except for the measurement of Mostovoi et. al. and Schumann et. al. all measurements of λ have been performed by measuring the beta asymmetry A or the triple correlation coefficient a. However, the current world average calculated by the Particle Data Group is currently scaled by a factor of 2.2 in order to account for the discrepancy between recent measurements performed by PERKEO II and UCNA and older measurements [PDG18]. This leads to the fact that the world average $\lambda = 1.2724(23)$ does not fully reflect the achieved precision by newer measurements.

For the neutron lifetime a similar observation can be made. Here the scaling for the world average is 1.9 to account for the discrepancy observed between storage experiments performed with ultracold neutrons and beam experiments. In typical storage experiments ultracold neutrons are stored in a magnetic or material trap and the number of remaining neutron is measured for different observation times. In beam experiments on the other hand the neutron decay probability is measured by counting the decay products for a neutron beam passing a well defined decay volume. This method requires a very precise determination of the geometry of the decay volume as well as a precise measurement of the neutron flux.

So far these discrepancies severely limit the potential power of neutron decay for testing the validity of the Standard Model and determining the parameters to describe the process of neutron decay.

1.2.5 Experimental Status of $|V_{ud}|$ from Neutron Decay

Using equation 1.14 and the current limits for λ and τ the value of V_{ud} from neutron decay is:

$$|V_{ud}| = 0.97585\,(18)_{\mathrm{RC}}\,(55)_{\tau}\,(146)_{\lambda} = 0.97585(157). \tag{1.22}$$

This result is currently limited dominantly by the experimental limit obtained for λ, which again illustrates the necessity for more precise experimental results.

The Standard Model requires the CKM matrix to be unitary. In order to check this, the overall norm of the first row is checked

$$\Delta = 1 - \left(|V_{ud}|^2 + |V_{us}|^2 + |V_{ub}|^2 \right), \tag{1.23}$$

where Δ is required to compatible with zero in order to confirm the Standard Model.

The most precise determination of V_{us} is obtained from different decay modes of Kaons [MB16] which are averaged to
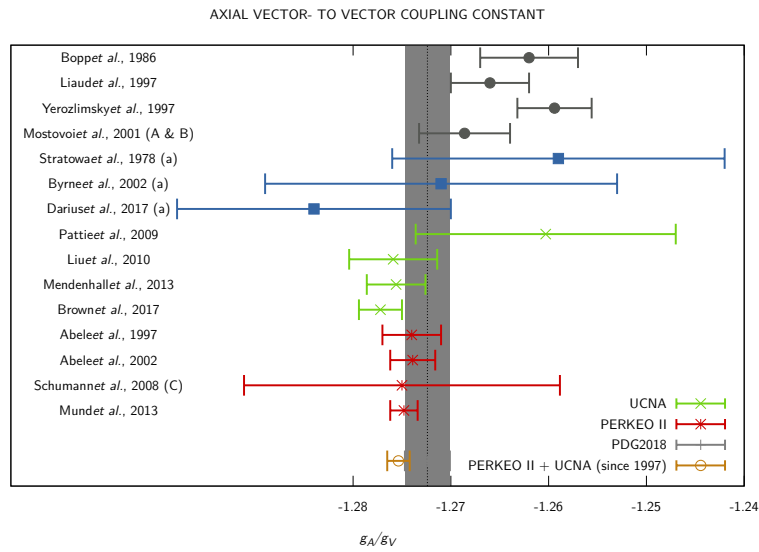
$$|V_{us}| = 0.2252(10). \tag{1.24}$$

Fig. 1.2: Comparison of λ measurements currently included in the world average. The letter in braces denotes the correlation coefficient measured to obtain λ if this is not A.
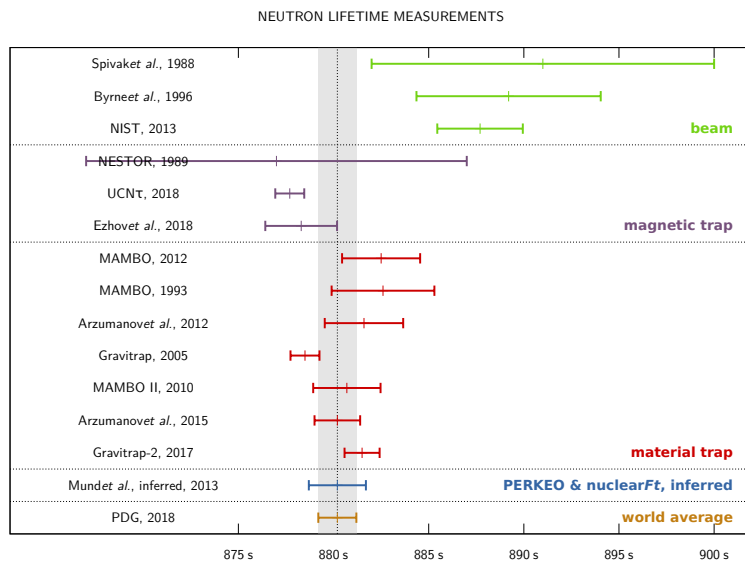

Fig. 1.3: Comparison of neutron lifetime measurements currently included in the world average.

Using this value and the current limit on V_{ud} (eq. 9.13) one obtains

$$\Delta = -3.0(3.1) \cdot 10^{-3}, \tag{1.25}$$

confirming the unitarity of the CKM matrix.

The best experimental limit on V_{ud} is currently obtained from superallowed nuclear beta decays [HT15], where the experimental ft values of 14 nuclei are averaged by including radiative and isospin-symmetry-breaking corrections individual to each nucleus. The validity of the applied corrections is simultaneously tested by this analysis and confirms the CVC hypothesis of the Standard Model. The value obtained is

$$V_{ud} = 0.97417(21), \tag{1.26}$$

which is a factor 7 more precise than the result obtained using neutrons. In this case the unitarity test leads to

$$\Delta = 2.3(6.0) \cdot 10^{-4}. \tag{1.27}$$

1.3 Neutron Decay and Physics Beyond the Standard Model

Neutron beta decay provides many more observables than free parameters required within the Standard Model (see section 1.2.2). This allows to check the consistency of different observables, effectively testing the validity of the Standard Model and its underlying assumptions.

In [JTW57] the decay correlations listed in table 1.1 are given in their most general form considering all potential couplings C_i. In the following only the amplitudes of potential scalar and tensor couplings are considered, but still accounting for the left-handedness of the weak interaction. The following leading order contributions to the decay observables are obtained:

$$
\begin{aligned}
a &= a_{\text{V-A}} - \frac{2}{3}\left(\frac{2}{1+3\lambda^2} - \frac{2 - C_S^2 + 3CT^2}{1 + C_S^2 + 3\lambda^2 + 3C_T^2}\right) \simeq a_{\text{V-A}} + \mathcal{O}(C_{S/T}^2), \\
b &= 2\frac{C_S + 3\lambda C_T}{1 + C_S^2 + 3\lambda^2 + 3C_T^2} \simeq 2\frac{C_S + 3\lambda C_T}{1 + 3\lambda^2} + \mathcal{O}(C_{S/T}^2), \\
A &= A_{\text{V-A}} + \frac{2}{1+3\lambda^2}\left(\frac{C_S^2\lambda(1+\lambda) + C_T^2(1 + 3\lambda + 6\lambda^2) + C_S(C_T + 3\lambda^2 C_T)}{1 + C_S^2 + 3C_T^2 + 3\lambda^2}\right) \\
&\simeq A_{\text{V-A}} + \mathcal{O}(C_{S/T}^2), \\
B &= \frac{2\left(C_T^2 + \lambda(\lambda - 1) - C_S C_T + \frac{m_e}{E_e}(-C_T(2\lambda - 1) - C_S\lambda)\right)}{1 + C_S^2 + 3\lambda^2 + 3C_T^2} \\
&\simeq B_{\text{V-A}} - \frac{m_e}{E_e}\frac{2(C_T(1 - 2\lambda) + C_S\lambda)}{1 + 3\lambda^2} + \mathcal{O}(C_{S/T}^2), \\
\tau &= \tau_{(V-A)} \cdot \frac{(1 + 3\lambda^2)}{1 + C_S^2 + 3\lambda^2 + 3C_T^2} \simeq \tau_{\text{V-A}} + \mathcal{O}(C_{S/T}^2).
\end{aligned}
\tag{1.28}
$$

The parameters τ, a and A only obtain corrections of quadratic order, but provide a stronger sensitivity on λ. Linear contributions are obtained for b and B.

This way neutron decay provides a sensitive probe to set limits on C_S and C_T or other potential non-Standard Model couplings by analysing multiple observables simultaneously.

1.3.1 The Fierz Interference Term

In case of non-zero scalar and tensor coupling the Fierz interference term also becomes non-zero. The spectra and experimental asymmetries accessed by experiments to extract the decay parameters then obtain additional changes due to the Fierz interference term (see eq. 1.15). The neutron beta decay rate is modified in an energy dependent fashion:

$$d\Gamma'_n\left(E_e\right) \to d\Gamma_n\left(E_e\right) \cdot \left(1 + b\frac{m_e}{E_e}\right). \tag{1.29}$$

This modification is transferred to the numerator of the experimental beta asymmetry (see eq. 1.19):

$$A'_{\exp}\left(E_e\right) \to A_{\exp}\left(E_e\right) \cdot \frac{1}{1 + b\frac{m_e}{E_e}}. \tag{1.30}$$

This then provides a first order dependence on scalar and tensor couplings and dominates the modification of the beta asymmetry A as derived in equation 1.28. Figure 1.4 shows the differences in the Neutron Beta Decay spectrum and the Experimental beta asymmetry for a Fierz interference term of $b = 0$ and $b = 0.1$.

Since it enters multiple spectra, there exist several options for the Fierz interference term to be extracted from neutron decay. The option most commonly used is to perform a combined analysis of multiple correlation coefficients fitting λ and b and to extract limits from this comparison [SBN06; WGH14]. In this case the energy dependent contribution of the Fierz interference term needs to be averaged over the whole energy region

$$A' \to A \cdot \frac{1}{1 + b\left\langle \frac{m_e}{E_e} \right\rangle}. \tag{1.31}$$

This method makes it very difficult to account for experimental details of each experiment as there usually limited information to account for the statistical sensitivity over the analysed energy region, background contributions and detector resolution correctly. These affect the parameter correlations between λ and b.

A first direct result on b extracted from the unpolarised decay spectrum measured with the UCNA spectrometer yields [Hic+17]

$$b = 0.067(0.005)_{\text{stat}} \left(^{+0.090}_{-0.061}\right)_{\text{sys}}, \tag{1.32}$$

where the result is limited severely by systematics related to electron detection. Although providing superior statistical sensitivity, a strong sensitivity on detector systematics is inherent to this method. The norm of the unpolarised decay spectrum is fitted simultaneously which reduces the signature of the Fierz interference term to a small spectral distortion. The statistical sensitivity is at least one order of magnitude larger
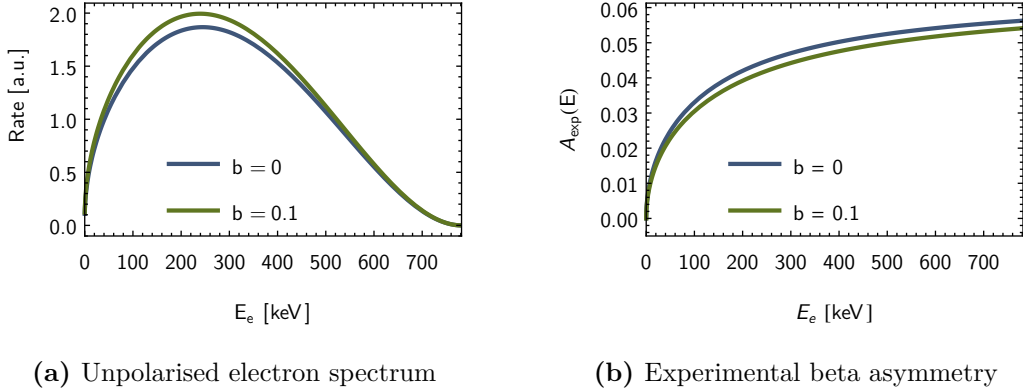
(a) Unpolarised electron spectrum

(b) Experimental beta asymmetry

Fig. 1.4: Comparison of the unpolarised electron spectrum from Neutron Beta Decay and the experimental beta asymmetry for a Fierz interference term of $b = 0$ and $b = 0.1$ according to equations 1.29 and 1.31.

compared to the beta asymmetry. For the PERKEO III data the improvement in statistical sensitivity is a factor of 13 for a fit range of 300-700 keV and increases strongly when including lower energies in the fit. Due to its superior statistical sensitivity such direct measurements are planned by the PERC collaboration at the FRMII [Dub+08; Kon+12a] and the Nab collaboration at the SNS [Bae+13] and also involve improved detector concepts.

Using the spectral analysis of an experimental asymmetry on the other hand provides limited statistical sensitivity. However, it allows to limit the contribution of detector and background systematics as the norm is not determined by the number of events detected [GJL95]. For the beta asymmetry such an analysis involves a combined λ-b-fit to the experimental beta asymmetry considering the full energy dependent contribution of the Fierz interference term as in equation 1.30.

Along with the analysis of the beta asymmetry data measured with PERKEO III this thesis deals with the understanding and improvement of systematic uncertainties. The present analysis provides the current best limit on b obtained from neutron decay (see chapter 6).

1.3.2 Current and future limits on Scalar and Tensor Interactions

The best limits on scalar couplings are dominated by the Fierz interference term obtained from comparing different superallowed nuclear decays [HT15] which leads to

$$b_F = -0.0028(26) \ \rightarrow C_S = \frac{-b_F}{2} = 0.0014(13) \ \ (68\% \ \text{C.L.}), \tag{1.33}$$

where b_F is only sensitive to scalar couplings due to the superallowed nature of the decays. A recent global analysis on multiple datasets provides limits on scalar and tensor currents assuming only coupling to left-handed neutrinos. This analysis includes nuclear and neutron decay data [GNS18] and provides consistency with the Standard Model

expectation $C_S = C_T = 0$. The projected single parameter limits are:

$$C_S/C_V = 0.0014(12) \quad (68\%\text{C.L.}),$$
$$C_T/C_A = 0.0020(22) \quad (68\%\text{C.L.}).$$

(1.34)

Since a potential tensor coupling does not modify the $0^+ \rightarrow 0^+$-decays, b_F directly limits the amplitude of C_S. The limits obtained for C_T are dominated by the measurement of neutron decay and other low energy nuclear decays such as ^{6}He. Similar limits on C_T are derived in [PHY13] where measurements of the beta asymmetry A in neutron decay, the neutron lifetime and C_S from superallowed Fermi decays are used. As illustrated in figure 1.5 the combination of the beta asymmetry and the neutron lifetime actually yields strong limits on the Fierz Interference term b, when the value of V_{ud} is constrained by superallowed Fermi decays. Using solely neutron decay data currently does not provide competitive limits as the simultaneous determination of V_{ud} and λ severely limits the sensitivity to other couplings. New results for λ and b are presented in this thesis.

Including a direct measurement of the Fierz interference term on the 10^{-3}-level combined with improved limits on several correlation coefficients would allow to extract more stringent limits from neutron decay data [Bha+12; Kon+12b; NG13].

Using an Effective Field Theory approach in the low energy limit the results obtained for the nucleon level couplings discussed above can be projected onto the quark-level [Bha+12; CGG13; CGH13] involving corrections for the nucleon structure from QCD lattice calculations. These calculations allow a comparison of the limits obtained for quark-level couplings from LHC data and precision measurements of nuclear and neutron decays. The results of these comparisons show that future limits of nuclear and neutron decay can provide limits which are complementary to those obtained by the LHC when including a direct Fierz interference term measurement from neutron decays.
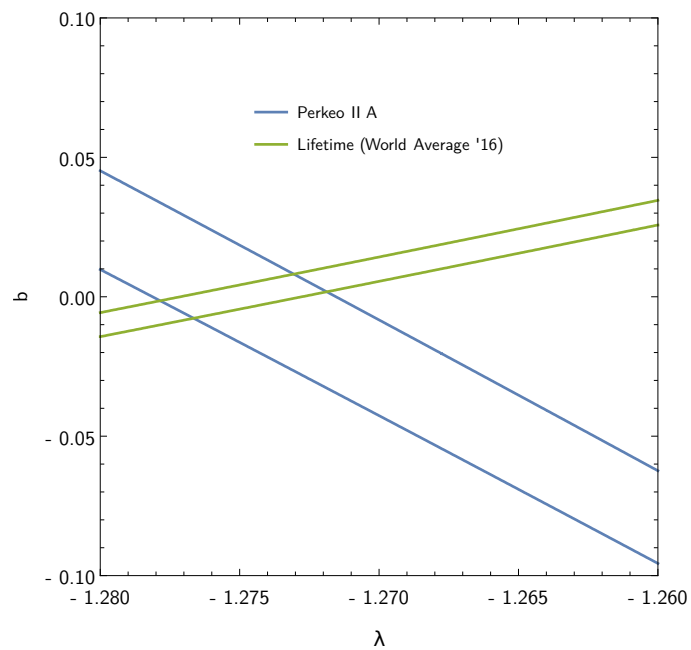
Fig. 1.5: 68.27% confidence regions of the beta asymmetry A as measured with PERKEO II [Mun+13] and the world average of the neutron lifetime [PDG18]. In order to infer the neutron lifetime the value of V_{ud} needs to be extracted from superallowed Fermi decays.

Chapter 2

The Phase Space of Neutron Decay and the Experimental Beta Asymmetry

With increasing precision of experiments also the influence of theoretical uncertainties on the obtained results become more important. Performing a spectral analysis, especially when aiming for the extraction of a Fierz interference term, requires the knowledge of the correct energy dependence of any corrections, in order to account for the varying statistical sensitivity due to influences of background and detector resolution.

Within this thesis the influence of theoretical corrections on the analysis of the experimental beta asymmetry is investigated. Most of these corrections have been applied in previous analyses already [Mun+13; Mes11]. In order to account for the improved precision of the PERKEO III data all relevant corrections are recalculated as given in the literature and corresponding uncertainties are investigated. This includes estimates on potential higher order contributions to the corrections and some refinements to previous calculations [Rei99] used for PERKEO. All relevant correction to the neutron decay phase space and the experimental beta asymmetry are implemented into the fitting routine which is used to analyse the spectra (see chapter 6). A compact analytical expression is calculated for the energy-dependence of the radiative corrections which provide a 10^{-3}-correction to the experimental beta asymmetry. Inclusion of this correction into the fit reduces the uncertainty related to this correction to $1 \cdot 10^{-4}$.

In the following chapter the relevant corrections and their uncertainties are summarised.

2.1 The Neutron Beta Decay Phase Space

The general shape of the electron energy distribution from neutron beta decay is defined by the phase space density ρ_0 (see equation 1.11).

$$\rho_0\left(E_e\right) = \left(E_0 - E\right)^2 E_e p_e. \tag{2.1}$$

This basic description of the decay phase space demands additional correction due to the interaction of charged decay products which are discussed in the following sections.

2.1.1 Coulomb Interaction

The change in phase space due to the coulomb potential of the proton is accounted for by the relativistic Fermi function [IPT13]

$$
F_R\left(E_e, Z=1\right) = \frac{2\left(1+\gamma\right)}{\Gamma\left(1+2\gamma\right)^2}\left(2r_p p_e \hbar\right)^{2(\gamma-1)} e^{\frac{\pi\alpha E_e}{cp e}}\left|\Gamma\left(\gamma+\frac{i\alpha}{cp_e}\right)\right|^2,
$$

$$
\text{with } \gamma = \sqrt{1+\alpha^2} \text{ and } \alpha = \frac{1}{137.036},
$$

(2.2)

whith the proton radius r_p and the electron momentum p_e. This changes the phase space density to $\rho\left(E_e\right) = \rho_0\left(E_e\right) F_R\left(E_e\right)$.

Previously, the non-relativistic approximation of the Fermi function has been used [Wil82; Rei99],

$$
F_{NR}\left(E_e, Z=0\right) = \frac{2\pi\alpha}{\beta\left(E_e\right)\left(1-e^{-\frac{2\pi\alpha}{\beta(E_e)}}\right)}.
$$

(2.3)

The deviation to the relativistic Fermi function results in an underestimation of the correction on the level of 10^{-3}.

In [Wil82] an estimate for the correction of the Fermi function to account for the proton recoil and thus the movement of the source field is derived. This is done by modifying $\beta\left(E_e\right)$ by adding the projection of the protons mean velocity along the electron direction to the electron velocity

$$
\beta\left(E_e\right) \rightarrow \beta\left(E_e\right) + \sqrt{\frac{E_e^2 + m_e^2}{m_e m_p}}\left(1 + \frac{1-\lambda^2}{1+3\lambda^2}\frac{E_0 - E_e}{3\left(E_e + m_e\right)}\right).
$$

(2.4)

Calculating these corrections using $\lambda = -1.2748$ one finds that the corrections to the Fermi function are $< 5 \cdot 10^{-5}$ for all possible electron energies.

The current deviation between the proton charge radius measured via proton-electron scattering and atomic energy levels with $r_p = 0.8751\,(61)$ fm on the one hand and the recent measurements of the lamb shift in muonic hydrogen with $r_p = 0.84087\,(39)$ fm [Poh+10; Ant+13] on the other hand, turns out to be uncritical as it gives a $2 \cdot 10^{-6}$ uncertainty in the value of the Fermi function.

2.1.2 Recoil Order Corrections

The Hamiltonian of the neutron decay as given in equation 1.7 is incomplete. Although only vector and axialvector couplings participate, additional terms need to be considered describing induced couplings resulting from the vector current conservation. When
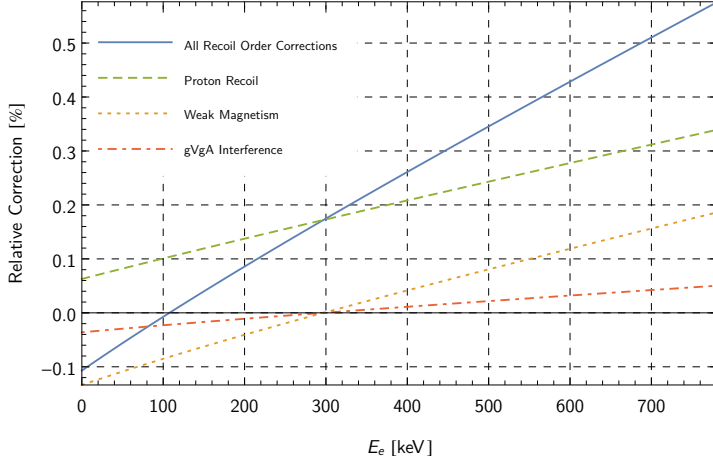
Fig. 2.1: Recoil order corrections to the electron phase space in neutron beta decay.

including these terms the hadronic currents in the Hamiltonian become [Hol74]:

$$
\begin{aligned}
J_\mu^{V,\text{hadr}}(x) &= G_F V_{ud} \bar\psi_p(x) \left\{ g_V \gamma_\mu + \frac{1}{2M} \left(g_{IS} q_\mu - i \left(g_M - g_V \right) \sigma_{\mu\nu} q^\nu \right) \right\} \psi_n(x), \\
J_\mu^{A,\text{hadr}}(x) &= G_F V_{ud} \bar\psi_p(x) \left\{ g_A \gamma_\mu \gamma^5 + \frac{1}{2M} \left(g_{IP} q_\mu \gamma^5 - i g_{IT} \sigma_{\mu\nu} q^\nu \gamma^5 \right) \right\} \psi_n(x),
\end{aligned}
\tag{2.5}
$$

where $M = (m_n + m_p)/2$ is the mass scale characteristic to the decay process. The first term of the hadronic currents describes the conventional vector and axialvector contributions. For the induced scalar coupling the assumption of strong conservation of the vector current implies that $g_{IS} = 0$. For the weak magnetism we get from the same assumption that

$$
g_{WM} = \frac{\mu_p^a - \mu_n^a}{2M} = \frac{\kappa}{2M}
\tag{2.6}
$$

where μ_p^a, μ_n^a are the anomalous magnetic moments of the proton and neutron, respectively [Wil82]. The induced tensor coupling constant is a so called second class current and it follows $g_{IT} = 0$ [CB83]. The resulting corrections as given in [Wil82] are:

Proton Recoil

$$
R_{Recoil}(W) = \frac{1}{(1 + 3\lambda^2) M} \left(2W + \lambda^2 \left(10W - \frac{2}{W} - 2W_0 \right) \right),
\tag{2.7}
$$

Weak Magnetism

$$
R_{WM}(W) = \frac{1}{(1 + 3\lambda^2) M} \left(2\lambda\kappa \left(2W_0 - 4W + \frac{2}{W} \right) \right),
\tag{2.8}
$$

$g_V - g_A$ **Interference**

$$R_{g_V - g_A}(W) = \frac{1}{(1 + 3\lambda^2) M} \left(\lambda \left(2W_0 - 4W + \frac{2}{W} \right) \right), \qquad (2.9)$$

with $W = (E_e + m_e) / m_e$ and $W_0 = (E_0 + m_e) / m_e$. These results are the same as given in [IPT13]. As shown in figure 2.1, the most dominant contribution is the proton recoil correction followed by the weak magnetism. The change to the measured decay rate is on the order of 10^{-3}.

The potential uncertainty of limiting the corrections to leading order $1/M$ is checked by including corrections of order $1/M^2$ for Proton Recoil as given in [Wil82].

$$R_{Recoil2}(W) = \frac{1}{(1 + 3\lambda^2) M^2} \left(\left(\frac{W_0^2}{2} - \frac{11}{6} + \frac{W_0}{3W} - \frac{4W_0 W}{3} + \frac{16W^2}{3} \right) \right.$$
$$\left. . + \lambda^2 \left(-\frac{W_0^2}{2} - \frac{77}{6} + \frac{7W_0}{3W} - \frac{28W_0 W}{3} + \frac{88W^2}{3} \right) \right). \qquad (2.10)$$

The contribution of these corrections is on the order of 10^{-6} and can be neglected.

2.1.3 Radiative Corrections

According to [Sir67; GT92] the radiative corrections can be separated into different contributions each being handled separately:

- Model independent part / "outer" radiative corrections (virtual photon exchange in external fermion lines)

- Model independent part / Bremsstrahlung

- Model dependent part / "inner" radiative corrections (virtual photon exchange on internal lines, depending on strong interaction)

- Coulomb interaction between final states of electron and proton (non-virtual photon exchange)

The radiative corrections account for higher order interactions involving photon exchange between the hadronic and fermionic currents. According to [Sir67] they may be separated into the model independent corrections, that are independent of the details of the strong interaction and a model-dependent part. When restricted to order-α this second part, also called "inner" radiative corrections, leads to contributions similar to those of the vector and axialvector couplings and may be absorbed in the usage of effective couplings constants

$$g'_v = g_v \left(1 + \frac{\alpha}{2\pi} Re(c) \right) \text{ and } g'_A = g_A \left(1 + \frac{\alpha}{2\pi} Re(d) \right) \qquad (2.11)$$

where c, d represent the contributions due to radiative corrections [Sha71]. These relative corrections are on the percent level and it is known that c and d are of similar order. They

modify the amplitude of the coupling constants and thus the neutron decay rate, though. The measured value of $\lambda = g_A/g_V$ inherently contains these corrections.

The model independent part on the other hand can be separated into the "outer" photonic corrections which describe the virtual photon exchange in external fermion lines and Bremsstrahlung.

As for the model independent part of the radiative corrections, an analytical expression for the correction of the electron phase space volume in unpolarised neutron decay has been derived considering contributions of order α [Sir67]

$$
\begin{aligned}
g(E_e) = {} & 3\ln\left(\frac{m_p}{m}\right) - \frac{3}{4} - \frac{4}{\beta}L_2\left(\frac{2\beta}{1+\beta}\right) \\
& + 4\left(\frac{\tanh^{-1}(\beta)}{\beta} - 1\right)\left(\ln\left(\frac{2(E_0 - E_e)}{m}\right) - \frac{3}{2} + \frac{E_0 - E_e}{3E_e}\right) \\
& + \frac{\tanh^{-1}(\beta)}{\beta}\left(2\left(1 + \beta^2\right) + \frac{(E_0 - E_e)^2}{6E^2} - 4\tanh^{-1}(\beta)\right),
\end{aligned}
\tag{2.12}
$$

which transforms the differential neutron decay rate as

$$
\mathrm{d}\Gamma_n = \frac{G_F^2\left|V_{ud}\right|^2}{32\pi^5}\left(1 + 3\lambda^2\right)\left(1 + \frac{\alpha}{2\pi}g(E_e)\right)\rho\left(E_e\right)\mathrm{d}E_e.
\tag{2.13}
$$

The overall effect on the decay rate due to the "outer" radiative corrections is 1.5 %. The theoretical uncertainty of the model-independent corrections is given by the missing higher order contributions which are yet to be calculated. However, a further suppression of order α would lead to contributions of order $1 \cdot 10^{-4}$.

This provides the dominant limit on the achievable precision for the calculation of the electron decay spectrum both integral and spectrally. Thus only corrections at or above $\mathcal{O}\left(10^{-4}\right)$ are considered for the corrected differential neutron decay probability. Other contributions given in [Wil82] as the effect due to lepton-nucleon convolution can be neglected.

The corrected neutron decay phase space then becomes

$$
\begin{aligned}
\mathrm{d}\Gamma_n = {} & \frac{G_F^2\left|V_{ud}\right|^2}{32\pi^5}\left(1 + 3\lambda^2\right)(E_0 - E_e)^2\,E_e p_e \\
& \times F\left(E_e, Z = 1\right)\left(1 + R\left(E_e\right)\right)\left(1 + \frac{\alpha}{2\pi}g\left(E_e\right)\right)\mathrm{d}E_e
\end{aligned}
\tag{2.14}
$$

$$
\text{with } R\left(E_e\right) = R_{Recoil}\left(E_e\right) + R_{WM}\left(E_e\right) + R_{g_V g_A}\left(E_e\right).
$$

A comparison of the uncorrected and corrected neutron decay spectrum is shown in figure 2.2.
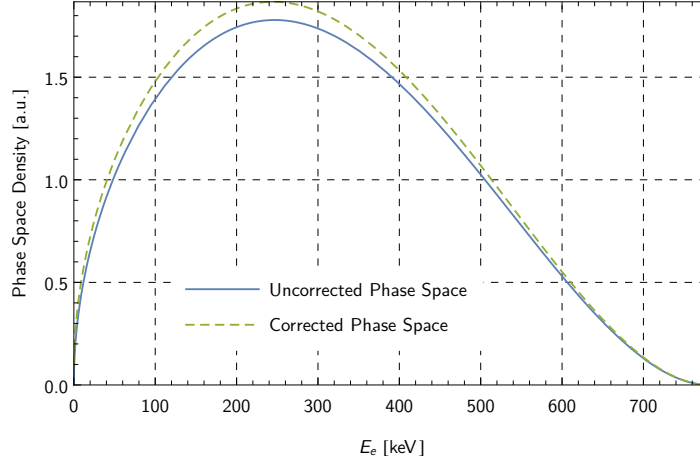
Fig. 2.2: Comparison of the electron phase space density in neutron decay with and without corrections applied.

2.2 The Experimental Beta Asymmetry

The measured spectrum used to extract the beta asymmetry is the experimental beta asymmetry as given in equation 1.19

$$A_{\exp}\left(E_e\right) = \frac{N^{\uparrow}(E_e) - N^{\downarrow}(E_e)}{N^{\uparrow}(E_e) + N^{\downarrow}(E_e)} = \frac{1}{2} A P_n \beta\left(E_e\right). \tag{2.15}$$

As the denominator basically represents an unpolarised neutron decay spectrum the same corrections apply as for the neutron decay phase space discussed in section 2.1. The relative corrections for the Coulomb interaction between the electron and proton are the same for both spin directions. Therefore the correction due to the Fermi-function cancels completely when performing a spectral analysis [1]. However, the vector and axial-vector contribution of the decay amplitudes are weighted differently in the numerator spectrum. This leads to different contributions from the recoil order and radiative corrections which do not cancel.

2.2.1 Recoil Order Corrections

The recoil order corrections discussed in section 2.1.2 for the experimental beta asymmetry become [Wil82]

---

[1]Note that if a non-spectral analysis of the Experimental Asymmetry is performed (i.e. only the integral counts of $N^{\uparrow}$ and $N^{\downarrow}$ are used) the correction for the Coulomb term needs to be considered and depending on the energy region actually changes the sign of the combined correction for Coulomb interaction and the radiative corrections.
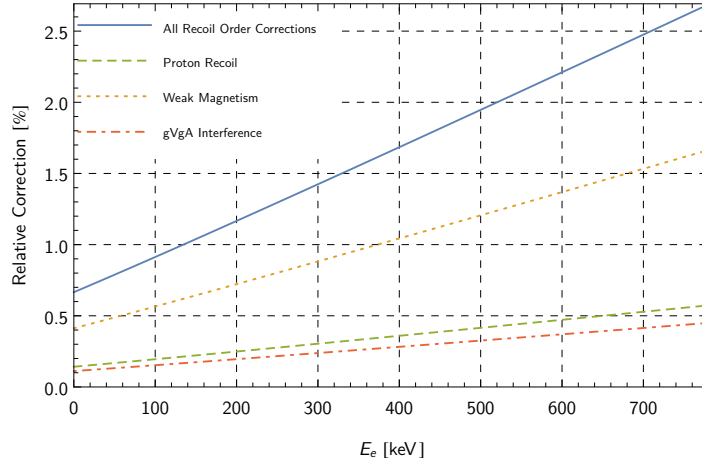
Fig. 2.3: Recoil order corrections to the experimental beta asymmetry.

Proton Recoil

$$R_{Recoil}(W) = \frac{\lambda}{\lambda(1+\lambda)(1+3\lambda^2)M} R_0(W),$$

$$\text{with } R_0(W) = \left(\lambda^2 - \frac{2}{3}\lambda - \frac{1}{3}\right)W_0 + \left(\lambda^3 - 3\lambda^2 + \frac{5}{3}\lambda + \frac{1}{3}\right)W + \frac{2\lambda^2(\lambda+1)}{W},$$

$$(2.16)$$

Weak Magnetism

$$R_{WM}(W) = \frac{-2\kappa}{\lambda(1+\lambda)(1+3\lambda^2)M} R_0(W), \qquad (2.17)$$

$g_V - g_A$ **interference**

$$R_{g_V-g_A}(W) = \frac{-1}{\lambda(1+\lambda)(1+3\lambda^2)M} R_0(W). \qquad (2.18)$$

The resulting corrections are shown in figure 2.3. The shape of these corrections is identical due to their common energy dependence $R_0(W)$. They increase the measured experimental beta asymmetry by 1 - 2.5 % depending on the energy window of the analysis. This consideration leads to an expected uncertainty of $\mathcal{O}(10^{-5})$ induced by neglecting the second order of the corrections.

2.2.2 Radiative Corrections

Similar to the $\mathcal{O}(\alpha)$ radiative correction to the decay phase space of an unpolarised neutron the corrections for a polarized neutron become [Sha71]

$$
\begin{aligned}
\rho\left(E_e\right) = \rho_0\left(E_e\right) \frac{1}{1+3\lambda^2} & \left[\left(1+3\lambda^2\right)\left\{1+\frac{\alpha}{2\pi}g(E_e)\right\}\right. \\
& \left. + \lambda\left(1-\lambda\right)P_n\beta\left(E_e\right)\cos\left(\theta\right)\left\{1+\frac{\alpha}{2\pi}h\left(E_e\right)\right\}\right].
\end{aligned}
\tag{2.19}
$$

Here $g(E_e)$ accounts for the common part for both spin directions and is the same as for the unpolarised spectrum (compare equation 2.12). $h(E_e)$ on the other hand accounts for the spin-dependent part of the decay rate and is given by [Sha71]

$$
\begin{aligned}
h\left(E_e\right) = 3\ln\left(\frac{m_p}{m_e}\right) & - \frac{3}{4} + 4\left(\frac{\tanh^{-1}\left(\beta\right)}{\beta} - 1\right) \\
& \times \left(\ln\left(\frac{2\left(E_0-E_e\right)}{m_e}\right) - \frac{3}{2} + \frac{E_0-E_e}{3E_e\beta^2} + \frac{\left(E_0-E_e\right)^2}{24E_e^2\beta^2}\right) \\
& + 4\frac{\tanh^{-1}\left(\beta\right)}{\beta}\left(1 - \tanh^{-1}\left(\beta\right)\right) - \frac{4}{\beta}L_2\left(\frac{2\beta}{1+\beta}\right).
\end{aligned}
\tag{2.20}
$$

These contributions modify the experimental beta asymmetry:

$$
\begin{aligned}
A_{\exp}\left(E_e\right) = \frac{N^{\uparrow}(E_e) - N^{\downarrow}(E_e)}{N^{\uparrow}(E_e) + N^{\downarrow}(E_e)} & = \frac{\lambda\left(1-\lambda\right)}{1-3\lambda^2}P_n\beta\left(E_e\right)\frac{1+\frac{\alpha}{2\pi}h\left(E\right)}{1+\frac{\alpha}{2\pi}g\left(E\right)} \\
& \simeq A_{exp,0}\left(E_e\right)\cdot\left(1+\frac{\alpha}{2\pi}g(E_e) - \frac{\alpha}{2\pi}h(E_e)\right) \\
& = A_{exp,0}\left(E_e\right)\cdot\left(1+\frac{\alpha}{\pi}f(E_e)\right),
\end{aligned}
\tag{2.21}
$$

with a common function $f(E_e)$ to account for the radiative corrections. Using equations 2.12 and 2.20 an analytical expression for $f(E_e)$ can be calculated as

$$
\begin{aligned}
2\cdot f\left(E_e\right) = h\left(E_e\right) & - g\left(E_e\right) \\
& = 4\left(\frac{\tanh^{-1}\left(\beta\right)}{\beta} - 1\right)\left(\frac{E_0-E_e}{3E_e\beta^2}\left(1+\frac{E_0-E_e}{8E_e}\right) - \frac{E_0-E_e}{3E_e}\right) \\
& - \frac{\tanh^{-1}\left(\beta\right)}{\beta}\left(2\left(1+\beta^2\right) + \frac{\left(E_0-E_e\right)^2}{6E_e^2} - 4\right),
\end{aligned}
\tag{2.22}
$$

which is in agreement with the expression given in [IPT13]. The correction to the experimental beta asymmetry is shown in figure 2.4. The effect is on the lower 10^{-3} level, increasing the absolute value of the measured beta asymmetry.

The analytical results obtained using equation 2.22 are in agreement with the numerical calculations performed in [GT92]. Within this thesis it has been found that the radiative corrections have been applied with opposite sign in previous publications. This is already
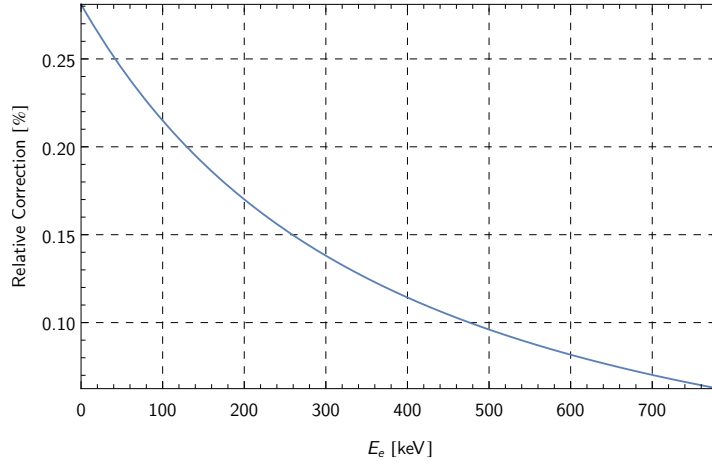
Fig. 2.4: $\mathcal{O}(\alpha)$ radiative corrections to the experimental beta asymmetry calculated according to equation 2.22.
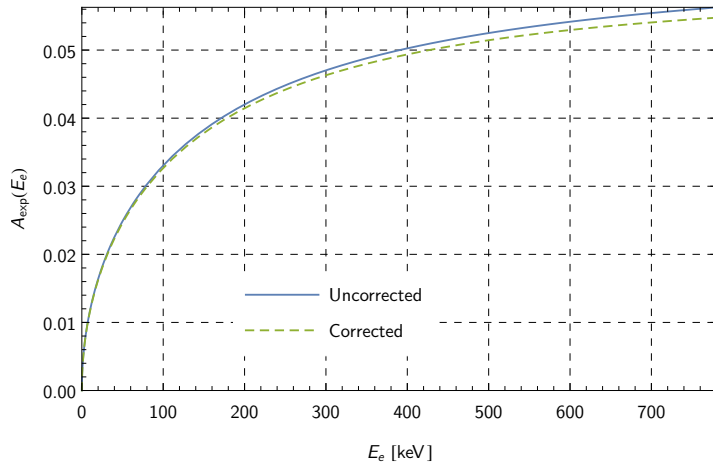
Fig. 2.5: Experimental beta asymmetry without any corrections and including radiative and recoil order corrections.

corrected in the most recent publication of the PERKEO II collaboration [Mun+13].

For the uncertainty of the radiative corrections, the expected amplitude of $\mathcal{O}(\alpha^2)$-corrections need to be considered. This would lead to a suppression by two orders of magnitude. However, the amplitude of the current correction is the result of two contributions which appear to cancel at the level of 10%. This is not necessarily the case for higher orders. Therefore, the conservative assumption of a $1 \cdot 10^{-4}$ uncertainty is made.

Figure 2.5 compares the experimental beta asymmetry without any corrections applied and including the radiative and recoil order corrections. While the correction is dominated by recoil order corrections the dominant uncertainty for the theoretical corrections to the experimental beta asymmetry is given by the 10^{-4} uncertainty of the radiative corrections.

Chapter 3

The Spectrometer Perkeo III

The spectrometer PERKEO III has been developed in 2006 with the aim to measure several correlation coefficients in neutron beta decay [Mär06]. In this chapter the basic principles of the PERKEO spectrometer are outlined, with a focus on the setup as used during the measurement of the beta asymmetry A in 2009. A more detailed description of the setup can be found in [Mes11; Wan13].

3.1 Operation principle of Perkeo III
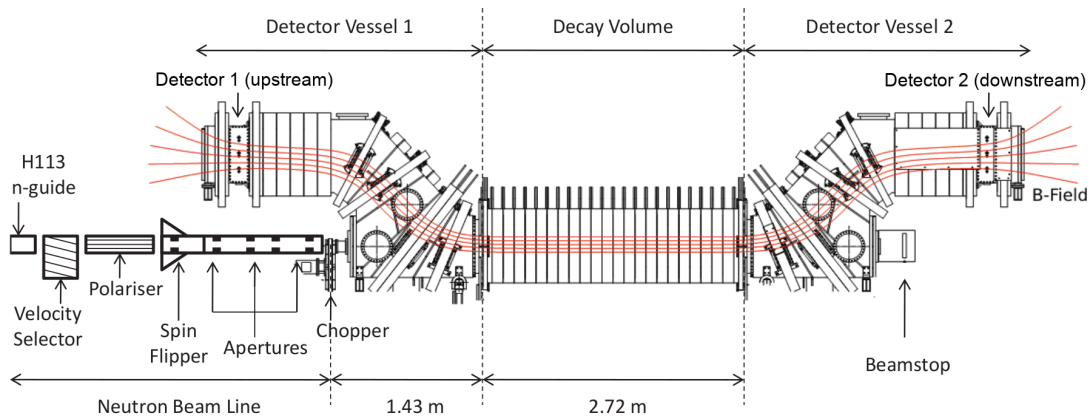
Fig. 3.1: Sketch of the PERKEO III experimental setup as utilized during the measurement of the beta asymmetry in 2009. The sketch shows the neutron beam preparation part of the setup and the main spectrometer including the magnetic field lines (indicated by the red lines) which guide the decay electrons to the detectors.

Figure 3.1 shows a sketch of the full setup as used during the 2009 beam time to measure the beta asymmetry. The setup can be separated into two major parts, the neutron beamline and beam preparation, and the spectrometer itself.

A beam of cold neutrons from the ILL reactor source (see section 3.2), guided by the neutron guide H113, features the source of neutrons that decay inside the spectrometer. The velocity distribution of neutrons inside the beam is filtered before entering the setup. Afterwards the beam is polarized using a polarisation sensitive transmission filter. An additional spin flipper allows to switch the direction of neutron polarisation by 180°. The last part of the beam preparation consists of a collimation system featuring five LiF

apertures and a mechanical disc chopper that allows to create a pulsed neutron beam. This pulsed beam enters the main spectrometer where a fraction of about 10^{-6} of these neutrons decay. The remaining neutrons are absorbed in a neutron beam stop made of enriched $^{10}\mathrm{B}_4\mathrm{C}$.

The spectrometer itself consists of a vacuum vessel build from non-magnetic, stainless steel with a residual pressure of 10^{-6} to 10^{-7} mbar and is surrounded by normal conducting coils that provide a curved magnetic field. Within the central part of the spectrometer the magnetic field is designed to be homogeneous and features the highest magnitude of 150 mT. The function of the field in this region is to provide a quantisation axis for the neutron spin, meaning that the spin of the neutrons is either aligned parallel of antiparallel to the magnetic field lines. At the same time the charged decay products will gyrate around and follow the magnetic field lines and are guided to the electron detectors.

Due to the homogeneous nature of the field in the central region of the spectrometer, electrons are guided to the detector which is placed in the direction of their initial emission. This effectively provides a separation into two half-spaces with respect to the neutron spin and allows to measure the electron distributions $N^{\uparrow,\downarrow}(E_e)$ for each spin direction separately and calculate the experimental beta asymmetry

$$A_{exp}(E_e) = \frac{N^{\uparrow}(E_e) - N^{\downarrow}(E_e)}{N^{\uparrow}(E_e) + N^{\downarrow}(E_e)}. \tag{3.1}$$

Using spectra from two detectors to calculate the experimental asymmetry is very challenging because an identical energy calibration of the two detectors is hard to achieve. To this end a spin flipper is applied to flip the direction of the neutron spin every ten seconds. Since the flight time of neutron through the setup is only about 7 ms, the necessary $N^{\uparrow,\downarrow}$ spectra are available for both detectors. This allows to calculate the experimental beta asymmetry for each detector individually.

Besides the fact that using two detectors increases the amount of recorded events by a factor of 2, the application of the symmetric two detector design allows to minimize systematic effects due to the remaining inhomogeneity of the magnetic field (Magnetic Mirror Effect), electron backscattering and noise related detector systematics. For this reason all instruments of the PERKEO series apply this principle.

3.2 Reactor source and guide

The measurements performed with PERKEO III take place at the PF1B beamsite at the neutron research centre Institut Laue-Langevin (ILL) in Grenoble. The reactor of the ILL features a thermal power of 54 MW and provides the most intense neutron source in the world. These neutrons are provided with different thermal properties (or velocities) to about 40 instruments specialized for a variety of research applications such as condensed and soft matter physics, magnetism, biology, nuclear and "fundamental" physics.

Cold neutrons, as used with PERKEO III, are created by cooling down thermal neutrons from the reactor moderator ($T \simeq 300$ K, $v \simeq 2200$ m/s) with a liquid hydrogen moderator to temperatures of $T = 40$ K ($v \simeq 800$ m/s). Due to their large wavelength of about 5 Å, these neutrons can be guided over distances of several 10 m using glass tubes with a

reflective coating. Traditionally, these coatings are made from Nickel that provides a very high reflectivity under small angles of incidence or from multiple materials in a multilayer structure that provide a slightly smaller reflectivity for but for larger angles of incidence.

The H113 neutron guide which provides neutrons to the PF1B has been installed at the ILL in 2000 [Häs+02]. It is the first so called ballistic supermirror guide that allows to benefit from a large acceptance of beam divergence of supermirrors even for longer cold neutron guides by significantly reducing the number of reflections [Abe+06]. The guide has a length of 74 m and a cross-section of 6×20 cm^2.

The capture flux[1] provided at the exit of the guide is $\Omega_c = 1.35 \cdot 10^{10}$ cm^{-2}s^{-1} making PF1B the strongest source of cold neutrons in the world.

In addition to the neutron guide PF1B features several options for beam preparation including a velocity selector and a polariser.

3.3 Neutron beam

After exiting the neutron guide the neutrons pass the beam preparation section (compare figure 3.1). The design and characterisation of the beamline are discussed in [Wer09]. A simulation of the resulting neutron beam profile inside the spectrometer is performed in [Wan13]. The main components of the beam preparation are:

Neutron Velocity Selector
The neutron guide H113 provides a broad spectrum of neutron velocities. When using a pulsed neutron beam this is detrimental as the longitudinal spread of the pulse would be very large. To this end only a certain wavelength range around the maximum of the spectrum is selected by the velocity selector which is a turbine of neutron absorbing blades. The selected wavelength region is $4.4 < \lambda < 5.6$ Å [Wan13].

Supermirror Polariser
The neutrons are polarized by applying a so called bender supermirror polariser. This device consists of multiple sheets parallel to the beam direction, which have a supermirror coating similar to that used for the neutron guide. A special feature of this particular coating is that the reflectivity is spin-dependent. The sheets, which are spaced by 2 mm, are bent such that the neutrons make at least two reflections when passing the system. This way neutrons with the "wrong" spin direction have a very low transmission probability, leaving a polarized neutron beam. The system used at PF1B has a length of 80 cm and is specified to achieve a beam polarisation of > 98 % [Sol+02].

Spin Flipper
In order to flip the neutron spin as described in section 3.1, an adiabatic resonance spin flipper is used [Baz+93]. In this system a static inhomogeneous magnetic field

---

[1]The capture flux is defined as the particle flux weighted by the inverse velocity of the neutrons normalized to the velocity of thermal neutrons and is common to account for the $1/v$-dependence of interaction cross-sections.

$\boldsymbol{B}_0(z)$ and perpendicular to it a rotating magnetic field $\boldsymbol{B}_{rot}$ with frequency ω are applied. The rotating frequency ω is chosen equal to the Larmor frequency of the neutron in the field $\boldsymbol{B}_0(z)$

$$\boldsymbol{\omega}_L = -\gamma_n \boldsymbol{B}_0, \tag{3.2}$$

where $\gamma = 1.83 \cdot 10^8 \ \mathrm{s}^{-1}\mathrm{T}^{-1}$ is the gyromagnetic ratio for the neutron. In the rotating frame moving with the neutron, the effective magnetic field becomes

$$\boldsymbol{B}_{\mathrm{eff}}(t) = \boldsymbol{B}_0(t) - \boldsymbol{\omega}/\gamma + \boldsymbol{B}_{rot}. \tag{3.3}$$

At the beginning, the spin of the neutron is oriented parallel to $\boldsymbol{B}_0(z = z_0)$. If the adiabatic condition $\mathrm{d}B\mathrm{d}t \ll \gamma B^2$ is met the neutron spin will follow the direction of B_{eff} when passing the flipper and is reversed at the end of the flipping region [LT84].

Collimation System
The typical divergence of the neutron beam delivered by the neutron guide H113 is $\theta \geq 7$ mrad (FWHM) [Abe+06]. The off-axis dimensions of the neutron beam within the spectrometer are critical for several aspects. Ideally, the neutron beam is confined in a region where the magnetic field is homogeneous in the central decay volume. This also ensures that the electrons emerging from neutron decay are transported to the detectors without making contact with the vacuum vessel, which would distort the measured data.

In order to limit the dimensions of the neutron beam which passes freely through the PERKEO III spectrometer, a collimation system of five LiF apertures with a diameter of $6 \times 6 \ \mathrm{cm}^2$ with a total length of 3.2 m is used before the neutron beam enters the spectrometer. Within the central region of the spectrometer this results in a beam with a cross-section of $10 \times 10 \ \mathrm{cm}^2$.

Rotating Disc Chopper
In order to create a pulsed neutron beam a Rotating Disc Chopper is used. This chopper consists of a disc with neutron absorbing plates made of ^{6}LiF attached to it. An opening window of 22.11 deg allows the neutrons to pass through the disc with a defined frequency f_{Ch} while the disc rotates.

The design of the chopper and the characterisation of the resulting neutron pulses are discussed in [Wer09]. During the measurement of the beta asymmetry two chopper frequencies, 94 Hz and 83 Hz, have been used.

Beamstop
After passing the spectrometer the neutrons are absorbed by the beamstop. Initially a ^{6}LiF tile was used which has been changed to a tile of ^{10}B$_4$C. While ^{6}Li produces no gamma background a high amount of secondary fast neutrons is generated. The delayed emission of these neutrons disturbs the background measurement within the background time window [Mes11]. ^{10}B on the other hand has a much lower probability to emit fast neutrons but produces a high gamma intensity. The detection of these gammas in the electron detectors produces the pronounced peak in the

count rate at around 8 ms in figure 3.2. Since the emission of these gammas is instantaneous they do not affect the background measurement.

3.3.1 Using a pulsed beam to minimize background systematics

During previous measurements with PERKEO II, background has been determined by performing separate measurements with the shutter of the neutron beamline closed paired with a continuous monitoring of the environmental background by additional detectors. A second background contribution that is created by the neutrons passing the beamline and spectrometer is estimated by analysing the measured spectra beyond the electron endpoint energy and comparing measurements with and without magnetic field [Mun+13]. The resulting uncertainty due to detector background for the measurement of the beta asymmetry is $\Delta A/A = 1.0 \cdot 10^{-3}$.

Using a continuous beam, the neutron decay rate within the PERKEO III spectrometer is $50 \cdot 10^3$ s^{-1} [Mär+09]. This is due to the fact that neither the velocity selector nor the rotating disc chopper are used. In this case detector background needs to be determined by additional measurements to obtain the clean electron spectra required for the experimental beta asymmetry.
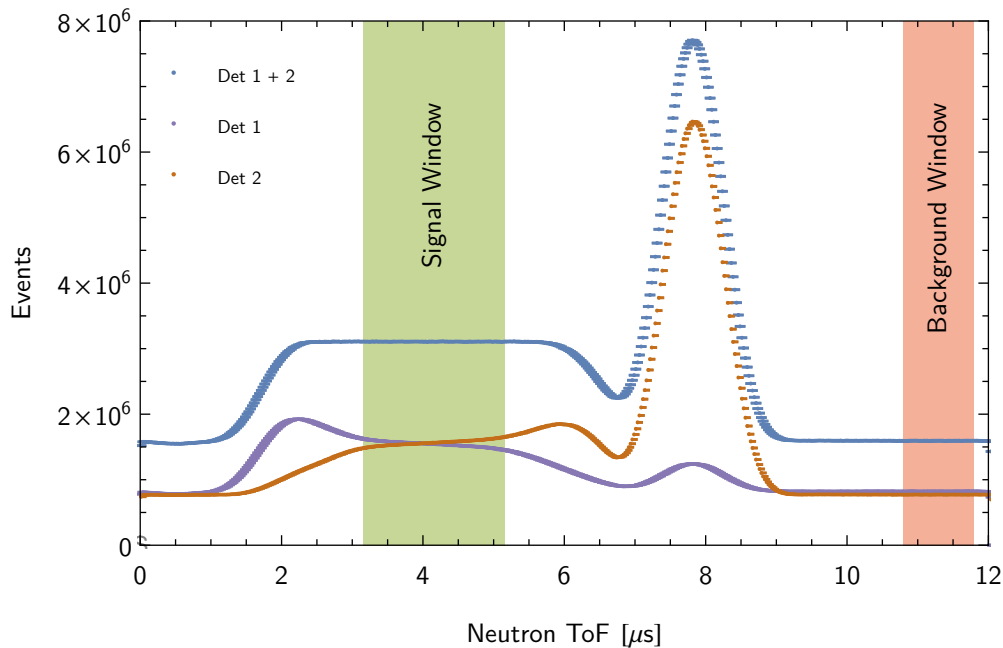
Fig. 3.2: Time-of-flight dependence of the detector count rates for detector 1 and 2.

For PERKEO III the scheme to determine the detector background is changed significantly by applying the pulsed beam method [Mär+09]. Figure 3.2 shows the number of events detected versus the time-of-flight of the neutrons inside the spectrometer. For the extraction of the electron spectra required to calculate the experimental beta asymmetry only events detected within a time window of 2 ms when the neutron beam is fully
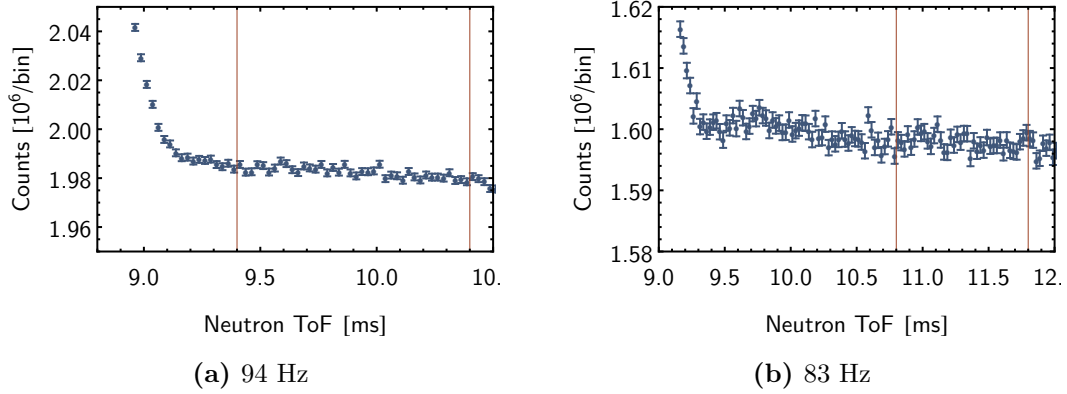
(a) 94 Hz

(b) 83 Hz

Fig. 3.3: Time-of-flight dependence of the count rate of detector 2 for both chopper frequencies. The red lines indicate the time windows used to extract the background spectra. The data is extracted with an energy cut of about 300-700 keV which corresponds to the energy window used in the analysis of the experimental beta asymmetry.

contained within the central decay volume are selected. Depending on the chopper frequency, these time windows have been chosen to minimize the systematic effect due to the magnetic field structure (see section 3.4.1)

$$
\begin{aligned}
3100 - 5100 \ \mu\text{s} \quad &(94 \text{ Hz}), \\
3150 - 5150 \ \mu\text{s} \quad &(83 \text{ Hz}).
\end{aligned}
\tag{3.4}
$$

Background is measured in another time window after the neutrons are absorbed completely in the neutron beamstop. This background contains environmental background as well as all background created in the neutron beamline and can be measured simultaneously with a time delay of a few ms only.

Figure 3.3 shows the detector count-rates after the absorption of neutrons in the beamstop. Even after the switch to $^{10}\text{B}_4\text{C}$ as absorber material (see section section 3.3) the structure of the count-rate is not perfectly constant for detector 2 which is closer to the beamstop. Potential reasons for this behaviour are delayed background components from the beamstop due to backscattered neutrons, the delayed emission of alpha particles or fast neutrons. In section 8.2 the impact of this effect on the beta asymmetry is shown to be on the order of $\Delta A/A = 1 \cdot 10^{-4}$.

To reduce the effect of the delayed background from the beamstop, the time-of-flight windows are chosen to be as late as possible. The chosen background time-windows for the analysis are

$$
\begin{aligned}
9400 - 10400 \ \mu\text{s} \quad &(94 \text{ Hz}), \\
10800 - 11800 \ \mu\text{s} \quad &(83 \text{ Hz}).
\end{aligned}
\tag{3.5}
$$

These time windows are slightly shifted compared to the ones used in [Mes11].

Due to the fact that the neutrons pass freely through the spectrometer before hitting the beamstop the only background component left, that is not covered by this measurement,

is the background created due to the chopper itself. The contribution of this background is estimated in section 8.2.

By applying the pulsed beam method, the overall uncertainties due to the detector background are reduced to a level of $\Delta A/A = 2 \cdot 10^{-4}$. Thanks to the longitudinal design of the magnetic field, which allows to dramatically increase the size of the decay volume, the instantaneous rate of detected decay events is still 10^3 s^{-1} which is a factor of three larger than that achieved with PERKEO II.

3.4 The spectrometer Perkeo III and its magnetic field
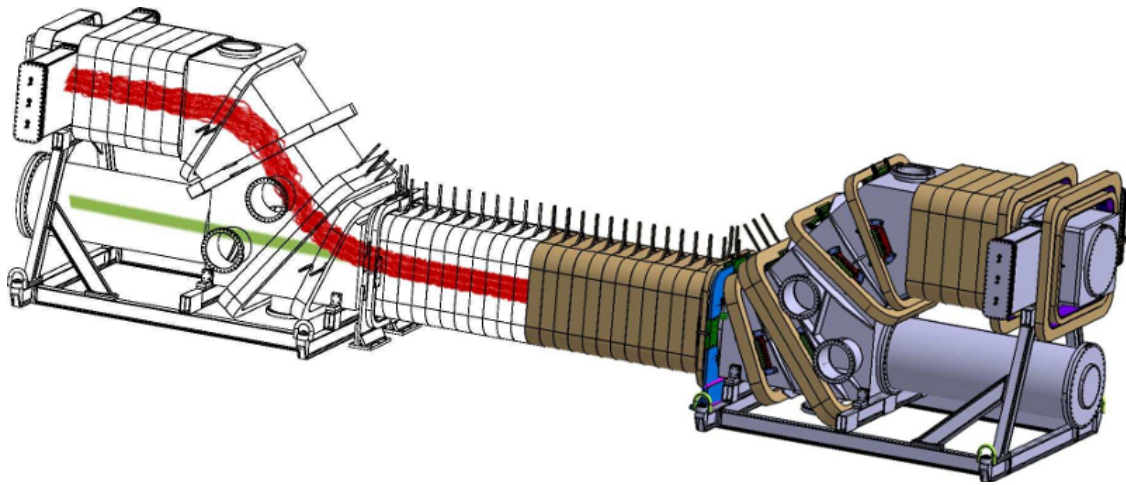
Fig. 3.4: The spectrometer PERKEO III. The image shows the coil system (brown) and vaccum vessel (blue). On the left side of the picture the neutron beam is shown as green line and the electron trajectories are indicated as red lines.

Figure 3.4 shows a model of the PERKEO III spectrometer. The main components of the spectrometer are a vacuum vessel with a vacuum of $10^{-6} - 10^{-7}$ mbar, pumped using two turbo molecular pumps, and the coil system consisting of 50 water cooled, normal conducting coils. The operating current for the nominal magnetic field strength is 600 A which is supplied by two power supplies. The total power consumption of the system is about 350 kW, most of which is lost as thermal power by the coils. Since the coils are operated in series the current is the same in all coils. The geometry of the magnetic field is thus solely given by the layout and design of the individual coils. The development of the spectrometer and optimisation of its general layout are discussed in [Mär06].

The spectrometer consists of three parts, the central solenoid, containing the main decay volume, and the two detector vessels. A cross section is shown in figure 3.1.

3.4.1 Central Solenoid

The central solenoid has a length of 2.7 m. The coils have a cross section of 60×60 cm^2 and the diameter of the vacuum vessel is 50 cm. The solenoid geometry provides a

homogeneous magnetic field with the highest magnetic field strength of 152 mT. The homogeneity of the field is critical in order to minimize corrections and uncertainties of the measurement due to the magnetic field.

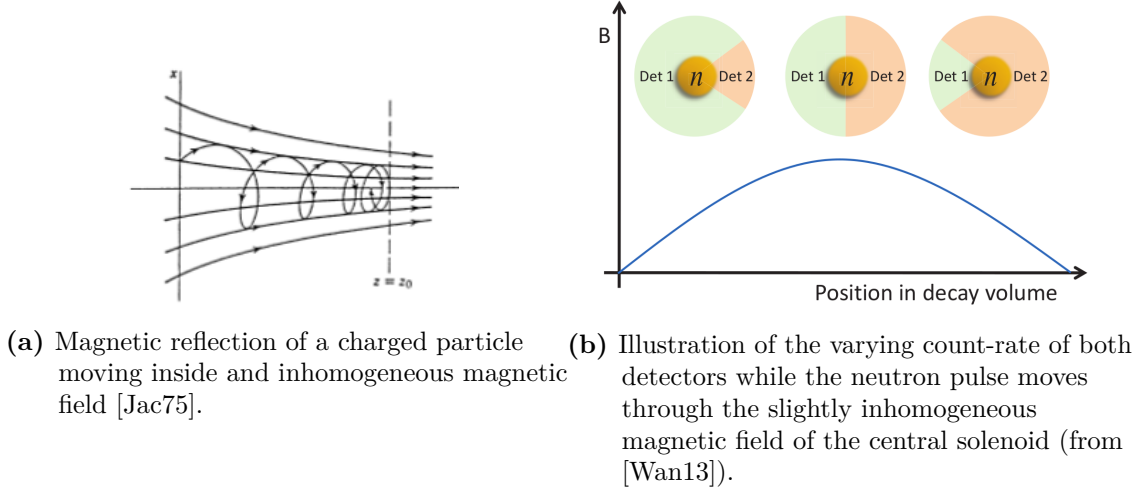**(a)** Magnetic reflection of a charged particle moving inside and inhomogeneous magnetic field [Jac75].

(b) Illustration of the varying count-rate of both detectors while the neutron pulse moves through the slightly inhomogeneous magnetic field of the central solenoid (from [Wan13]).

Fig. 3.5: Illustration of a magnetic reflection of a charged particle inside an inhomegeneous magnetic field (a). This leads to a different solid angles for electrons created in different positions of the decay volume (b).

For particles moving towards an increasing magnetic field, their critical angle of emission perpendicular to the magnetic field lines is given by [Wan13]

$$\theta_c = \arcsin\left(\sqrt{B(z_0)/B_{max}}\right), \tag{3.6}$$

where $B(z_0)$ is the magnetic field strength at the point z_0 of particle emission and B_{max} is the maximum magnetic field strength. For particles emitted in lower field regions of the spectrometer this leads to potential reflections at the point of maximum field strength, which is in the centre of the central solenoid, if their initial angle relative to the magnetic field vector is larger than θ_c. Due to this effect the count rates of the detectors vary while the neutron pulse moves through the central solenoid, leading to a higher count rate if the pulse is between the detector and the maximum of the magnetic field (compare figure 3.2). Not only does this affect the count rates of both detectors, it also affects the magnitude of the experimental beta asymmetry as the beta asymmetry induces an anisotropic angular distribution of decay electrons. The symmetric two detector setup of PERKEO III also helps to minimize this effect as the magnetic mirror effect partially cancels when summing over both detectors. Details on the calculation of the magnetic field and simulations of particle trajectories inside the system can be found in [Wan13]. The final analysis of the magnetic mirror correction is derived in a separate analysis.

The signal window mentioned in section 3.3.1 is optimized to minimize the contribution of the magnetic mirror effect. This is achieved by choosing the centre of the signal window to be at the point where the neutron pulse is in the centre of the active decay volume. As

this is the point of maximum field strength the count rate of both detectors at this point is expected to be the same. In [Mes11] these points, in terms of the neutrons time-of-flight, have been determined to be 4100 μs ($f_{chop} = 94$ Hz) and 4150 μs ($f_{chop} = 83$ Hz). The width of the signal window is set to 2 μs which provides a reasonable amount of statistics while providing a lossless projection of the decay electrons on the detector and keeping the uncertainties due to the magnetic mirror effect small. This leads to the signal time windows stated in equation 3.4.

3.4.2 Detector Vessels

The detector vessel features a magnetic field of 80 mT. While the electrons move from the higher magnetic field regions of the central solenoid to the smaller field of the detector vessel, the momentum fraction of the electrons total momentum parallel to the magnetic field increases due to the same principles of motion that lead to the magnetic mirror effect. The following relation describes this effect [Jac75]

$$p_\parallel = p^2 - p_{\perp,0} \cdot \frac{B(z)}{B(z_0)}, \tag{3.7}$$

where $p_{\perp,0}$ is the particle momentum perpendicular to the magnetic field at the point of emission, and $B(z_0)$ is the magnetic field strength. For particles emitted in the centre of the decay volume with the maximum angle of $\theta_{max} = 90°$ to the magnetic field vector, the angle at the detector becomes

$$\theta_{\text{det}} = \arcsin\left(\sqrt{\frac{80 \text{ mT}}{150 \text{ mT}}}\right) = 47°. \tag{3.8}$$

This forward focussing of the electron momenta helps to reduce the backscattering at the detectors as the backscattering probability becomes larger for lower angles of incidence. In the case that backscattering occurs, higher angles of electron emission are more likely. Due to the high critical angle it occurs that a fraction $> 60\%$ of backscattered electrons are reflected back to the same detector. This reduces systematic effects related to backscattering as discussed in section 7.4 which generally scale linearly with the fraction of backscattering events that reach the opposite detector.

3.5 Electron Detectors

The electron detectors used to measure the beta asymmetry with PERKEO III are plastic scintillators which are read out via acrylic light-guides. A schematic of the detector is shown in figure 3.6.

The scintillator is a Bicron BC-400 plastic scintillator [Bic] with a refractive index of $n = 1.58$ and an emission wavelength of $\lambda = 423$ nm. The size of the scintillator is 43×45 cm^2 which is large enough to cover the whole electron beam created when neutrons decay inside the decay volume. The scintillation light is transmitted via acrylic light-guides to the photomultipliers. They provide a similar refractive index $n = 1.49$ as the scintillator
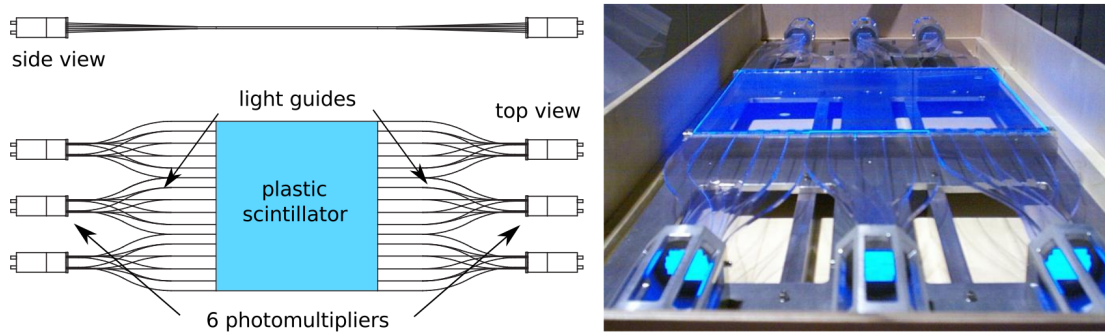
Fig. 3.6: Schematic of the electron detectors (from [Mes11]). The detectors consists of a plastic scintillator and are read out by 6 fine-mesh photomultipliers which are connected via acrylic light-guides.

itself. For the detection of scintillation light fine-mesh photomultipliers of type Hamamatsu R5504 / R5924 are used. Compared to conventional photomultipliers these fine-mesh photomultipliers provide a superior performance when operated inside magnetic fields. The absorption spectrum of the photocathode ranges from $\lambda = 300 - 650$ nm and has its maximum at $\lambda = 420$ nm which matches the emission wavelength of the scintillator.

3.5.1 Readout system

To read out the detector, a VME based data acquisition system is used. For each channel this system features linear fan-outs (LeCroy 748) to split the signals from the photomultipliers. One line is fed into a discriminator (CAEN V812, CAEN C808) and the other line passes a cable delay line with length $t_{delay} \simeq 300$ ns before being fed into a charge-to-digital converter (QDC). The trigger signal generated by the discriminators is evaluated by a digital logic module that generates a global trigger if two out of six photomultipliers are triggered for one of the detectors. This signal is used to trigger the QDC modules that measure the charge integral of the delayed pulses from each channel.

One important feature of the system is that a global trigger always triggers the complete detector system including both detectors. This way the full energy of the detected electrons is recorded, even in case backscattering from the scintillator surface occurs. The timing of the individual photomultiplier triggers generated in the discriminators relative to the global trigger is measured using a TDC with a resolution of 0.8125 ns. This allows to identify which detector triggered first in case both detectors are triggered due to electron backscattering.

More details on the readout system including the timing scheme and several improvements made to the QDCs in preparation of the 2009 measurement are discussed in [Mes11].

The generated data is recorded using the data acquisition software *dackel* which has been developed at the University of Heidelberg. The data is organized in measurement cycles of a fixed length for each measurement run and for each run a file is saved using the ROOT data analysis framework. Measurement cycles are numbered consecutively

and this number is used as main identifier of the data.

For each event the following information is stored:

- Amplitudes of the 12 photomultiplier tubes as measured with the QDCs,

- global event time and time of the last chopper opening (giving the time-of-flight of the neutrons inside the spectrometer),

- TDC data for the detector trigger and individual PMT triggers,

- type of measurement,

- current spin flipper setting (on / off),

- number of the measurement cycle.

Additional information concerning the monitoring of measurement times and chopper and selector frequencies are stored per cycle in the same file. Another important information stored is the consistency of the data stored, which is signalled to be valid by the data acquisition software if the assembling of the data streams from the different modules into separate events is successful. This is generally the case for count rates below 10 kHz but occasionally fails for higher count rates.

3.5.2 Detector calibration

The main part of the measurement has been spent with measuring neutron decay electrons. In order to monitor and calibrate the detectors, multiple electron conversion sources are installed inside the decay volume of PERKEO III providing five peaks and Auger electrons covering an energy range of 0 to 1 MeV (see table 3.1). This provides a higher sensitivity to check the linearity of the detector system compared to the neutron decay spectra. The sources are mounted on ultra thin carbon foils with a thickness of about 100 nm which are installed in a scanner device which is shown in figure 3.7. This device allows to move the sources in 2D to map out the whole detector response.

In the measurements performed with PERKEO II, the calibration of the detectors has been determined from neutron decay spectra [Mun+13]. More precisely, the denominator spectrum $N^{\uparrow}(E_e) + N^{\downarrow}(E_e)$ and the numerator spectrum $N^{\uparrow}(E_e) - N^{\downarrow}(E_e)$ of the experimental asymmetry have been used. This determination of the detector calibration is in general not statistically independent from the beta asymmetry as the same data is used. Since the dominating uncertainty of the detector calibration is obtained by comparing the results obtained for both spectra and is systematic in nature, this should pose no major problem. However, when calibrating using these spectra certain assumptions about the validity of the Standard Model are necessary. For example the unpolarised decay spectrum $N^{\uparrow}(E_e) + N^{\downarrow}(E_e)$ is modified in shape by a non-zero Fierz Interference Term (compare equation 1.29). This likely reduces the sensitivity for the detection for contributions of physics beyond the Standard Model or at least requires to consider the assumptions made in the calibration process when extracting limits.

Although radioactive sources were available in the PERKEO II spectrometer, the background for the measurement of these sources, due to gammas from the same sources,
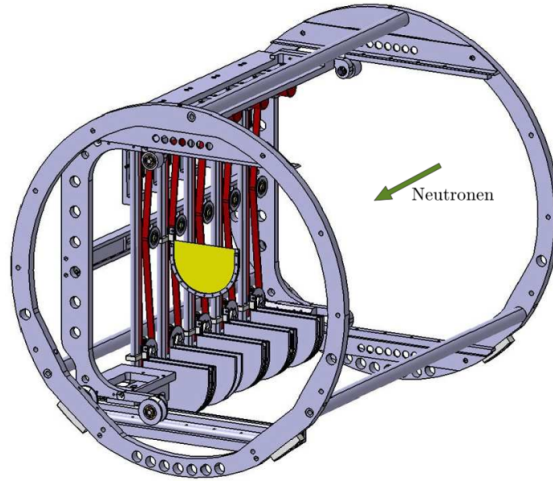
Fig. 3.7: Schematic of the scanner device used to move the five calibration sources inside the decay volume (from [Wil07].

could not be determined well enough. The geometry of the PERKEO III spectrometer for the first time allowed the use of electron conversion sources for all parts of the detector calibration. This has been achieved with the long distance between decay volume and the detectors. The movement of electron sources within the decay volume does not change the solid angle covered for gamma radiation significantly.

Isotope	Energy peak [keV]	Half life	Decay Mode	Rate [10^3 s^{-1}]
^{139}Ce	75	137.6 d	ε + Augers	3.17
^{207}Bi	503, 995	32.9 y	ε + Augers	2.36
^{113}Sn	369	115.1 d	ε + Augers	3.25
^{137}Cs	630	30.1 y	ε + Augers, β^-	32.0

Tbl. 3.1: Calibration sources used during the 2009 measurement. The energy values given represent the nominal energy of the conversion electrons while the measured spectra also contain Auger electrons etc. detected in coincidence.

Using this setup the neutron decay measurements are interrupted regularly in order to monitor the detector properties. More precisely the following measurements are performed:

Drift Monitoring (hourly)
The detector drift is monitored once per hour during the measurement allowing to correct for the detector drift in the data reduction (see section 4.2.6). For the monitoring of the detector drift, a single electron conversion source is used at a fixed position with the neutron beam closed by a shutter. In total 978 drift measurements have been performed having two to four measurement cycles of 150 s length. The drift measurements are followed by a background measurement. This is measured over the same duration with the source moved back into the parking position.

Full Calibration (twice a day)
Twice a day a full calibration using all of the sources has been measured in order to determine properties of the detector model. Between measurements with different sources a background measurement has been performed in order to have statistically independent background measurements for each source spectrum. 114 of these calibration measurements have been performed during the beamtime.

2D Detector Scan (every few days)
In order to monitor the spatial response of the detector, scan measurements have been performed. For each of those scans measurements similar to the drift measurements have been performed at different positions on the detector surface consecutively.

The calculation of the detector response is discussed in chapter 5. The calibration fits performed to extract the relevant detector properties are discussed in section 6.1.

Chapter 4

Data Reduction

The aim of this chapter is to describe the data reduction process from the recorded single events to the final spectra. Systematic effects related to the data reduction process are discussed whereas systematics related to the background and the properties of the electron detection system are discussed in later chapters. Within this thesis a new software tool chain, *p3reduce* has been developed in order to automatize the data reduction process, which has been used successfully in the data analysis of the most recent Perkeo III beamtime in 2015 as well [Raf16].

4.1 Collected data

In this section an overview of the data collected during the 2009 beamtime is given. Here we focus on the "production" part of the measurement during which the data, relevant for the analysis of the beta asymmetry, have been taken. This part of the measurement ranges from measurement cycles 211906 to 627900. Several other measurements to characterize the setup including magnetic field measurements, background checks and measurements of the neutron beam polarisation have been performed. For more details on these measurements see [Mes11].

4.1.1 Datasets

For the data reduction process and analysis the recorded data is divided into datasets. A natural separation that occurs throughout all datasets is the separation of data assigned to an individual detector. The spectra for both detectors are evaluated and analysed separately to reduce systematic effects of the detector response.

In the following the other important steps of data separation are discussed, where the data is grouped concerning certain properties. While for some parts of the analysis and data reduction process larger datasets are more convenient to use, in some cases (e.g. detector calibration) a more fine grained separation of the data is necessary to account for the individual properties of the datasets correctly.

Calibration Sets

The main part of the measurements has been spent with measuring neutron decay events. As mentioned in section 3.5.2 these measurements have been interrupted regularly to perform measurements to monitor and characterize the detector properties. For the

analysis the neutron decay measurements are grouped into datasets (calibration sets) containing the data between two consecutive full calibration measurements. For each of these datasets the detector calibration is obtained by fitting a theoretical description of the calibration spectra with the detector function applied as described in section 6.1. The calibration used for each dataset is the one measured before the dataset.

Subsets

The calibration sets can be grouped into bigger datasets where the same settings to operate the detector system and spectrometer are used. The critical parameters for this selection are:

- **Chopper frequency:** Changing the chopper frequency implies changing the neutron time-of-flight pattern which requires different parameters for extracting signal and background spectra. Due to potentially different background conditions data taken with different chopper frequencies is kept separated.

- **High voltage:**
  Changing the high voltage of the photomultipliers obviously modifies the detector gain. The PMT high voltages have been recalibrated once during the beamtime.

- **Drift measurement:**
  The detector drift has been monitored using different electron conversion sources and has been measured at different positions on the detector surface, changing the amplitude of the drift peak due to the non-uniformity of the detector. Hence, the drift corrected detector amplitude (see section 4.2.6) is not the same.

- **Discriminator level:**
  The discriminator level chosen does not affect the neutron decay spectrum or the beta asymmetry in the energy range used in the analysis. For analysis and checks which critically depend on the trigger function the data is split up into parts where the same discriminator level is used.

Table 4.1 shows the subsets resulting from this separation. The main motivation of separating these datasets is to renormalise the detector gain to the same value for all of these subsets. This then allows to create four larger datasets where only the separation of data for both detectors and the chopper frequency is maintained (chopper sets) which provide a convenient way to analyse some systematic effects. However, a normalized detector amplitude for the different datasets does not imply the exact same detector calibration. For this reason the asymmetry extraction which depends critically on the knowledge of the detector function is performed for each single calibration set.

4.1.2 Chopper sets

For many studies of small systematic effects (e.g. the study of background systematics) it is sufficient to group the data into even larger datasets. This is done by grouping all subsets during which the same chopper frequency has been used. This also implies the

Set	Cycles		Chopper	Drift measurement		Electronics	
	First	Last	f [Hz]	Source	Pos. (x/y [cm])	HV	Discr.
1	211906	230756	94	Bi	90/140	1	8
2a	230757	260912	94	Sn	100/140	1	8
2b	260913	273937	94	Sn	100/140	1	5
3	273938	299440	94	Sn	100/140	2	5
4	299441	342355	94	Sn	0/140	2	5
5	342359	430453	94	Sn	100/140	2	5
6	430457	446494	83	Sn	80/140	2	5
7	446526	470622	83	Sn	80/140	2	5
8	470991	500152	83	Sn	80/140	2	5
9	500157	503300	83	Cs	-/-	2	5
10	503301	623102	83	Sn	80/140	2	5
11	623106	627900	83	Cs	-/-	2	5

Tbl. 4.1: Datasets having the same detector and drift measurement parameters. The shown listed information for each subset includes the chopper frequency and drift measurement parameters. The last columns shows different settings used for the PMT high-voltage and discriminator threshold. The numbers given in the"HV" column refer to one of the two high-voltage configurations used and whereas the "Discr" column contains the threshold setting of the discriminator, where a higher number means a larger threshold. The detector amplitude can be assumed to be stable within each one of these sets.

same neutron time-of-flight windows to select signal and background spectra throughout these datasets. The datasets are listed in table 4.2.

Set	Cycles		Subsets	Chopper
	First	Last		f [Hz]
1	211906	430453	1-5	94
2	430457	627900	6-11	83

Tbl. 4.2: Datasets having the same chopper frequency.

4.1.3 Data Selection

For the analysis of the experimental beta asymmetry only data where the operation parameters of the setup are stable are selected. The following hardware parameters have been monitored and used to filter the data for the analysis:

- **Magnetic field** At certain points during the measurements the power supplies for the magnet coils have been switched off due to failure in the cooling water supply or overheating. Data affected by these shutdowns is discarded in the analysis.

- **Chopper and selector frequency** The chopper frequency is monitored by the data acquisition system. While the selector ran stable most of the time throughout

the measurement, the chopper frequency measurement failed a few times due to sensor problems. Beta decay data where the chopper or selector frequency do not match the set frequencies are ignored.

- **Flipper** During some measurements the flipper did not work as intended. The affected measurements are discarded.

- **Detector high-voltage** On a few occasions the detector high-voltage switched off because the measured current exceeded the set limit. The data affected by these shutdowns as well as a certain time after switching the high-voltage on again are discarded. The latter allows for the detector amplitudes to stabilize after ramping up the high-voltage.

In some cases the data acquisition system monitored the status of the hardware and marked the affected data as invalid. In other cases the data has been filtered manually in the beginning of the data analysis.

For the analysis only data are selected for which valid drift measurements are available. Additionally, each dataset needs to start with a calibration measurement. If any of the operation parameters is changed the data until the next calibration measurement is ignored.

Calibration Measurements

The spectra for full calibration measurements are measured consecutively. The measurement with each source is followed by a background measurement in order to subtract the background for each individual source. Out of the 114 full calibration sets only the data are selected where consistent data has been written. This is true for most of the spectra with the exception of some measurements performed with Caesium during the beginning of the beamtime. Here the data streams of the different data acquisition modules were inconsistent due to the high intensity of the Caesium source.

Other criteria for data selection are the correct positioning of the sources relative to the centre of the neutron beam as well as the stability of of the background count rates. To this end the count rate of the different measurement cycles within a single file is compared. This count rate is expected to be stable for the same source type as well as for the background measurement. However, in case the environmental background changes during a source measurement, e.g. due to opening or closing of neighbouring neutron beamlines, the count rate between the measurement cycles fluctuates. The calibration measurements have been performed using four measurement cycles with a duration of 30s each. The detected count rate of the individual cycles is required to be consistent with a p-value of at least 10^{-5}. If this criterion is not fulfilled the measurement of the affected source is discarded. If a background measurement is found to have inconsistent count rates for different measurements cycles it is discarded and a different background measurement from the same calibration run is used, if possible.

In addition, the availability of drift data is checked. Since drift correction is crucial for the calibration measurements, only those with drift measurements available 1.5 hours
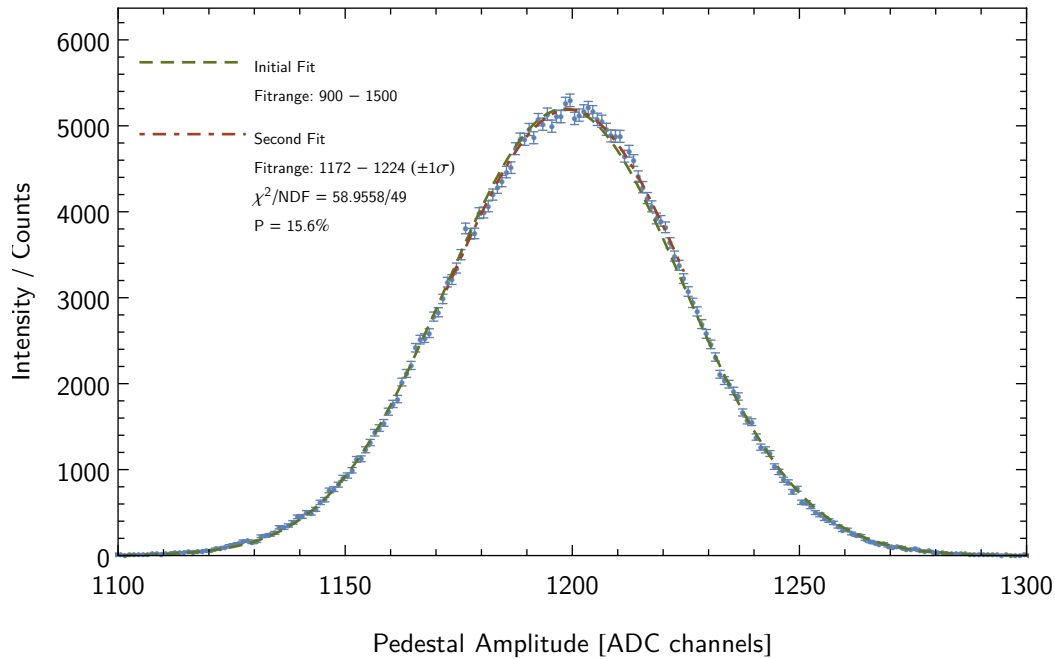
Fig. 4.1: Pedestal spectrum for a single datafile and the corresponding fits to determine pedestal width and position.

before or after the calibration measurement are accepted. This is done, in order to limit the effect of linear interpolation between the drift measurements.

After applying all these criteria 58 calibration sets with all four calibration spectra, 33 with three calibration spectra and one measurement with only two calibration spectra available are selected and used for the detector calibration in the analysis.

4.2 Detector Amplitude

In this section the extraction of the detector amplitude from the raw data is discussed. This involves a few corrections to the data. Their influence on recorded data and the detector amplitude is studied as well. Except for the drift of the detectors, no effects are found which have a significant impact on the results from the measurement.

4.2.1 Detector Pedestals

The first step in the data reduction process is the determination of the detector pedestals. The photomultipliers are read out by QDCs consisting of an integrator circuit being read out by 16-bit ADCs [Mes11]. The amplitude measured by the ADCs contains a bias voltage that determines the value of the QDC amplitude if the PMT did not generate a signal but a trigger is present.

In order to determine the baseline of the resulting spectra, this pedestal is determined for each PMT/QDC channel by performing Gaussian fits to spectra generated from

events where the corresponding detector has not triggered. Here, a sequence of two fits is performed. The first fit is carried out with a broad fitrange that surely contains the pedestal peak. The second peak is performed over a range of $\pm 1\sigma$ as obtained from the first fit. Figure 4.1 shows an example of such a spectrum and the corresponding fits. The QDC pedestals are determined on a file by file basis for each individual channel. In the data reduction process the QDC pedestals are subtracted from the measured amplitudes to obtain offset free spectra.

The fit results also contain the width of the pedestal for each PMT. Since the detector amplitude is calculated as the sum of the individual PMT amplitudes the corresponding broadening to the complete detector is given as square root of the sum of squares of the individual PMT pedestals

$$\sigma_{det\ j} = \sqrt{\sum_{i=1}^{6} \sigma_{ji}^2},$$

$$\sigma_{total} = \sqrt{\sigma_{det1}^2 + \sigma_{det2}^2}. \tag{4.1}$$

(a) Pedestal Position   **(b)** Pedestal Width
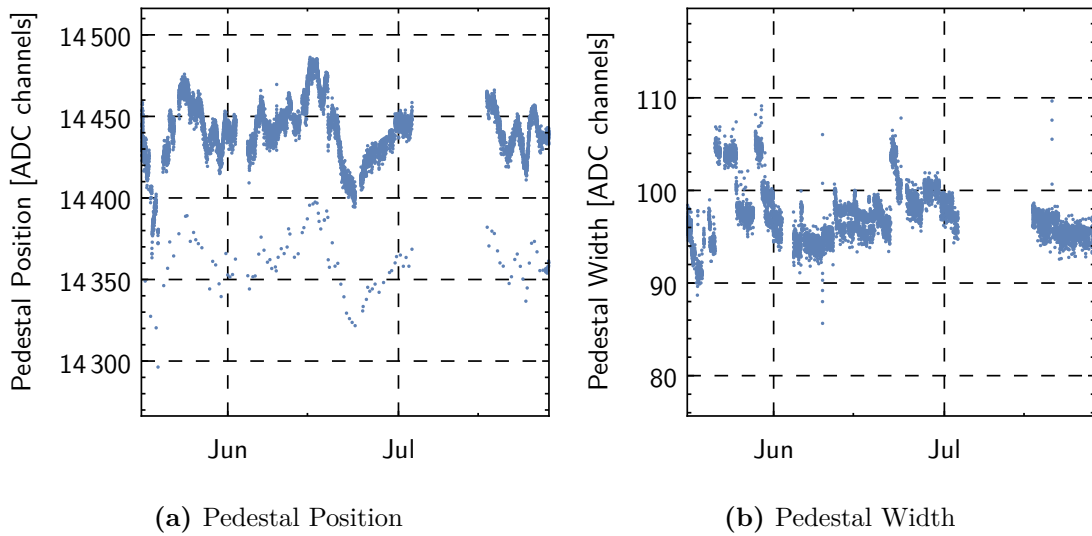
Fig. 4.2: Pedestal position and width for all datafiles taken into account in the analysis. The drop in pedestal position observed for some of the files is due to the high count rate of the Cs source in conjunction with a rate dependence of the QDCs. This effect is discussed in more detail in section 4.2.4.

Figure 4.2 shows the extracted pedestal positions for all files during the measurement. The variation of the pedestal position over time is about 80 ADC channels which corresponds to a relative variation of 0.5%. The mean value of the pedestal width is 97.6 ADC channels with a standard deviation of 3.0 due to a variation over time. This width is considered in all fits to the data in the detector response model as discussed in section 5.4.

4.2.2 Spin Dependence of the Pedestal

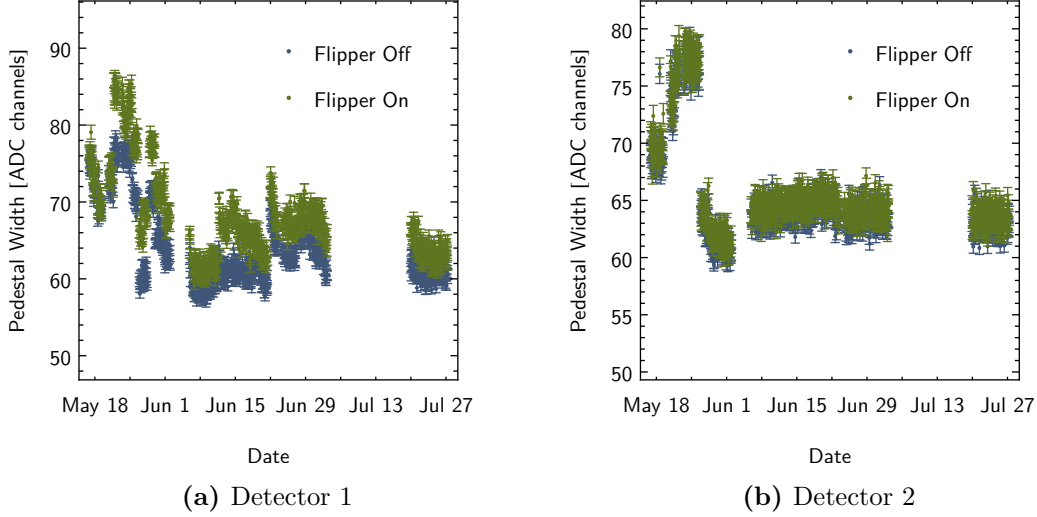**(a)** Detector 1 **(b)** Detector 2

Fig. 4.3: Contributions of both detectors to the total detector pedestal width.

When splitting the pedestal extraction with respect to the state of the flipper device, a dependence of the pedestal width with respect to the spin state is observed. Figure 4.3 shows the individual detector pedestals (compare equation 4.1) for both spin settings which are significantly higher when the flipper is running. The average differences in pedestal width are:

$$\sigma_{1,on} - \sigma_{1,off} = 4.1(2.3) \text{ ADC channels,}$$
$$\sigma_{2,on} - \sigma_{2,off} = 0.7(1.0) \text{ ADC channels,} \tag{4.2}$$

where the errors are calculated as standard deviation from the data in order to account for non-statistical fluctuations. A likely explanation for this effect is that noise is introduced from the spin-flipper or its driver into the signal lines of the detectors. Since detector 1 is much closer to the flipper, the effect is expected to be stronger for detector 1. The observed shifts in pedestal position are ≤ 0.1 ADC channels for both detectors which is considered negligible.

For the data analysis the actual difference between the magnitude of the pedestal width shift for the detectors does not play a role since both detector amplitudes are summed up for each event. The width shift for the total detector pedestal is

$$\sigma_{total,on} - \sigma_{total,off} = 3.4(1.8) \text{ ADC channels.} \tag{4.3}$$

For the experimental beta asymmetry a spin-dependence of the signal broadening can play a significant role as the spectra $N^{\uparrow}$ and $N^{\downarrow}$ are affected differently. The resulting spectral difference is amplified when calculating the difference of these spectra for the numerator of the beta asymmetry. In the calculation of the detector response, as will be presented in chapter 5, the spin-independent average for the width of the detector pedestal is assumed.

The effect of neglecting the spin-dependence has been studied by assuming a difference in the electronic noise contribution for $N^\uparrow$ and $N^\downarrow$ before calculating the experimental beta asymmetry. The resulting spectral corrections for the Experimental Asymmetries of detector 1 and 2 are plotted in figure 4.4.
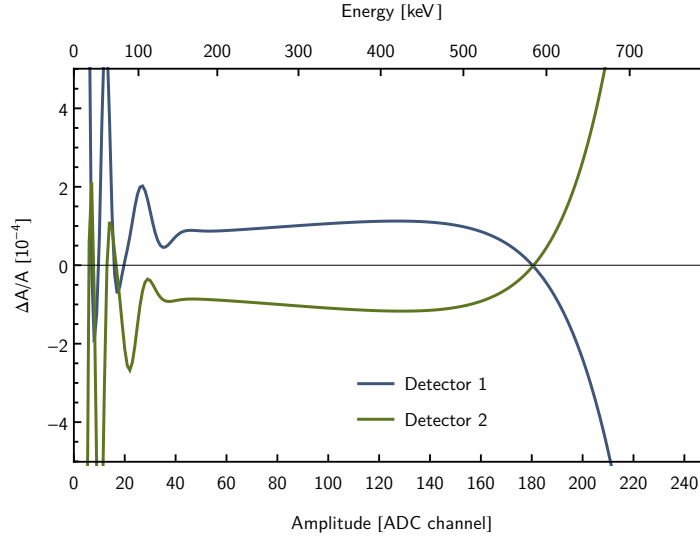

Fig. 4.4: Relative correction functions for the experimental beta asymmetry to account for the spin-dependence of the pedestal width for both detectors. The oscillating structure at lower amplitudes is due to the broadening of the signal generated by a discrete number of photoelectrons. The corrections for both detectors cancel due to the fact that the same pedestal width applies for different spin states.

At lower amplitudes the broadening of the signal around a discrete number of detector photoelectrons creates an oscillating structure. Within the energy window used to fit the data ranging from ADC channel 85 to 215 the amplitude of the correction is on the level of $1 \cdot 10^{-4}$. When applying the correction in the fit the, following integral relative corrections are obtained:

$$\begin{aligned}
(\Delta A/A)_{\text{Det1}} &= -0.76 \cdot 10^{-4}, \\
(\Delta A/A)_{\text{Det2}} &= 0.76 \cdot 10^{-4}
\end{aligned} \tag{4.4}$$

The exact value of the correction has a strong dependence on the overall broadening of the spectrum (i.e. other noise contributions). However, the absolute value of the correction for both detectors is the same, while being different in sign. This is due to the fact that the effect is correlated with the flipper state, which affects different spin directions for the detectors. The total correction when averaging over both detectors cancels up to a level of $\Delta A/A = 10^{-6}$ which can be neglected safely.
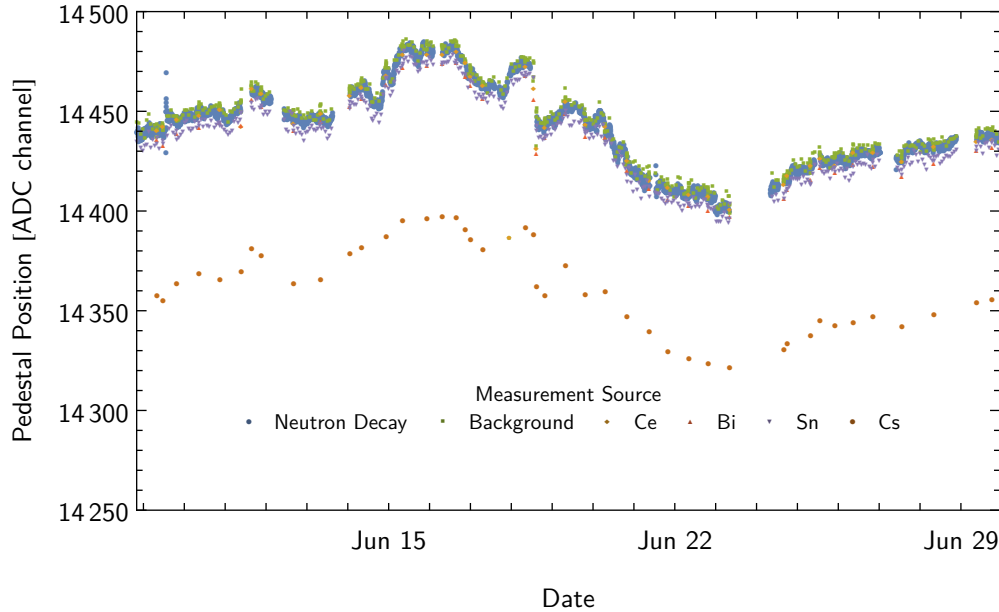
Fig. 4.5: Pedestal position for individual measurement source for 5000 files.

4.2.3 Calculating the full Detector Amplitude and Trigger Information

Using the extracted pedestals the raw total detector amplitude is extracted for each event by calculating the sum of all QDC values with the pedestals subtracted.

$$A_{tot,raw} = \sum_{i=1}^{2} \sum_{j=1}^{6} \left(A_{ij} - P_{ij} \right) \tag{4.5}$$

Here A_{ij} represent the individual QDC amplitudes obtained from the raw data for detector i and channel j and P_{ij} denote the corresponding pedestals (compare section 4.2.1). For the assignment of the events the data measured with the TDC is used to determine which detector triggered first.

Using the raw detector amplitude from equation 4.5 and the trigger information allows to histogram the detector amplitude obtaining the measured spectra for each file.

4.2.4 Rate dependence of the QDC Amplitude

Figure 4.5 shows the detector pedestals for each datafile broken down to the type of measurement performed. The apparent effect here is that the pedestals for the measurements with Caesium consistently are 84 channels lower compared to other measurements. In a first analysis this effect has been explained with a rate-dependence of the QDC amplitudes [Mes11]. In the following a more detailed analysis of this effect and its implications for the present analysis are performed.

Table 4.3 shows the average shift of the pedestal for each calibration source compared

Source	Pedestal Shift to Background		Count Rate
	Position [ch]	Width [ch]	[cnts/s]
Background	-	-	930
Neutron Decay	-1.7	+1.28	2200
Ce	-5.1	+0.7	3170
Bi	-7.1	+0.7	2360
Sn	-7.2	+0.4	3250
Cs	-83.8	+2.6	32000

Tbl. 4.3: Pedestal shifts and count rates for different measurement types. The rates given are total rates including background events. The rate for neutron decay is the detection rate including background within the ToF signal window (compare section 4.3).

to background measurements performed after each calibration and drift measurement. The shifts for the other sources are much smaller. This is consistent with the hypothesis of a rate-dependent effect. However, although measured with lower count rate the pedestals during the Cerium measurements are shifted less compared to those of the Bismuth measurements. This additionally indicates a dependence on the deposited energy which is much higher for Bismuth.

Figure 4.6a shows the shift of the pedestal and peak position for all Sn measurements versus the time since the previous detector trigger. The behaviour illustrates that the pedestal shift and the shift in the total detector amplitude are the same, which confirms that this particular behaviour of the QDCs can be explained as a shift in the pedestal only. Figure 4.6b shows the pedestal behaviour broken down into different trigger constellations where it is distinguished if the previous event triggered the same, the other or both detectors. The data shows that the shift in the pedestal position is dominant if the same detector has been triggered in the previous event which equates to a higher energy deposition. If the previous event only triggered the other detector this equates to an energy deposition below the trigger threshold and leads to a smaller shift in pedestal.

The Sn peak analysis shows that the shift in the pedestal position depends on the time elapsed since the previous detector event and the amplitude detected in the respective event. The shift of the measured QDC amplitude may then be written in the form

$$A_{QDC}\left(A_0, t\right) = A_0 + \sum_{i=1}^{\infty} f\left(t_i, A_i\right), \tag{4.6}$$

where A_0 determines the "real" amplitude as opposed to the measured amplitude A_{QDC}, $f\left(t_i, A_i\right)$ describes the dependence of the shift on the "Delta-Time" t_i, the time between events, and the amplitude of the preceding event A_i. The index i in theory runs over all preceding events.

During the beam time and offline test of the QDC channels has been performed where two pulsers, one having a slightly detuned frequency compared to the other have been used
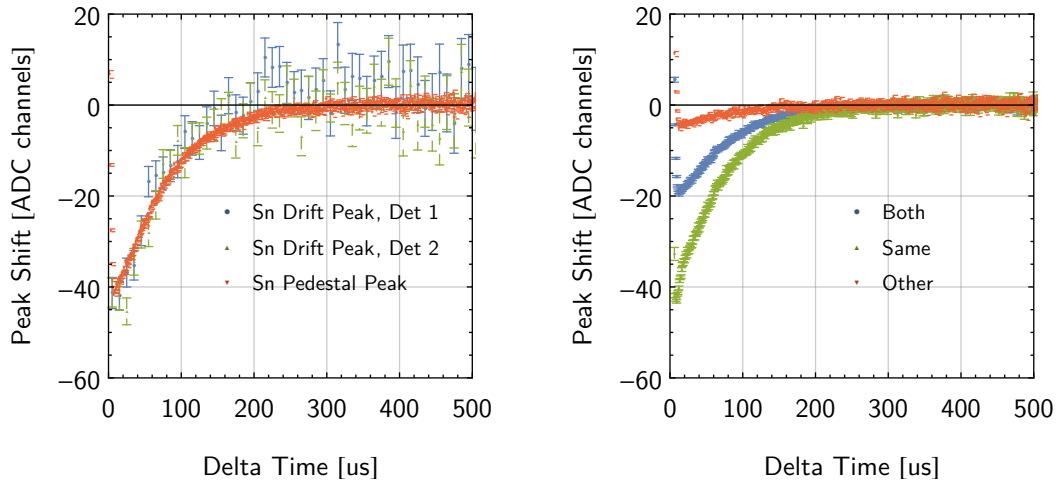
(a) Comparison of peak position and pedestal for both detectors.

(b) Comparison of pedestal shift depending on previous trigger for detector 1.

Fig. 4.6: Behaviour of the pedestal and peak position of the Sn drift measurements versus the time elapsed since the previous trigger. For shorter times between events the drift peak position is shifted to smaller channels by the same amount as the pedestal is shifted (a). The effect for the pedestal is stronger when the previous event triggered the same detector (b).

to feed signals into all QDC channels. This way all possible "Delta-Times" between events from 0 to $1/f$ are recorded with the same input amplitude which allows to determine the function $f(t)$. Figure 4.7 shows the measured amplitude versus the delta-time where the relative shift in the measured amplitude for each channel is equal to a few percent and independent of the total signal amplitude. This justifies the linear dependence of the correction on the detector amplitude $f(t_i, A_i) = A_i \widetilde{f}(t_i)$. The correction data obtained from this measurement are used to fit three exponential functions in order to describe $\widetilde{f}(t)$. Due to the two pulser constellation the delta-times of all preceding events with even index i originate from the same pulser that also triggers the signal under investigation. This reduces accumulation effects. The resulting description of $\widetilde{f}$ should thus provide a good estimate.

In order to check the influence on the beta asymmetry an inverse correction of this effect based on the estimate of $\widetilde{f}$ has been applied to six calibration sets where only the first order effect has been corrected

$$A_{\text{corr}}(A_{\text{QDC}}, t) = A_{\text{QDC}} - A_1 \widetilde{f}(t_1, A_1). \tag{4.7}$$

This correction has been applied to each single PMT amplitude in the pedestal analysis and creation of spectra before summing up the amplitudes. The resulting mean shifts in pedestal are summarized in table 4.4. The differences in pedestal position between the background measurements and the other measurements is reduced by a factor of two or more when correcting the QDC amplitude. The remaining differences as well as the still significant deviation for the Cesium measurements can be explained by accumulation
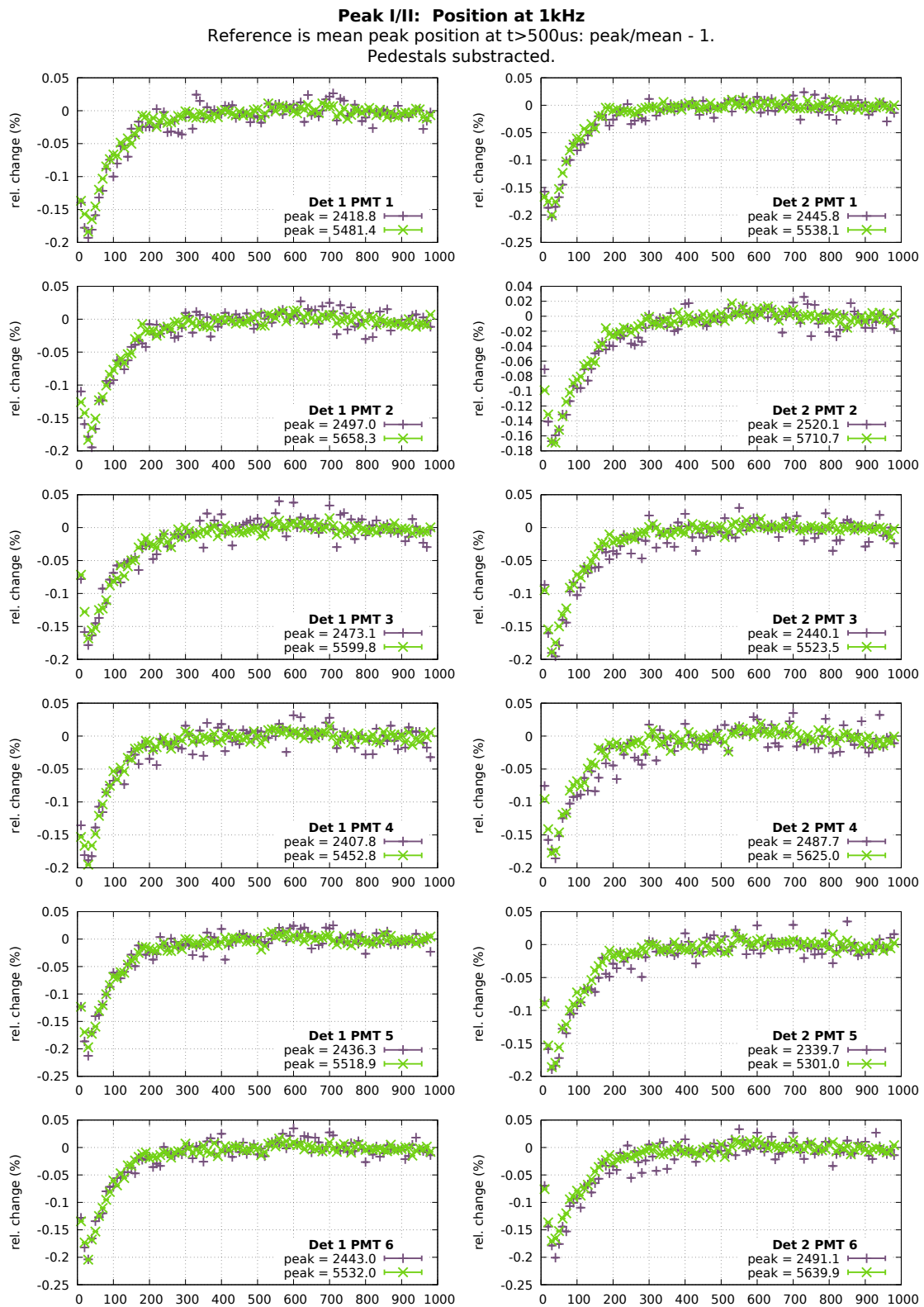
Fig. 4.7: Relative shift in pedestal measured with a floating pulser setup for different pulse amplitudes.

effects according to equation 4.6 which is not corrected for in this analysis.

Source	Uncorrected		Corrected	
	Position [ch]	Width [ch]	Position [ch]	Width [ch]
Background	-	-	-	-
Neutron Decay	-4.4	+2.1	-2.2	+1.9
Ce	-2.6	+2.7	+1.1	+2.5
Bi	-5.6	+7.9	-1.3	+6.3
Sn	-10.1	+3.7	-4.7	+2.8
Cs	-105.8	+11.5	-86.0	+10.2

Tbl. 4.4: Average deviation of the detector pedestal between background and other measurements with and without correcting the QDC amplitude.

Since the delta-time dependence of the QDC amplitude affects the pedestal and the measured signal amplitude in the same way, no effect on the measured spectra is expected. This is checked by comparing the results for the beta asymmetry for the six calibration sets with and without correcting the QDC amplitude in the raw data processing. For each dataset the detector calibration is obtained separately using the same correction applied to the Neutron Decay measurements. The deviation for the single datasets varies between $\Delta A/A = 1 \cdot 10^{-3}$ and $-2.5 \cdot 10^{-3}$. This is well below the statistical uncertainties for these datasets. A likely cause of the variation being a modification of the binned spectra due to the correction of amplitudes for individual events. The deviations observed when averaging over the detectors gives

$$\Delta A/A_{\text{Det1}} = 1.9 \cdot 10^{-4},$$
$$\Delta A/A_{\text{Det2}} = -1.8 \cdot 10^{-4}. \tag{4.8}$$

The total average is $\Delta A/A < 1 \cdot 10^{-5}$. This indicates that applying the correction has no significant impact. Vice-versa the pedestal subtraction mechanism used is considered to account for the rate-dependence sufficiently. As a consequence of this analysis however, for the neutron decay measurements a time-of-flight dependent extraction of the detector pedestal for signal and background time windows is performed to obtain the correct pedestals for each spectrum.

4.2.5 Recalibration of the PMT Amplitudes

In [Mes11] a recalibration of the individual PMT channels is derived in order to make the detector more spatially uniform. For this the 2D maps measured during the beamtime have been analysed and the amplitudes of the individual PMTs have been rescaled in a way that the map follows the expectation of a cosh-shape. The resulting rescaling factors c_{ij} for each PMT are included in the data reduction process by modifying the detector
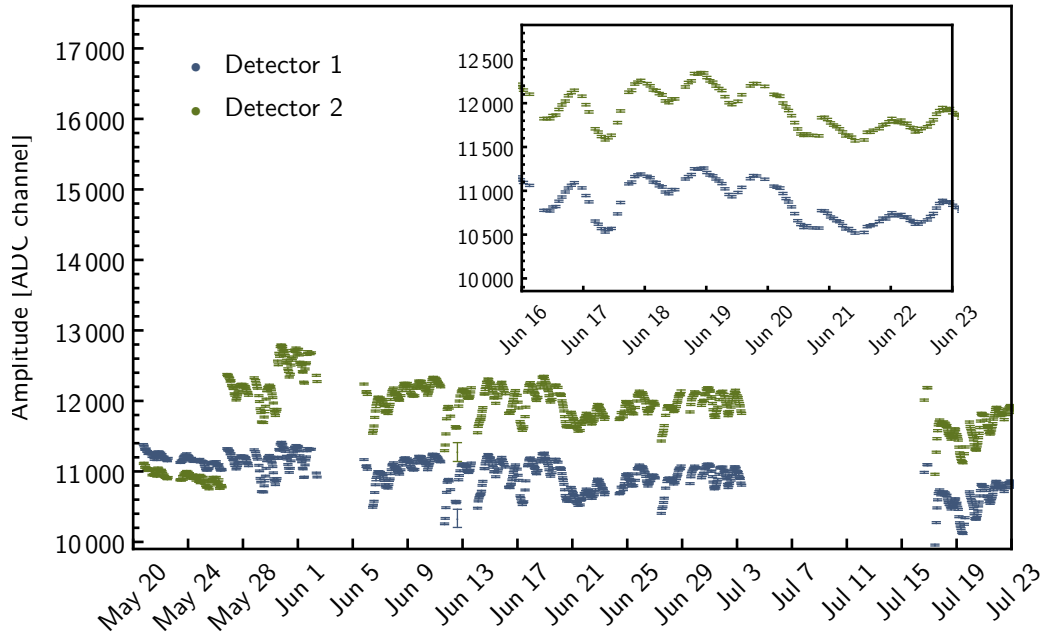
Fig. 4.8: All drift measurements performed with ^{113}Sn.

amplitude given in equation 4.5

$$A_{tot} = \sum_{i=1}^{2} \sum_{j=1}^{6} c_{ij} \left(A_{ij} - P_{ij} \right).$$ (4.9)

Including these correction factors gives a more uniform detector response with a homogeneity of ± 2.5 % over the area covered by the decay electrons from neutron decay.

4.2.6 Drift Correction

The hourly single point calibration measurements are performed mostly using the ^{113}Sn source in a fixed position of the scanner device. This provides a measurement of the relative evolution of the raw detector amplitudes as shown in figure 4.8 for all measurements performed with ^{113}Sn. The data has been extracted using Gaussian fits to the main peak of ^{113}Sn, the mean amplitude being represented by the mean value of the fit. The drift data shows a day-night variation of the detector amplitudes of about 2% as well as long-term drifts. The likely origin of both effects is a temperature variation of the photomultipliers sitting close to the magnet coils. As mentioned in section 3.4 these coils are normal conducting and water cooled. The temperature of the coils in operation depends on the temperature of the cooling water which is not regulated.

The variation of the detector amplitude for the beta data itself just results in a reduced energy resolution. However, since the calibration measurements take place at a fixed time during this variation, the application of the calibration may be shifted compared to the average detector amplitude for the beta data. In order to reduce this effect, a
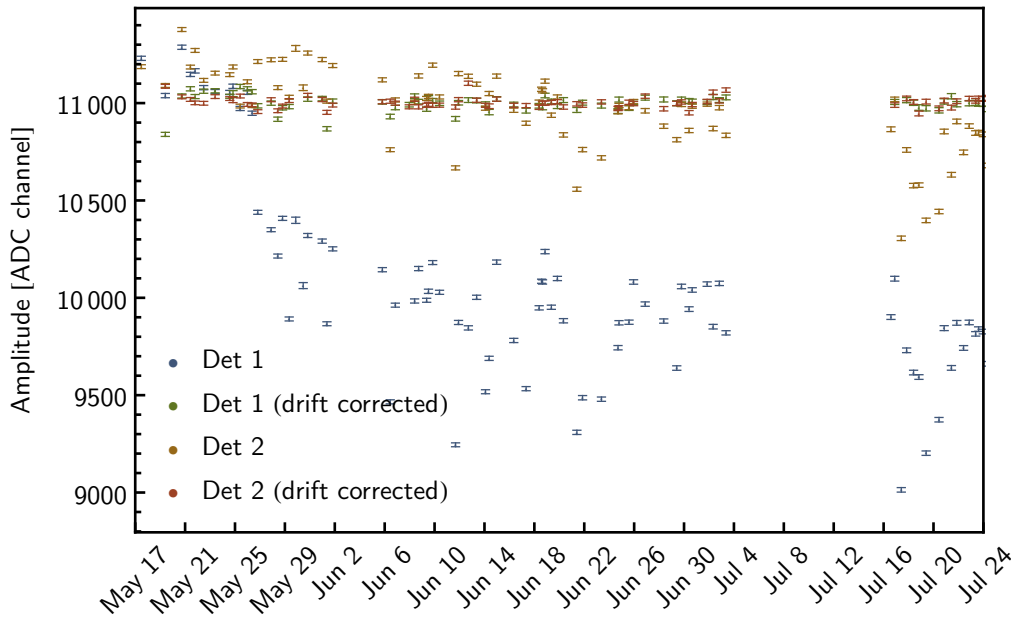
Fig. 4.9: Comparison of the ^{113}Sn main peak position for the calibration measurements with and without drift correction.

drift correction is derived for both detectors by linear interpolation of the drift peak measurements. This correction is applied during the data reduction process for all neutron decay and calibration measurements giving a drift corrected detector amplitude

$$A_{tot,drift} = \sum_{i=1}^{2} d_i r_i \sum_{j=1}^{6} c_{ij} \left(A_{ij} - P_{ij} \right), \tag{4.10}$$

where d_i are the drift correction factors for detector 1 and 2 respectively. The additional rescaling factors r_i in equation 4.10 are necessary in order to correct for changes in the measurement of the drift data between different sets(see table 4.1).

Although mostly measured with ^{113}Sn, a few measurements have been performed with other sources and the position on the detector at which the drift is measured has been changed a few times during the beamtime. In order to obtain comparable detector amplitudes throughout the whole beamtime, the data is grouped in sets which use the same set of parameters for the drift measurement. In contrast to the drift measurements, the full calibration measurements have always been measured in the centre of the detector which allows to use the ^{113}Sn peak position to derive the correction factors r_i for each of those sets by requiring this peak position to be the same. The accuracy of these rescaling factors is not important for the final result as the data is analysed for each calibration set separately during which the drift parameters are stable. However, this renormalisation allows to create larger datasets (subsets and chopper sets, compare section 4.1.1) for a more convenient analysis of systematic effects.

The result of drift correction is illustrated by comparing the peak positions of the

Set	Rescaling		χ^2/NDF		Add. Rel. Uncertainty	
	Det 1	Det 2	Det 1	Det 2	Det 1	Det 2
1	1.00391	1.00414	-	-	-	-
2	1.01147	1.00071	25.2/10	28.3/10	$1.19 \cdot 10^{-3}$	$1.19 \cdot 10^{-3}$
3	1.08487	1.00001	34.1/5	33.0/5	$2.41 \cdot 10^{-3}$	$2.13 \cdot 10^{-3}$
4	1.10661	1.00464	135.7/4	40.7/4	$5.84 \cdot 10^{-3}$	$2.82 \cdot 10^{-3}$
5	1.10300	0.99603	126.6/20	123.8/20	$2.51 \cdot 10^{-3}$	$2.24 \cdot 10^{-3}$
6	1.10328	0.99596	17.5/5	3.6/5	$1.71 \cdot 10^{-3}$	$0. \cdot 10^{-3}$
7	1.12883	0.99847	4.5/3	1.1/3	$0.80 \cdot 10^{-3}$	$0. \cdot 10^{-3}$
8	1.10010	0.99629	24.1/6	26.0/6	$2.00 \cdot 10^{-3}$	$1.84 \cdot 10^{-3}$
9	1.10024	0.99721	-	-	-	-
10	1.10010	0.99629	47.6/25	174.6/25	$1.17 \cdot 10^{-3}$	$3.27 \cdot 10^{-3}$
11	1.10024	0.99721	-	-	-	-
Average					$\mathbf{1.91 \cdot 10^{-3}}$	$\mathbf{2.20 \cdot 10^{-3}}$

Tbl. 4.5: Rescaling factors used to account for differences in drift measurements for the different subsets. The reduced χ^2 values show that the remaining variance in the drift corrected ^{113}Sn peak positions is larger than expected just from statistics. The increased scattering of data points can be described by an additional uncertainty contribution (according to equation 4.11) that accounts for interpolation uncertainties and statistical uncertainties of the drift measurement and is listed as relative uncertainty in detector gain in the last columns. This uncertainty is considered for all subsets where the reduced χ^2 is bigger than one and is assumed to be 0 otherwise. Generally this shows that the drift correction works on a relative $2 \cdot 10^{-3}$ level.

^{113}Sn spectra in the full calibration measurements with and without drift correction as shown in figure 4.9. Among a correction of the individual detector drift also a relative normalisation of both detector amplitudes is achieved. This leads to similar calibrations for both detectors which is important for full energy reconstruction in case of backscattering events.

The remaining variation of the drift corrected ^{113}Sn peaks within the mentioned datasets is bigger than expected from the statistical fluctuations as indicated by the reduced χ^2 values listed in table 4.5. This shows that the drift correction is limited due to interpolation between the drift measurements. The additional relative uncertainties in table 4.5 are calculated by introducing an additional uncertainty contribution to the χ^2 calculation and forcing the reduced χ^2 to be 1 for each set:

$$\chi^2/\text{NDF} = \sum_i \frac{(x_i - \langle x \rangle)^2}{\sigma_i^2 + \omega^2} \overset{!}{=} 1. \tag{4.11}$$

The non-statistical uncertainty ω then is a measure of the additional fluctuations in the drift correction. This uncertainty is only assumed if the χ^2/NDF value for the dataset is larger than one. However, choosing a higher bound for the reduced χ^2 (larger confidence regions) does not impact the result as most subsets show a very large χ^2.

4.3 Neutron Time-of-Flight and Detector Background

For each event the time relative to the last chopper opening is determined simply by subtracting the time of the last chopper opening from the time stamp of the event. This difference gives the time-of-flight of the neutrons within the spectrometer. The resulting time-of-flight dependence of the count rates of the individual detectors has been discussed in section 3.3.1.

4.3.1 Signal and Background spectra

For the extraction of beta decay spectra only events from within the signal time window are selected. This time windown is defined by the time-of-flight when the neutron pulse is in the central decay volume (see section 3.3.1). The events are histogramed with the detector amplitude calculated according to equation 4.10. The same procedure is used to extract the background spectra. These need to be rescaled by a factor of 2 to account for the shorter length of the background time window.

Given the detected rate $\dot{N}$, the real rate $\dot{N}'$ can be calculated from the non-extensible dead-time τ to be [Leo87]:

$$\dot{N}' = \frac{\dot{N}}{1 + \dot{N} \cdot \tau}, \tag{4.12}$$

where the dead-time has been set to be $\tau = 1.5~\mu$s. The required dead-time corrections to the signal and background spectra are applied to both spectra automatically by the data reduction software. The measured event rate is calculated from the number of detected events divided by the number of chopper rotations in the respective dataset multiplied with the length of the time window.

The obtained signal and background spectra as well as the background free electron spectrum are shown in 4.10.

Chapter chapter 8 contains furhter discussions of the background subtraction and related systematics.

4.3.2 The Experimental Beta asymmetry

In a general formulation where background may depend on the spin the experimental beta asymmetry is given by the following equation:

$$A_{exp}(E) = \frac{\left(N^\uparrow(E) - B^\uparrow(E)\right) - \left(N^\downarrow(E) - B^\downarrow(E)\right)}{(N^\uparrow(E) - B^\uparrow(E)) + (N^\downarrow(E) - B^\downarrow(E))}. \tag{4.13}$$

For the case that background can be assumed to be independent ($B^\uparrow = B^\downarrow = B/2$) of
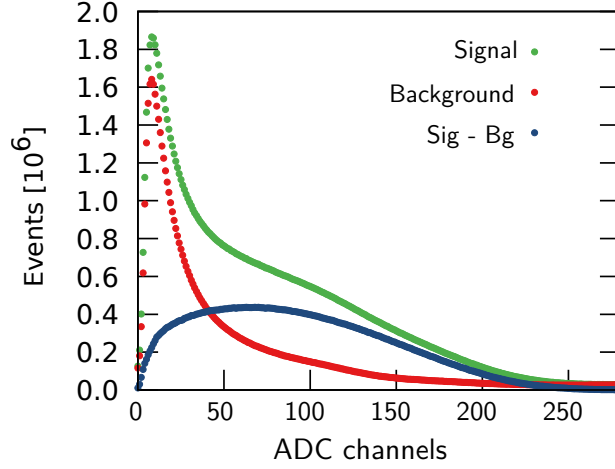
Fig. 4.10: Spectra obtained by selecting data according to their neutron time-of-flight within the spectrometer. The signal spectrum is obtained by selecting data for which the neutron pulse is contained within the central decay volume. For the background spectrum on the other hand only data recorded after all neutrons are absorbed in the beamstop is considered. The background spectrum is scaled in order to account for the shorter length of the background time window. The difference of the signal and background spectra finally gives a background free electron spectrum.

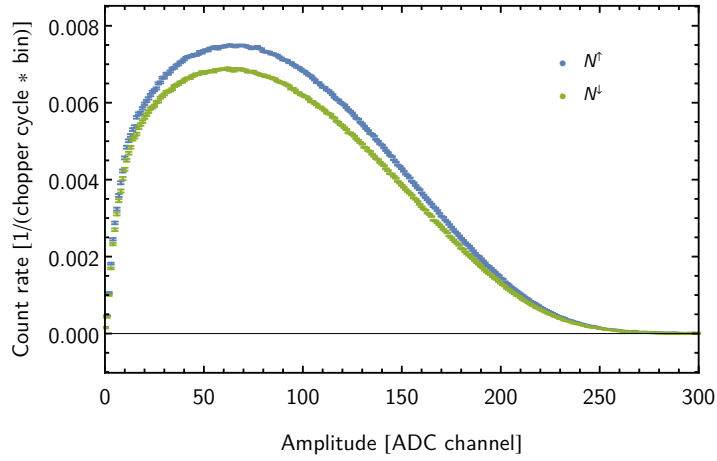the spin direction equation 4.13 becomes:

$$A_{exp}(E) = \frac{N^\uparrow(E) - N^\downarrow(E)}{N^\uparrow(E) + N^\downarrow(E) - B(E)}. \tag{4.14}$$

The contribution of the statistical uncertainty of the background δB is given by:

$$(\delta A_{exp})_{bg,si} = \sqrt{\frac{\left(N^\uparrow - N^\downarrow\right)^2 \delta B^2}{\left(N^\uparrow + N^\downarrow - B\right)^4}}. \tag{4.15}$$

for the case of spin-independent background. In case the measured background would depend on the spin-direction the statistical uncertainty would become

$$
\begin{aligned}
(\delta A_{exp})_{bg} &= \sqrt{\left(\frac{\partial A_{exp}}{\partial B^\uparrow}\right)^2 \cdot \delta B^{\uparrow 2} + \left(\frac{\partial A_{exp}}{\partial B^\downarrow}\right)^2 \cdot \delta B^{\downarrow 2}} \\
&= 2 \cdot \sqrt{\frac{\left(B^\uparrow - N^\uparrow\right)^2 \cdot \delta B^{\uparrow 2} + \left(B^\downarrow - N^\downarrow\right)^2 \cdot \delta B^{\downarrow 2}}{\left(B^\uparrow + B^\downarrow - N^\uparrow - N^\downarrow\right)^4}}.
\end{aligned}
\tag{4.16}
$$

(a) Spin up / Spin down spectra with background subtraction.
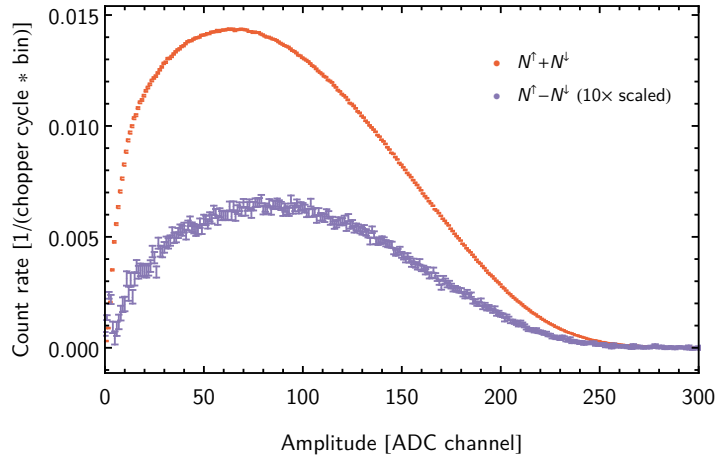
(b) Denominator and numerator spectra of the experimental beta asymmetry.
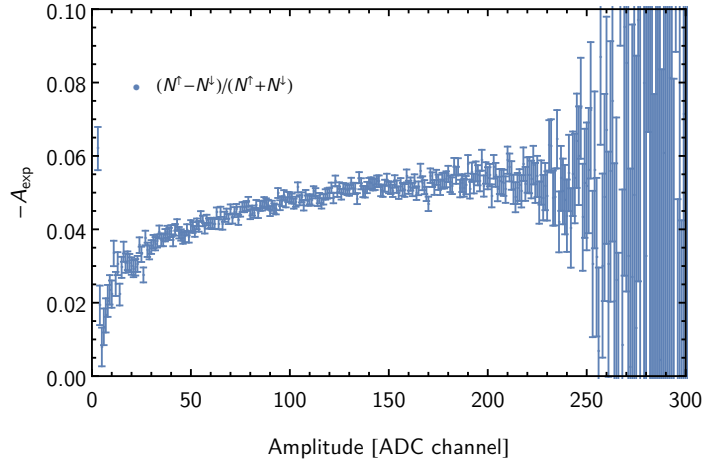
(c) Experimental beta asymmetry.

Fig. 4.11: Extracted spectra to calculate the experimental beta asymmetry. The plots are created from the combined dataset for detector 1 with chopper frequency 83Hz.

For a signal-to-background ratio of 2 and an energy region of $300 - 700$ keV the statistical sensitivity per decay event N for both cases is:

$$
\begin{aligned}
(\delta A_{exp})_{bg} &\simeq 4.80 \cdot P/\sqrt{N} \\
(\delta A_{exp})_{bg,si} &\simeq 4.14 \cdot P/\sqrt{N}
\end{aligned}
\tag{4.17}
$$

with the neutron beam polarisation P. Hence the statistical sensitivity is increased by 20% if the background can be considered spin independent. The validity of this assumption is justified in chapter 8.

Figure 4.11a shows the extracted background free electron spectra for both spin directions. The spin dependent background is subtracted for illustration purposes only. For the calculation of the experimental beta asymmetry as shown in figure 4.11c according to equation 4.14 only the spin-independent total background is considered.

Chapter 5

Model of the Detector Response

The spectral analysis of the Beta Asymmetry and the calibration measurements is performed by fitting the theoretical spectra, modelled with a description of the detector response, to the measured data. While the next chapter deals with the spectral analysis of the data itself, this chapter is dedicated to outline the details of modelling the detector response.

The description of the detector response is based on forward modelling of all relevant physical processes ranging from electrons of a certain energy hitting the scintillator surface to the charge accumulation in the QDCs and analog-to-digital conversion. This technique has been used for the previous analyses of PERKEO data and limits the number of necessary corrections to the measured spectra, such as unfolding to account for the detector resolution. This would imply a considerable information loss and limit statistical accuracy.

A critical part in the analysis is the fitting of calibration spectra in order to obtain the detector properties independent of neutron decay spectra. Within this thesis several improvements to the actual implementation have been made which especially improve the description of the detector non-linearity and energy resolution. A phyiscally more motivated description of the scintillator non-linearity is implemented, which accounts correctly for events where multiple electrons hit the detectors at the same time. Further improvment is achieved by implementing a precise approximation for the noise created by the photomultiplers. Both changes strongly improve the fit quality achieved when fitting the calibration spectra and extract the detector non-linearity from these fits. For the first time this allows to analyse a PERKEO measuremnt solely with independent calibration data. Additionally, the description of the photomultiplier noise is an important ingredient for the exact calculation of the detector trigger function [Roi18], which is necessary to analyse systematics related to backscattering (see section 7.4.2).

The following sections describe the steps in calculating the actual fit function and the mentioned improvements.

5.1 Electron energy distribution

The initial electron energy distribution is calculated as a binned histogram. The range of spectra implemented covers all relevant electron spectra from neutron beta decay (see section 2.2) as well as a description of the used calibration sources [Roi18].
One important peculiarity about the spectra of the electron conversion sources is that typically Auger electrons are emitted shortly after the emission of the conversion electron.
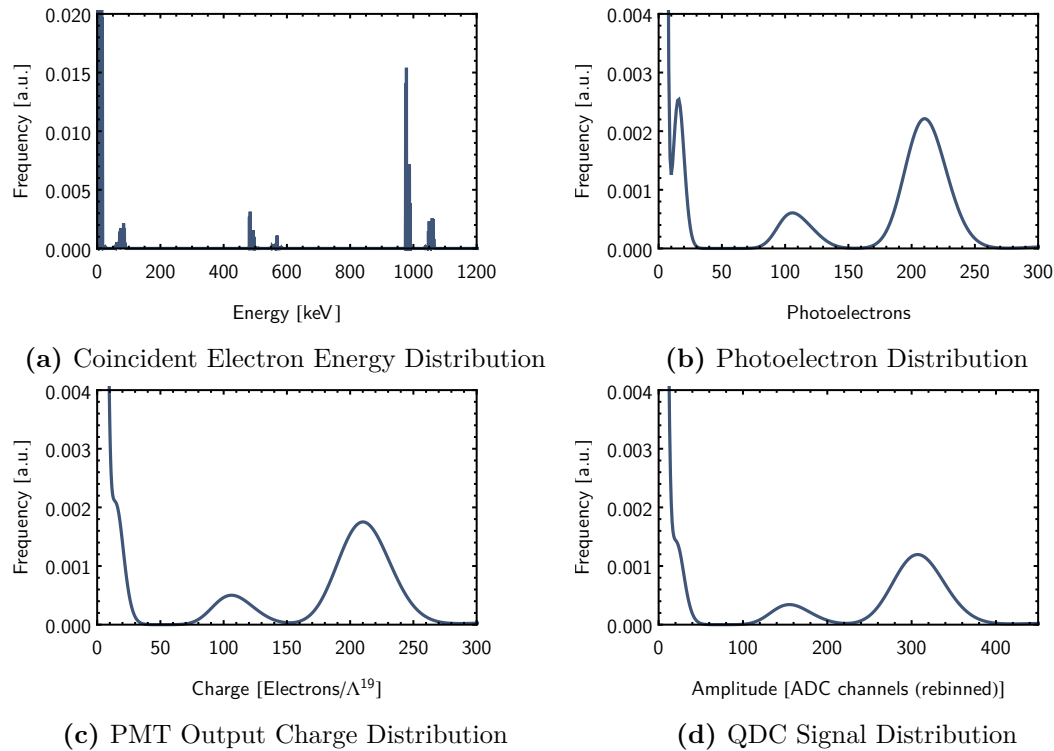
(a) Coincident Electron Energy Distribution

(b) Photoelectron Distribution

(c) PMT Output Charge Distribution

(d) QDC Signal Distribution

Fig. 5.1: Evolution of the measured spectrum for different stages of the detector response for Bi^{207}. The shown spectra are: The discrete line spectrum, including coincident Auger electrons (a), the resulting photoelectron distribution at the dynodes of the PMT (b), the spectrum after calculating the noise contribution of the photomultipler (c) and the spectrum measured by the QDC (d).

Since these Auger electrons may arrive at the detector within the same QDC integration window, they contribute to the measured amplitude. The calculation of the calibration spectra take these effects into account by calculating all possible combinations, considering the length of the QDC integration window. The amplitudes of the combined events is then calculated when filling the theoretical histogram. Image 5.1a shows the result of such a calculation for the theoretical spectrum of Bi^{207} which is one of the used calibration sources.

5.2 Scintillation

The first step of electron detection is their absorption in the scintillator of the electron detection system (see section 3.5). Along their path inside a scintillator electrons deposit all or part of their kinetic energy predominantly by interacting with other electrons, leading either to ionization or molecular excitations of the bulk material. The resulting secondary radiation has a much lower energy and may excite the primary fluors of the scintillator. which deexcite by emitting photons in the UV range. A wavelength shift is achieved by means of secondary fluors, leading to a photon emission spectrum ranging

from 400 to 500 nm wavelength, with the most probable wavelength being 420 nm or 3 eV.

The maximum number of potentially generated photons is thus on the order of 10^5 per MeV, whereas the expected number of photons for plastic scintillators is typically on the order of $a = 10^4$ MeV^{-1}. This allows describing the number of generated photons per electron energy in terms of a Poisson distribution:

$$p_{\text{scint}}\left(n_{\text{ph}}, E, a\right) = \frac{(a \cdot E)^{n_{\text{ph}}}}{n_{\text{ph}}!} e^{-a \cdot E}, \tag{5.1}$$

where the mean number of photons per energy is described by the factor a.

5.2.1 Scintillator Non-linearity

A known property of organic scintillators is that they posses an intrinsic non-linearity. In a general formulation a, non-linear scintillation output would modify equation 5.1 in a way that the expectation value $a \cdot E$ would be replaced by a non-linear relation $a \cdot E_{\text{nl}}(E)$ which is equivalent to an energy-dependent light yield.

$$p_{\text{scint}}\left(n_{\text{ph}}, E, a\right) = \frac{(a \cdot E_{\text{nl}}\left(E\right))^{n_{\text{ph}}}}{n_{ph}!} e^{-a \cdot E_{\text{nl}}(E)}. \tag{5.2}$$

This formulation is valid for any kind of non-linear light output, that does not or only slightly increase the variance of the light yield.

The non-linearity of plastic scintillators is commonly described using a quenching model developed by J.D. Birks [Bir51]. In this model the non-linearity is described as a local quenching or saturation effect of the scintillation molecules along the charged particle track. In regions where the stopping power is high, the amount of scintillation photons generated is reduced as some of the scintillation molecules are damaged or already excited. The differential light output along an infinitesimal track length dx in this model is defined by

$$\frac{\mathrm{d}L}{\mathrm{d}x} = \frac{a \cdot \frac{\mathrm{d}E}{\mathrm{d}x}}{1 + k_B \cdot \frac{\mathrm{d}E}{\mathrm{d}x}}, \tag{5.3}$$

where a is the linear proportionality between electron energy deposit and light output (compare equation 5.1), dE/dx is the differential energy deposit or stopping power and k_B, the Birks coefficient, accounts for the non-linearity and its value depends on the scintillator material and the primary particle species. Without loss of generality equation 5.3 can be rephrased in terms of an effective energy deposit inside the scintillator that is proportional to the light output

$$\frac{\mathrm{d}E_{\text{nl}}}{\mathrm{d}x} = \frac{\frac{\mathrm{d}E}{\mathrm{d}x}}{1 + k_B \cdot \frac{\mathrm{d}E}{\mathrm{d}x}}. \tag{5.4}$$
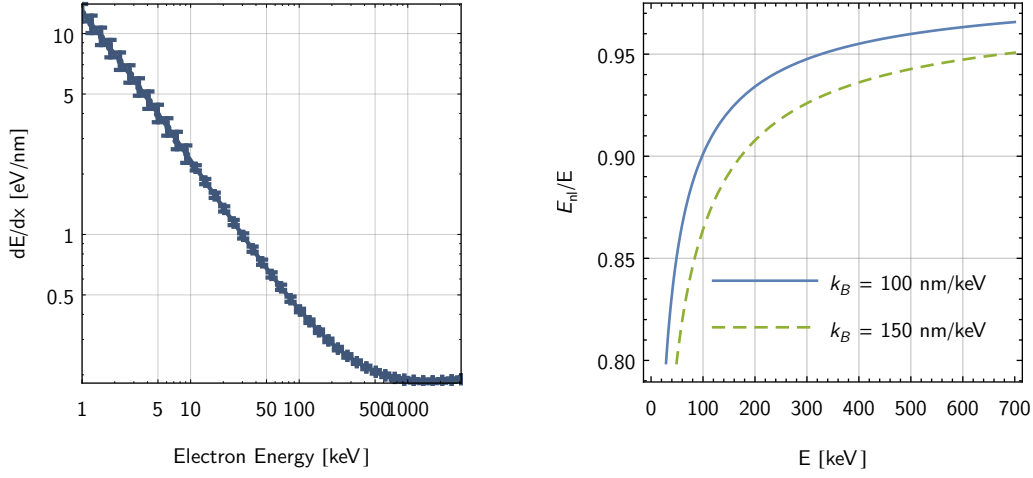
(a) dE/dx from ESTAR data with log-log-linear interpolation.

(b) Relative effective energy for $k_B = 100$ and $k_B = 150$ nm/keV

Fig. 5.2: Energy loss of electron in Polyvinyltoluene from ESTAR data. The effective energy contains the intrinsic scintillator non-linearity according to equation 5.6.

From this relation the dependence of the effective energy E_{nl} on the electron kinetic energy E follows to be

$$\frac{dE_{nl}}{dE} = \frac{1}{1 + k_B \cdot \frac{dE}{dx}(E)}, \tag{5.5}$$

where $dE/dx(E)$ denotes the stopping power for a certain energy E. The effective energy is the calculated by integrating over the complete electron energy loss:

$$E_{nl}(E) = \int_a^E \frac{1}{1 + k_B \cdot \frac{dE'}{dx}(E')\,dE'}. \tag{5.6}$$

In contrast to the previous implementation [Mes11] the Birks non-linearity is now calculated from ESTAR data [Ber+05] for the stopping power of electrons inside the scintillator material Polyvinyltoluene and implemented as an effective energy (proportional to the light yield) instead of assuming a non-linear energy-channel-relation.

The interpolating function between two nodes i and $i+1$ of the dE/dx data may be written as $k_i \cdot E_i^y$. The integral 5.6 is then given by

$$E_{nl}(E) = \left(\sum_{i=0}^{i=j} \int_{E_i}^{E_{i+1}} \frac{dE'}{1 + k_B \cdot k_i \cdot E'^{y_i}} dE' \right) + \int_{E_j}^{E} \frac{dE'}{1 + k_B \cdot k_j \cdot E'^{y_j}} dE', \tag{5.7}$$

where E_i is the energy of the i-th node and the index j is chosen such that $E_j < E$ with the highest possible node index. The integral to calculate the individual terms can be

written as

$$
\int_{E_1}^{E_2} \frac{\mathrm{d}E}{1 + k \cdot E^y} =
\begin{cases}
\frac{E_2 - E_1}{1 + k} & , y = 0 \\[2ex]
{}_2F_1\left(1, 1/y, 1 + 1/y; -k \cdot E_2^y\right) E_2 & , E_1 = 0, y > 0 \\[2ex]
\begin{aligned}
& {}_2F_1\left(1, 1/y, 1 + 1/y; -k \cdot E_2^y\right) E_2 \\
& - \frac{k^{-1/y} \pi \csc\left(\pi/y\right)}{y}
\end{aligned} & , E_1 = 0, y < 0 \\[3ex]
\begin{aligned}
& {}_2F_1\left(1, 1/y, 1 + 1/y; -k \cdot E_2^y\right) E_2 \\
& - {}_2F_1\left(1, 1/y, 1 + 1/y; -k \cdot E_1^y\right) E_1
\end{aligned} & , E_1 \neq 0, y \neq 0
\end{cases}
\tag{5.8}
$$

where ${}_2F_1\left(a, b, c; z\right)$ is the ordinary hypergeometric function.

Using these relations an efficient implementation is achieved by tabulating the sum in equation 5.7 for a given k_B so that for each energy only the last integral needs to be calculated. The log-log interpolation is based on 40 nodes in the range of 1 keV up to 3.1 MeV as shown in figure 5.2a. For plastic scintillators typical values of k_B are on the order of 100 - 150 nm/keV [Abe+11]. The resulting fraction of detected non-linear energy versus real electron energy is shown in figure 5.2b.

Multi-electron events

One peculiarity about the correct calculation of the non-linearity is its application to multi-electron events of the calibration sources. The electrons from these kind of events impinge on the detector separately, both spatially and in time. This leads to the fact that - especially when explained as a local saturation effect - the non-linearity needs to be applied separately for those electrons instead of being calculated for the summarized amplitude that is usually considered. To this end the non-linearity is applied to the single electron energies separately before summing up the detector amplitude

$$
E_{\mathrm{tot}} = \sum_i E_{\mathrm{nl}}\left(E_i\right).
\tag{5.9}
$$

Due to the separation in arrival time and the short signals produced by the detector, the argument of separated events still holds when considering other types of non-linearities (e.g. due to electronics).

5.2.2 Light Transport inside the Scintillator

The efficiency of light transport from the origin of scintillation to the photomultiplier tubes depends on the light transport efficiency inside the scintillator and light guides. Due to the refractive index of the scintillator material of $n_{\mathrm{scint}} = 1.58$ the critical angle for inner total reflection of photons can be calculated to be:

$$
\theta_{\mathrm{crit}} = \arcsin\left(\frac{n_{\mathrm{vac}}}{n_{\mathrm{scint}}}\right) \simeq 39.3°,
\tag{5.10}
$$

where the refractive index of vacuum is $n_\text{vac} = 1$. All photons hitting the scintillator surface below this angle are reflected and guided to the light guides. The refractive index of the light guide material PMMA is $n_\text{PMMA} \simeq 1.5$ which means that nearly no refraction occurs on the interface between scintillator and light guides and the condition for total inner reflection is almost the same as inside the scintillator. However, due to surface roughness and the fact that the interface usually contains a small slit, typical transmission efficiencies for the interfaces are on the order of 0.8 [Plo00]. Another important aspect to light transport is the self absorption of light inside the material. The attenuation length of BC400 is 250 mm ([Bic]) whereas the typical light attenuation in PMMA is 1000 mm.

Image 5.3 shows the result of a light transport simulation inside the detector system. The full geometry of the scintillator and light guides are implemented into an optical ray tracing simulation performed with Geant4 [Ago+03] in order to better understand several aspects of the light transport. If the surfaces of the scintillator and light guides are assumed perfectly event the total light output measured on all 6 PMTs is averaged over the scintillator surface is $f_\text{polish} = 0.193$ with a standard deviation of 0.5% over the surface. This variation is due to the structure of the light guides and their curvature.

The optical photon transport code of Geant4 allows to parametrize the surface roughness using the "polish" parameter of the Glisur model. The assumption in this model is that a rough surface consists of multiple micro facets and the effective surfaces on which photons reflect are tilted against the perfect surface. The polish parameter describes the amount of tilt of the micro-facets against the perfect surface where a value of 0 corresponds to maximum roughness and 1 corresponds to a perfectly polished surface. The effect of varying this surface property for the scintillator and the light guides has been studied in order to check how the light output and detector uniformity are influenced. Figure 5.4a shows the light yield versus the roughness parameter of the light guides assuming a perfect scintillator surface while figure 5.4b shows the same for varying the scintillator roughness parameter only. The drop in light yield for the same roughness value is much bigger for the light guides as for the scintillator as the path length inside the light guides is longer which leads to more reflections. However, the roughness of the light guide surfaces does not influence the uniformity of the detector. For the scintillator on the other hand the roughness also increases the non-uniformity of the detector as the number of reflections inside the scintillator is generally higher for photons originating from the centre of the scintillator.

A more realistic 2D light yield profile has been extracted where a polish value of 0.6 has been assumed for the scintillator. In this case the average light output drops to $f_\text{rough} = 0.10$ with a standard deviation of 13%. However, for the part of the detector that is actually covered by the decay electrons, the standard deviation is still 0.8%. This roughly resembles the measurements of the spatial detector response and is in agreement with an analysis of the spatial response performed in [Mes11]. This matching is performed only qualitatively and has potential for future improvement. Conservatively a large uncertainty is assumed in the analysis of detector systematics related to the spatial response (see section 7.3).

Concerning the mathematical treatment within the detector, the effect of light transport efficiency can generally be described as a Binomial distribution. If one assumes a number of generated scintillation photons n_ph at the origin of scintillation and their momenta
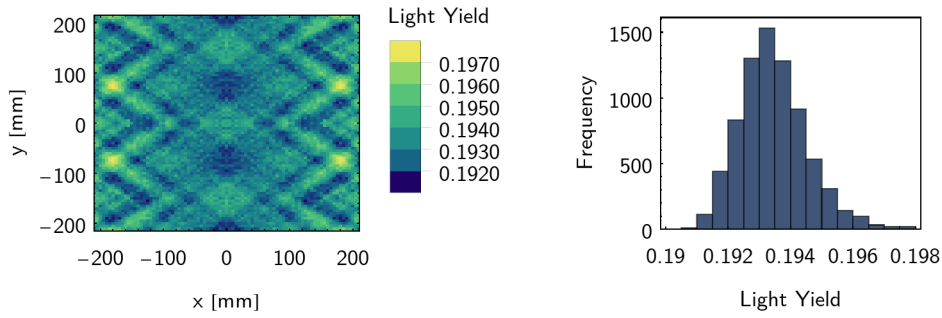
(a) Light yield without surface roughness.
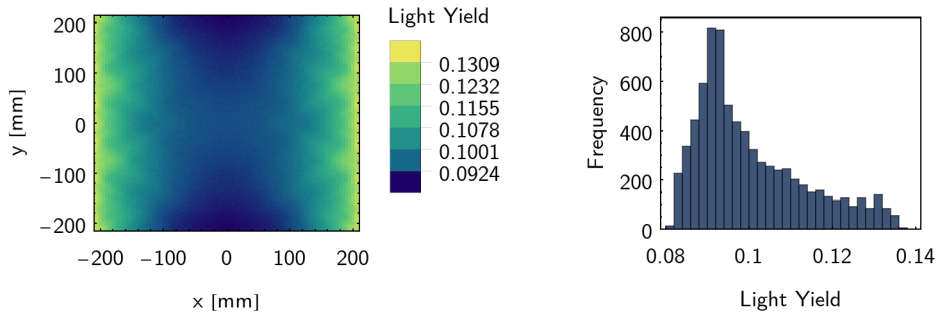
(b) Light yield with a scintillator surface roughness $f_{\text{polish}} = 0.6$.

Fig. 5.3: Comparison of the spatial light yield distribution for the PERKEO III detector simulated with Geant4 with and without surface roughness. The first image shows the spatial variation of the detector amplitude and a histogram for uniform illumination of the scintillator surface (a). The line structure in the detector response results from the geometry of the light guides. This structure vanishes if the scintillator surface is assumed to be rough because the variation of the detector response is dominated by the transport efficiency of the scintillator (b). This is modelled by using the Glisur model of Geant4 that parametrizes the surface roughness by a single parameter f_{polish}.

(a) Light guides

(b) Scintillator

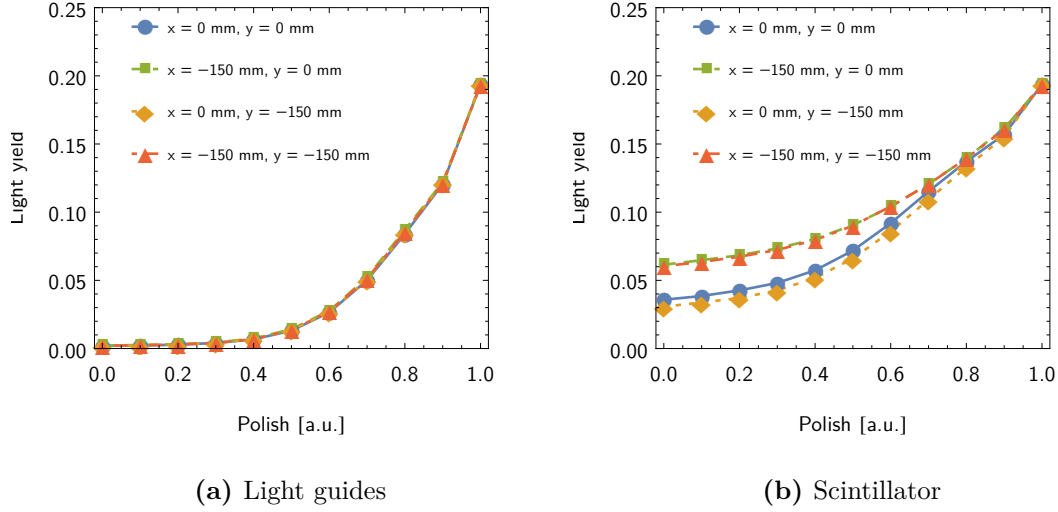**Fig. 5.4:** Comparison of the simulated light yield for the PERKEO III detectors when varying the surface roughness. The surface roughness of the light guides and scintillator are varied seperately and studied for different points on the scintillator surface to investigate the effect on the detector uniformity. The light yield is given as the fraction of 10^6 simulated photons at each point that reach one of the photomultipliers.

being distributed isotropically, this distribution of photons that reach the photomultipliers can be written as:

$$p_{\text{trans}}\left(n_{\text{t}}, n_{\text{ph}}, t\right) = \binom{n_{\text{ph}}}{n_{\text{t}}} t\left(\vec{x}\right)^{n_{\text{t}}} \left(1 - t\left(\vec{x}\right)\right)^{n_{\text{ph}} - n_{\text{t}}}, \tag{5.11}$$

where $t\left(\vec{x}\right)$ describes the transmission probability for a single photon which depends on the origin, $\vec{x}$, of the photon inside the scintillator. In the following $t\left(\vec{x}\right) = t$ is assumed to be a constant as the results of the light transport simulations show that the spatial variance is small. The error made by this assumption is investigated in [Roi18] based on the simulations described above. The results of this analysis are discussed in section 7.3.

One can calculate the combined distribution of scintillation and light transport by making use of cumulant and moment generating functions (CGF and MGF) of the respective distribution. The moment generating function of the Poisson process of scintillation (equation 5.1) is given as

$$M_{\text{scint}}\left(s; E\right) = e^{(e^s - 1)aE} \tag{5.12}$$

whereas that of the Binomial process (equation 5.11) for a single scintillation photon is given as

$$M_{\text{trans}}\left(s; t\right) = \left((e^s - 1)\, t\right). \tag{5.13}$$

The Moment generating function of the combined process is then given by nesting the logarithm of the MGF (also known as cumulant generating function) of the second process

into the MGF of the first process.

$$M_{\text{photon}}\left(s; n_{\text{ph}}, t\right) = M_{\text{scint}}\left(\ln M_{\text{trans}}\left(s, t\right)\right) = e^{(e^s - 1)aEt} \tag{5.14}$$

Comparing this expression to equation 5.12 one can identify the MGF of a Poisson process with mean aEt,

$$p_{\text{photon}}\left(n_{\text{t}}; E, a, t\right) = \frac{\left(a \cdot Et\right)^{n_{\text{t}}}}{n_{\text{t}}!} e^{-aEt}, \tag{5.15}$$

which describes the probability distribution of photons reaching the photomultipliers n_t.

5.3 Photomultipliers

The photons successfully transported through the scintillator and light-guides are detected using Hamamatsu R5924 fine mesh photomultipliers. In this section the influence of the photoelectron conversion as well as the gain process inside the photomultiplier on the measured spectra are discussed.

5.3.1 Photoelectron Production

The probability for conversion of a single photon reaching the photomultiplier surface is given by the so called quantum efficiency, which is specified to be $\sigma = 22\%$ in the range of the absorption maximum of 420 nm [Ham96]. This conversion process is independent for any single photon. Thus, for a bunch of photons this again can be described as a Binomial process:

$$p_{\text{pe}}\left(n_{\text{pe}}, n_{\text{t}}, \sigma\right) = \binom{n_{\text{t}}}{n_{\text{pe}}} \sigma^{n_{\text{pe}}} \left(1 - \sigma\right)^{n_{\text{t}} - n_{\text{pe}}}, \tag{5.16}$$

with the number of generated photoelectrons n_{pe} and initial photons n_{t}. Making use of the fact that a Poisson process followed by a Binomial process can be described as Poisson process (compare section 5.2.2) the combined probability distribution for the generated photoelectrons n_{pe} for a certain electron energy E can be written as:

$$p_{\text{pe}}\left(n_{\text{pe}}; E, f_{\text{pe}}\right) = \frac{\left(f_{\text{pe}} \cdot E\right)^{n}_{\text{pe}}}{n_{\text{pe}}!} e^{-f_{\text{pe}} \cdot E}, \text{ with } f_{\text{pe}} = at\sigma. \tag{5.17}$$

Where the characteristic property f_{pe} of the detector gives the characteristic number of photoelectrons per detected energy and is determined by calibration measurements.

In case the non-linearity of the scintillator mentioned in section 5.2 is considered, the photoelectron distribution may be modified so that the electron energy is replaced by an effective energy that resembles the shape of the non-linear light output

$$E_{\text{nl}}\left(E\right) = c \cdot L\left(E\right) \tag{5.18}$$

where $c \simeq 1/a$ is a constant to rescale the light output to units of energy. This way the definition of f_{pe} in equation 5.17 remains unchanged. Figure 5.1b shows the resulting photoelectron distribution for the discrete line spectrum of Bi^{207}. Within the fitting tool

this is implemented as a discrete histogram that contains the folding of the theoretical input spectrum with the photoelectron distribution in equation 5.17.

5.3.2 Photoelectron Multiplication

Usually the detector response is described in terms of the photoelectron distribution for a certain electron energy as given in equation 5.17, which ignores the contribution of the gain process of the photomultipliers to the energy resolution. This description leads to effective f_{pe} values which are smaller than the "real" number of photoelectrons per energy but typically provide a sufficient description of the energy resolution at higher energies.

In the following section the influence of the photomultiplier gain process is investigated. A description for the photomultiplier response is derived which describes the additional variance as well as higher order momenta of the resulting signal distribution. Although this higher order contributions do not have an impact on fits of the beta asymmetry, especially for conventional energy windows above 300 keV, they improve the description of the measured calibration spectra. Additionally, the gain process also modifies the expectation value for signal extinction compared to the Poisson description and is thus crucial for the determination of a correct trigger function.

Inside the photomultiplier the photoelectrons initially generated are amplified using multiple dynodes. A high voltage circuit (usually a simple voltage divider) is used to set the dynodes to an electric potential increasing with their distance to the first dynode. This leads to electrons being accelerated from one dynode to the other starting with the photocathode. If the acceleration potential is high enough, the electrons hitting the dynodes release secondary electrons from the dynode material. These are accelerated onto the next dynode. If the electron multiplication factor per stage, Λ, is greater than one this finally leads to the well known avalanche of electrons arriving at the last dynode.

The amplification of a single electron between two dynodes can be described as a Poisson process with mean value Λ, so that the probability distribution for a certain number of electrons n_e after this amplification stage is given by

$$p_1\left(\Lambda; n_e\right) = \frac{e^{-\Lambda}\Lambda_e^n}{n_e!}.$$
(5.19)

For multiple initial electrons n_0 the gain process for each electron stays the same and the resulting distribution $p_1(n_e)$ is a n_0-fold convolution of p_1 for a single primary electron

$$p_1\left(n_0, \Lambda; n_e\right) = \left(p_1\left(n_0 - 1, \Lambda\right) * p_1\left(1, \Lambda\right)\right)\left(n_e\right) = \frac{e^{-n_0\Lambda}\left(k\Lambda\right)^{n_e}}{n_e!} = p_1\left(n_0\Lambda; n_e\right)$$
(5.20)

Here, an idealised photomultiplier is considered where no screening of the electric field due to the electron cloud occurs. This assumption is usually fulfilled when photomultipliers are operated in the proportional regime.

In case of two stages the outcome can be calculated in the following way

$$p_2\left(n_0, \Lambda; n_e\right) = \sum_{n_1=0}^{\infty} p_1\left(n_0, \Lambda; n_1\right) p_1\left(n_1, \Lambda; n_e\right).$$
(5.21)

(a) Different number of stages N.

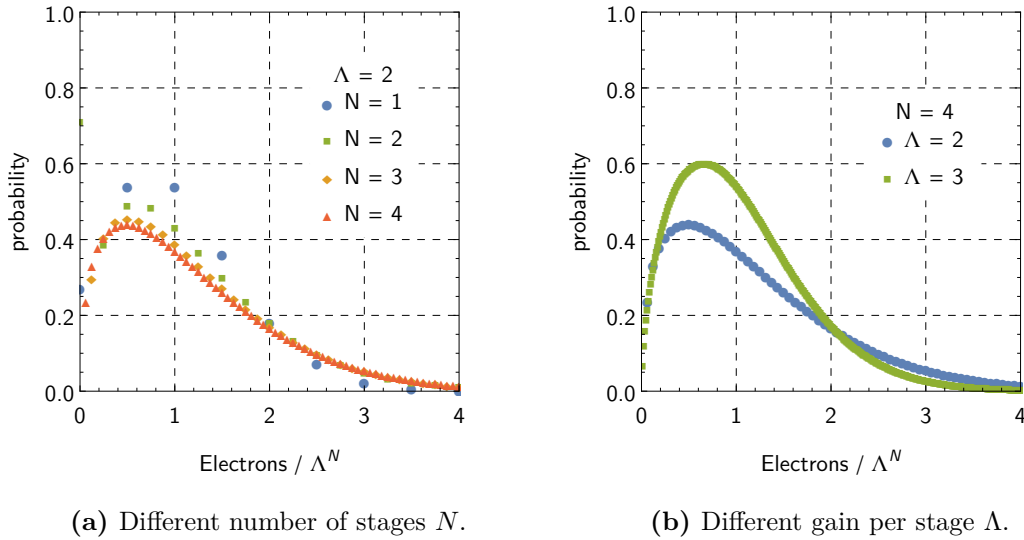**(b)** Different gain per stage Λ.

Fig. 5.5: Electron number distribution inside a photomultiplier. The plots compare the electron number distributions for N gain stages with mean amplification Λ and a single initial electron. Distributions are renormalized by Λ^{-N} for better comparison.

Figure 5.5 shows the resulting distributions for a different number of stages and different amplification. Obviously, the skewness of the distribution increases asymptotically with higher number of stages. The probability for having no electron at all is increasing with increasing N.

For $N = 19$ stages the correct implementation for the photomultiplier response inside a Monte Carlo simulation is trivial, calculating the exact analytical expression explicitly requires to carry out 18 sums over Poisson distributions with mean values of the order of the total photomultiplier gain $g = 10^6 - 10^8$ which is impracticable.

Galton-Watson Process

A way to overcome this problem is to use mathematical techniques initially developed to describe population growth. The discrete-time Galton-Watson process describes the development of a population where each individuals' probability, for having a certain number of descendants in the next generation, is given by the same offspring distribution $p(n)$ [Har89]. Such a process is identical to the electron amplification inside a photomultiplier, if the dynodes are identified as generations and the offspring distribution is the Poisson distribution 5.19.

The moment generating function of the probability density describing the number of

individuals in the k-th generation is given by

$$M_k\left(s\right) = M_{k-1}\left(C_1\left(s\right)\right),$$

$$\text{with } M\left(s\right) = E\left(e^{sn}\right) = \sum_{n=0}^{\infty} e^{isn} p\left(n\right), \tag{5.22}$$

$$\text{and } C_1\left(s\right) = \ln M_1\left(s\right).$$

Here the moment generating function $M(s)$ of a discrete probability density function $p(n)$ is defined by its Z-transformation and the cumulant generating function $C(s)$ is the logarithm of the moment generating function.

In the present case of a Poisson offspring distribution the cumulant generating function becomes

$$C_1\left(s; \Lambda\right) = \left(e^s - 1\right)\Lambda \tag{5.23}$$

as already discussed in section 5.2.2. Assuming a discrete distribution of initial photoelectrons of the form

$$p_{\text{pe}}\left(n; n_{\text{pe}}\right) = \begin{cases} 1 & n = n_{\text{pe}} \\ 0 & n \neq n_{\text{pe}} \end{cases} \tag{5.24}$$

the moment generating function for this distribution is given by

$$M_0\left(s; n_{\text{pe}}\right) = e^{sn_{\text{pe}}}. \tag{5.25}$$

From this the moment generating function of the full Galton-Watson process for the k-th generation becomes

$$\begin{aligned} M_k\left(t; \Lambda, n_{\text{pe}}\right) &= M_0\left(C_1\left(C_1\left(..., \Lambda\right), \Lambda\right), n_{\text{pe}}\right) \\ &= e^{\left(e^{\left(e^{\cdots}-1\right)\Lambda}-1\right)\Lambda n_{\text{pe}}} \end{aligned} \tag{5.26}$$

where the dots denote that nesting should continue up to the k-th level.

Instead of the discrete photoelectron distribution, the Poisson distribution from equation 5.17 can be used which has the following moment generating function:

$$M_0\left(t; E, f_{\text{pe}}\right) = e^{\left(e^t-1\right)f_{\text{pe}}\cdot E}. \tag{5.27}$$

The k-th generation MGF then becomes

$$M_k\left(t; E, f_{\text{pe}}, \Lambda\right) = e^{\left(e^{\left(e^{\left(e^{\cdots}-1\right)\Lambda}-1\right)\Lambda}-1\right)f_{\text{pe}}E}, \tag{5.28}$$

which defines the complete detector response.
As the name suggests the moments of the distribution can be obtained from the moment generating function via

$$m_n = \frac{\mathrm{d}^n M}{\mathrm{d}t^n}\left(t = 0\right), \tag{5.29}$$

where m_n denotes the n-th moment. The mean μ and variance σ^2 are then given by

$$\mu = m_1 = f_{\text{pe}}E\Lambda^K,$$
$$\sigma^2 = m_2 - m_1^2 = f_{\text{pe}}E\Lambda^K \left(\sum_{k=0}^{K} \Lambda^k \right). \tag{5.30}$$

The relative width of the signal distribution for a total number of stages N can then be approximated as

$$\left(\frac{\sigma}{\mu}\right)_{Det} = \frac{1}{\sqrt{f_{\text{pe}}E}} \cdot \sqrt{\frac{\sum_{k=0}^{N} \Lambda^k}{\Lambda^N}} \underset{N\to\infty}{=} \frac{1}{\sqrt{f_{\text{pe}}E}} \sqrt{\frac{\Lambda}{\Lambda - 1}} = \left(\frac{\sigma}{\mu}\right)_{\text{pe}} \cdot \sqrt{\frac{\Lambda}{\Lambda - 1}}. \tag{5.31}$$

For typical values of the photomultiplier gain $g = \Lambda^N \simeq 10^7$ the variance of the full detector response is a factor of 1.75 bigger than that of the photoelectron distribution.

Another important property of the photomultiplier response is the extinction probability which defines the probability that no signal is generated for a certain number of initial photoelectrons. For this the probability generating function $P(t)$ of the offspring and initial photoelectron distributions need to be calculated which are defined as the expectation value of t^n of a discrete PDF with variable n

$$P(t) = \sum_{n=0}^{\infty} p(n) t^n = \sum_{n=0}^{\infty} E(t^n). \tag{5.32}$$

The important property for this concern being that $P(0)$ defines the expectation value $E(0)$. For the initial photoelectron distribution 5.24 the PGF is given by

$$P_0(t; n_{\text{ph}}) = t^{n_{\text{pe}}}, \tag{5.33}$$

whereas the PGF for the Poisson offspring distribution can be calculated to be

$$P_1(t; \Lambda) = e^{(t-1)\Lambda}. \tag{5.34}$$

For a Galton-Watson-Process the PGF for the k-th generation then is defined by nesting the PGFs of each generation

$$P_k(t; \Lambda, n_{\text{pe}}) = p_0(p_1(p_1(\cdots, \Lambda), \Lambda), n_{\text{pe}}) = \left(e^{\left(e^{(\cdots - 1)\Lambda} - 1 \right)\Lambda} \right)^{n_{\text{pe}}} \tag{5.35}$$

Although a bit lengthy this expression allows the exact calculation of the extinction probability for any finite number of stages and gain values.

The complete electron number distribution representing the photomultiplier response can be calculated by performing the inverse Z-transformation of the moment generating function given in equation 5.26. However, there is no closed analytical solution for the required integral and numerical integration is challenging due to the highly oscillating nature of the integrand.

Diffusion Approximation

In order to obtain an analytical approximation for the photomultiplier response a Diffusion Approximation [Fel51] can be used. In [Tan82] this approximation method has been used with a similar motivation.

The basic idea of this approximation is to approximate the behaviour of the discrete time Markov Chain by a continuous time Markov Chain. This results in the following moment generating function:

$$M\left(t; A, B\right) = e^{\frac{-At}{1+Bt}}.$$
(5.36)

Compared to the MGF for the detector response derived above (compare equation 5.26) the advantage of this formulation is that the inverse Laplace-transformation gives a closed analytical expression as has been derived in [Tan82]

$$p\left(x; A, B\right) = e^{-A/B}\left(\delta\left(x\right) + \frac{e^{-x/B}\sqrt{A/x}}{B}I_1\left(\frac{2\sqrt{Ax}}{B}\right)\right),$$
(5.37)

where $I_1\left(x\right)$ is the modified Bessel function of the first kind. The discrete number of electrons n has been replaced with the continuous variable x. Using equations 5.36 and 5.29 the mean and variance can be calculated to be

$$\begin{aligned} \mu &= A, \\ \sigma^2 &= 2AB. \end{aligned}$$
(5.38)

Comparing this to the moments of the photomultiplier signal distribution given by equation 5.26

$$\begin{aligned} \mu &= n_{\mathrm{pe}}\Lambda^N, \\ \sigma^2 &= n_{\mathrm{pe}}\Lambda^N\left(\sum_{k=0}^{N-1}\Lambda^k\right) \end{aligned}$$
(5.39)

the parameters A and B of the Diffusion Approximation follow

$$\begin{aligned} A &= n_{\mathrm{pe}}\Lambda^N, \\ B &= \sum_{k=0}^{N-1}\Lambda^k/2. \end{aligned}$$
(5.40)

This fully defines the probability density given in equation 5.37.

Improved approximation

Figures 5.6a and 5.6b show a comparison between the simulated and calculated photomultiplier response where $N = 19$ stages have been simulated as single Poisson processes with a photomultiplier gain of $\Lambda = 2$. Especially the response for $n_{\mathrm{pe}} = 1$ obviously does not represent the simulation well. This is due to the fact that the extinction probability

(a) Diffusion Approximation, $n_{pe} = 1$

(b) Diffusion Approximation, $n_{pe} = 10$

(c) Improved Approximation, $n_{pe} = 1$

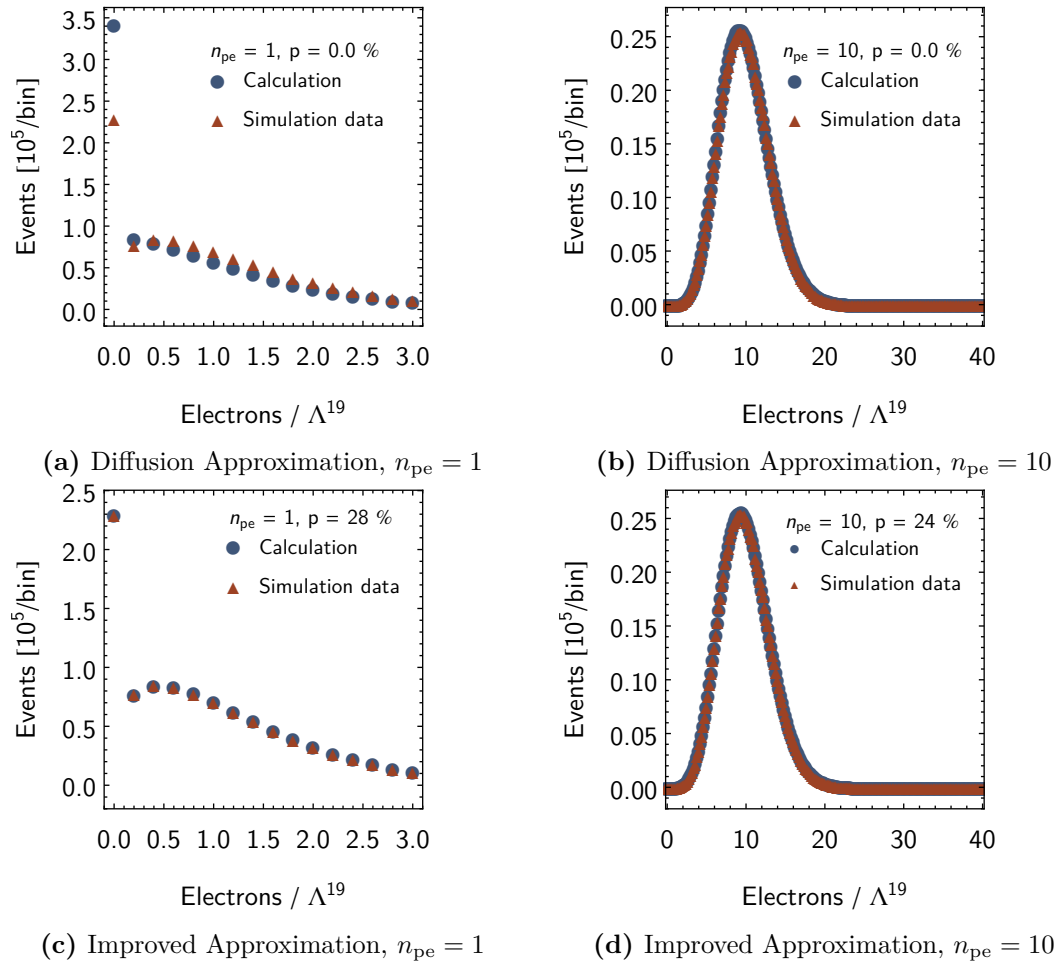**(d)** Improved Approximation, $n_{pe} = 10$

Fig. 5.6: Comparison calculated photomultiplier response with the Diffusion Approximation according to equation 5.37 (a and b) and Improved Approximation according to equation 5.41 (c and d). The photomultiplier gain has been set to $\Lambda = 2$ and the data are binned in units of $0.2\Lambda^{19}$. The calculation results have been averaged by numerical integration over the corresponding bins.

$p(0, A, B)$ is defined as $e^{-A/B}$. This is not a goof approximation for the exact solution derived in equation 5.35. However, even in the case of $n_{\mathrm{pe}} = 10$ where the extinction probability is negligible, the χ^2 results in a probability of 0.0 %. Reasonable performance is achieved for $n_{\mathrm{pe}} = 100$ and above. With a typical value of $f_{\mathrm{pe}} = 0.25$ keV^{-1}, this is equal to an energy of $E = n_{\mathrm{pe}}/f_{\mathrm{pe}} = 400$ keV.

In order to improve the approximation, first the value for $p(0, A, B)$ is calculated according to equation 5.35. Moreover, for lower numbers of initial photoelectrons the Poisson distribution describing the electron distribution after the first photomultiplier stage is calculated explicitly and then the Diffusion Approximation for $N - 1$ stages is applied. This is repeated recursively for up to 4 stages and can be written in the form

$$p(x; \Lambda, n_{\mathrm{pe}}, n) = \begin{cases} P_n(0; \Lambda, n_{\mathrm{pe}}) & x = 0, \\ \sum_{i=1}^{\infty} p_1(i; \Lambda, n_{\mathrm{pe}}) * p(x; \Lambda, i, n-1) & x <= 20, \ n > 14 \\ e^{-A/B}\left(\delta(x) + \frac{e^{-x/B}\sqrt{A/x}}{B} I_1\left(\frac{2\sqrt{Ax}}{B}\right)\right) & x > 20 \end{cases}, \quad (5.41)$$

where the definitions of A and B in equation 5.40, P_n according to equation 5.35 and p_1 from equation 5.20 are used. This improved approximation provides a sufficient description of the simulated photomultiplier response even for a single initial photoelectron as illustrated in figure 5.6c.

Within the fitting routine the photomultiplier response is included by calculating the response spectrum for each photoelectron bin. The resulting distribution is binned in units of $0.2 \cdot \Lambda^{19}$ where for lower initial photoelectron numbers trapezoidal integration is used to calculate the binned response function. The resulting spectrum as shown in figure 5.1c is then calculated as a composition of these response spectra according to the photoelectron distribution.

The exact shape of the signal distribution only changes slightly with Λ so that variations in the total photomultiplier gain of $g = \Lambda^{19} = 10^6 - 10^8$ only change the number of photoelectrons f_{pe} and have no impact on the result of the analysis. During the analysis a gain of $G \simeq 10^7$ is assumed which gives $\Lambda = 2.34$. The number of photoelectrons extracted during the calibration analysis (see section 6.1) is then

$$f_{\mathrm{pe}} = 0.25 \text{ keV}^{-1}. \quad (5.42)$$

5.4 Energy-channel relation

The resulting charge output of the photomultiplier is measured with a charge integrating QDC resulting in a binned amplitude. Due to the intrinsic resolution and noise of the QDCs the resulting output for a discrete signal is a distribution of amplitudes that is described by a Gauss distribution

$$p(ch; x, G, \sigma_{\mathrm{QDC}}) = \frac{1}{\sigma_{\mathrm{QDC}}\sqrt{2\pi}} e^{-\frac{1}{2}\left(\frac{ch - x \cdot G}{\sigma_{\mathrm{QDC}}}\right)^2}, \quad (5.43)$$

where the relation between the measured charge signal x and the QDC channel number ch is given by the gain factor G. The characteristic width of the distribution is given by the detector pedestal, $\sigma_{\mathrm{QDC}} \simeq 1$ ch. Since the pedestals are subtracted during the raw data reduction the energy-channel relation is a linear function without offset.

Folding the charge output spectrum with the resolution function 5.43 finally gives the output spectrum describing the measured data. In order to decorrelate the number of photoelectrons per electron energy f_{pe} and the gain factor an effective gain in units of channels per keV is used as a fit parameter

$$G = g \cdot f_{\mathrm{pe}} \cdot \Lambda^{19} \simeq 0.33 \text{ ch/keV}. \tag{5.44}$$

When fitting the detector model this way the light output f_{pe} is solely determined by the width of the spectrum whereas G is determined by the relation between the measured peak position in QDC channels and the theoretical peak position in energy.

5.5 Multi-PMT model

Since multiple PMTs are used to read out the detector, the generated scintillation light is distributed among several PMTs. For each of these photomultipliers and light-guides the same photoelectron distribution as in equation 5.17 is valid. The fraction of scintillation light reaching another PMT may be absorbed into a lower light transport probability. For simplification readout by two photomultipliers with photoelectron numbers $f_{\mathrm{pe,a}}$ and $f_{\mathrm{pe,b}}$ is assumed. Here $f_{\mathrm{pe,a}}$ and $f_{\mathrm{pe,b}}$ may account for different light transport probabilities and different quantum efficiencies of the PMTs. The combined photoelectron distribution of the two PMTs is then given by folding the two respective photoelectron distributions

$$\begin{aligned} p_{\mathrm{pe}}\left(n_{\mathrm{pe}}; E, f_{\mathrm{pe,a}}, f_{\mathrm{pe,b}}\right) &= \sum_{i=0}^{n_{\mathrm{pe}}} \frac{(f_{\mathrm{pe,a}} \cdot E)^i}{i!} e^{-f_{\mathrm{pe,a}} \cdot E} \frac{(f_{\mathrm{pe,b}} \cdot E)^{n_{\mathrm{pe}}-i}}{(n_{\mathrm{pe}}-i)!} e^{-f_{\mathrm{pe,b}} \cdot E} \\ &= \frac{((f_{\mathrm{pe,a}} + f_{\mathrm{pe,b}}) E)^{n_{\mathrm{pe}}}}{n_{\mathrm{pe}}!} e^{-(f_{\mathrm{pe,a}} + f_{\mathrm{pe,b}})E}. \end{aligned} \tag{5.45}$$

This again follows a Poisson distribution with mean value $f_{\mathrm{pe,a}} + f_{\mathrm{pe,b}}$. For this reason the photoelectron distribution for multiple PMTs even in the case of different quantum efficiencies is correctly described using a single photoelectron number f_{pe}.

Due to its nature as a Galton-Watson process the photoelectron multiplication for each initial photoelectron is independent from the total number of photoelectrons in this PMT. It is obvious that this also implies that the gain process is not affected by using multiple photomultipliers with the same gain. However, the light transport and photocathode of the single photomultipliers can not be considered perfectly equal. Since the individual high voltages of the PMTs have been adjusted to give the most uniform detector response it is likely that the output signal of the photomultipliers can be assumed to be equal for the same amount of light input. This means that a potential variation of the light transport and photocathode efficiencies is compensated by different gain factors in the photomultiplier.
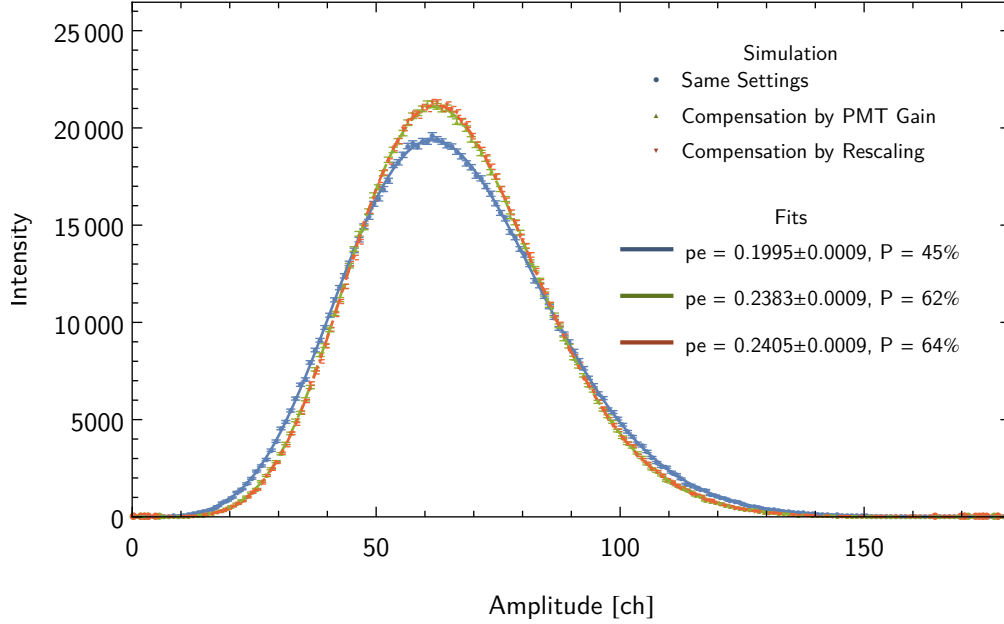
Fig. 5.7: Simulated detector response for events with 100 keV electron energy for a scintillator read out by two photomultipliers. (1) $f_{\text{pe,a}} = f_{\text{pe,b}} = 0.1$ MeV^{-1}, $\lambda_{\text{a}} = \lambda_{\text{b}} = 2$, $G_{\text{a}} = G_{\text{b}} = 0.33$ch / keV, (2) $f_{\text{pe,b}} = 0.15$MeV^{-1}, $\lambda_{\text{b}} = 1.97$, (3) $f_{\text{pe,b}} = 0.15$, $G_{\text{b}} = 0.22$. The fits to the simulations have been performed using the detector model described in previous sections for a single PMT. The QDC gain factor G and PMT gain factor λ are fixed in the fit using f_{pe} and a norm as only parameters. The results show that the model still describes the data well with an effective photoelectron number that is slightly reduced compared with the expectation.

Figure 5.7 shows a comparison of combined spectra of 2 photomultipliers. The first simulation has been performed assuming two PMTs with equal photoelectron number $f_{\text{pe}} = 0.1$ 1/MeV and same gain $\lambda = 2.$, whereas in the second simulation a higher photoelectron number for the second PMT of $f_{\text{pe,a}} = 0.15$ 1/MeV is compensated by a lower gain of $\lambda_2 = 2.251$ and in the third case this compensation is made by linearly rescaling the amplitude of the second PMT. For all simulations an initial electron kinetic energy of 100 keV is used and 10^6 events are simulated.

The detector model derived above is fitted to the data where only the photoelectron number f_{pe} and a norm have been used as free parameters and the photomultiplier gain has been fixed to $\lambda = 2$ in all cases. In both cases the fits describe the data well with a slightly reduced number of photoelectrons compared to the expectation of $f_{\text{pe}} = f_{\text{pe,a}} + f_{\text{pe,b}} = 0.25$. Due to the higher average photoelectron number, the resulting the peak width for the second simulation is reduced as expected. The slight reduction of the photoelectron number when comparing the rescaling due to PMT gain versus linear rescaling is due to the increase to the PMT response contribution to the standard deviation according to equation 5.31. Although the total photomultiplier gain is reduced by 33% the gain reduction per PMT step is just 2%. The same analysis has been performed assuming
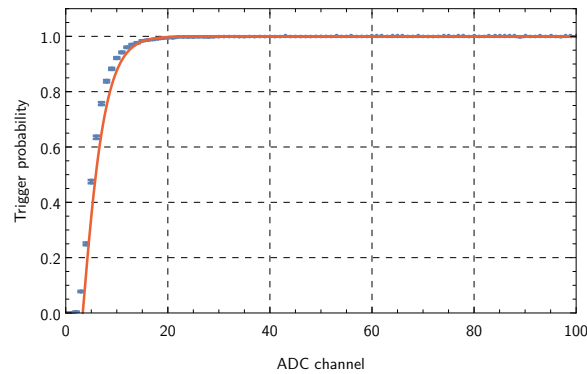
Fig. 5.8: Triggerfunction extracted from backscattering data according to equation 5.47 and a fit of the trigger function model.

an initial electron energy of 500 keV, which yields consistent results for the value of the effective photoelectron number.

Bearing in mind that the resulting f_{pe} value is an effective parameter, this shows that the detector model is sufficient to describe data resulting from a detector setup with multiple PMTs where different photoelectron numbers of the single PMTs are compensated by their gain settings or linear rescaling of the amplitudes in the data reduction.

5.6 Trigger function

To account for the trigger efficiency of the detectors an effective model for trigger function is used [Mun06]

$$T(ch) = 1 - (1-p)^{a \cdot ch} \left(1 + \frac{a \cdot ch \cdot p}{1-p} \right), \tag{5.46}$$

where p is the probability for a photon to trigger a certain photomultiplier and $a \cdot ch$ is the number of photons present for a certain channel. The trigger function can be derived from the data by calculating the spectrum

$$T(ch) = \frac{P_3(ch)}{P_2(ch) + P_3(ch)},$$

with $P_1(ch)$: events that trigger only detector 1, $\tag{5.47}$

$P_2(ch)$: events that trigger only detector 2,

$P_3(ch)$: events that trigger both detectors and detector 1 first.

Such a spectrum is shown in figure 5.8. Fitting the trigger function model to this spectrum gives

$$a \simeq 0.32, \ p \simeq 0.78. \tag{5.48}$$

In the present analysis no fits to the spectra below ADC channel 25 are performed. Here the trigger function is essentially one and described sufficiently well by the trigger function

in equation 5.46. However, for systematic analysis of backscattering systematics this description is insufficient. Extensions to this model including the correct photoelectron statistics [Fri08; Mes11] only lead to a partial improvement. A new calculation of the trigger function, motivated by the analysis of undetected backscattering corrections is performed in [Roi18] and includes the complete model of the photomultiplier signal described in section 5.3.2 as well as the spatial dependence of the light distribution.

Chapter 6

Spectral Analysis

In this chapter the analysis of the measured spectra is outlined. The detector model described in the previous chapter is applied to the theoretical spectra. This is necessary to analyse the calibration measurements and to extract the free parameters of the detector model. This information is then used to analyse the experimental beta asymmetry. The latter is performed in two ways, a single parameter analysis extracting the beta asymmetry parameter A, under the assumption of full validity of the Standard Model and an energy-dependent analysis dealing with the simultaneous extraction of the Fierz interference term, b, and λ, the ratio of axialvector and vector coupling constants.

The blinded analysis of the beta asymmetry has been carried out before the combined analysis of λ and b in order to eliminate any potential bias implied by the consistency of the result with the Standard Model. Both analyses are related concerning major parts of the analysis, though.

This chapter focusses on the results of the analysis including statistical uncertainties. The detailed consideration of systematic effects is then covered in the following chapters.

6.1 Calibration Fits

In order to obtain the remaining free parameters of the detector model described in chapter 5, a simultaneous fit to spectra of each full calibration measurement is performed. As opposed to the detector calibration scheme used previously [Mun+13], where neutron decay spectra are used, this method provides a clean detector calibration in the sense that it is independent of any assumptions about hypothetical additional effective couplings for charged currents. This fulfils a major requirement for the analysis of physics beyond the Standard Model.

Figure 6.1 shows the spectra and the corresponding fit for one of these calibration sets.

The analysis is performed separately for each calibration measurement. The free parameters which require extraction from fitting the calibration spectra are the detector gain, G (see section 5.4), the effective number of photoelectrons, f_{pe} (see section 5.3.1) and the Birks coefficient k_B to describe the detector non-linearity (see section 5.2.1). In addition the norms of the spectra are used as free fit parameters as well.

The results of such a calibration fit is shown in figure 6.1. Figure 6.2 shows the extracted calibration parameters for all calibration measurements analysed. The individual parameter sets obtained are not necessarily compatible with each other.

The comparatively strong scattering of the number of photoelectrons can be attributed to the fact that, as discussed in section 5.5, the effective number of photoelectrons as a
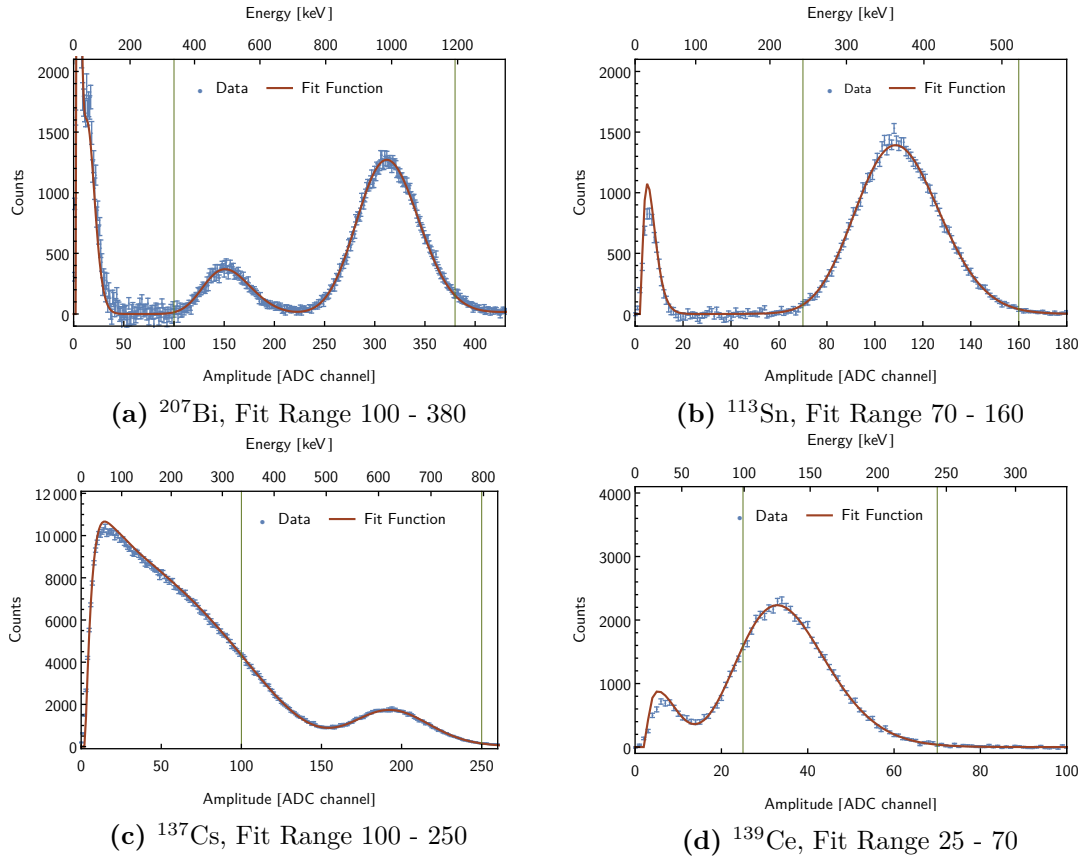
(a) ^{207}Bi, Fit Range 100 - 380

(b) ^{113}Sn, Fit Range 70 - 160

(c) ^{137}Cs, Fit Range 100 - 250

(d) ^{139}Ce, Fit Range 25 - 70

Fig. 6.1: Example for the measured calibration spectra and the simultaneous fit performed to extract the free parameters of the detector response model (see chapter 5).

measure of detector resolution will vary when rescaling the detector amplitude differently (e.g. when applying the drift correction). In the beginning of the measurements the detector function differs in the extracted parameters. This is because of a different high voltage setting and rescaling parameters used, which affects the energy resolution, the detector non-linearity and, due to a strong correlation of about 0.97 between G and k_B, also the extracted detector gain. The deviation observed in the last parts of the measurement on the other hand is correlated with the absence of measurements with ^{207}Bi, which are due to a malfunction of the scanner device. Both these observations indicate that only considering scintillator non-linearities for the description of the complete detector non-linearity is not necessarily correct with respect to the underlying physics. A systematic analysis of the detector non-linearity and its impact on the measurement of the beta asymmetry is discussed in section 7.2.

The averaged reduced χ^2 of these fits is 1.18 for detector 1 and 1.26 for detector 2. The number of degrees of freedom varies between 282 and 562 depending on which spectra are available in each individual calibration set. The improvements made to the detector model provide a huge enhancement in the overall fit quality compared to the previous analysis. Previously, reduced χ^2 values on the order of 1.5 have been obtained for much
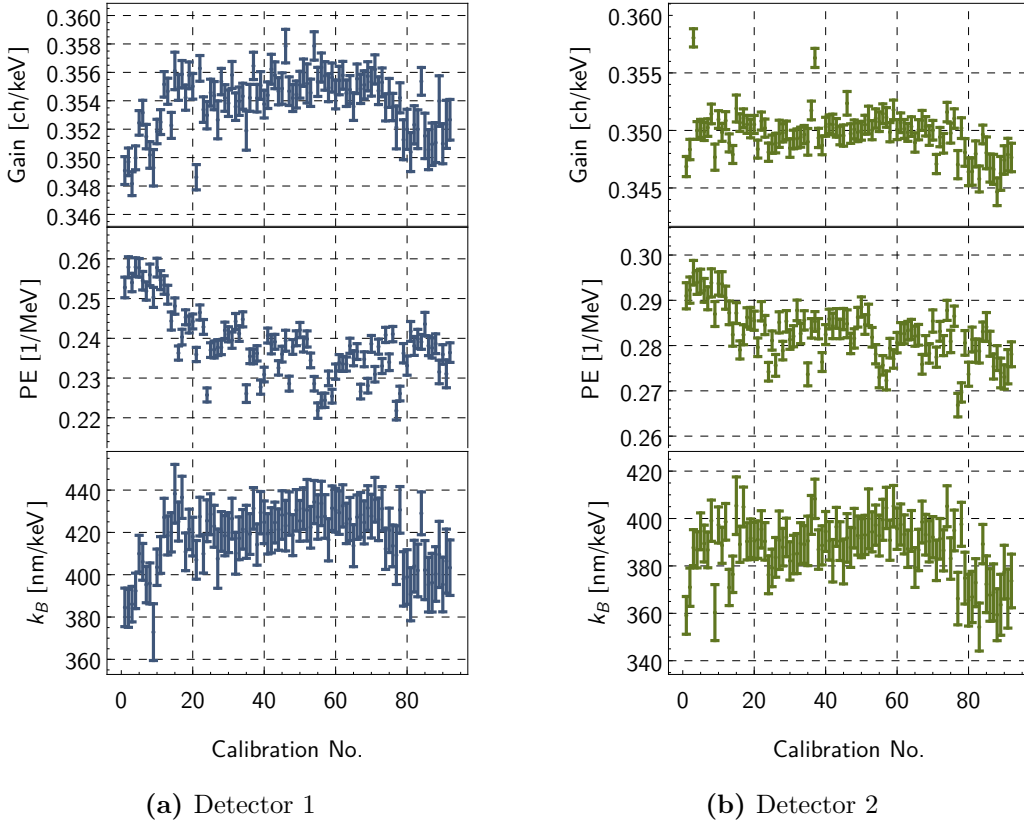
Fig. 6.2: Results of the fits to the calibration spectra. Error bars are given as 68.23% C.L. for three free parameters including parameter correlations.

narrower fit ranges [Mes11]. The remaining deviation from 1 can be attributed to detector drifts in between different measurements of calibration sources, in conjunction with an imperfect drift correction. This would slightly shift the different spectra with respect to each other and thus cause an increase in χ^2. This statement is supported by the fact that performing fits to the individual spectra leads to lower χ^2 values.

For each of these calibration fits the best fit parameters for G, f_{pe} and k_B including the full covariance matrix are extracted. For the calibration fit shown in figure 6.1 the results for the calibration are:

$$G = 0.3544(10) \text{ keV/ch}, \ f_{\mathrm{pe}} = 0.2316(19) \text{ keV}^{-1}, \ k_{\mathrm{B}} = 430.5(10.3) \text{ nm/keV}, \ (68.27\%\text{C.L.})$$

$$\rho_{G,f_{\mathrm{pe}},k_{\mathrm{B}}} = \begin{pmatrix} 1 & 0.16 & 0.98 \\ 0.16 & 1 & 0.14 \\ 0.98 & 0.14 & 1 \end{pmatrix}.$$

(6.1)

The average calibrations for the four chopper datasets are listed in table 6.1.

Dataset	$G[\text{keV/ch}]$	$f_\text{pe}[\text{keV}^{-1}]$	$k_\text{B}[\text{nm/keV}]$
Det1 / 94 Hz	0.35493(14)	0.24196(29)	428.5(1.4)
Det1 / 83 Hz	0.35566(16)	0.23447(31)	437.2(1.6)
Det2 / 94 Hz	0.35105(12)	0.28548(34)	401.3(1.2)
Det2 / 83 Hz	0.35070(14)	0.28065(35)	402.6(1.4)

Tbl. 6.1: Weighted average of the calibration fit results for different chopper frequencies and detectors. The uncertainties are the correlated 68.27% uncertainties without considering any systematics.

6.1.1 Spatial Response Correction

As mentioned in section 5.2.2, the amplitude of the detector response varies over the detector surface, giving lower amplitudes in the centre of the detector. This needs to be taken into account when applying the calibration extracted from the calibration measurements to the neutron decay data. To first order, neglecting the point spread of the electrons due to their motion within the magnetic field [Dub15], the electron conversion sources are assumed as point-like sources as opposed to the spread rectangular source of the neutron beam.

In a first analysis [Mes11], based on the 2D scan measurements performed during the beamtime, this effect has been studied by calculating the mean detector amplitude under the area covered by the neutron beam and its variation. Figure 6.3 shows the relative detector gain as measured during the scan measurements. From these measurements the detector uniformity within the area covered by the neutron beam is calculated to be 1% and the mean detector amplitude relative to a point source is 1.0032(15). However, in this analysis the point spread of electrons is neglected. The result is a detector response which appears more homogeneous as it just represents the variations of the detector amplitudes measured in the scan measurements.

A more detailed calculation of the effect of the detectors spatial response has been performed in [Roi18]. This new analysis is based on the detector response simulations performed in this thesis (see section 5.2.2) and also includes the magnetic point spread of electrons inside the magnetic field according to [Dub15]. Using this description the detector uniformity within the same area is 2.5%.

For the results presented in this chapter a first correction is included based on the old analysis. The detector gain G and light yield f_pe extracted from the calibration measurements are scaled by the factor of 1.0032. Moreover, an additional Gaussian broadening with a width of 1% is considered. A refinement of this correction and related uncertainties, based on the new analysis, are discussed in section 7.3.
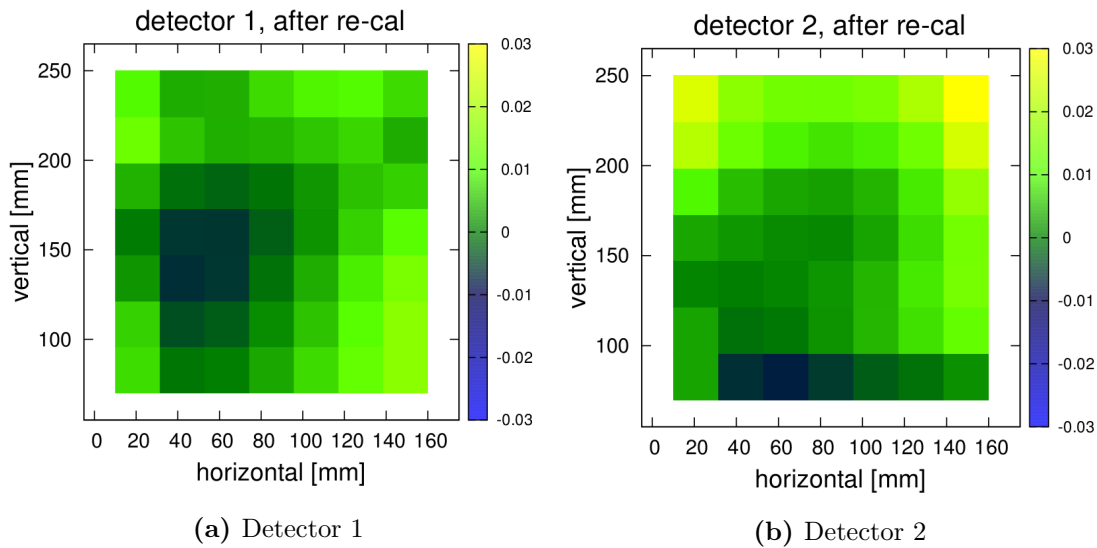
(a) Detector 1   **(b)** Detector 2

Fig. 6.3: Scan measurements performed during the 2009 beamtime taken from [Mes11]. The variation of the measured detector amplitude within the area covered the neutron beam is 1%.

6.2 Fitting the Beta Asymmetry

The spectra for the experimental beta asymmetry are extracted for each calibration dataset corresponding to the data reduction process outlined in section 4.3.2. This is done for all beta data between two calibration measurements resulting in 89 datasets for each detector. Each of these is assigned to the calibration measurement performed in advance, using the extracted calibration parameters. For the extraction of the beta asymmetry parameter A from these datasets, the spectra are fitted using the experimental beta asymmetry including recoil order and radiative correction as described in section 2.1. The fit parameter used in this case is in fact λ instead of A. This is due to the fact that the fit includes the recoil and radiative corrections that are a function of λ (compare section 2.2.1). Most of the systematics however, can be best described as a relative correction to the beta asymmetry $\Delta A/A$, independent of the central value A. For this reason the fit results are given in terms of the beta asymmetry A rather than λ.

Figure 6.4 shows the fits to the combined 4 datasets for each detector and chopper frequency for a fit range of 291 - 694 keV. The calibration parameters used are the average of the respective individual calibrations.

6.2.1 Weighted mean of individual Datasets

The statistical uncertainty obtained from the fit of the experimental beta asymmetry gives the dominant contribution to the overall uncertainty for each dataset. Another contribution comes from the statistical uncertainty of the calibration fits. Given the three parameters detector gain G, f_{pe}, k_B the uncertainty contribution to the beta asymmetry

(a) Detector 1, 94 Hz

(b) Detector 1, 83 Hz

(c) Detector 2, 94 Hz
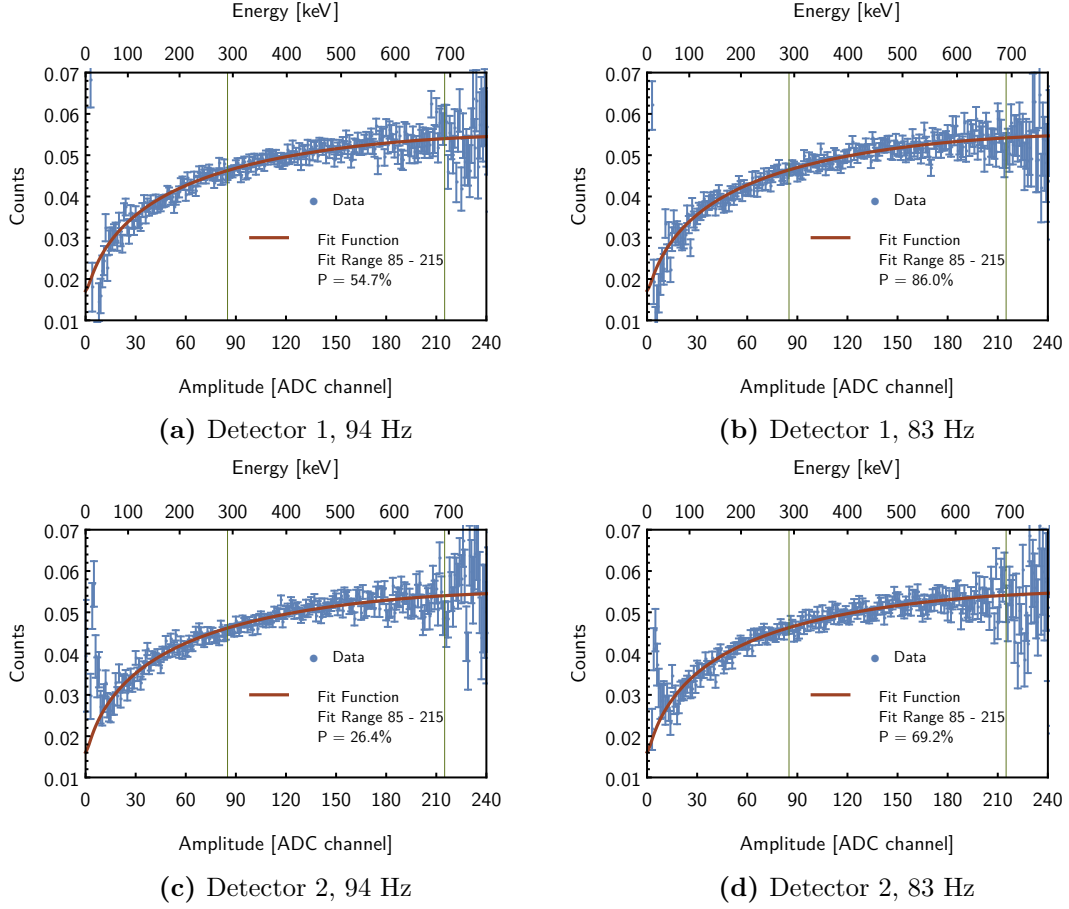
(d) Detector 2, 83 Hz

Fig. 6.4: Fits to the combined experimental beta asymmetry spectra for each detector and chopper frequency. For these fits a mean detector calibration has been used.

can be calculated from the covariance matrix Σ_{cal} of the calibration:

$$(\delta A)_{\text{cal}} = \sqrt{\begin{pmatrix} \frac{\partial A}{\partial G} & \frac{\partial A}{\partial pe} & \frac{\partial A}{\partial k_B} \end{pmatrix} \cdot \Sigma_{\text{cal}} \cdot \begin{pmatrix} \frac{\partial A}{\partial G} \\ \frac{\partial A}{\partial pe} \\ \frac{\partial A}{\partial k_B} \end{pmatrix}}. \tag{6.2}$$

This way the strong correlations between the calibration parameters are considered correctly. The required partial derivatives have been analysed by varying the values of the individual calibration parameters in the fits of the beta asymmetry,

$$\begin{aligned}
\frac{\partial A}{\partial G} &\simeq -0.06 \ \frac{\text{keV}}{\text{ch}} \\
\frac{\partial A}{\partial f_{\text{pe}}} &\simeq 1.9 \cdot 10^{-3} \ \text{MeV (Det1)}, \ 1.4 \cdot 10^{-3} \ \text{MeV (Det2)} \\
\frac{\partial A}{\partial k_{\text{B}} B} &\simeq 6 \cdot 10^{-6} \ \frac{\text{keV}}{\text{nm}}.
\end{aligned} \tag{6.3}$$

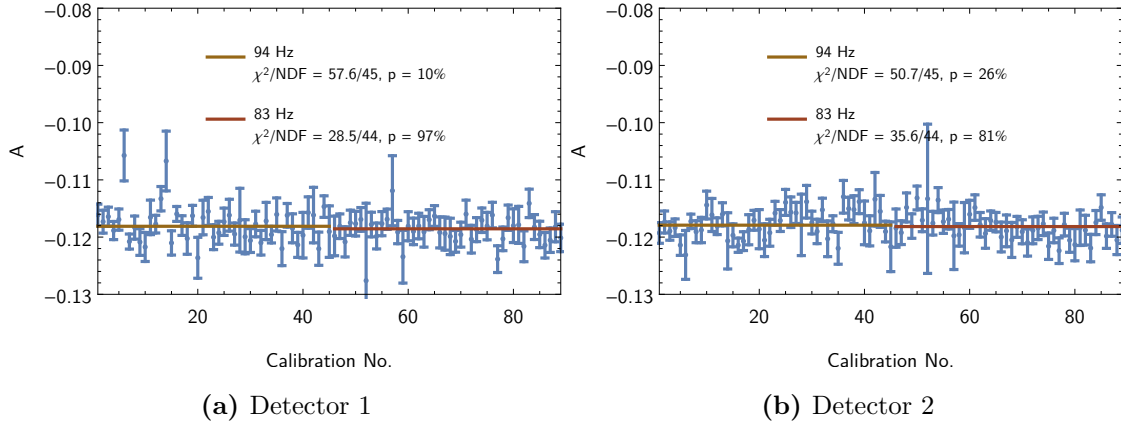**(a)** Detector 1   **(b)** Detector 2

Fig. 6.5: Results of the fits to the experimental beta asymmetry for each dataset. The error bars denote the statistical error as obtained from the fits. Differences between the average for different chopper frequencies and detectors are expected due to the magnetic mirror effect (see section 3.4.1).

The contribution to the uncertainty of the beta asymmetry is $(\delta A)_{\text{cal}} = 1.6 \cdot 10^{-5}$ for a typical calibration. This is small compared to the typical statistical uncertainty of $(\delta A)_{\text{stat}} = 2.6 \cdot 10^{-3}$.

Dataset	A	χ^2/NDF	P-Value
Det1 / 94 Hz	-0.11812(33)	57.3/44	10.4%
Det1 / 83 Hz	-0.11859(35)	28.4/43	96.7%
Det2 / 94 Hz	-0.11795(31)	50.3/44	27.0%
Det2 / 83 Hz	-0.11819(34)	35.6/43	81.2%

Tbl. 6.2: Averages of the beta asymmetry fits for each detector and chopper frequency over multiple datasets. The uncertainties include the minor contribution from the statistical uncertainty of the detector calibration.

In order to calculate the mean result over multiple datasets, the total uncertainty for each dataset is calculated

$$(\delta A)_{\text{tot}} = \sqrt{(\delta A)_{\text{stat}}^2 + (\delta A)_{\text{cal}}^2}, \tag{6.4}$$

and the weighted mean over all datasets is taken. The results of the individual datasets are plotted in figure 6.5 together with the weighted mean for each detector and chopper frequency which is summarized in table 6.2.

6.2.2 Fit Range Dependence

The analysis above has been reperformed varying the lower bound of the fit range. The results are summarized in figure 6.6 and table 6.3. Obviously, shifting the lower bound to

Fit Range	$\delta A/A$		Goodness of Fit	
	Stat.	Calib.	χ^2/NDF	Prob.
85-215 (291-694 keV)	$14.0 \cdot 10^{-4}$	$0.10 \cdot 10^{-4}$	128.1/130	0.53
70-215 (244-694 keV)	$13.1 \cdot 10^{-4}$	$0.12 \cdot 10^{-4}$	142.8/145	0.54
55-215 (197-694 keV)	$12.5 \cdot 10^{-4}$	$0.13 \cdot 10^{-4}$	158.1/160	0.53

Tbl. 6.3: Statistical uncertainties and reduced χ^2 values for different fit ranges in the analysis of the experimental beta asymmetry.

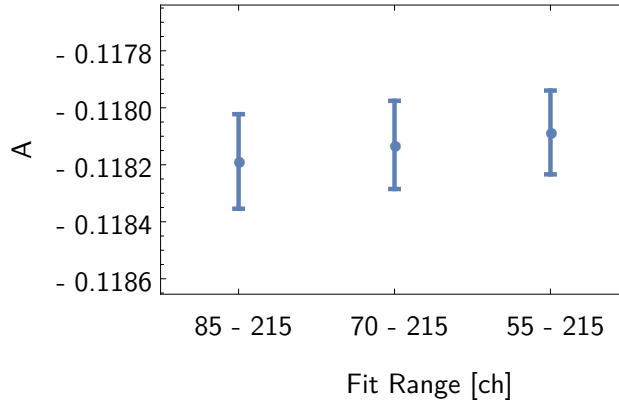smaller energies increases the statistical sensitivity.

Fig. 6.6: Comparison of the mean result of A when using different ranges for the fit (given in rebinned ADC channels). The results are listed also in table 6.3.

When reducing the lower bound of the fit ranges to smaller energies, the result of the fit is slightly shifted to smaller asymmetries. Between the 85-215 and 55-215 fit range this shift is $\Delta A/A = 9 \cdot 10^{-4}$. To check the hypothesis that the observed fluctuations are purely caused by statistical fluctuations the value for the 55-215 fit range may be composed as the weighted mean of the result for the 85-215 fit range and an additional component accounting for the lower energies.

$$A_{85\text{-}215} = -0.11819(17),$$
$$A_{55\text{-}85} = -0.11771(32).$$
(6.5)

The reduced χ^2 when combining these two datasets is 1.76 which corresponds to a probability of 0.18. Although some energy dependent systematic corrections are missing in the analysis at this stage, the result does not contradict the hypothesis of statistical fluctuations. A comparison of the fit range dependent results including the full systematics is presented in section 9.1.1.

6.3 The Fierz Interference Term and the experimental beta asymmetry

The analysis of the experimental beta asymmetry presented above has been extended to a combined spectral analysis concerning the Fierz interference term, b, and λ as discussed in section 1.3.1. This analysis takes advantage of the fact, that a non-zero Fierz Interference term gives a spectral signature in the asymmetry spectrum which allows to simultaneously extract λ and b, when fitting the following function

$$A'_{exp}\left(E_e\right) \rightarrow A_{exp}\left(E_e\right) \cdot \frac{1}{1 + b\frac{m_e}{E_e}} = -\frac{\lambda(\lambda+1)P_n\beta(E_e)}{(1+3\lambda^2)\left(1 + b\frac{m_e}{E_e}\right)}. \tag{6.6}$$

For this analysis the same data as for the beta asymmetry analysis is used. However, for the first three subsets (compare section section 4.1.1) insufficient data to extract the trigger function and spatial response is available, which is necessary to correct for undetected backscattering and the spatial response. For this reason the affected data is ignored. Table 6.4 shows the datasets used in the analysis.

Set	Cycles		Subsets	Chopper
	First	Last		f [Hz]
1	273938	430453	3-5	94
2	430457	627900	6-11	83

Tbl. 6.4: Datasets used to analyse the Fierz Interference term. Compared to the data used for the beta asymmetry, data in the cycle range 211906 - 273937 are removed since some energy-dependent corrections are not available.

The analysis of the beta asymmetry is performed on individual calibration sets which leads to datasets with statistically independent detector calibrations. While this is possible for a single parameter fit of λ (or A) the small amount of statistics available in the individual fits does not result in a symmetric χ^2 environment when performing the combined λ-b-fit.

For illustration figure 6.7 shows the extracted confidence regions for the full 83Hz dataset for detector 1 and a smaller subset. The fact illustrated in these figures is that the extracted confidence regions become asymmetric for smaller datasets. This in turn leads to the fact that the extraction of the fit results in form of the best fit values and a covariance matrix provides incomplete information. A more complex treatment would be required in order to perform the fit on the smaller data sets with individual calibrations. To this end the analysis is performed on the four large datasets using an average calibration (see section 6.3.1). Although this method does not account for the fact that the calibration results vary for the individual small datasets the systematic error made is negligible compared to the complete statistical uncertainty of the λ-b fit. This can be seen by the fact that the statistical uncertainty of the calibration (see section 6.3.1) is much smaller even if it is scaled by a factor of 2 to account for the non-statistical variations between
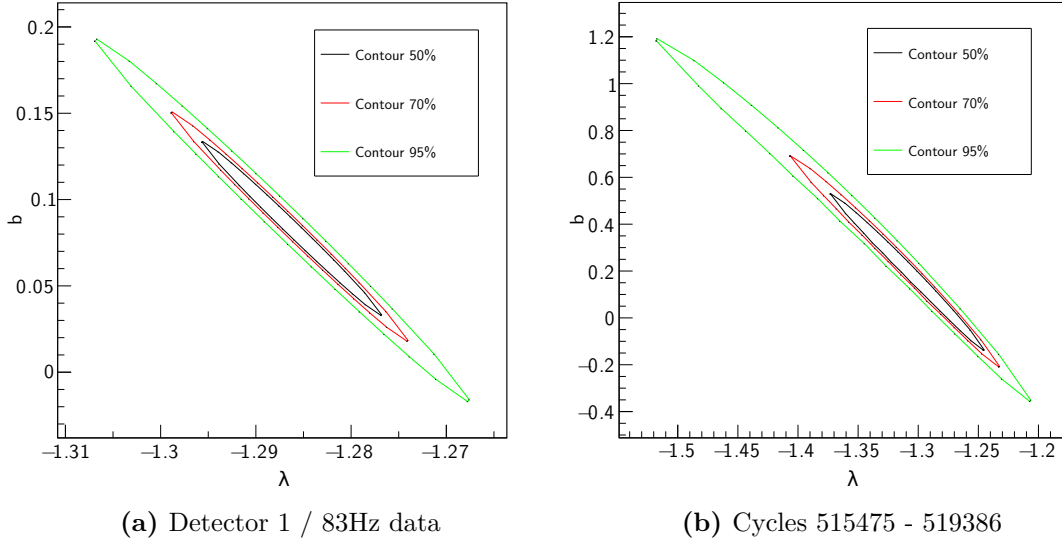
(a) Detector 1 / 83Hz data

(b) Cycles 515475 - 519386

Fig. 6.7: Comparison of the resulting confidence regions from a λ-b-fit to a larger and smaller dataset for detector 1. The asymmetry of the confidence regions of the smaller dataset indicates a non-Gaussian likelihood function.

the individual calibration fits.

Set	λ	$\delta\lambda$	b	δb	ρ	χ^2/NDF
Det 1 - 94 Hz	-1.278	0.013	0.010	0.066	-0.993	166.6/159 (32%)
Det 1 - 83 Hz	-1.288	0.012	0.064	0.063	-0.993	136.7/159 (90%)
Det 2 - 94 Hz	-1.285	0.012	0.051	0.065	-0.993	190.1/159 (5%)
Det 2 - 83 Hz	-1.274	0.010	-0.015	0.054	-0.993	139.3/159 (87%)
Total	-1.2806	0.0059	0.025	0.031	-0.993	

Tbl. 6.5: Results of the individual datasets. The uncertainties denote the correlated errors at the 68.27% confidence level for a fit region of 197 - 694 keV. The combined results of these datasets is calculated as the weighted mean of the individual datasets. These results already include corrections for polarisation and the magnetic mirror effect but no corrections for detector and background systematics.

The results of the combined fits for the individual datasets are shown in figure 6.8 and are found to be consistent within the given 68.27% confidence intervals. The fits are carried out over an energy range of 197 - 694 keV. Individual results as well as their weighted mean are listed in table 6.5.

6.3.1 Calibration Uncertainty

The uncertainty in the result of the analysis due to the statistical uncertainties of the calibration parameters can be estimated using a similar method as for the beta asymmetry
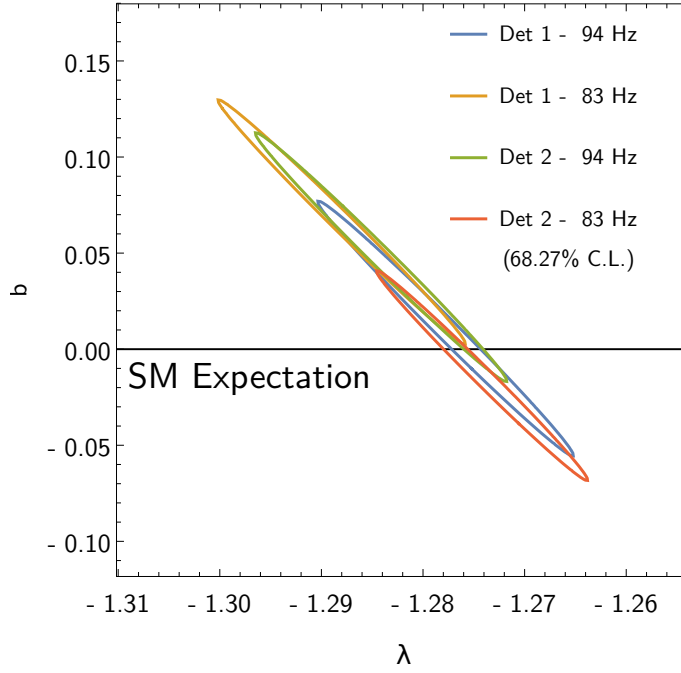
Fig. 6.8: Results of the λ-b-fits including corrections for polarisation and the magnetic mirror effect. Corrections for detector and background systematics are not included. The results of the individual datasets are consistent within the statistical uncertainties shown.

analysis section 6.2.1. For the beta asymmetry, the covariance matrix of the calibration fits has been projected onto A. Due to the additional free parameter in this analysis, the variation of a single calibration parameter induces correlated variations in λ and b which can not be accounted for by a single derivative as these are individual to each calibration parameter. This is overcome by mapping the parameter uncertainties of the calibration and to project the corresponding variations in the calibration onto the result (λ, b).

The 69.27% confidence level contour described by the covariance matrix of the calibration analysis can be visualized as an ellipsoid as illustrated in figure 6.9 for the 83 Hz / Det 1 dataset (see table 6.4). In order to achieve a meaningful presentation, the covariance matrix Σ_{cal} is rescaled with a scaling matrix S to obtain the correlation matrix C_{cal} using the relation:

$$\Sigma_{\mathrm{cal}} = S \cdot C_{\mathrm{cal}} \cdot S, \text{ with } S = \mathrm{diag}(\Sigma)^{1/2} = \begin{pmatrix} \sigma_G & 0 & 0 \\ 0 & \sigma_{pe} & 0 \\ 0 & 0 & \sigma_{k_B} \end{pmatrix}. \tag{6.7}$$

The resulting ellipsoid is discretized into disjoint triangles (meshed) using the geometric computation capabilities of *Wolfram Mathematica* [1]. From the corners of these triangles 42 points on the surface of the ellipsoid are generated to represent variations of the

---

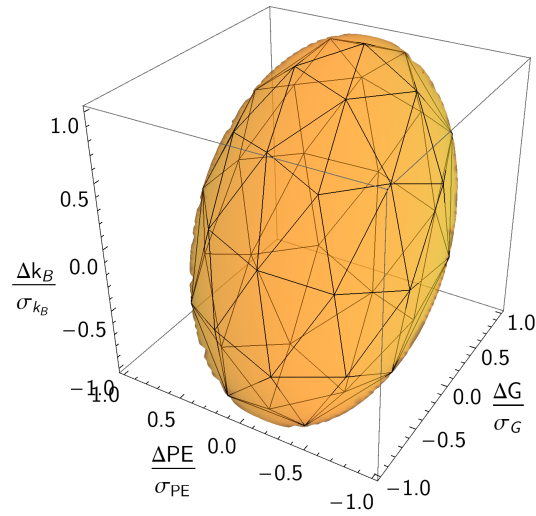[1]Wolfram Mathematica is a feature rich software package for computational algebra by Wolfram.

Fig. 6.9: Illustration of the covariance matrix of the calibration analysis for the 83 Hz / Det 1 dataset. The corresponding ellipsoid is meshed using 42 points on the surface as illustrated by the nodes of the mesh. These points are used to map the changes of the fit results λ, b when varying the calibration parameters.
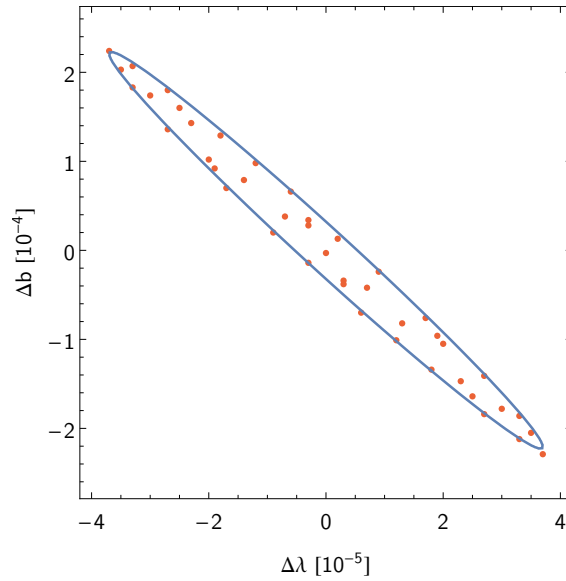

Fig. 6.10: Shifts in (λ, b) when varying the calibration parameters on the 68.27% confidence contour. The points are obtained by refitting the experimental beta asymmetry using shifted calibration parameters as represented by the nodes of the meshed ellipsoid in Fig. 6.9. The plot shows the difference to the result obtained when using the best fit value for the calibration parameters. The ellipse constructed around the data points defines an upper limit on the 68.27% covariance due to the statistical uncertainty of the detector calibration.

calibration on the surface of the 68.27% confidence region. These variations are mapped to shifts in λ and b by refitting the data with the varied calibration parameters. The results are illustrated in figure 6.10 as shifts around the central value. Also shown is an ellipse constructed containing all the data points which defines an upper limit on the covariance due to the statistical uncertainty of the calibration.

For the given dataset the resulting parameter uncertainties and correlations are

$$\sigma_\lambda = 3.7 \cdot 10^{-5}, \ \sigma_b = 2.2 \cdot 10^{-4}, \ \rho_{\lambda,b} = -0.99. \tag{6.8}$$

Similar results are obtained for the other datasets.

The uncertainties are more than two orders of magnitude smaller than the statistical uncertainties of λ and b (compare table 6.5). In analogy to the beta asymmetry analysis the combined covariance matrix including both statistical contributions is calculated before forming the weighted mean of all datasets. This refinement, however, does not lead to significant changes when compared to the results listed in table 6.5.
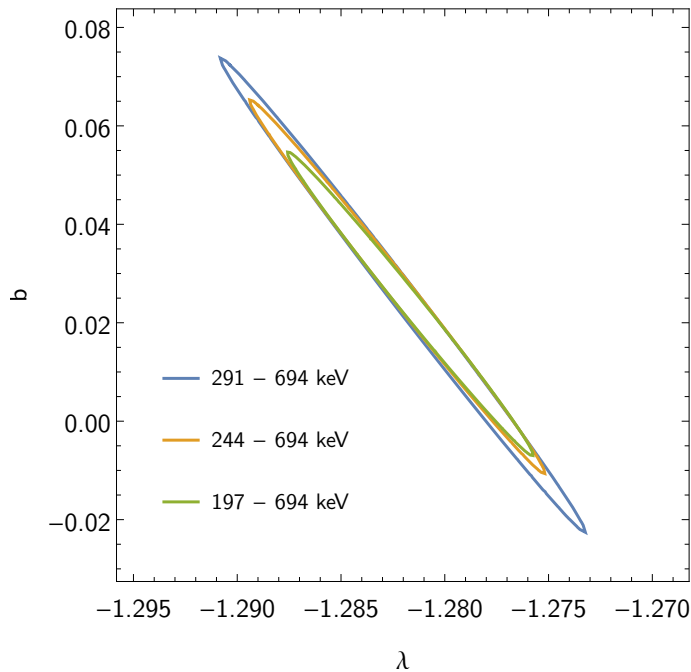
6.3.2 Fit Range Dependence

Fig. 6.11: Comparison of the 68.27% confidence region when using different fit ranges. Using a reduced lower fit range bound decreases the correlation between λ and b.

While extending the fit range to lower energies only results in a slight increase in statistical sensitivity for the beta asymmetry, the benefit in a combined fit with the Fierz interference is significant. This is due to the fact that the signature of a potential Fierz term is larger for lower energies, which in turn leads to a higher statistical sensitivity and

less correlation between λ and b when including lower energies in the fit range. Figure 6.11 shows a comparison of the combined results for different fit ranges. Without quantitative analysis it is obvious that the results are consistent with each other.

The optimal choice of fit range, however, minimises the overall uncertainty including all systematic effects. These include detector and background systematics which are discussed in the following two chapters. A final comparison of the result for different fit ranges including systematics is presented in section 9.2.

Chapter 7

Detector Systematics

In this chapter the analysis of systematic effects specific to the detector and its response model is presented.

The dominant contributions to the error budget arise from the stability of the detector amplitude and the detector non-linearity. Several offline measurements and checks on the calibration spectra are performed in order to improve the understanding of the detector non-linearity and to rule out some of its potential origins. Combined with the improved implementation described in section 5.2.1, this in the end yields an acceptable uncertainty related to the non-linearity, which is essential to perform energy-dependent analysis.

For most systematics the analysis is done by implementing corrections into the fit function and refitting the experimental beta asymmetry as presented in the previous chapter. The shifts observed directly allow the extraction of the respective correction for the individual systematic effects. The uncertainty related to the strength of the respective effect can be easily translated into a systematic uncertainty for the result.

This scheme is used in both analyses, the analysis of the beta asymmetry and the λ-b analysis, and based on the same corrections. However, for the analysis of the beta asymmetry A, the projection of the systematic effect onto a single parameter is of interest, while in case of the two-parameter analysis of λ and b correlations between the parameters need to be considered. The method used to estimate the correlated uncertainties is described in detail in section 7.1 and then used for most systematic effects later on. The differences in these methods and the fact that corrections and uncertainties are calculated for different points in the λ-b parameter space yield slight differences in the result.

Some of the systematics effects discussed here are found to be negligible and are not considered in the final error budget. The same is true for the rate dependence of the QDCs and the spin-dependence of the pedestals (see chapter 4) which are not further discussed in this chapter.

The effect of most systematic effects is studied for the different fit ranges used in chapter 6 to allow optimisation of the total error budget and also test if results are consistent. In cases, where this provides insight on the nature of the correction, the results for the individual fit ranges are compared or explicitly stated. However, to avoid repetitiveness, in some cases only the result for the final choice of fit range is given.

7.1 Drift uncertainty

The correction of the detector drift is based on hourly measurements with a single calibration source as described in section 4.2.6 and included in the data reduction process.

The current scheme of drift correction allows to stabilize the detector amplitude on a level of 10^{-3} as shown in section 4.2.6. The remaining uncertainties in the detector gain for any drift corrected measurement are

$$\left(\frac{\delta G}{G}\right)_{\text{Det1}} = 1.91 \cdot 10^{-3}, \quad \left(\frac{\delta G}{G}\right)_{\text{Det2}} = 2.20 \cdot 10^{-3}. \tag{7.1}$$

For the continuously measured neutron decay spectra, however, such fluctuations will average out, leading only to a slightly reduced energy resolution. For the non-continuous calibration measurements on the other hand, any insufficiency in the drift correction becomes relevant, as the drift correction for these spectra is usually just derived from one drift measurement before and one after the calibration measurement. When applying the calibration parameters as extracted in section 6.1, the above uncertainties need to be considered in addition to the statistical uncertainties.

Relative variations in the detector gain can be related to variations in the beta asymmetry parameter A, simply by repeating the fits of the experimental beta asymmetry with a modified gain. The result of such fits is:

$$\begin{aligned}
\frac{\Delta A}{A} &\simeq s_A \cdot \frac{\Delta G}{G}, \\
\text{with } s_A &= 0.18 \quad (297\text{-}694 \text{ keV}) \\
s_A &= 0.18 \quad (244\text{-}694 \text{ keV}) \\
s_A &= 0.19 \quad (197\text{-}694 \text{ keV}),
\end{aligned} \tag{7.2}$$

given for different fit ranges of the experimental beta asymmetry. Based on this relation the uncertainty due to the remaining detector drift can be estimated to be

$$\left(\frac{\Delta A}{A}\right)_{\text{Det1}} = 3.4 \cdot 10^{-4}, \quad \left(\frac{\Delta A}{A}\right)_{\text{Det2}} = 3.9 \cdot 10^{-4}, \tag{7.3}$$

for a fit range of 297 - 694 keV. In [Mes11] the uncertainty of the drift correction has been studied by repeating the analysis with and without correcting for the detector drift. The difference between the results is given as $\frac{\Delta A}{A} = 4 \cdot 10^{-4}$ which is of similar magnitude as the uncertainty estimated here directly from the drift and calibration data.

For the combined λ-b analysis this discussion needs to be extended to multiple parameters. To extract the effect on λ and b for a variation in the detector gain a similar method as for the beta asymmetry isused. However, uncertainties in b can only be given in terms of absolute numbers. To this end all corrections and uncertainties relating to this part of the analysis are given as absolute values $\Delta\lambda$ and Δb. In order to relate the variation of the detector gain to uncertainties in λ and b, the fits performed in section 6.3 have been re-performed with a gain shifted by $\Delta G = 0.003$, which roughly equals 1%. The observed shifts in λ and b are

$$\begin{pmatrix} \Delta\lambda \\ \Delta b \end{pmatrix} = \begin{pmatrix} 0.00048 \\ -0.0055 \end{pmatrix}, \tag{7.4}$$

where both parameters are free parameters in the fit. Usually the extraction of the covariance matrix is based on calculating the derivates of the observable (λ, b) with respect

to the varied parameter G. This would lead to

$$C_{\text{Drift}} = \begin{pmatrix} \left(\frac{\partial\lambda}{\partial G} \cdot \delta G\right)^2 & 0 \\ 0 & \left(\frac{\partial b}{\partial G} \cdot \delta G\right)^2 \end{pmatrix}.$$ (7.5)

The required derivatives can be estimated by the shifts of the parameters λ and b when changing the gain leaving the other parameter fixed

$$\frac{\partial\lambda}{\partial G} = \frac{\Delta\lambda}{\Delta G} \simeq -0.17, \ \frac{\partial b}{\partial G} = \frac{\Delta b}{\Delta G} \simeq -0.95.$$ (7.6)

This method, however, neglects the fact that the variations in λ and b are correlated to a certain extent. This is obvious as the resulting shifts in λ and b are larger when both parameters are free fit-parameters (see equation 7.4). Figure 7.1a illustrates the resulting covariance matrix as an error ellipse.
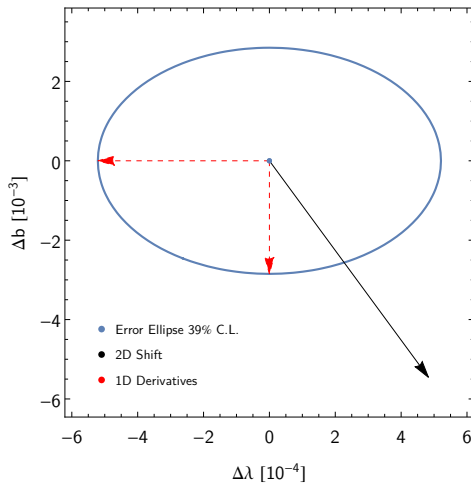
(a) Diagonal covariance matrix constructed in the unrotated parameters space.
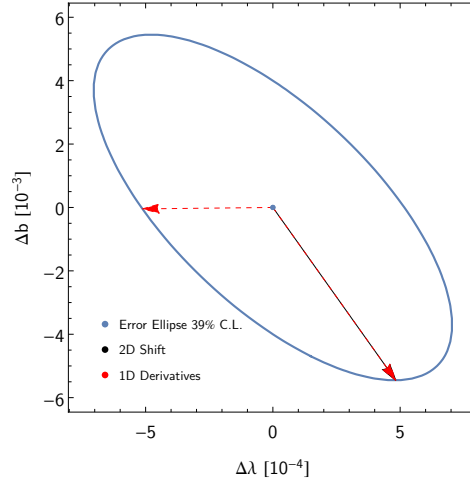
(b) Covariance matrix constructed as a diagonal covariance matrix in a rotated parameter space to account for parameter correlations.

Fig. 7.1: Comparison of the constructed covariance ellipses with and without considering correlation in the covariance matrix.

A more realistic estimate of the covariance matrix can be obtained by rotating the parameter space $(\lambda, \ b)$:

$$\begin{pmatrix} \lambda' \\ b' \end{pmatrix} = \begin{pmatrix} \lambda \\ b \end{pmatrix} \cdot R, \ \text{with } R = \begin{pmatrix} \cos(\theta) & -\sin\theta \\ \sin(\theta) & \cos(\theta) \end{pmatrix}.$$ (7.7)

The rotation angle θ is chosen such that the shift in equation 7.4 is accounted for as a

shift of a single parameter

$$\begin{pmatrix} \Delta\lambda \\ \Delta b \end{pmatrix} \cdot R^{-1} = \begin{pmatrix} \Delta\lambda' \\ 0 \end{pmatrix}. \tag{7.8}$$

In the present case of gain variations this leads to $\theta \simeq -1.48$. In this rotated parameter space the covariance matrix can be constructed in analogy to equation 7.5

$$C' = \begin{pmatrix} \left(\frac{\partial\lambda'}{\partial G} \cdot \delta G\right)^2 & 0 \\ 0 & \left(\frac{\partial b'}{\partial G} \cdot \delta G\right)^2 \end{pmatrix}. \tag{7.9}$$

The individual derivates are obtained by including the rotation into the fitting routine, allowing to perform fits in the rotated parameter space. The covariance matrix for the unrotated system C is now obtained by simply applying the rotation matrix:

$$C = R^{-1} \cdot C' \cdot R. \tag{7.10}$$

Using the gain variations from equation 7.1 the final covariance matrix describing the uncertainty due to detector drift for detector 1 and 83 Hz reads

$$C_{\text{Drift}} = \begin{pmatrix} 5.61 \cdot 10^{-8} & -2.25 \cdot 10^{-7} \\ -2.25 \cdot 10^{-7} & 2.95 \cdot 10^{-6} \end{pmatrix}. \tag{7.11}$$

Repeating the same extraction for the other datasets leads to similar results. The diagonal elements of this covariance matrix describe correlated uncertainties and are scaled by a factor of 2.29 to give a 68.27% confidence region in the two parameter space. The corresponding uncertainties and correlation are

$$\sigma_{\lambda,\text{Drift}} = 2.37 \cdot 10^{-4}, \ \sigma_{b,\text{Drift}} = 1.72 \cdot 10^{-3}, \ \rho_{\lambda b,\text{Drift}} = -0.553. \tag{7.12}$$

The uncorrelated uncertainties can be calculated to be:

$$\sigma_{\lambda,\text{Drift,uncorrel.}} = 1.97 \cdot 10^{-4}, \ \sigma_{b,\text{Drift,uncorrel.}} = 1.43 \cdot 10^{-3}. \tag{7.13}$$

The uncertainty in λ corresponds to a relative uncertainty of $\Delta A/A = 3.7 \cdot 10^{-4}$ for detector 1 for the beta asymmetry, when scaled down to a 1σ uncertainty. This is slightly larger than the relative uncertainty derived in the beta asymmetry analysis (see equation 7.3). This can be mainly attributed to the larger fit range used.

7.2 Detector Non-linearity

So far Birks has been assumed during the analysis to account to account for the detector non-linearity (see section 6.1). However, with a value of $400 - 450$ nm/keV the extracted Birks coefficient k_B is bigger than the expected 150 nm/keV. To this end some checks concerning the scintillator and other detector non-linearities are performed to investigate potential origins of the increased detector non-linearity. This includes spectral analysis of the calibration data as well as some offline tests of the electronics used to read out the
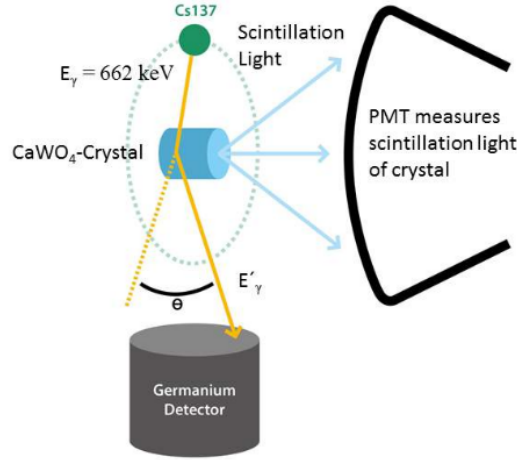
Fig. 7.2: Compton-coincidence setup to measure the intrinsic scintillator non-linearity as used in [Opp16]. The monoenergetic gammas emitted from the ^{137}Cs-source produce Compton electrons within the scintillator. The resulting scintillation light is measured with a photomultiplier in coincidence with the gamma that is detected by a Germanium detector. Image taken from [Opp16].

photomultipliers. Finally, a comparison between different models to describe the detector non-linearity is used in order to evaluate the systematic uncertainty quantitatively.

7.2.1 Measurement of the Scintillator Non-linearity

For the measurement of the scintillator non-linearity an existing setup to measured the scintillator response of Compton-Electrons created inside the scintillator from a monoenergetic Gamma source. Usually this setup is used to characterize the scintillators of several neutrino and dark matter experiments[1].

The used setup is described in [Opp16] for the measurement of self-grown CaWO$_4$-crystals produced at TUM for the CRESST-experiment. Figure 7.2 shows an image of the setup. Only slight mechanical adaptations to the setup have been made in order to perform a similar measurement with a plastic scintillator. Due to the lack of an appropriate sample a Bicron-408 scintillator has been used instead of the Bicron-400 that has been utilized in the PERKEO III measurement.

The scintillation light created by Compton-electrons induced by monoenergetic Gammas from a ^{137}Cs source are measured by a photomultiplier. These signals are measured in coincidence with the remaining Gamma which is measured with a Germanium detector. The energy of the Compton electron is then known from the relation:

$$E_{el} = E_0 - E_\gamma, \tag{7.14}$$

where $E_0 = 662$ keV is the energy of the Cs-gammas. This energy is then compared with
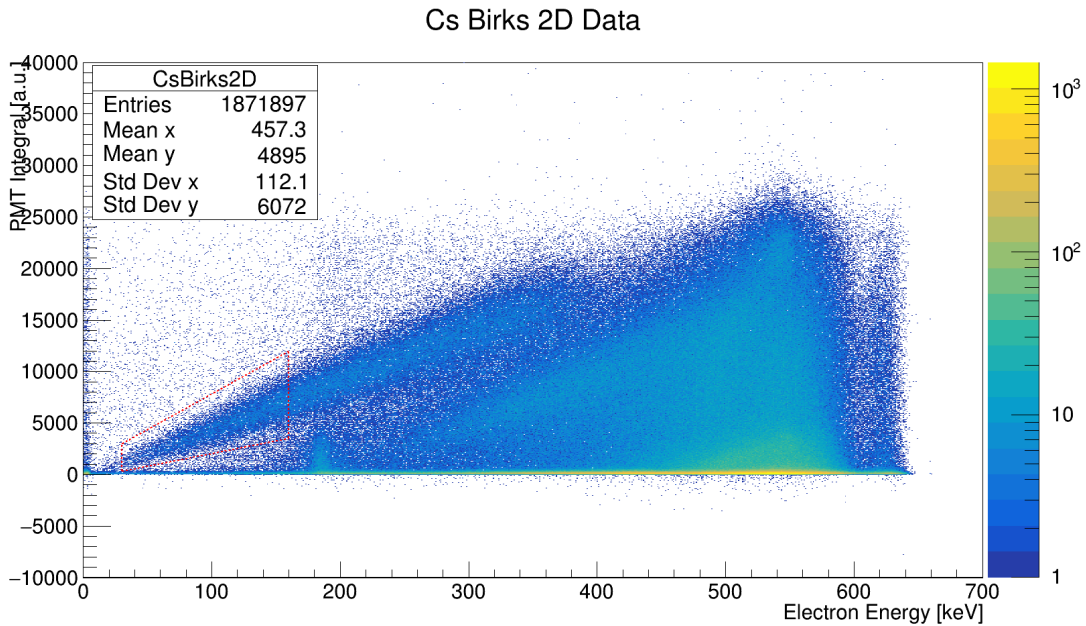

Fig. 7.3: Histogram of the measured integral PMT amplitude versus energy determined from the residual gamma energy (compare equation 7.14). The region inside the red lines marks the data selection for the analysis.

the integrated amplitude of the photomultiplier as shown in figure 7.3.

Due to the fact that the measured electrons are created within the bulk material of the scintillator, this measurement is insensitive to surface effects of the scintillator. The resulting non-linearity curve then only represents the intrinsic scintillator non-linearity as described by the Birks model (see section 5.2.1). Additionally, electronics non-linearities might influence this measurement. However, in this setup a fast sampling ADC is used, which is expected to behave sufficiently linear.

In a first analysis only data in the energy region of 30 - 160 keV has been selected. For energies beyond this multiple Compton scattering processes within the scintillator and the Germanium detector make the description of the measured data more complex.

In the analysis the spectra for the PMT integral for each energy bin of 2 keV width are fitted simultaneously. For this task the fitting tool *PMTSpecFit* has been developed which is capable of analysing 1D and 2D spectra. It is based on the same algorithms as the fitting tool *p3fit* used in the main analysis but uses binned log-likelihood instead of χ^2 minimisation. Given a certain input energy for each spectrum, this tool calculates the resulting spectrum considering the whole detector response as discussed in chapter 5. In the present case of analysing 2D spectra, these a represented as an array of 1D slices which are fitted simultaneously. The number of parameters used to describe the norms of the 1D slices is reduced by describing these by a fifth order polynomial in energy.

In addition to the Compton signal also background due to random coincidences is observed in the selected energy region. Within the fit this background is described by combining the PMT spectrum for energy 0 and the energy spectrum for PMT amplitude 0
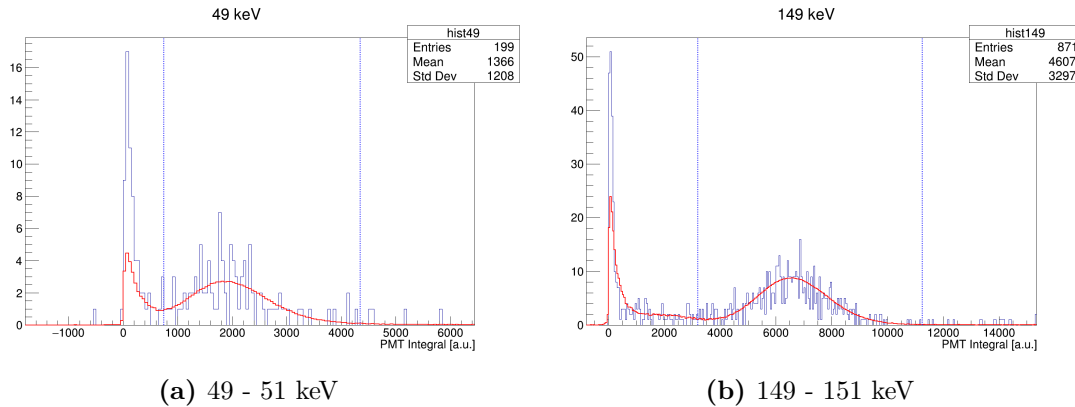
(a) 49 - 51 keV   **(b)** 149 - 151 keV

Fig. 7.4: Spectra of the integral PMT amplitude for two different energy bins. The red lines represent the best fit obtained by simultaneously fitting all spectra in the region of 30 - 160 keV. The fit function models the expected detector response for a single electron energy including the scintillator non-linearity with an additional background contribution due to random coincidences.

with a common normalisation constant.

The full fit includes the QDC Gain G, effective photoelectron number PE and the Birks coefficient k_B as free parameters in addition to the norms of the spectra and the overall background normalisation constant. The result obtained for the Birks coefficient is

$$k_B = 123(14) \text{ nm/keV}. \tag{7.15}$$

When varying the fit range and extending the background normalisation to a third-degree polynomial in energy a shift in k_B of up to 10 nm/keV is observed. This is considered as a first measure of systematic uncertainties. For a final result a more detailed study of systematic uncertainties including detector drifts, background checks and the investigation of the influence of the calibration of the Germanium detector is required.

The preliminary result of this measurement, however, is in good agreement with the expectations of $k_B = 100 - 150$ nm/keV and agrees well with similar measurements of other plastic scintillators [Abe+11].

7.2.2 Surface Effects

The difference between the non-linearity observed in the calibration measurements and the intrinsic scintillator non-linearity as presented in section 7.2.1 may be the result of reduced light generation close to the scintillator surface. Possible reasons for such effects are "dead-layers" on the scintillator, that describe a layer of non-scintillating material on top of the scintillator either due to damage of the fluors of the scintillator close to the surface or condensed matter such as water. Previously such dead-layers have been discussed as a potential reason for the difference between measured and calculated trigger functions. However, these differences are not observed when calculating the trigger function correctly under consideration of the photomultiplier signal distribution (compare section 5.6).

Another effect that might lead to similar observations has been described by Birks as a loss of scintillation excitations close to the surface [Bir52] for short range particles. In the differential light yield such losses are accounted for by an additional multiplicative factor ϕ, that depends on the distance to the surface

$$\left(\frac{dL}{dx}\right)_{\text{exp}} = \phi\left(x\right) \cdot \left(\frac{dL}{dx}\right)_{\text{theor}},$$

$$\text{with } \phi\left(x\right) = 1 - \frac{e^{-x/a_0} + \frac{x}{a_0}Ei\left(-x/a_0\right)}{2}. \tag{7.16}$$

Here $Ei\left(z\right)$ is the exponential integral $-\int_{-z}^{\infty}\exp\left(t\right)/t\,dt$ and a_0 is the characteristic length for excitations to travel inside the scintillator. In case of a dead-layer the same relation can be used replacing $\phi\left(x\right)$ with the relation

$$\phi\left(x\right)_{\text{deadlayer}} = \begin{cases} 1 & x > a_0 \\ 0 & x \le a_0 \end{cases}. \tag{7.17}$$

This would correspond to a layer of thickness a_0 of the scintillator in which no scintillation takes place. Due to the similar energy dependence of the stopping power, this description may also be used for other dead layers such as water or other organic materials.

A comparison of the resulting relative effective energy is plotted in figure 7.5. The curves are calculated by numerical integration of equation 7.16 using the approximation that the penetration depth inside the scintillator is equal to the path length. To test this approximation a simulation has been performed using PENELOPE [SFS11]. Here the angular distribution of incident electrons as well as backscattering are considered. The effective energy is calculated assuming the same description as for the analytical curves and summarizing over each step of the simulation. The comparison between the calculation and simulation shows a good agreement between the approximate calculation and the simulated data despite some smaller deviations for electron energies between 10 and 100 keV.

Comparing the different calculated models shows the effect of a_0 which changes the effective non-linearity for low energies. The signature of a non-linearity with $k_B = 158$ nm/keV combined with $a_0 = 12$ μm is similar to that for $k_B = 450$ nm/keV. This transition happens for energies of about 20 keV and below. For higher electron energies the dead layer model resembles the same non-linearity as the surface effect described by Birks when the value of a_0 is adapted to smaller values. For lower energies however the dead layer assumption leads to a more significant drop in the measured energy approaching 0 when the electron path length drops below the dead layer thickness.

In order to check whether the non-linearity found in the measured calibration spectra can be explained by such surface effects, the calibration fits have been repeated using the modified Birks non-linearity of equation 7.16. The formulation of ϕ has been modified to
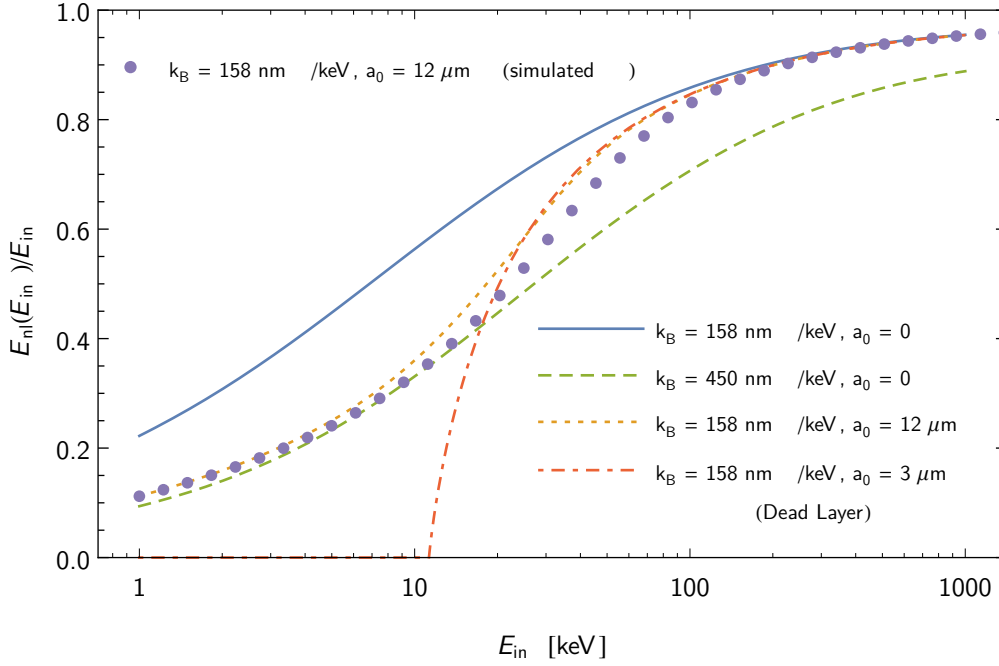
Fig. 7.5: Effective energy normalized to the incident electron energy for different strength of the Birks non-linearity with and without surface effects ($a_0 \neq 0$).

allow for negative values of the thickness parameter a_0,

$$\phi\left(x\right) = \begin{cases} 1 - \frac{e^{-x/a_0} + \frac{x}{a_0} Ei(-x/a_0)}{2} & a_0 \geq 0, \\ 1 + \frac{e^{-x/a_0} + \frac{x}{a_0} Ei(-x/a_0)}{2} & a_0 < 0 \end{cases} . \tag{7.18}$$

which would cause an increased effective energy. This avoids using boundaries for the parameter a_0, which would disturb the fit for values close to zero. However, when performing calibration fits to the measured calibration data, the fit converges to values of $a_0 < 0$ and slightly higher values of k_B for all full calibration fits as shown in figure 7.6. For fits not including Bismuth spectra the resulting a_0 converges to values slightly greater zero but the observed shifts in the Birks coefficient are still small. The big error bars for the a_0 parameter are the result of a high correlation between the fit parameters. The above results show no significance of surface effects that would explain a major effect on the measured non-linearity.

7.2.3 Electronics Non-linearities

In the previous section potential effects increasing the observed non-linearity related to the scintillator have been found to be neglibile. Another potential contribution to the detector non-linearity is the electronics. A first indication that such effects are present could already be observed by the dependence of the detector non-linearity on the photomultiplier voltage (see section 6.1). In this section investigations concerning the origin of such an
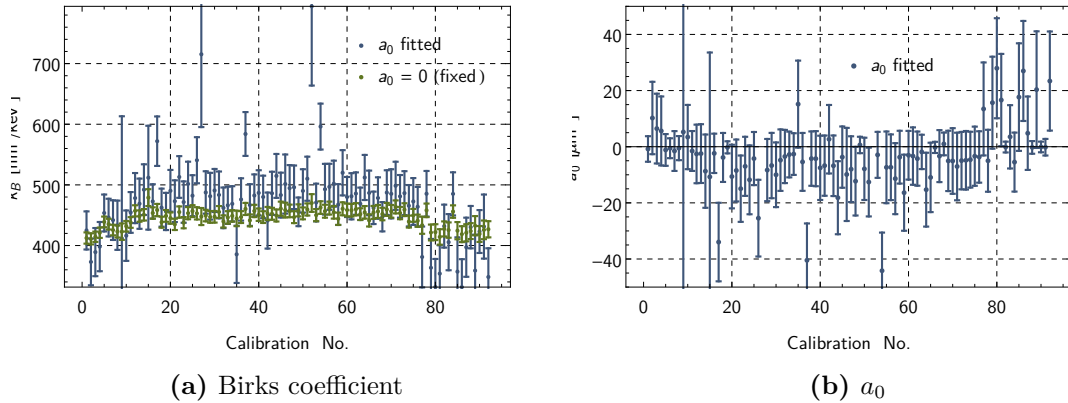
(a) Birks coefficient

(b) a_0

Fig. 7.6: Comparison of the resulting Birks coefficient k_B with and without considering surface effects within the fit and the resulting thickness parameter a_0.

effect are presented which have been carried out by offline tests of the used electronics.

Pulser Tests

In order to check the linearity of the Linear Fan-Outs and QDCs a first check on the response to static rectangular pulses have been performed within the Bachelor's thesis of R. Sachsenhauser [Sac16].
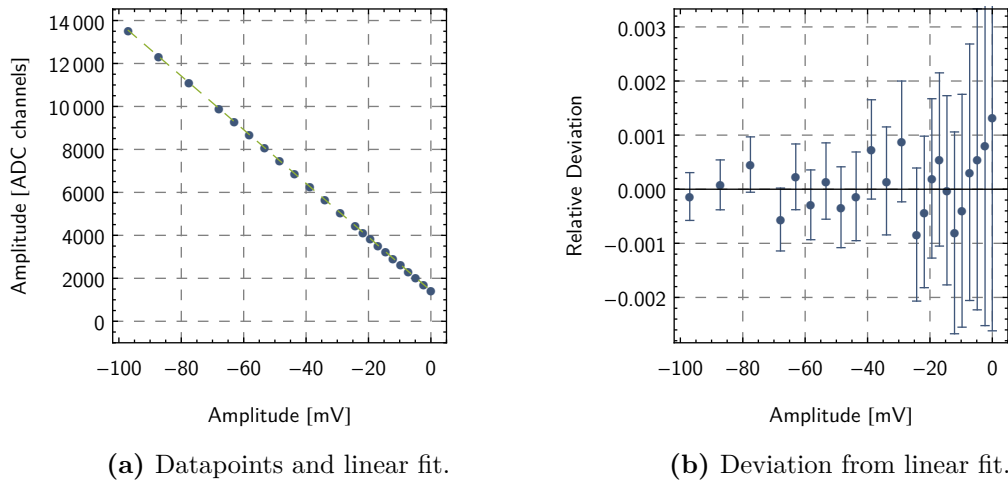

(a) Datapoints and linear fit.

(b) Deviation from linear fit.

Fig. 7.7: Measurement of the QDC linearity for a single QDC channel. The errorbars consist of statistical errors for the determination of the peak center and the systematic uncertainty in the voltage measuremet projected on the QDC axis which induces correlations.

In this test a Digital Pulser (RIGOL D4062) is used using trapezoidal pulse of 80 ns total length with a rise- and fall-time of 15 ns. The pulser signal is fed into multiple QDC channels using the Linear Fan-Out. The integral over these pulses is then measured with individual QDC channels and the peak center is used as response value. For a precise amplitude reference the voltage drop for these pulses over a 50 Ω resistance has

been measured with a digital multimeter using longer pulses with the same amplitude. The uncertainty for the measured reference voltage is 0.04mV which is given by the reproducability of the voltage measurement for amplitude and baseline voltage. Image 7.7 shows the results of such a measurement for the first QDC. The results for the other QDC channels give similar results and indicate that the measurement is limited by the precision of the voltage measurement.r Within the precision of the measurement no non-linearity is found. From figure 7.7b an upper limit on the the combined Fan-Out / QDC non-linearity is estimated to be $< 2 \cdot 10^{-3}$. This is one to two orders of magnitude smaller than the effect observed within the calibration data.

Real Photomultiplier Pulses

The static pulser setup described above gives a limit on the Fan-Out / QDC linearity for longer trapezoidal signals. However, the pulses generated by the PMTs for real scintillator signals are much shorter and have a broader spectral bandwidth spectrum. In contrast to the QDCs which are designed to detect fast PMT pulses, the Linear Fan-Outs have a limited bandwidth of 200 MHz. This might result in an amplitude dependent response.

In order to check the linearity of the electronic components for real detector signals a measurement scheme initially implemented in [Sac16] has been improved. The basic idea is to feed the same signal generated by a Mesh-photomultipler coupled to a scintillator through one or two fan-out stages into multiple QDCs. Assuming the effect of the Linear Fan-Out can be described via a function $F(A)$ that describes the relative effect of the Fan-Out on the signal amplitude A, the ratio of the measured amplitudes can be written as

$$\frac{A_2}{A_0} = \frac{Q_2\left(F\left(F\left(A\right)\right)\right)A}{Q_0\left(F\left(A\right)\right)A}, \tag{7.19}$$

where the factors Q_0 and Q_2 account for the potentially different response of the QDCs. Assuming small deviations from linearity this dependence can be approximated as

$$\frac{A_2}{A_0} \simeq \frac{Q_2\left(A\right)F^2\left(A\right)A}{Q_0\left(A\right)F\left(A\right)A} = \frac{Q_2\left(A\right)}{Q_0\left(A\right)} \cdot F\left(A\right), \tag{7.20}$$

where the relation $F(F(A)) \simeq F^2(A)$ is used. Switching QDC channels inversely changes the effect of the Fan-Out:

$$\frac{A_2}{A_0} \simeq \frac{Q_2\left(A\right)}{Q_0\left(A\right)} \cdot \frac{1}{F\left(A\right)}. \tag{7.21}$$

Dividing equations 7.20 and 7.21 and calculating the square root gives F

$$F\left(A\right) = \sqrt{\frac{\left(A_2/A_0\right)_a}{\left(A_2/A_0\right)_b}}. \tag{7.22}$$

In order to measure F for the Fan-Outs used in the Perkeo III, a setup using a photomultiplier measuring background of a scintillator is used. The photomultiplier signal passes either one or two Fan-Out stages before being fed into different QDC-channels. Pedestal and drift measurements are realised by interrupting the background measurements
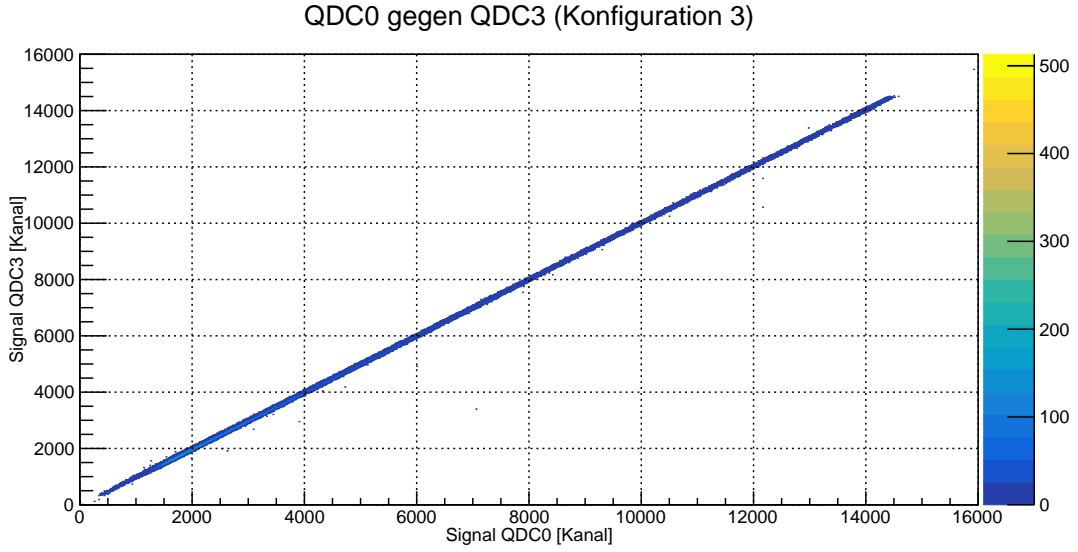
Fig. 7.8: Scintillator background measured with a PMT. The signal is fed into two QDCs via Linear Fan-Outs and the amplitudes are compared. Pedestals and drift of individual QDC channels are corrected.

and measuring pulses generated with a LED-pulser. The pedestals are subtracted and the drift is corrected by rescaling the data of each individual channel. In figure 7.8 the resulting amplitudes of the two QDC channels are plotted against each other. This data is binned with respect to the amplitude of channel 0 and the mean value of the second channel is calculated for each bin. The ratio of the amplitudes according to equation 7.19 is plotted in figure 7.9a. Due to different intrinsic noise of the QDC channels the ratio shows a drop of the ratio as the spectrum of channel 2 is shifted to lower amplitudes close to the trigger threshold. This behaviour should not influence the present analysis as it is constant for both measurements performed. However, amplitudes below channel 1000 are not considered in the analysis for this reason. The Fan-Out response is calculated from these datasets according to equation 7.22 and plotted in figure 7.9b.

The observed non-linearity in the data due to the Fan-Out response is on a level of $4 \cdot 10^{-3}$ and may become stronger for amplitudes below channel 1000.. The constant offset from 1 may describe the general damping produced by a second Fan-Out stage but may as well be the result of imperfect drift correction. The behaviour of the data for medium amplitudes (QDC channels 2000 - 12000) can be approximated with a quadratic function as illustrated. When including lower amplitudes (QDC channels 800 - 8000) a better approximation is achieved by a $1/A$-dependence

$$F(A) = a + b \cdot (A + A_0)^2,$$
$$a = 0.99560(5),\ b = -2.26(10) \cdot 10^{-11}\ 1/\text{ch}^2,\ A_0 = 240(100)\ \text{ch}.$$

(7.23)

From this approximation the expected non-linearity for signal amplitudes close to zero can be estimated to be 1.5 %. The observed non-linearity itself can not explain the deviation
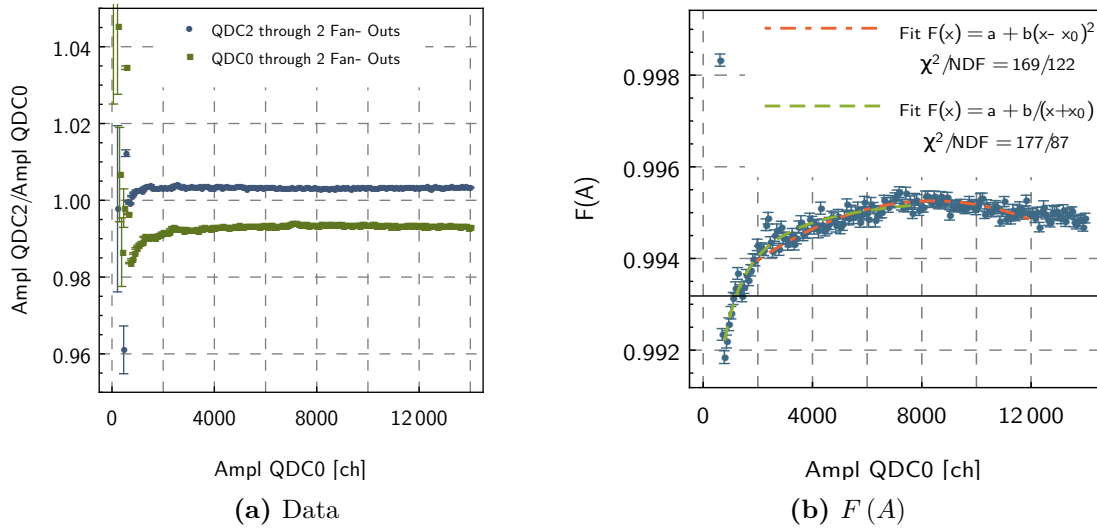
(a) Data

(b) $F(A)$

Fig. 7.9: Comparison of the measured amplitudes when guiding PMT pulses through a single or two fan-outs. Calculating $F(A)$ according to equation 7.22 shows that the damping in the second fan-out stage is amplitude dependent.

between the observed non-linearity and the measured scintillator non-linearity. However, the present experiment only tests for the effect in the second Fan-Out stage. Without knowing the specific origin of this non-linearity no conclusion can be made for a single fan-out stage.

This measurement leaves amplitude dependence of the fanouts as one of the potential origins for the detector non-linearity.

7.2.4 Effect on the Beta Asymmetry

In order to evaluate the potential effect of different models for the detector non-linearity the complete analysis (see chapter 6) is reperformed. The models used in this investigation are found to provide a good description of the calibration and neutron decay spectra. These models don't exactly resemble the shape of the electronics non-linearity found in section 7.2.3. The reason is that the results for the fan-out non-linearity can not be applied to the fit function as the non-linearity. The exact shape and strength of the effect is not known and may be different for each setup. Moreover, this kind of non-linearity would apply to every individual PMT channel and not the complete detector amplitude. A correct implementation would require also the inclusion of the light distribution among the PMTs.

The used models are

- **Birks**

  This is the model used in the initial fits. Although it is meant to describe non-linearity effects in the scintillator it can account for other effects if the resulting shape of the non-linearity is similar.
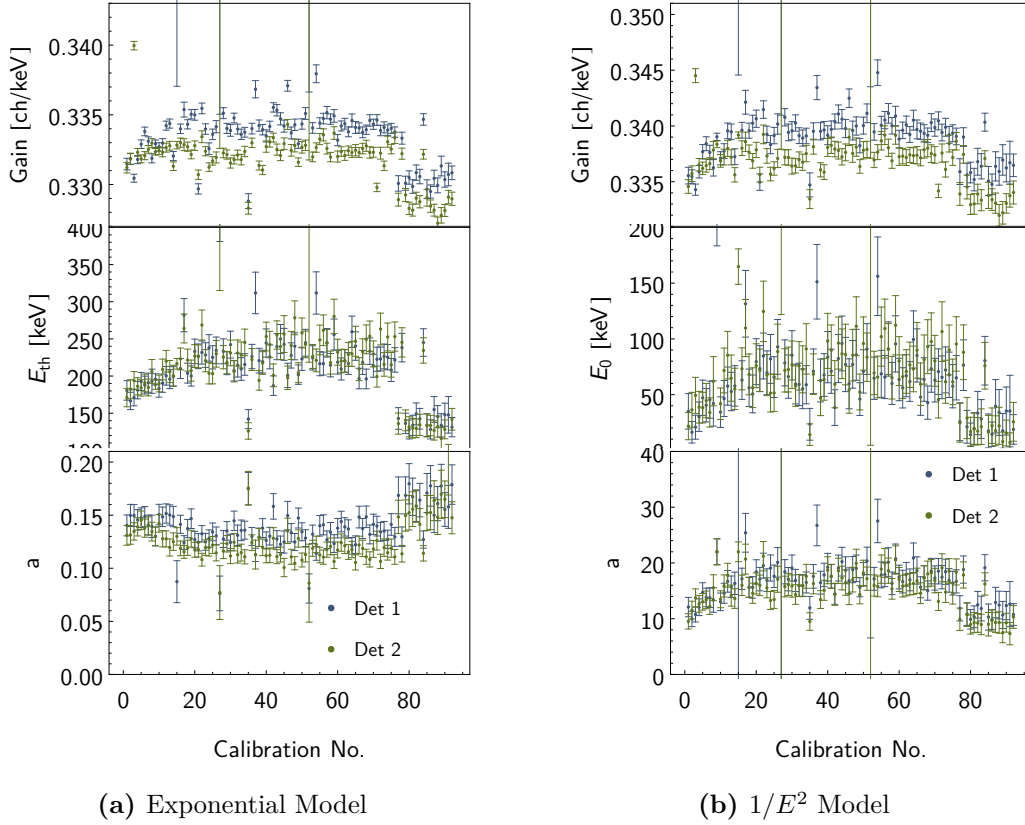
(a) Exponential Model   **(b)** $1/E^2$ Model

Fig. 7.10: Results for the individual calibration parameters when extending the scintillator non-linearity (with $k_B = 150$ nm/keV) with an Exponential or $1/E^2$ model. The errorbars denote the correlated uncertainties for the parameters.

- **Exponential**

  This model describes an exponential non-linearity with strength a and a specific threshold energy E_{th}:

$$E_{nl}(E) = E \cdot \left(1 - a \cdot \exp\left(-\frac{E}{E_{\text{th}}}\right)\right). \tag{7.24}$$

- **$1/\text{E}^2$**

  This model is motivated by the shape of the non-linearity observed in the Fan-Out tests (see section 7.2.3).

$$E_{nl}(E) = E \cdot \left(1 - \frac{a}{(E + E_0)^2}\right) \tag{7.25}$$

Except for the Birks model, which is the same that is used in chapter 6, these models are considered as extension to the known scintillator non-linearity. The energy E used as input for the additional non-linearity contribution already has the Birks non-linearity
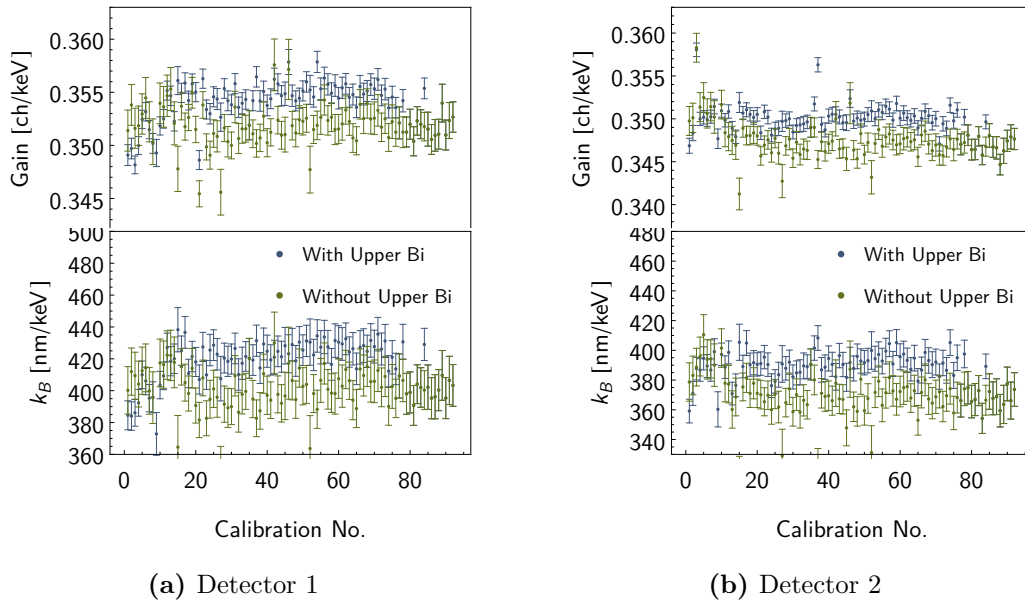
(a) Detector 1 **(b)** Detector 2

Fig. 7.11: Comparison of the detector calibration with and without the upper ^{207}Bi-peak included in the fit using the Birks model with k_B free. Reducing the calibration fit range leads to less variations of the detector gain and non-linearity when comparing the individual results.

applied with a fixed value of $k_B = 150$ nm/keV. This is within measurement uncertainties of the measured Birks coefficient (see section 7.2.1).

Figure 7.10 shows the results of the calibration fits for the gain and non-linearity parameters for each calibration dataset. The extracted parameters show a similar behaviour for the different models. The later measurements performed without the ^{207}Bi-source result in a lower gain and smaller non-linearity. Similarly, the gain and the non-linearity are different for the first measurements performed with different PMT high voltages. While the latter effect is expected when the additional non-linearity is assumed to be an electronics effect, the dependence on the source selection shows that the description of the non-linearity does not provide an exact description over the whole energy range.

Although these models are primarily meant to describe additional non-linearities due to the electronics they are implemented in the same way as the pure scintillator non-linearity. The reasoning behind this is that, as already indicated in section 5.2.1, the non-linearity generally requires seperate handling of the individual amplitudes in multi-electron events as they appear e.g. within the calibration measurements[2].

To account for this fact, the analysis for all models is repeated again. This time the higher ^{207}Bi-peak is excluded from the fits. This reduces the upper limit of the calibration fit range from 1.2 MeV to 750 keV which is closer to the energy range used for the fits of

---

[2]This is also true for effects in the electronics as the non-linearity occurs for every single detector hit due to the fast response time of the detector. Realizing this in higher layers (e.g. the energy-channel relation) of the detector response model becomes very inefficient and only has a minor effect on the obtained results.
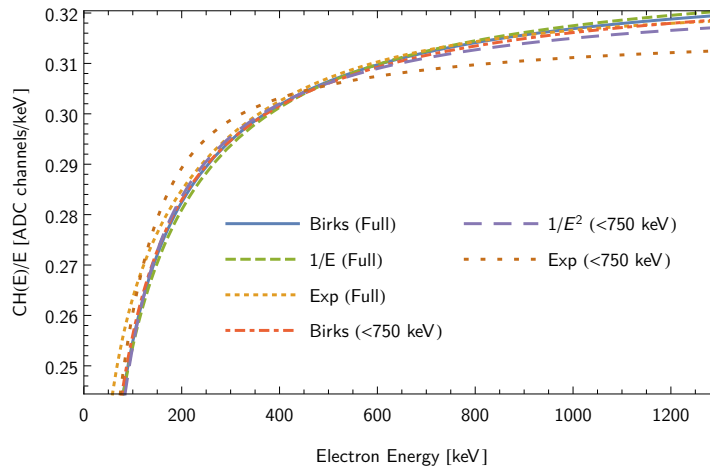
Fig. 7.12: Comparison of the resulting gains for detector 1 and the different non-linearity models. For all models the analysis has been performed using the full calibration fit range and limiting the fit range to energies below 750 keV. The plot shows the energy-channel-relation normalized with the incident electron energy.

the experimental beta asymmetry. The results of the calibration parameters for the Birks model for each dataset are shown in figure 7.11 and compared to the previous results. The fits performed with the reduced fit range are not sensitive to the availability of the Bi-data although the first peak at around 500 keV is still used. This shows that in the energy range up to 750 keV a consistent description of the detector non-linearity is achieved.

The results of the calibration fits for the different models are illustrated in figure 7.12 in terms of the energy-channel-relation normalized with the incident electron energy. The results for the beta asymmetry and the Fierz term analysis relative to the pure Birks calibration are listed in table 7.1 and illustrated in figures 7.13 and 7.14. The resulting detector calibrations differ for very low and very high energies. Within the fit range used for the analysis of the experimental beta asymmetry the differences are small. The only exception to this is the exponential model when fitting the calibration only with lower fit ranges. Here the resulting detector response becomes much more linear for higher energies and dominantly non-linear for very low energies. However, even for this case the shift relative to the Birks model is smaller when using the full calibration fit range. This illustrates that although the exact shape of the detector response may vary with respect to the selection of fit ranges the available calibration peaks are composed well to pin the detector response for the energies relevant in the fits of the experimental beta asymmetry.

For the models having two parameters the resulting calibration uncertainty is generally higher than for the pure Birks fit (compare figure 6.2) which is due to strong parameter correlations. This also holds for the case of the reduced fit range which does not affect the statistical calibration uncertainty much. This is mainly due to the fact that in this energy range the detector non-linearity is described better for any of these models providing a sharper χ^2-minimum and consequently smaller uncertainties relative to the available statistics.

The reduced χ^2 values for the calibration fits for all of these models are similar,
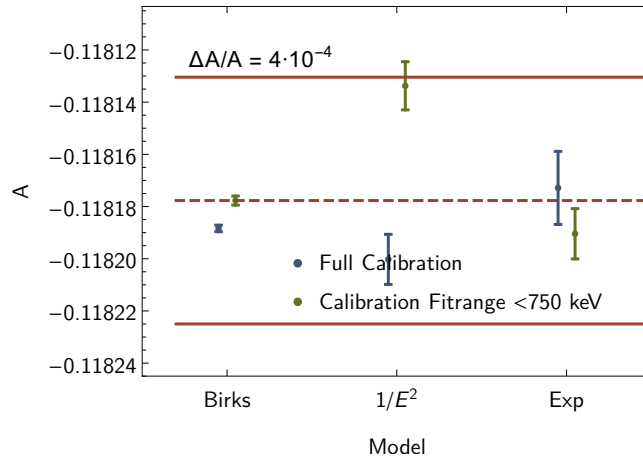
Fig. 7.13: Comparison of the combined result for the beta asymmetry A, when using different non-linearity models and fit ranges for the extraction of calibration parameters. The errorbars represent the projected calibration uncertainty of the given model. The region indicated by the red lines represents the estimate for the uncertainty. The results are also summarized in table 7.1.
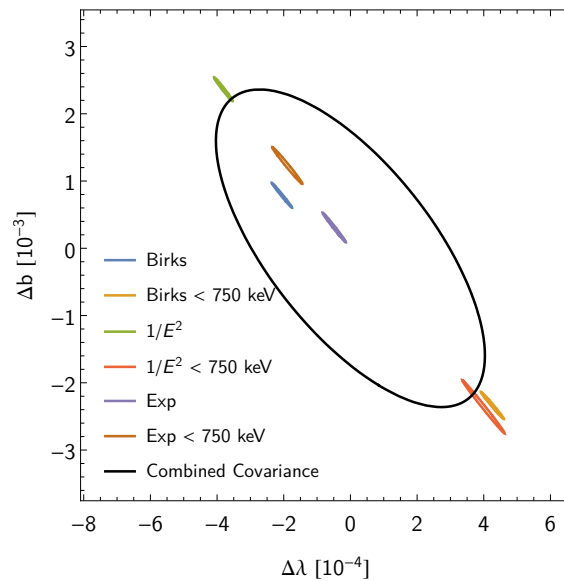
Fig. 7.14: Comparison of the combined result for λ and b, when using different non-linearity models and fit ranges for the extraction of calibration paramters. The error ellipses for the individual model correspond to the respective calibration uncertainty. The black ellipse represents a constructed ellipse that contains all models and represents the uncertainty for the detector non-linearity. The results are also summarized in table 7.1.

Model	Calibration		Results		
	Fit Range	$\langle \chi^2/\mathrm{NDF_{calib}} \rangle$	$\Delta A/A\ [10^{-4}]$	$\Delta \lambda\ [10^{-4}]$	$\Delta\ b[10^{-3}]$
Birks	Full	1.18/1.25			
	< 750 keV	1.09/1.15	-0.9	6.3	-3.1
$1/E^2$	Full	1.15/1.20	1.0	-1.7	1.6
	< 750 keV	1.08/1.13	-4.6	6.0	-3.1
Exp	Full	1.22/1.25	-1.3	1.6	-4.8
	< 750 keV	1.08/1.12	-1.7	1.7	-4.4

Tbl. 7.1: Comparison of the combined result for the beta asymmetry A and the λ-b analysis, when using different non-linearity models and fit ranges for the extraction of calibration parameters.

with slightly smaller values when removing the upper Bi peak. This allows no further discrimination of the selected models. Since the results obtained with the reduced calibration fit range generally provide a better goodness-of-fit and agreement with each other, the Birks result for the reduced fit range is used as final model for the beta asymmetry. For the uncertainty related to the detector non-linearity an interval is choosen that contains all results of the different models. For the λ-b analysis an error ellipse is constructed which again contains all models. An additional requirement is that the uncorrelated uncertainty in λ should reflect the single parameter uncertainty for A.

Fit Range	Beta Asymmetry	λ-b		
	$\delta A/A\ [10^{-4}]$	$\delta \lambda\ [10^{-4}]$	$\delta b\ [10^{-3}]$	$\rho_{\lambda,b}$
297 - 694 keV	4	5	3	-0.91
244 - 694 keV	5	5	3	-0.85
197 - 694 keV	6	4	2	-0.68

Tbl. 7.2: Systematic uncertainties due to detector non-linearity for the beta asymmetry and λ-b. The uncertainties given for λ and b represent the correlated uncertainties.

The final uncertainties for the detector non-linearity for both analysis are given in table 7.2. While the uncertainty for A increases for larger fit ranges, the correlated uncertainties for λ and b even decrease due to the reduction in correlation.

7.3 Spatial Detector Response

The non-uniformity of the light output of the detectors leads to slight variations in the measured spectra compared to a uniform detector. This is caused by the magnetic point spread of the electron beam [Dub15] as well as the spread of the neutron beam. So far only the change in the mean light yield is accounted for when applying the detector calibration to the experimental beta asymmetry (see section 6.1.1). In this section some refinements

to this assumption are discussed which yield additional corrections to the calibration as well as the beta asymmetry measurement.

Both corrections are calculated in [Roi18] and include the mentioned magnetic point spread of electrons and use the simulation of the light transport efficiency presented in section 5.2.2 as input. The simulations are matched to the measured detector response.

The correction of the calibration measurements includes additional effects concerning the energy-loss of electrons inside the sample holder (thin carbon foil) and the potential mixing of detectors in multi-electron events. The correction for the beta asymmetry on the other hand includes the Asymmetric PSF which describes the influence of the beta asymmetry on the angular distribution of electrons and thus the point-spread.

Due to the complexity of these calculations, which involve an extension of the detector response calculations, it is not efficient to include the full corrections into the production fits. Instead the results when including these corrections are extracted only once for a reduced but representative dataset of 14 calibration sets and compared to the uncorrected results of the beta asymmetry for these datasets. The individual corrections are shown in figure 7.15. The effect is much stronger for detector 2. This is due to the fact that the foils supporting the calibration sources are pointing to detector 2 and electrons emitted towards this detector loose some of their energy. For the individual detectors the variation between indidual datasets is rather strong. This is caused by considering the mixing of detectors for multi-electron events in the calibration. When combining both detectors for each dataset the resulting correction is stable.
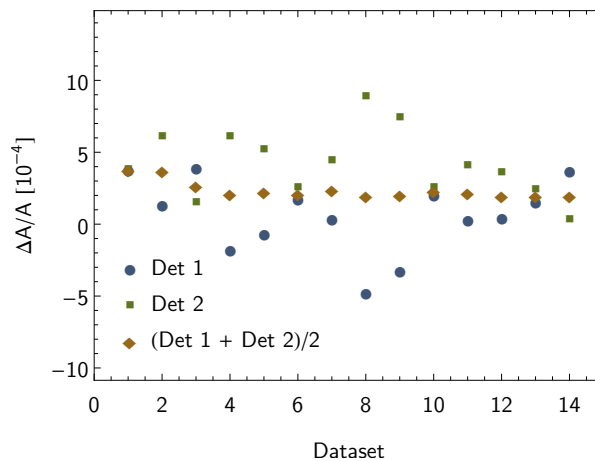

Fig. 7.15: Spatial response correction for the beta asymmetry for 14 datasets. The correction includes effects of the magnetic point-spread of electrons in the magnetic field of PERKEO III, the non-uniformity of the detector response, energy loss of electrons in the calibration foil holder and detector mixing in multi-electron events.

The average correction for all used datasets becomes $\Delta A/A = 4.2(2.1) \cdot 10^{-4}$. The uncertainty is assumed to be 50% and accounts for the fact that the light transport

simulations are not yet matched perfectly to the scan measurements. Another potentially important uncertainty arises from the fact that the position of the calibration scanner and detectors are not known. This effect has been studied by varying the beam center for the calibration and beta asymmetry measurements individually by 5 mm horizontally and vertically. The resulting changes in the correction are on a level of $\Delta A / A = \mathcal{O}(10^{-5})$ and can be neglected.

The fit results presented in section 6.2 already include an initial correction to account for the different detector coverage in calibration and neutron decay measurements (see section 6.1.1). The effect of this first order correction is $\Delta A / A = 5.6 \cdot 10^{-4}$. The net correction to be applied to the fit results is then given as the difference:

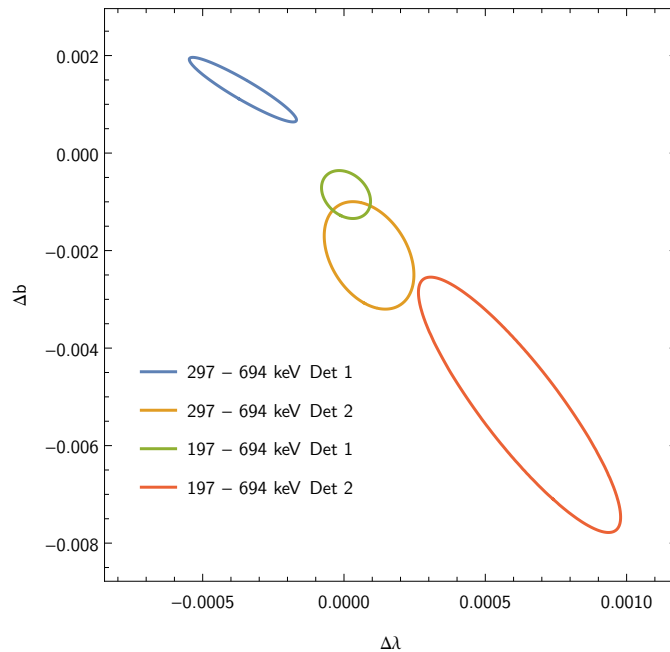$$\frac{\Delta A}{A} = -1.4(2.1) \cdot 10^{-4}. \tag{7.26}$$

Fig. 7.16: Spatial response correction in the combined λ-b analysis for each detector and fit range. The correction includes effects of the magnetic point-spread of electrons in the magnetic field of PERKEO III, the non-uniformity of the detector response, energy loss of electrons in the calibration foil holder and detector mixing in multi-electron events. The ellipses denote the 68.27% uncertainty and the corrections are the centre of the ellipses.

The analysis is repeated for the combined λ-bb analysis. Due to the high computational effort only the $291 - 694$ keV and $197 - 694$ keV energy ranges have been used for this analysis and the corrections are averaged for each detector. Figure 7.16 shows the corrections and uncertainties for each detector and fitrange. Similar to the analysis of the beta asymmetry the effect is larger for detector 2 due to the orientation of the sample

holders. With decreasing the lower limit of the fit range the correction becomes larger.

For the 197 - 694 keV fit range the correction obtained is

$$\Delta\lambda = 1.6(2.7) \cdot 10^{-4}, \ \Delta b = -1.1(1.9) \cdot 10^{-3}, \ \rho_{\lambda,b} = -0.87, \tag{7.27}$$

where the errors are given as correlated 68.27% uncertainties and $\rho_{\lambda,b}$ is the correlation as extracted from the covariance matrix. This correction is that necessary to correct the fit results obtained in section 6.3. It already accounts for the fact that the fit results include an initial correction.

7.4 Electron Backscattering

One important effect when detecting electrons in the keV-MeV energy range is that they can backscatter from the detector surface. For plastic scintillators the backscattering probability for electrons is angle and energy dependent. The typical backscattering probability for electrons from neutron decay is about 11%. This is compared to other detector types, e.g. Silicon based detectors, and makes scintillators a good for beta spectroscopy. When being backscattered electrons usually deposit a large fraction of their energy before escaping the scintillator.

In addition to reducing systematics related to the magnetic field, the symmetric two-detector design of the PERKEO instruments allows to reconstruct the full electron energy even in case that backscattering occurs. Backscattered electron either follow the magnetic field lines to the opposite detector or depending on the backscattering angle, are reflected back onto the same detector by the magnetic potential of the decay volume (see section 3.4.1). Every time one of the two detectors is triggered, the charge integral for all PMTs of both detectors is measured and recorded. This allows to reconstruct the full electron energy as both the energy deposited in the primary and secondary detector can be summed up.

Figure 7.17 shows a measured neutron decay spectrum of detector 1 compared to the amplitude measured in detector 2 with and without the trigger condition being satisfied for detector 2. The increased number of events in case that the trigger condition is not fulfilled for the second detector is mainly due to the detector pedestal (QDC noise). Due to the magnetic mirror effect the fraction of triggered backscattering on the second detector is 3.8%.

In this section two important systematic effect related to backscattering are discusssed. The first effect deals with the dependence of the full energy reconstruction on the integration time window used in the QDCs. The second effect accounts for events, where the energy deposit of the electron before it is backscattered is below the trigger threshold.

7.4.1 Short gate-time of the QDCs

One requirement for full energy reconstruction in case of backscattering is a sufficient integration time window of the QDCs. The effect of the limited gate time of the used QDCs has been investigated by Monte-Carlo simulations of backscattering spectra in
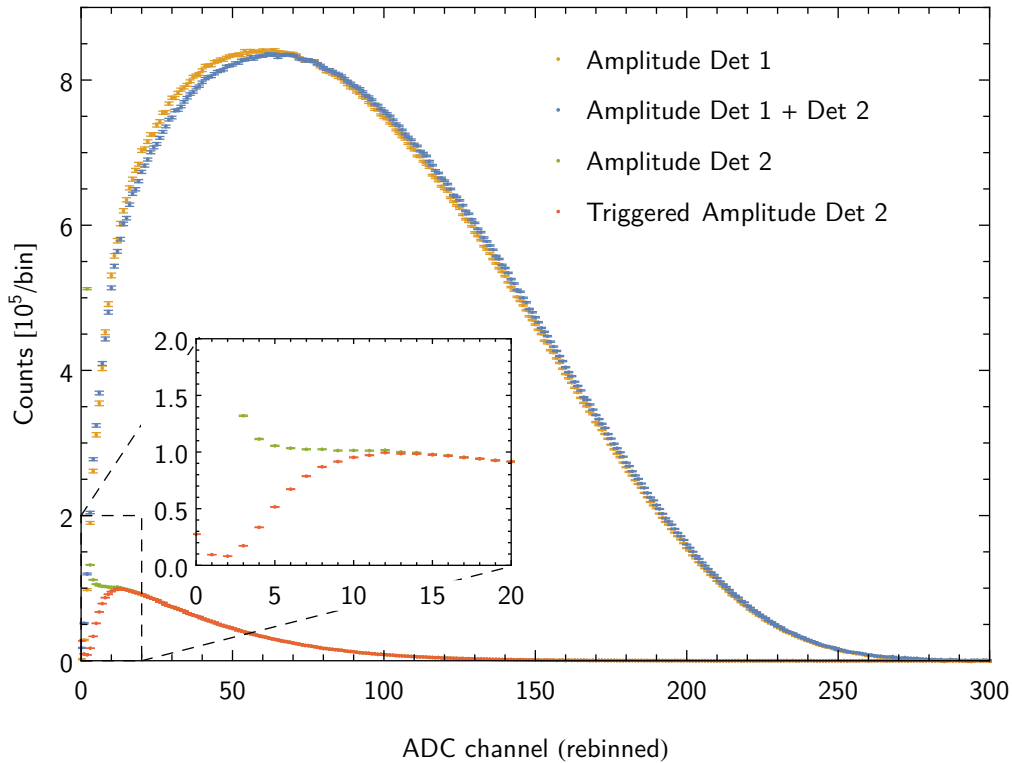
Fig. 7.17: Neutron decay spectrum of detector 1 and the simultaneously measured backscattering spectra on detector 2 with and without trigger condition fulfilled.

[Mes11]. The expected shift of the measured beta asymmetry is

$$\frac{\Delta A}{A} = 0.1(1.4) \cdot 10^{-4}. \tag{7.28}$$

The analysis is limited by the number of simulated events and while the correction itself can be considered negligible its uncertainty applies to the final result for the beta asymmetry.

7.4.2 Undetected and wrongly assigned backscattering

When backscattering occurs there is a certain probability that the energy deposit within the primary detector is small and the trigger condition is not satisfied. If in these cases the backscattered electron generates a trigger in the other detector, the event is assigned to the wrong detector. Moreover, the fraction of the energy deposited in the primary detector is now missing from the event independent of which detector detects the remaining electron energy. These undetected backscattering events are by their nature not identifiable within the data.

In case of polarized neutron decay the wrong assignment of events makes the magnitude of the beta asymmetry smaller. The incomplete energy deposition on the other hand
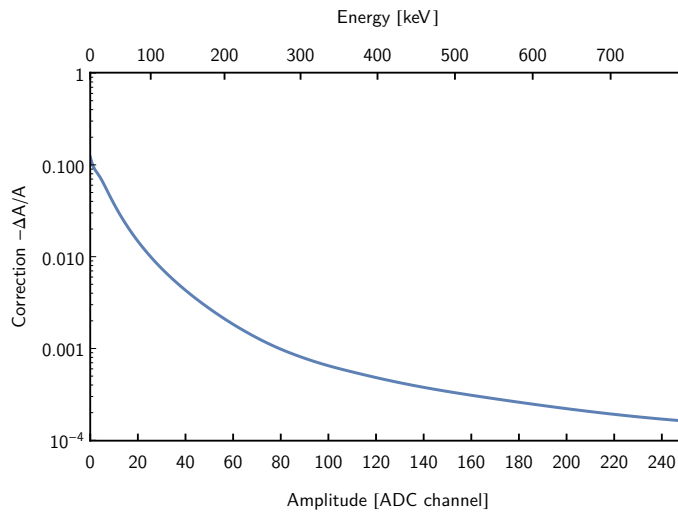
Fig. 7.18: Correction to the fit function for the experimental beta asymmetry for detector 1. The correction accounts for undetected and wrongly assigned backscattering events making the measured asymmetry smaller.

counteracts this effect as in the experimental beta asymmetry higher energetic events with a larger asymmetry are shifted towards lower energies.

For PERKEO III these effects have been studied in [Mes11] based on the calculations made for PERKEO II [SA08]. However, in this analysis the correct trigger function and fractional energy deposition have not been considered. To this end a new estimate for the effect on the beta asymmetry has been done [Roi18]. This analysis uses the response model for the photomultipliers as derived in section 5.3.2 to calculate the correct trigger function for the detector system. The detector calibration used is the one derived in section section 6.1 and the backscattering simulations performed with GEANT4 are matched to reproduce the backscattering data shown in figure 7.17.

The correction is derived as an energy dependent relative correction to the fit function for the experimental beta asymmetry similar to the method used for the correction of the detector's spatial response in section 7.3. Figure 7.18 shows the correction for detector 1. Applying this correction when fitting the beta asymmetry leads to a correction of

$$\frac{\Delta A}{A} = 4.6(1.3) \cdot 10^{-4}, \tag{7.29}$$

for the 297 - 694 keV fit range, where the uncertainty accounts for uncertainties in deriving the trigger function from the data and in the backscattering simulations.

The resulting correction for the λ-b analysis is shown in figure 7.19. The correction and its uncertainty become larger when reducing the lower limit of the fit range. Due to the symmetric setup the correction is almost the same for both detectors. For the 197 - 694 keV fit range the correction obtained is

$$\Delta\lambda = 9.9(4.6) \cdot 10^{-4}, \ \Delta b = -6.4(2.9) \cdot 10^{-3}, \ \rho_{\lambda,b} = -0.97, \tag{7.30}$$
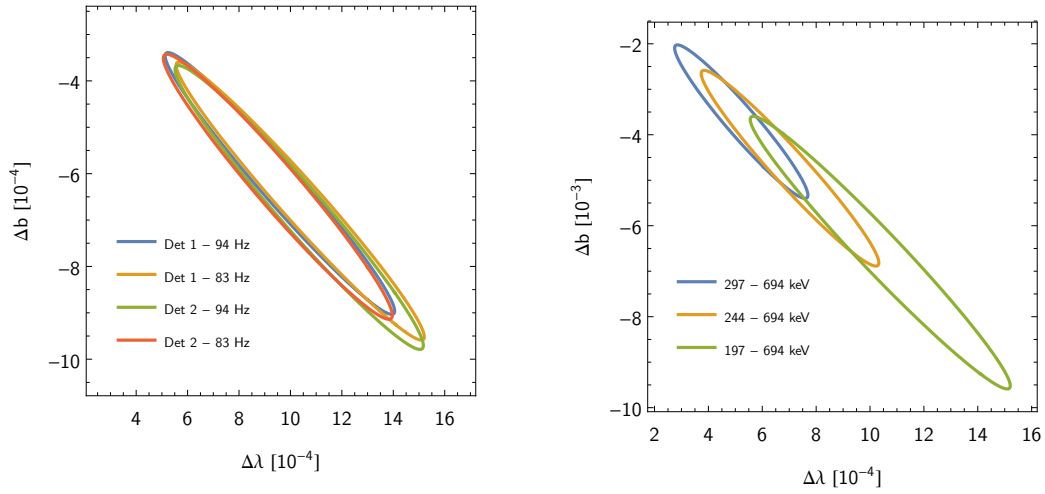
(a) Individual Datasets, Fit Range 197 - 694 keV.

(b) Different fit ranges, Det 1 - 83 Hz.

Fig. 7.19: Correction for undetected backscattering of electrons from the scintillator. The ellipses denote the 68.27% uncertainty and the corrections are the centre of the ellipses.

where the errors are given as correlated 68.27% uncertainties and $\rho_{\lambda,b}$ is the correlation as extracted from the covariance matrix.

Chapter 8

Detector Background

As discussed in section 4.3 the background subtraction is based on measuring with a pulsed neutron beam. The neutron beam is pulsed using a rotating disc chopper. This chopper is closed while the neutron pulses passes the central decay volume and still remains closed while the neutron pulse is absorbed by the beamstop. The neutron decay signal is extracted from events within the signal time window, which is choosen such that the neutron pulse is in the central decay volume. A second time window after the neutrons are absorbed is used to extract the detector background. Subtraction of the measured background, with appropriate scaling for the different lengths of both windows, from the signal finally gives a background free neutron decay spectrum.

This method allows to measure all kinds of background that are stable over the time of a single chopper rotation. This covers all beam-independent background originating from the reactor environment and other experiments as well as background produced within the beam preparation of the PERKEO III experimental setup. However, beam-dependent background, meaning background that is somehow produced by or correlated with the neutron pulses passing the spectrometer is not fully covered by this method as it may contribute differently within the signal and background time windows.

In this chapter the limitations of the background subtraction method are investigated including potential sources of beam-dependent background. Some of these effects have been addressed in [Mes11] and are updated to account for the different choice of background time windows (see section 3.3.1). In particularx the checks for beam-dependent background from the chopper as well as limits on the precision of the dead-time correction are performed for the first time.

8.1 Sensitivity to background in the Experimental Beta Asymmetry

As discussed in section 4.3.2, the contribution of the background to the statistical uncertainty is already included in the calculation of the experimental beta asymmetry. To investigate the effect of background uncertainties other than the statistical one the influence of background shifts to the experimental beta asymmetry needs to be known. This is obtained by calculating the relative shift in the beta asymmetry for fractional shifts in the Background intensity:

$$\frac{\Delta A}{A} = \frac{\frac{\partial A}{\partial B} \cdot \Delta B}{A} = \frac{\Delta B}{B} \cdot \frac{r \cdot B(E)}{N^\uparrow(E) + N^\downarrow(E) - r \cdot B(E)} = \frac{\Delta B}{B} \cdot \mathrm{SF}(E). \qquad (8.1)$$

The statistical suppression function SF (E) describes the energy dependent relation between background shifts and shifts in the beta asymmetry.
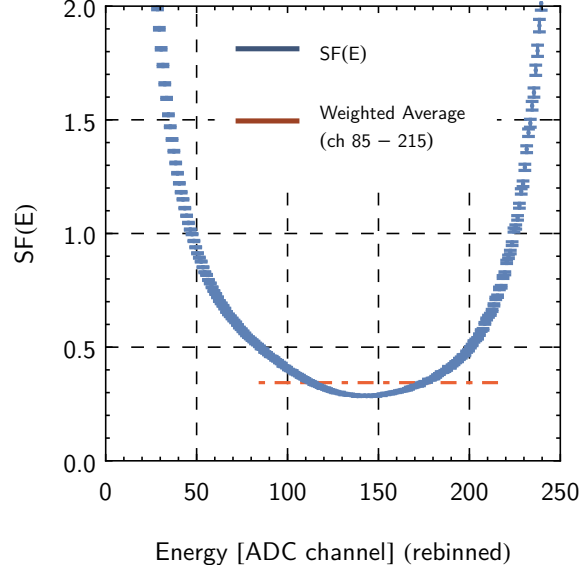

Fig. 8.1

Fig. 8.2: Statistical suppression function SF (E) for Det1 / 94Hz that relates relative shifts in background intensity to relative shifts in the beta asymmetry according to equation 8.1. The weighted average of SF (E) is used to obtain the net correction for the whole analysis energy region of 300 to 700 keV.

Dataset	$\langle$SF $(E)\rangle$
Det1 / 94Hz	0.344
Det2 / 94Hz	0.239
Det1 / 83Hz	0.329
Det2 / 83Hz	0.238

Tbl. 8.1: Weighted average of the statistical suppression function for the different datasets.

The net effect is obtained by performing a weighted average of SF (E) over the fit region used for the analysis. As this function depends on the actual signal-to-noise ratio, different results are obtained for individual datasets and detectors which are summarized in table 8.1.

In order to estimate the same effect for the λ-b analysis, generally the derivatives $\partial\lambda/\partial B$ and $\partial b/\partial B$ are required. However, to extract small systematic corrections it is sufficient to apply fractional changes in the background intensity. A linear rescaling factor r is used. A modified background intenstiy $B'(E)$ then can be written as

$$B'(E) = r \cdot B(E),\tag{8.2}$$

where $B(E)$ is the background spectrum as measured. This treatment includes the assumption that the background spectrum does not change significantly for the systematics discussed.

Additional datasets are created where background is rescaled by a factor $r = 1.03$. Refitting and calculating the shifts relative to the data without rescaled background allows to obtain the shifts necessary to calculate the derivatives $\partial\lambda/\partial r$ and $\partial b/\partial r$. To give a full covariance matrix for the uncertainty, the parameter system is again rotated with respect to the observed shifts. The diagonal covariance matrix created in the rotated parameters system then becomes a non-diagonal covariance matrix including an estimate for the correlation when rotating back. This method is explained in more detail in section 7.1.
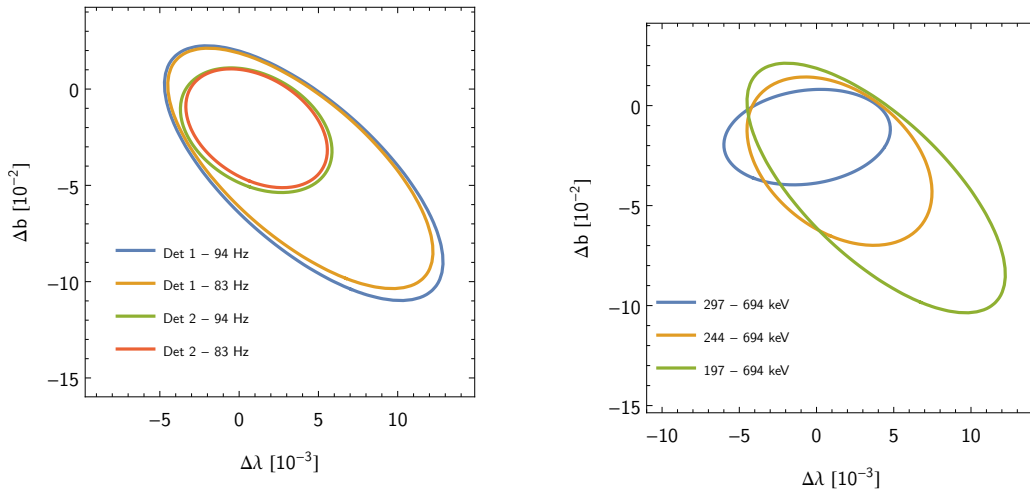
(a) Individual Datasets, Fit Range 197 - 694 keV.

(b) Different fit ranges, Det 1 - 94 Hz.

Fig. 8.3: Resulting correction, denoted by the centre of the ellipses, and the corresponding uncertainties when assuming a systematic correction in the background rescaling $\Delta r = 0.03(3)$.

Figure 8.3 shows the corrections and uncertainties resulting from a background rescaling of $\Delta r = 0.03(3)$. Due to different signal-to-noise ratios and background spectra the results are individual to each dataset and especially different for both detectors. This has already been observed for the statistical suppression function used for the beta asymmetry (see table 8.1). Changing the fit range significantly changes the observed shifts in magnitude and direction, which is expected due to the spectral shape of the background spectrum.

8.2 Time variation of background

In [Mes11] the time variation of the background count-rate is investigated. This investigation mainly addresses beam-dependent background that is created by a delayed signal from the beamstop (see section 3.3.1) which is present only within the background time window. In this section this analysis is repeated considering the statistical suppression function for the individual datasets and the new background time windows.

The time variation of the background signal is investigated by linear fits to the detection rate vs. the time-of-flight where an energy cut of 300-700 keV has been applied to the data. The resulting slopes of the linear fit indicate the amount of time variation present within the background window. The "real" detector background that is also present within the signal-window is assumed to be constant in time. Hence the slope is interpreted as additional signal which must not be considered when subtracting the background.

Dataset	Constant Fit		Linear Fit			
	χ^2/NDF	Prob.	χ^2 / NDF	Prob.	Slope $[10^{-3}/\text{ms}]$	$\Delta A/A[10^{-4}]$
Det1 / 94 Hz	55.5/39	0.20	49.3/38	0.21	$-1.0(0.9)$	$-1.8(1.6)$
Det2 / 94 Hz	33.5/39	0.72	31.2/38	0.77	$-1.7(1.1)$	$-2.0(1.3)$
Det1 / 83 Hz	39.3/39	0.46	38.0/38	0.47	$1.2(1.1)$	$2.0(1.7)$
Det2 / 83 Hz	37.7/39	0.53	36.3/38	0.55	$-0.8(1.2)$	$-0.9(1.5)$
Total						$-0.8(0.8)$

Tbl. 8.2: Results of linear and constant fits performed within the count rate vs. neutron time-of-flight histogram for each dataset. The fraction of background described by the slopes is considered as additional background (e.g. due to the beamstop) that is not present within the signal window. The correction for the beta asymmetry is calculated by applying the statistical suppression function as derived in section 8.1.

The results of these fits including the corresponding corrections to the beta asymmetry for each dataset are summarized in table 8.2 where the average statistical suppression functions from table 8.1 have been used to calculate the correction for the beta asymmetry. In order to test the significance of this slope, also constant fits have been performed which show that the time variation can not be assumed as zero. The correction to the beta asymmetry is smaller compared to the previous analysis, which result only in slight improvements in the goodness of fit. Since the uncertainties of the individual corrections are statistical in nature and independent, Gaussian uncertainty propagation is applied when averaging over multiple datasets.

For the λ-b analysis the corresponding corrections are calculated accordingly reinterpreting the slope as an error in the rescaling factor r. The total correction obtained for the 197 - 694 keV fit range is:

$$\Delta\lambda = 0.4(4.9) \cdot 10^{-5}, \ \Delta b = 0.6(3.5) \cdot 10^{-4}, \ \rho_{\lambda,b} = -0.58. \qquad (8.3)$$

As opposed to the results of the beta asymmetry analysis, here the uncertainty is much larger than the correction itself. The corrections for the individual datasets cancel almost completely. Projecting the covariance to a single parameter uncertainty in A (by assuming $b = 0$) leads to $\delta A/A = 1.1 \cdot 10^{-4}$ when also considering the same fit range as for the beta asymmetry analysis. The difference in the uncertainty is partly due to the fact that part of the 94 Hz data is ignored in the analysis. Also the correction is developed using different degrees of freedom around a different point in the λ-b parameter space. Thus one

can expect different estimates for the uncorrelated parameter uncertainties, in particular when the effects are small compared to the statistical uncertainty of the experimental beta asymmetry.

8.3 Chopper background

Another source of beam-dependent background is the chopper itself. A measurement of the background created by the chopper has been performed after installation of the full experimental setup [Wer09]. A NaI counter has been placed close to the chopper in order to detect *gamma*-radiation that is generated while the chopper rotates. Figure 8.4 shows the detected count-rate vs. the chopper rotation angle for different chopper frequencies. During the opening of the chopper at 18 ° the measured count rate is strongly decreased. However, the created background shows a dependence on the chopper angle even if the chopper is fully closed. This leads to differences in the background generated during the signal and background time windows. The fact that the structure of the measured count-rate is independent from the chopper frequency indicates that the background is generated instantaneously.
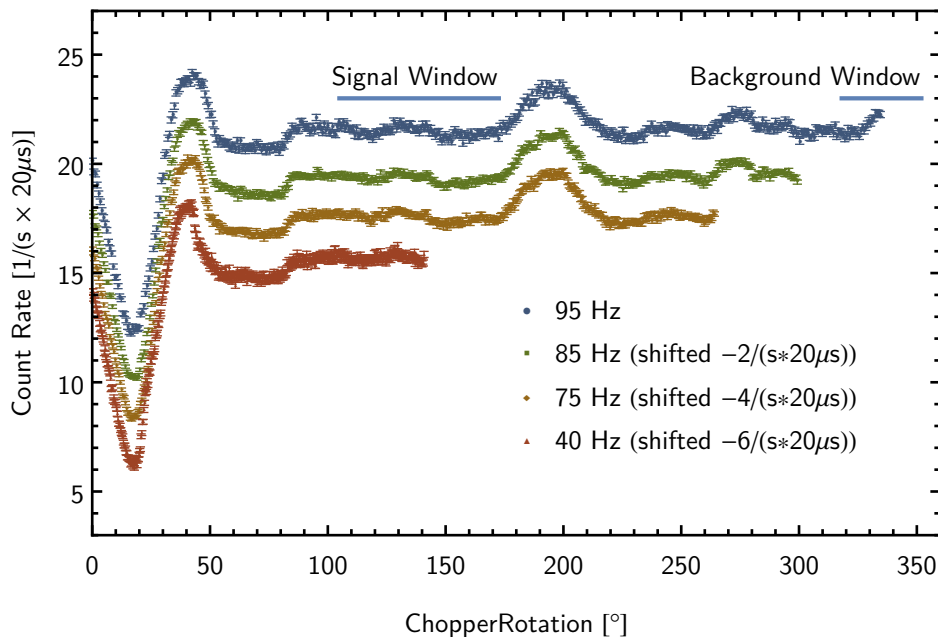
Fig. 8.4: Measurement of the chopper background using a NaI-counter for different chopper frequencies. The data show the reduction of background during the chopper opening at around 18 ° and a variation of the background while the chopper rotates. This variation induces differences of the background measured within the signal and background window. The intensity is normalized to the counts per second and time-of-flight bin with a bin width of 20 μs.
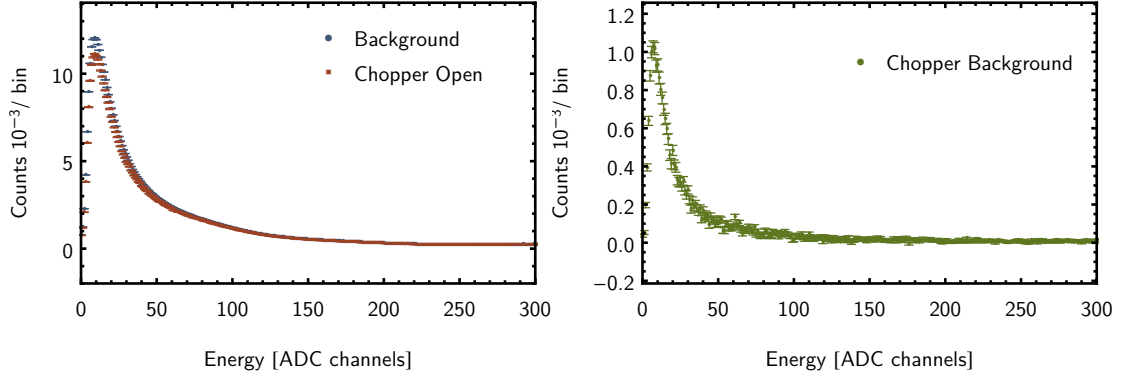
(a) Pulse height spectra extracted from the background time window and a time window that corresponds to the chopper being completely open (see equation 8.4.

(b) Spectrum of the background created by the chopper. This spectrum is obtained by subtracting the two spectra shown in figure 8.5a.

Fig. 8.5: Pulse height spectra to extract the chopper background.

Sensitivity of the Perkeo III detectors to Chopper Background

In order to estimate the influence of the varying chopper background on the measurement, the spectral sensitivity of the electron detectors to this background needs to be estimated. To this end the background measured within the background time window and during chopper opening are compared. A corresponding time window is defined. Its center is assumed to be 18° and the width to be 2°, which matches the chopper opening window determined in [Wer09]. The spectra used to extract the data have a neutron time-of-flight binning of 25 μs. This leads to time windows of

$$
\begin{aligned}
475 - 525 \ \mu\text{s} \ (94 \text{ Hz}), \\
525 - 600 \ \mu\text{s} \ (83 \text{ Hz}).
\end{aligned}
\tag{8.4}
$$

Figure 8.5a shows a comparison of the spectra extracted from the background time window and the mentioned time window where the chopper is open. The spectrum of the chopper background is rescaled to account for the different lengths of the time-of-flight windows. The difference of these spectra shown in figure 8.5b gives the spectral contribution of the background created by the chopper. The spectrum shows that the background priduced is predominantly low energetic, as expected for gamma radiation.

To estimate the effect of variations in the chopper intensity for the experimental beta asymmetry a similar method as the one used to calculate the sensitivity for overall background changes is used (see section 8.1). This time the statistical suppression function is calculated only for variations of the chopper background to obtain the relation

$$
\frac{\Delta A}{A}(E_e) = \text{SFC}(E_e) \cdot \frac{\Delta C}{C}(E_e).
\tag{8.5}
$$

The description of the experimental beta asymmetry 4.14 is modified

$$A_{exp}(E) = \frac{N^{\uparrow}(E_e) - N^{\downarrow}(E_e)}{N^{\uparrow}(E_e) + N^{\downarrow}(E_e) - B'(E_e) - C(E_e)}, \tag{8.6}$$

where the background contribution in the denominator is split into the chopper background $C(E_e)$ and the remaining background $B'(E_e)$. These two spectra are not accessible directly, but can be rewritten in the form of the accessible spectra $B(E_e)$, which is the usual background term, and $C_{\text{open}}(E_e)$, which is the spectrum measured during the opening window of the chopper scaled to account for the length of the time windows.

$$\begin{aligned} C(E_e) &= B(E_e) - C_{\text{open}}(E_e), \\ B'(E_e) &= C_{\text{open}}(E_e). \end{aligned} \tag{8.7}$$

Assuming the chopper background during the background time window is changed by a small fraction, the background that needs to be subtracted in the beta asymmetry needs to be reduced accordingly:

$$B(E_e) \rightarrow B(E_e) + (r-1) \cdot C(E_e) = r \cdot B(E_e) + (1-r) \cdot C_{\text{open}}(E_e), \tag{8.8}$$

where $r = 1 - \Delta C/C$ describes the rescaling of the chopper background. Inserting this into the experimental beta asymmetry and using $r \simeq 1$ after calculating the derivative, allows to extract the statistical suppression function

$$\frac{\Delta A}{A} = \frac{\frac{\partial A}{\partial r} \cdot \Delta C}{A} = \frac{\Delta C}{C} \cdot \frac{B(E_e) - C_{\text{open}}(E_e)}{N^{\uparrow}(E_e) + N^{\downarrow}(E_e) - B(E)} = \frac{\Delta C}{C} \cdot \text{SFC}(E_e). \tag{8.9}$$

The effect on the beta asymmetry is given by the weighted average $\langle \text{SFC}(E_e) \rangle$ over the respective fit region. These averages are listed in table 8.3 for each dataset for the 297-694 keV fit range. Due to the larger distance the sensitivity of downstream detector 2 is five times smaller compared to updstream detector 1. The uncertainties of the given results are statistical uncertainties dominated by the statistical uncertainty of the chopper background spectrum.

Variations of the chopper background

To estimate the relative variation of the chopper background $\Delta C/C$ from the NaI measurement the 95 Hz data is used. Only this dataset provides partial coverage of the background time window. The average intensity of the NaI measurement during the chopper opening is $\dot{N}_{\text{open}} = 12.43(4)$ $(\text{s} \times 20~\mu\text{s})^{-1}$. The average chopper background intensity within the signal window is $\dot{N}_{\text{sig}} = 21.47(1)$ $(\text{s} \times 20~\mu\text{s})^{-1}$.

The average intensity within the background time window is more difficult to estimate due to the fact that the background time window is not covered fully by the data and the count rate not being constant. Figure 8.6 shows the count rate measured with the NaI detector within this window. Beyond the statistical uncertainties of the data points the weighted average includes an additional uncertainty contribution that is introduced to account for the fact that the data is not constant. This uncertainty contribution is

Dataset		Correction	
Detector	f_{Chopper}	$\langle \text{SF}(E_e) \rangle$	$\Delta A/A$
1	94 Hz	$10.7(0.4) \cdot 10^{-3}$	$-3.3(1.3) \cdot 10^{-4}$
1	83 Hz	$9.7(0.4) \cdot 10^{-3}$	$-3.0(1.2) \cdot 10^{-4}$
2	94 Hz	$2.1(0.4) \cdot 10^{-3}$	$-0.7(0.3) \cdot 10^{-4}$
2	94 Hz	$1.8(0.3) \cdot 10^{-3}$	$-0.6(0.2) \cdot 10^{-4}$
Total			$-1.9(0.7) \cdot 10^{-4}$

Tbl. 8.3: Averages of the statistical suppression function $\langle \text{SF}(E_e) \rangle$ for the chopper background and each chopper set. These have been calculated for a fit region of 85 - 215 ADC channels. The given errors denote the statistical uncertainty of the result which is dominated by the statistical uncertainties of the chopper background spectrum (figure 8.5b). The correction values $\Delta A/A$ are obtained by multiplying $\langle \text{SF}(E_e) \rangle$ with $\Delta C/C$ from equation 8.11

determined by forcing the modified reduced χ^2 to be one,

$$\frac{\chi^2}{\text{NDF}} = \sum_{i=1}^{N} \frac{(x_i - \langle x \rangle)^2}{(N-1)\left(\delta x_i^2 + \Delta^2\right)} \stackrel{!}{=} 1. \tag{8.10}$$

With $\Delta = 0.342$ the weighted mean for the background time window becomes $\dot{N}_{\text{bg}} = 21.76(34) \ (\text{s} \times 20 \ \mu\text{s})^{-1}$.

Figure 8.6 also shows the count rate of detector 1 within the background time window. To infer this data an upper energy cut of 30 ADC channels is applied, in order to increase the sensitivity to the low energetic chopper background. The fraction of the chopper background in this energy region is 5.97 % as determined by comparing the spectra in figure 8.5a. The contribution of all other background is subtracted and the data is then rescaled to match the intensity of the NaI measurement. The inferred count rates show that the choice of a constant count rate within background time window is justified.

Using these results the shift of the chopper background between signal and background time window is given by

$$\frac{\Delta C}{C} = \frac{\dot{N}_{\text{sig}} - \dot{N}_{\text{bg}}}{\dot{N}_{\text{bg}} - \dot{N}_{\text{open}}} = -3.1(1.2)\%. \tag{8.11}$$

The relative corrections to the measured beta asymmetry are obtained using relation 8.9. The uncertainties for the individual datasets are dominated by the uncertainty of $\Delta C/C$ which is common for all datasets. Hence, the total correction and its uncertainty is given by the average of all datasets.

In the λ-b analysis the same procedure as described in section 8.1 is performed. Relation 8.8 is used to extract the experimental beta asymmetry for $r = 1 - 0.03$. Refitting the spectra to extract the correction and again using the explicit construction technique for
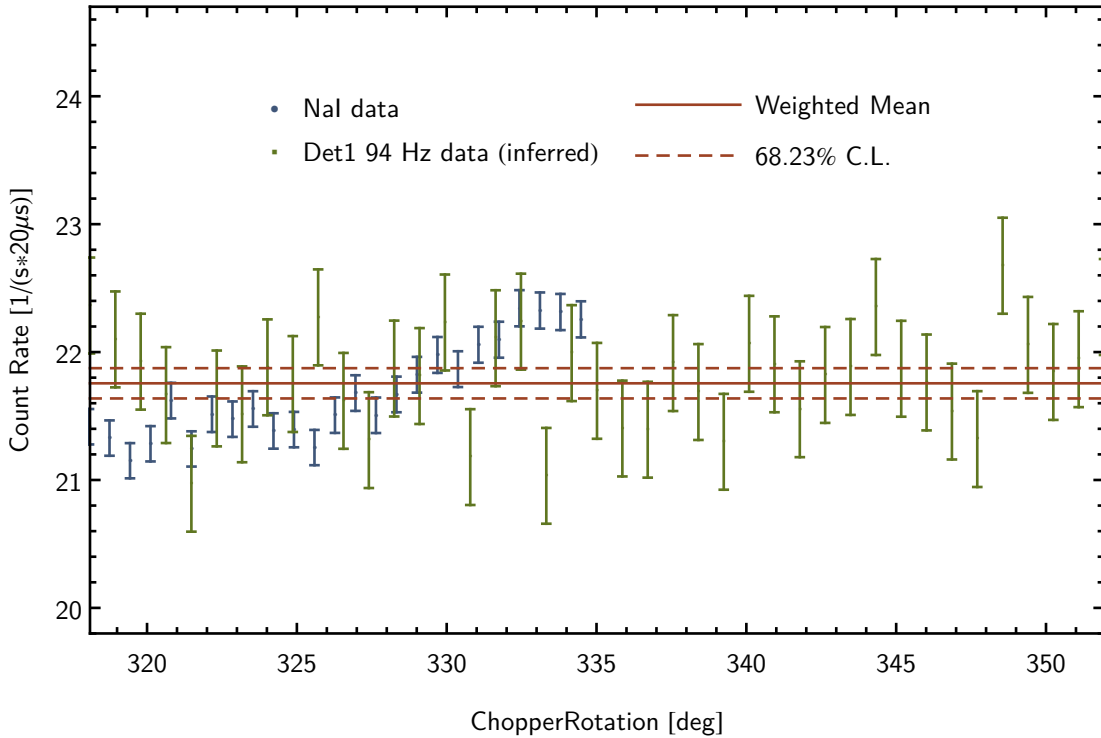
Fig. 8.6: Count rate of the NaI measurement of the chopper background within the background
time window only. In order to account for the non-statistical structure of the count
rate, the uncertainty of the weighted mean is scaled by a factor of 7 to obtain a 68.23%
confidence level. The background count rate of detector 1 with an energy
≤ 30 ADC channels is inferred by subtracting the fraction of the background that is not
produced by the chopper and rescaling the data to the same intensity as the NaI data.

the covariance matrix introduced in section 7.1.

The resulting corrections for different datasets and fit ranges are shown in figure 8.7.
The effect is much more dominant for detector 1 due to its larger sensitivity. Since the
chopper background spectrum is dominated by low amplitudes the correction becomes
much larger when the fit range is stretched to lower energies. The combined correction
for the 197 - 694 keV fit range is compatible with zero.

$$\Delta\lambda = -0.3(0.9) \cdot 10^{-4}, \ \Delta b = 5.3(6.4) \cdot 10^{-4}, \ \rho_{\lambda,b} = -0.58. \tag{8.12}$$

8.4 Dead time correction

After being triggered and recording an event the readout electronics of the detectors is
inactive until the QDCs are able to detect another event. This dead-time is set to be
$1.5\mu s$. Any detector signal creating during this non-extensible dead-time is ignored. Given
the detected rate $\dot{N}$, the real rate $\dot{N}'$ can be calculated from the dead-time τ to be [Leo87]
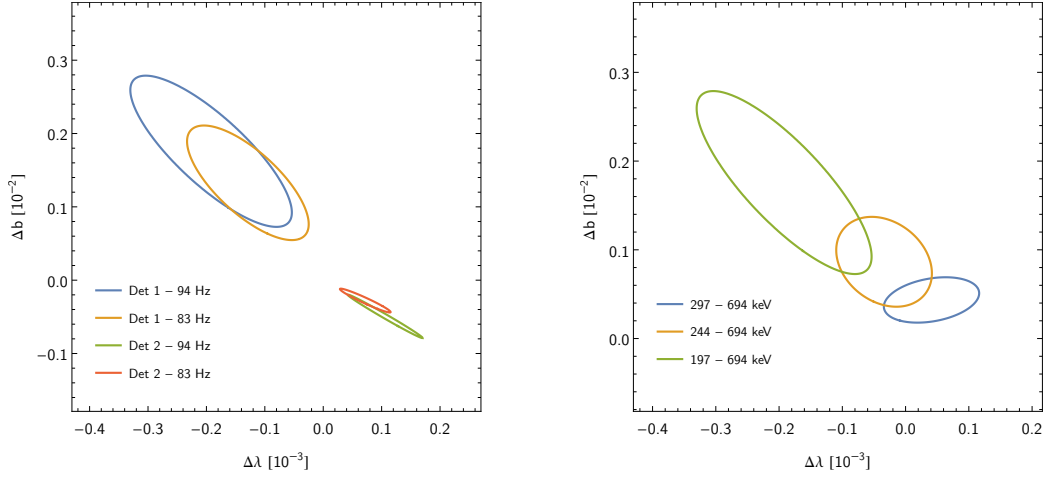
(a) Individual datasets, fit range 197-694 keV. **(b)** Different fit ranges, Det 1 - 94 Hz.

Fig. 8.7: Resulting correction, denoted by the centre of the ellipses, and the corresponding uncertainties for the chopper background.

$$\dot{N}' = \frac{\dot{N}}{1 + \dot{N} \cdot \tau}. \tag{8.13}$$

The required dead-time corrections to the signal and background spectra are applied before subtracting the background by rescaling signal and background spectra. Here the measurement rate is calculated from the number of detected events divided by the number of chopper rotations in the respective dataset times the length of the time window.

In [Mes11] the resulting dead-time correction has been calculated considering a dead time of $\tau = 1.5(1)$ μs to be

$$\frac{\Delta A}{A} = 5(2) \cdot 10^{-4}. \tag{8.14}$$

As mentioned this correction is already applied in the data reduction process. This way no correction to the asymmetry needs to be taken into account while the uncertainty still needs to be considered.

The above correction of the dead-time is derived under the assumption of the detector-events being distributed exponentially in time according to a Poisson process. The expected delta-time distribution is only determined by the mean event rate $\langle r \rangle$

$$N(t) = N_0 e^{-t\sqrt{\langle r \rangle}}, \tag{8.15}$$

where t is the time difference of an event to the previous event and N_0 a normalisation constant.

For very short times between events the count-rate is increased compared to a Poisson like behaviour, though. A corresponding plot is shown in figure 8.8. These events may appear due to afterpulses of the photomultipliers or the slow component of the scintillation process. In a previous analysis these events have been shown to have an energy of less
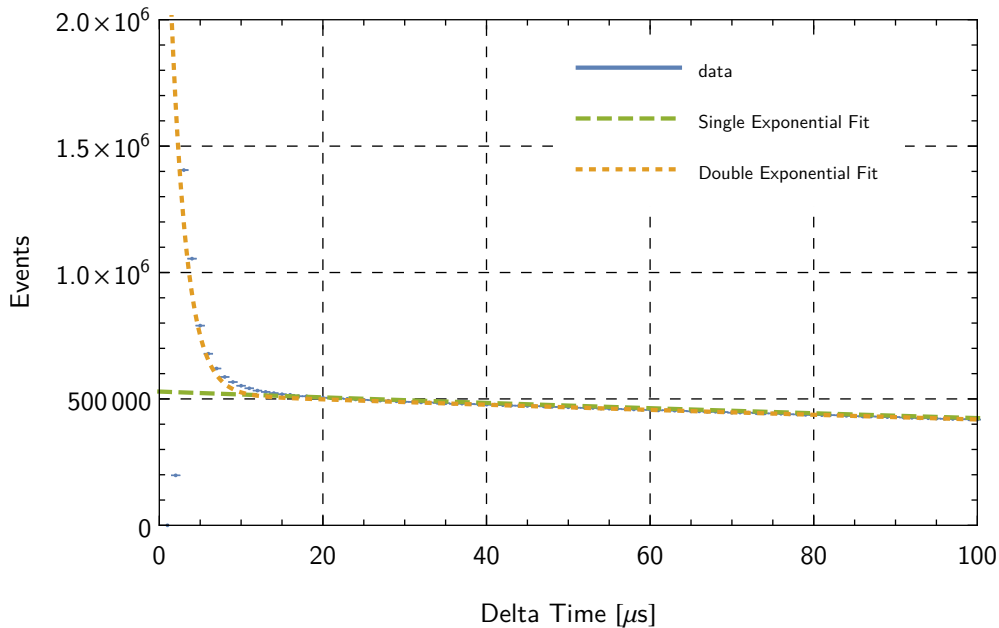
Fig. 8.8: Number of events vs. time between two events. The data shows an increased number of events for short delta-times compared to the expected exponential behaviour. These events are resulting from afterpulses of the photomultipliers and the slow component of scintillation and can be approximated by another exponential component.

than 30 keV [Mes11] and to not spectrally contribute in the energy region used in the analysis. However, these events may influence the behaviour of the detector in terms of dead time. The dead time after detecting afterpulses, provides an additional suppression of electron or background events.

In order to check the influence of afterpulses on the dead time correction a Monte-Carlo event simulation has been performed that distributes events according to an exponential delta-time-distribution and also includes event non-detection due to dead time. In addition a 2% probability for afterpulses with a short decay time of 2.5 μs is assumed. These parameters are estimated by a double exponential fit to the delta-time distribution of events in figure 8.8. The results of this simulation are summarized in table 8.4. Not including afterpulses 10^{11} events have been simulated assuming a rate of 2200 s^{-1} of which a fraction of 0.996656(3) has been simulated to be detected. Hence the real dead time correction required to scale the detected rate to the simulated rate is

$$\Delta_{\text{real}} = 1.003354. \qquad (8.16)$$

The naive dead time correction on the other hand is estimated according to equation 4.12 where the detected rate includes afterpulses. This leads to

$$\Delta_{\text{naive}} = 1.003336. \qquad (8.17)$$

This means that the resulting shift in the dead time correction due to afterpulses is on

Primary Events	10^{11}
Mean Rate	2200 $1/s$
Dead time	$1.5 \cdot 10^{-6}$ s
Afterpulse Probability	0.02 1/Event
Afterpulse Rate	$4 \cdot 10^5$ $1/s$
Detected Primary Events	$0.9966563 \cdot 10^{11}$
Detected Afterpulses	$1.094000 \cdot 10^9$
Detected Total	$1.007596 \cdot 10^{11}$
Naive Dead Time Correction	1.003336
Real Dead time Correction	1.003354
Difference	$1.8 \cdot 10^{-5}$

Tbl. 8.4: Parameters and results of a Monte-Carlo simulation performed to estimate the effect of afterpulses on the dead time correction. In this simulation events are distributed according to an exponential time distribution. The occurrence of afterpulses for each event is modelled with another exponential time distribution with a much shorter decay length. Via this simulation the number of detected "real" events is determined and compared to a conventional dead time correction.

the order of $2 \cdot 10^{-5}$ which is much smaller than the estimated uncertainty in equation 8.14. Even for the case of this shift being different for signal and background spectra the resulting uncertainty for the beta asymmetry would be below 10^{-6} which is considered negligible for this analysis.

8.5 Test of background subtraction

The method presented above explicitly tests for time-variations of the background signal in the same energy region as the one used for the fits to the experimental beta asymmetry. A complementary check can be performed by testing the background subtraction in the energy region above which electron signals from neutron decay are observed. Here the background free electron spectra are expected to be zero. Such a test is performed by a constant fit to the unpolarised decay spectrum $N^\uparrow(E_e) + N^\downarrow$ using ADC channels 400 to 800. This corresponds to energies of about 1.25 to 2.5 MeV. Figure 8.9 shows that the signal and background spectra still contain enough background statistics within this energy region to allow for this kind of analysis.

The results of the fits and the corresponding correction for each datasets are listed in table 8.5. For the 94 Hz dataset small deviations from 0 are observed. The resulting corrections are calculated by using the statistical suppression functions derived in section 8.1. It is important to note that this check has limited significance to test for beam-dependent background contributions since it relies on the assumption that the spectral shape is the same for different types of background. However, this method gives a much more stringent limit on the uncertainty of the dead-time correction as the rescaling of spectra affects all energy regions equally. The resulting correction on the other hand is not considered as it is small and may have the same origin as the time-variation of the background that is
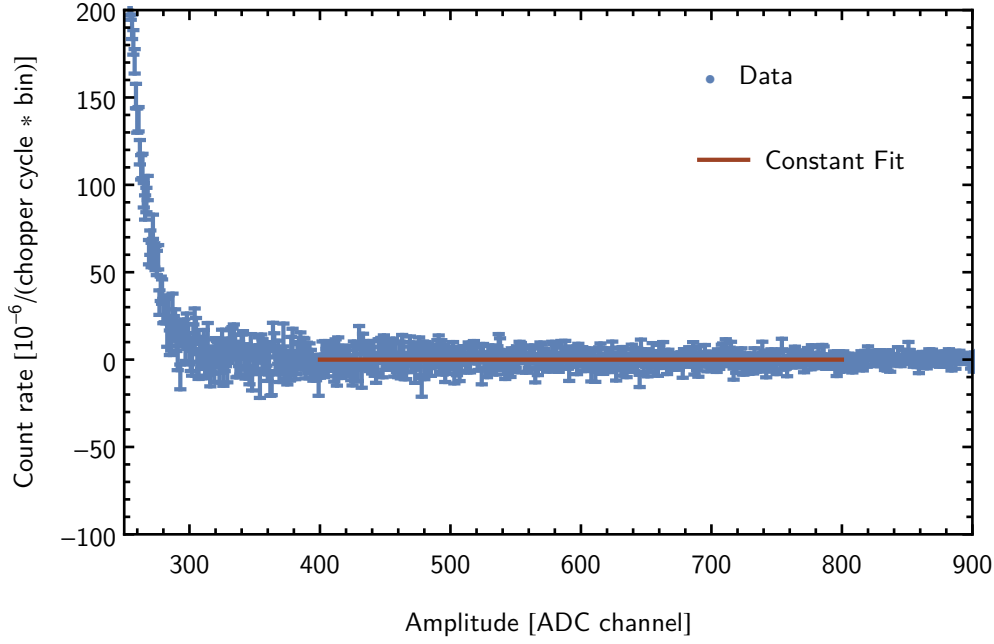
Fig. 8.9: Fit to the electron spectrum $N^\uparrow(E_e) + N^\downarrow$ for detector 1 / 83 Hz above the electron endpoint energy. This fit is used to determine how well the background subtraction works. The results of these fits for all datasets are summarized in table 8.5.

already accounted for.

The total correction obtained for the 197 - 694 keV fit range in the λ-b analysis is

$$\Delta\lambda = 0.1(2.9) \cdot 10^{-5}, \ \Delta b = 0.4(2.1) \cdot 10^{-4}, \ \rho_{\lambda,b} = -0.61. \tag{8.18}$$

When comparing this to the correction for the beta asymmetry, the same behaviour as for the time variation of the background is observed.

8.6 Spin dependence of Background

As already discussed in section 4.3.2 the statistical sensitivity of the measurement is increased if the background can be considered spin-independent. When considering the background being spin-independent in the analysis, remaining spin dependent contributions to the background may provide a contribution to the experimental asymmetry that shift the value of the extracted beta asymmetry A. An expression for such a contribution may be obtained from equation 4.13 by isolating the background terms in the numerator:

$$A_{\mathrm{exp,bg}}(E) = \frac{B^\downarrow - B^\uparrow}{N^\uparrow + N^\downarrow - B^\uparrow - B^\downarrow}. \tag{8.19}$$

Dataset	Constant [cnts/(bin · s)]	Correction $\Delta A/A$
Det1 / 94 Hz	$2.6(1.6) \cdot 10^{-7}$	$1.3(0.8) \cdot 10^{-4}$
Det2 / 94 Hz	$-6.2(1.7) \cdot 10^{-7}$	$-1.8(0.5) \cdot 10^{-4}$
Det1 / 83 Hz	$-0.3(1.9) \cdot 10^{-7}$	$-0.1(0.9) \cdot 10^{-4}$
Det2 / 83 Hz	$0.4(2.0) \cdot 10^{-7}$	$0.1(0.6) \cdot 10^{-4}$
Total		$-0.2(0.3)$

Tbl. 8.5: Results of a constant fit to the electron spectrum $N^{\uparrow}(E_e) + N^{\downarrow}(E_e)$ between ADC channels 400 to 800. These fits are used to test background subtraction in and energy region is beyond the electron endpoint energy where no signal is expected. The calculation of the correction for the beta asymmetry is performed by normalizing the result of the constant fit with the total background intensity and multiplying with the statistical suppression function $\mathrm{SF}(E)$ obtained in section 8.1.

The relative correction for the experimental asymmetry is then given by

$$\delta A_{\mathrm{exp,bgspin}}\left(E\right) = \frac{B^{\downarrow} - B^{\uparrow}}{N^{\uparrow} - N^{\downarrow}}. \tag{8.20}$$

Dataset	Fit Result		Goodness of Fit	
	Constant	Error	χ^2/NDF	Probability
Det 1 / 94 Hz	$-7 \cdot 10^{-4}$	$21 \cdot 10^{-4}$	113.7/109	0.36
Det 2 / 94 Hz	$9 \cdot 10^{-4}$	$18 \cdot 10^{-4}$	94.7/109	0.83
Det 1 / 83 Hz	$10 \cdot 10^{-4}$	$23 \cdot 10^{-4}$	106.7/109	0.54
Det 2 / 83 Hz	$2 \cdot 10^{-4}$	$20 \cdot 10^{-4}$	112.7/109	0.38

Tbl. 8.6: Fit results for the spin-dependent background spectra according to equation 8.20. The fit region ranges from channels 85 to 215 (equivalent to about 300-700 keV).

In order to check if the treatment of the background being "unpolarised" is justified the spectra corresponding to equation 8.20 are generated from the raw data for all four datasets and analysed by constant fits in the same fit region used for the beta asymmetry. The results summarized in table 8.6 show that there is no signature of a spin-dependence of the background in any of the datasets. This analysis is clearly limited by overall background statistics. Since the statistical uncertainty induced by the background and its subtraction is already included within the experimental asymmetry no further uncertainties are considered for its spin-dependence.
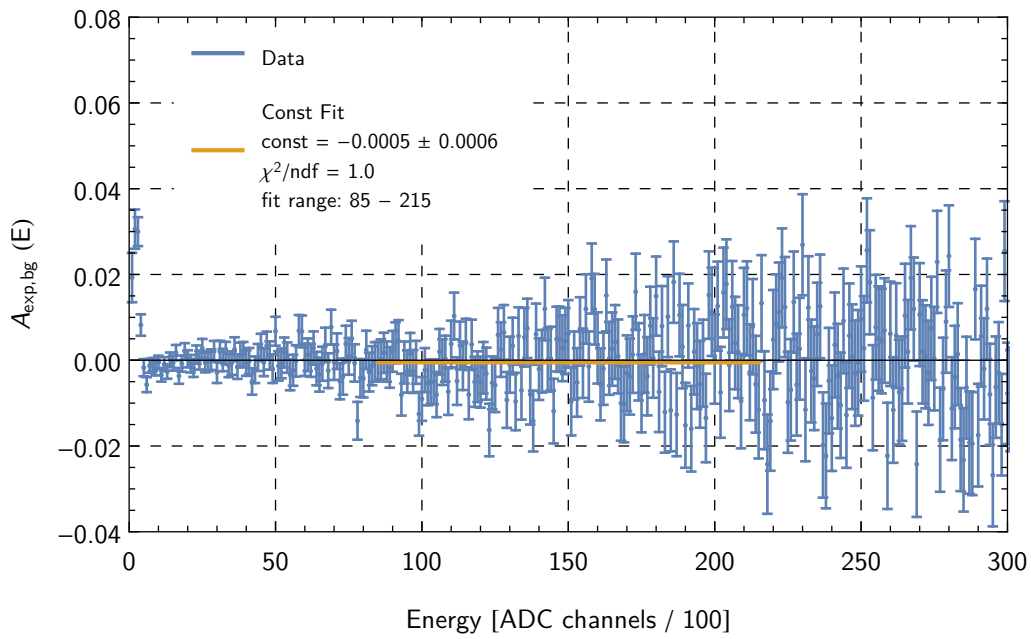
Fig. 8.10: Constant fit to the background asymmetry spectrum of one of four datasets according to equation 8.20. The results are limits by the number of background events and show no spin-dependence of the background.

Chapter 9

Results and Outlook

In this chapter the results of the analysis of the experimental beta asymmetry are summarized and their potential impact on the low energy sector is studied. An additional outlook gives an overview on future efforts on improving these results and relates these to the findings of the present analysis.

9.1 Beta Asymmetry

The corrected results for the beta asymmetry are calculated based on the result obtained in section 6.2.1. The corrections derived in chapters 7 and 8 are applied to the results of the individual chopper sets.

Figure 9.1 illustrates the individual corrections and uncertainties for the combined result. With $\Delta A/A = -0.02 \cdot 10^{-4}$ the correction applied to fit results obtained in chapter 6 due to detector and background systematics is rather small. However, since this is a combination of many individual corrections the combined uncertainty of these corrections is $\delta A/A = 6.4 \cdot 10^{-4}$. The dominant contributions to the uncertainty from background and detector systematics are due to detector drift and non-linearity.

Averaging over all datasets the combined result including these corrections becomes

$$A = -0.11819(6)_{sys}(17)_{stat} = -0.11819(18), \ (68.27\% \ \text{C.L.}). \tag{9.1}$$

The final results of the analysis including all corrections is presented later in section 9.1.3.

9.1.1 Fit Range Analysis

During the analysis several fit ranges have been used in order to check for consistency and potentially optimize the overall uncertainty of the beta asymmetry. A comparison of the fit results obtained for different fit ranges is presented in section 6.2.2. Additionally, the systematic uncertainties have been evaluated for the different fit ranges. The results are summarized in table 9.1 and illustrated in figure 9.2.

The increased statistical sensitivity when stretching the fit range to lower energies is largely compensated by increasing systematics where the dominant contributions arise from the detector non-linearity, spatial response corrections and undetected backscattering.

A check of the hypothesis that the variation between the fit ranges is consistent with statistical fluctuations can be performed by extracting asymmetries for different energy

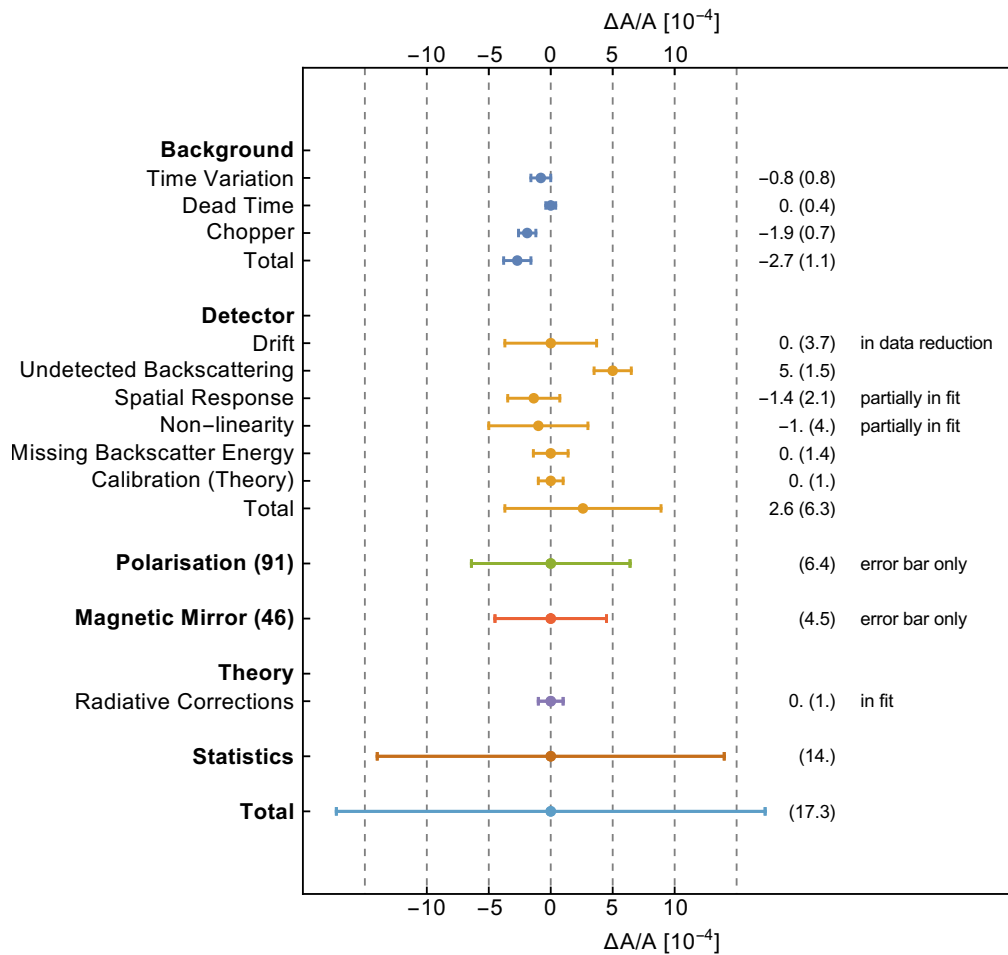**Fig. 9.1:** Error Budget for the analysis of the beta asymmetry using a fit range of 297 - 604 keV. The corrections shown refer to the corrections necessary to correct the fit result obtained in section 6.2. The neutron beam polarisation and magnetic mirror effect corrections result from a seperate analysis and were blinded during the analysis. Both are shown only with the corresponding errorbars.
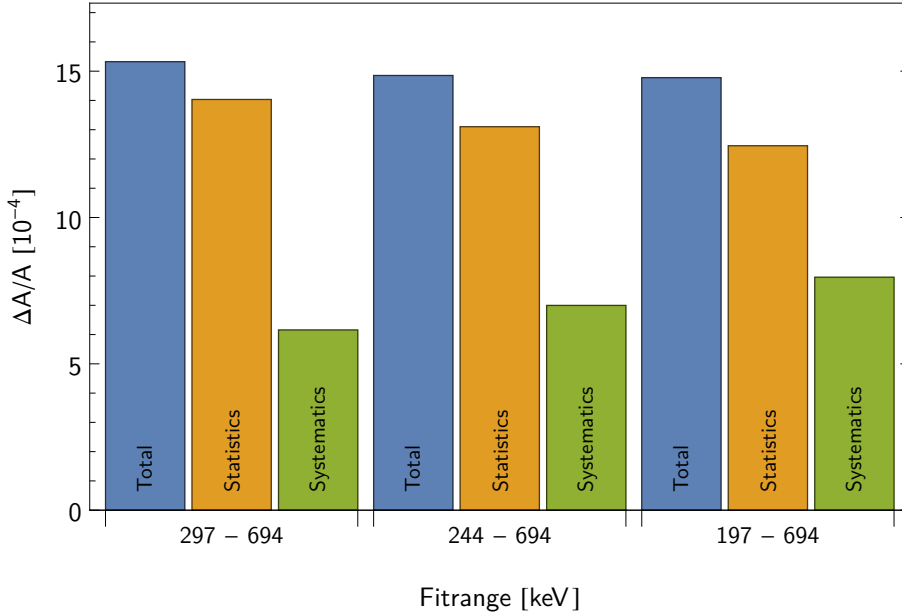
Fig. 9.2: Comparison of the experimental uncertainties when extracting the beta asymmetry using different fit ranges. The systematic uncertainties include effects related to background and electron detection. Not included in this overview are the contributions from polarisation and magnetic mirror effect, which are not energy-dependent.

regions

$$A_{85\text{-}215} = -0.11819(17),$$
$$A_{55\text{-}85} = -0.11794(32),$$

(9.2)

where only the statistical uncertainties are considered since the systematic uncertainties are correlated for these results. The reduced χ^2 for these datasets is 0.51 which corresponds to $P = 47.6\%$ and represents perfect agreement with the hypothesis.

By using larger fitranges, no significant improvement in the precision of the result for the beta asymmetry is achieved. For the final result the 297 - 694 keV fit range is choosen since this provides the smallest systematic uncertainty.

9.1.2 Neutron Beam Polarisation and Magnetic Mirror Effect

Not included in the results above are the correction for the magnetic mirror effect and the neutron beam polarisation. The analysis of these effects is performed in seperate analysis and the corresponding corrections were blinded while the analysis has been carried out.

The neutron beam polarisation P_n and flip efficiency F_n have been measured several times during the beam time directly after the neutron beamline and behind the Perkeo III spectrometer using polarised helium cells as analyser. The measured results are [Sol18]

$$P_n = 0.9910(6), \quad F_n > 0.99964.$$

(9.3)

Fit Range	Result		Statistics	Systematics	
	A	$\delta A/A$	$\delta A/A$	$\Delta A/A$	$\delta A/A$
291-694 keV	-0.11819	$15.4 \cdot 10^{-4}$	$14.0 \cdot 10^{-4}$	$-0.02 \cdot 10^{-4}$	$6.4 \cdot 10^{-4}$
244-694 keV	-0.11816	$14.8 \cdot 10^{-4}$	$13.1 \cdot 10^{-4}$	$1.9 \cdot 10^{-4}$	$7.0 \cdot 10^{-4}$
197-694 keV	-0.11814	$14.6 \cdot 10^{-4}$	$12.5 \cdot 10^{-4}$	$3.8 \cdot 10^{-4}$	$7.6 \cdot 10^{-4}$

Tbl. 9.1: Results of the beta asymmetry analysis when using different fit ranges. The corrections and uncertainties given are those for detector and background systematics. The increased statistical sensitivity is compensated by increased systematic uncertainties.

Using the relation

$$A_{\exp}(E_e) = \frac{(1 + F_n)\, P_n A \beta(E_e)}{4} \tag{9.4}$$

the correction for the final asymmetry becomes

$$\left(\frac{\Delta A}{A}\right)_{\mathrm{pol}} = \frac{2}{(1 + F_n)\, P_n} - 1 = 90.8(6.4) \cdot 10^{-4}. \tag{9.5}$$

The magnetic mirror effect (see section 3.4) is determined from several offline measurements of the magnetic field, neutron pulse shape and neutron velocity [KM18]. The data obtained from these measurements reproduce the neutron time-of-flight profile measured with the electron detectors.

Dataset		MM Correction
Detector	Chopper Freq.	$\Delta A/A [10^{-4}]$
1	94 Hz	23.7
1	83 Hz	41.7
2	94 Hz	61.4
2	83 Hz	57.6
Total		**46.1(4.5)**

Tbl. 9.2: Magnetic mirror effect corrections for the individual datasets and the combined correction [KM18]. The systematic uncertainty for the combined correction accounts for correlations between the uncertainties of the individual corrections.

Due to different chopper frequencies and the diverging behaviour of the neutron beam the resulting corrections for each detector and chopper frequency are different. The individual corrections for each dataset are listed in table 9.2. The uncertainty given for the total correction accounts for the fact that the uncertainty becomes smaller when averaging over both detectors.

Both corrections have been assumed to be zero in the fits performed to obtain the uncorrected value of the beta asymmetry. This changes the value of A and consequently λ. Applying the corrections for both the neutron beam polarisation and magnetic mirror
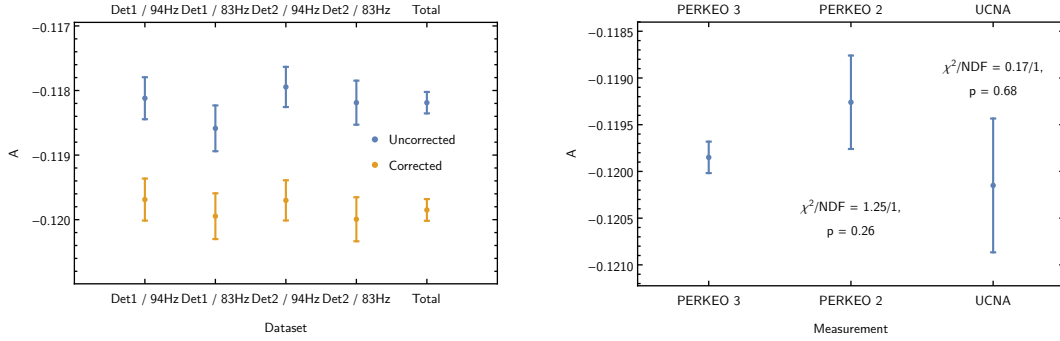
(a) Individual datasets with and without systematic corrections applied. After applying the corrections the individual datasets are consistent with $P = 86\%$.

(b) Comparison of the result obtained with PERKEO III with the combined result of PERKEO II [Mun+13] and UCNA [Bro+18], which are in good agreement.

Fig. 9.3: Comparison of the results of the individual datasets with and without systematic corrections and comparison of the final result with the two most recent measurements of the beta asymmetry.

effect the beta asymmetry becomes

$$A = -0.11981(21), \lambda = -1.27632(56). \tag{9.6}$$

However the change in λ also implies a change in the energy-dependent recoil-order corrections (see section 2.2). These corrections are applied based on the value of λ which corresponds to the value of A during the fit. Considering the corrections for neutron beam polarisation and magnetic mirror effect in the fit function and comparing to the previous result an additional correction is obtained:

$$\frac{\Delta A}{A} = 3.0(2) \cdot 10^{-4}. \tag{9.7}$$

Although this additional correction is two orders of magnitude smaller compared to the correction for the Polarisation and Magnetic Mirror Effect itself, it certainly needs to be considered at the current level of precision.

9.1.3 Final Result

Applying the corrections for the Polarisation and the Magnetic Mirror Effect, including the higher order contributions due to the recoil-order corrections, the final standard model result ($b = 0$) for the beta asymmetry and λ becomes

$$\begin{aligned}
A &= -0.11985(12)_{sys}(17)_{stat} = -0.11985(21) \\
\lambda &= -1.27641(56) \ (68.27\% \text{ C.L.}).
\end{aligned} \tag{9.8}$$

Figure 9.3a shows a comparison of the results for the individual datasets with and without systematic corrections. The total systematic correction to the raw fit result is

1.399%. After applying these corrections the χ^2-probability for consistency between the individual datasets increases from $P = 56\%$ to $P = 86\%$.

Figure 9.3b shows the result together with the two most recent measurements of the beta asymmetry by Perkeo II [Mun+13]:

$$A_{\text{Perkeo II}} = -0.11926(^{+47}_{-53})$$
$$\lambda_{\text{Perkeo II}} = -1.2748(^{+13}_{-14})$$
(9.9)

and UCNA [Bro+18]

$$A_{\text{UCNA}} = -0.12015(72)$$
$$\lambda_{\text{UCNA}} = -1.2772(19).$$
(9.10)

The results are in good agreement as indicated by the χ^2-probabilities. Comparing the result of Perkeo III to the current world average [PDG18]

$$A_{\text{PDG18}} = -0.1184(10)$$
$$\lambda_{\text{PDG18}} = -1.2724(23).$$
(9.11)

one finds a deviation of almost 2σ. Still this leads to $P = 15\%$ due to the larger uncertainty of the world average, as it includes a scaling of the uncertainty by 2.2. Figure 9.4 gives on overview over all measurements of λ entering the world average and the new results. Recent quantum chromodynamics calculations of the axialvector coupling reach a relative precision of 1% [Cha+18].

Using λ and the neutron lifetime, τ, one can calculate V_{ud} (see section 1.2.4 and section 1.2.5) solely from neutron data. Using the current world averages ($\tau_n = 880.2(1.0)$ s) this becomes:

$$|V_{ud}| = 0.97584\,(19)_{\text{RC}}\,(55)_\tau\,(146)_\lambda = 0.97584(158)$$
$$\Rightarrow \Delta = 1 - \left(|V_{ud}|^2 + |V_{us}|^2 + |V_{ub}|^2\right) = -0.30(0.31)\%,$$
(9.12)

confirming unitarity of the CKM-matrix. Considering the Perkeo III result from above the uncertainty on $|V_{ud}|$ is significantly improved

$$|V_{ud}| = 0.97323\,(19)_{\text{RC}}\,(55)_\tau\,(35)_{\lambda(\text{PIII})} = 0.97323(68)$$
$$\Rightarrow \Delta = 0.21(14)\%.$$
(9.13)

The increased precision in λ leads to a significant improvement in the overall precision which is now limited by the precision of the neutron lifetime. This result indicates a 1.5σ deviation from CKM-unitarity. This would likely not be considered significant, especially since the CKM-unitarity is tested to higher precision in superallowed Fermi-decays [HT15]. Conversely this deviation can be interpreted as a slight tension between the result obtained for λ and the neutron lifetime.

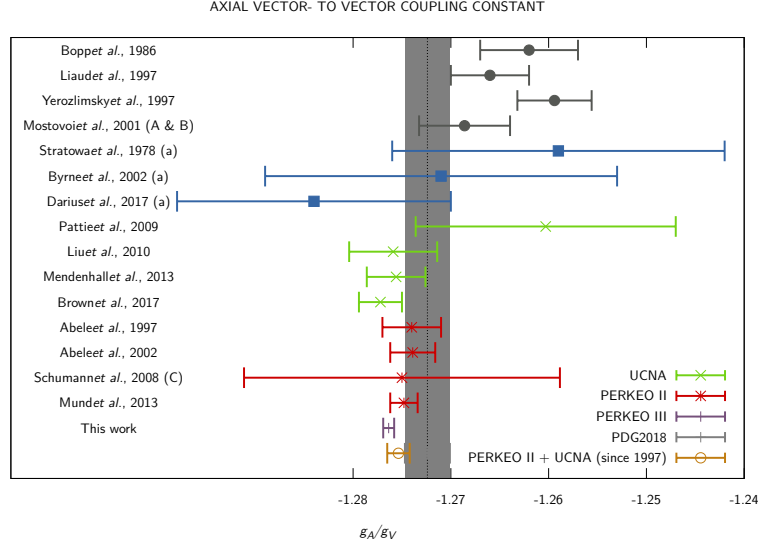Using $\overline{\mathcal{F}t} = 3072.27(72)$ from [HT15] in order to calculate the neutron lifetime from the

AXIAL VECTOR- TO VECTOR COUPLING CONSTANT

Fig. 9.4: Comparison of λ measurements currently included in the world average and the new result presented in this thesis. The letter in braces denotes the correlation coefficient measured to obtain λ if this is not A. All measurements performed since 1997 are in agreement including the new result.

PERKEO III result for λ gives:

$$\tau_{\mathrm{n,PERKEO\ III}} = 878.5(0.7)\ \mathrm{s}. \tag{9.14}$$

This results is consistent with recent measurements of the neutron lifetime performed with magnetic storage of ultracold neutrons which give a shorter neutron lifetime, $\tau_{\mathrm{UCN}\tau} = 877.7(0.7)$ [Pat+18], than the current world average.

9.2 The Fierz Interference Term

In chapters 7 and 8 several studies of systematic effects are summarized. Being analysed with a focus on their energy-dependence, the resulting corrections and uncertainties can be applied to the energy-dependent analysis of λ and b. The combined effects for detector and background systematics can be written in terms of corrections to λ and b, the corresponding correlated uncertainties and correlation:

$$\begin{aligned} \text{Detector:} \quad & \Delta\lambda = 13.5(7.1) \cdot 10^{-4}, \ \Delta b = -8.3(4.6) \cdot 10^{-3}, \ \rho_{\lambda,b} = -0.82, \\ \text{Background:} \quad & \Delta\lambda = -0.2(1.1) \cdot 10^{-4}, \ \Delta b = 0.6(0.8) \cdot 10^{-3}, \ \rho_{\lambda,b} = -0.71. \end{aligned} \tag{9.15}$$

Figure 9.5 shows the respective individual contributions. Note that the spatial response correction is the correction relative to the fit results in section 6.3. These already include a first order correction. The effect of the spatial response for an uncorrected fit is of similar order as the correction for undetected backscattering.

(a) Detector Systematics

(b) Background Systematics

Fig. 9.5: Systematic effects related to background and the electron detector for the combined λ-b analysis. The corrections are represented by the centre of the ellipses, which denote the corresponding 68.27% C.L. uncertainty.

(a) Systematic effects
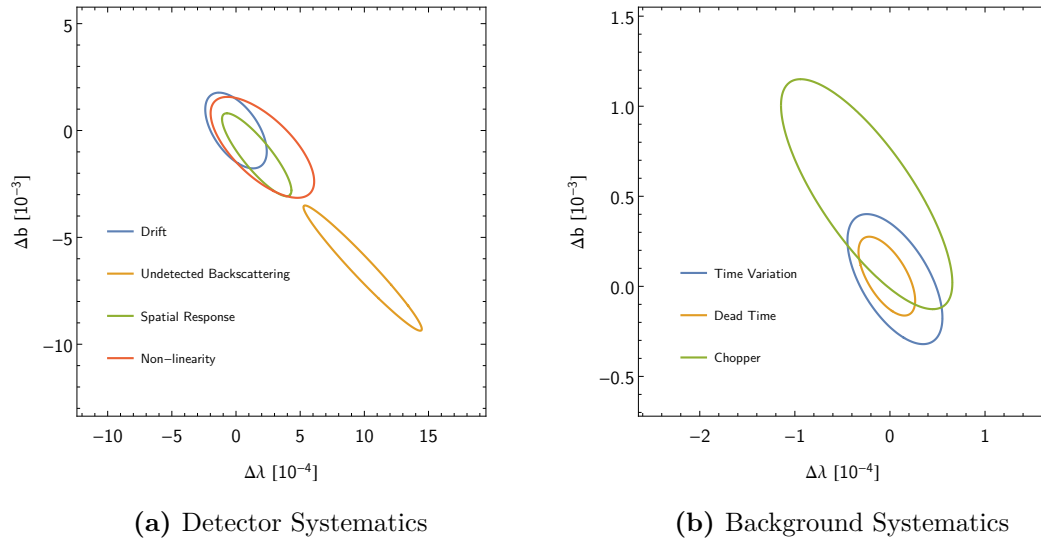
(b) Systematics and statistics

Fig. 9.6: Systematic effects related to background and the electron detector for the combined λ-b analysis. The corrections are represented by the centre of the ellipses, which denote the corresponding 68.27% C.L. uncertainty.
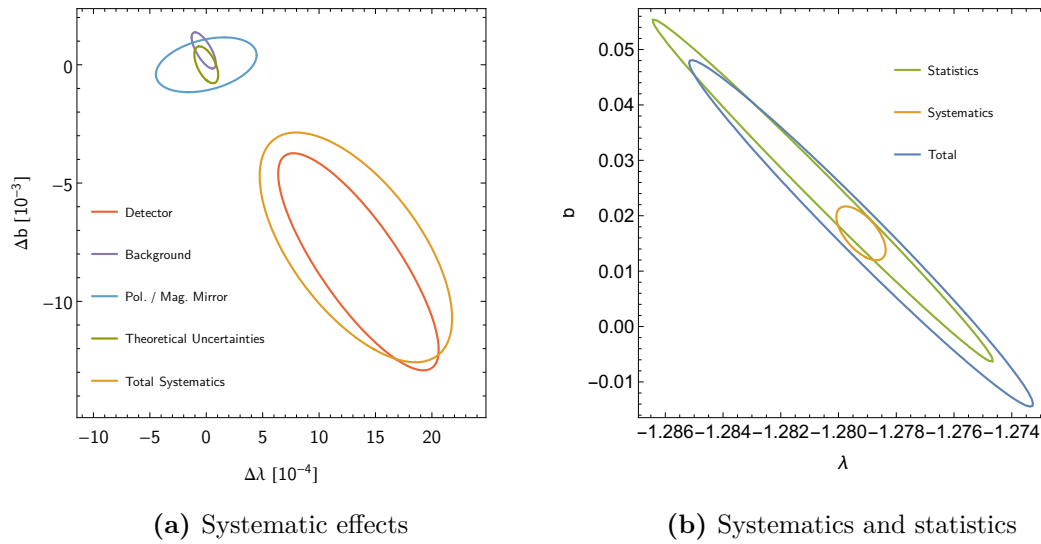
The estimates for the correction for Polarisation and the Magnetic Mirror Effect mentioned in section 9.1.2 are already included in the fits described in section 6.3. To first order, these effects only provide a scaling of the experimental beta asymmetry and thus λ. However, due to recoil-order corrections and their energy-dependence also an uncertainty in b is induced. Figure 9.6a compares all systematic contributions. The full result including statistics is illustrated in figure 9.6b. The measurement uncertainty is clearly dominated by statistics and the combined two-parameter result for the fit range of 197 - 694 keV is:

$$\lambda = -1.2792(60), \ b = 0.017(0.031), \ \rho_{\lambda,b} = -0.985 \ \ (68.27\% \ \text{C.L.}). \tag{9.16}$$

This result is in agreement with the Standard Model assumption $b = 0$.

The parameter limits obtained may be reinterpreted as a single result for b by integration over λ,

$$b = 0.017(21) \ \ (68.27\% \ \text{C.L.}), \tag{9.17}$$

which is the most precise limit on b obtained from a single measurement in neutron decay.

9.2.1 Fit Range Analysis

The fit range used for the result above is optimized to give the lowest overall uncertainty. A comparison of the statistical uncertainty for different fit ranges is presented in section 6.3.2. It shows that the statistical sensitivity is much higher when including lower energies in the combined fit. In the beta asymmetry analysis this benefit is much lower due to the fact that the signal-to-noise ratio is worse for lower energies. In the two-parameter analysis, however, the signature of b becomes much more dominant for lower energies which reduces the correlation between the parameters. When dealing with systematic effects a similar behaviour is observed. The systematic uncertainties increase in the beta asymmetry analysis when including lower energies usually due to the fact that the systematic corrections here get larger. For the combined analysis this also holds for the uncorrelated uncertainties of λ and b. The correlated uncertainties however decrease even slightly, which again is the result of reduced correlation between the parameters. This is illustrated in figure 9.7 which also shows the reduced overall uncertainty for the 197 - 694 keV fit range.

The precision of this result could likely be improved by stretching the fit range to even lower energies. However, this would require a detailed study of additional systematics which are not included in the present analysis. Examples for such effects are the trigger function of the detector system, which is known but difficult to implement in production fits due to the complexity of the calculation [Roi18], and afterpulses of the detector system which don't contribute at the present level.
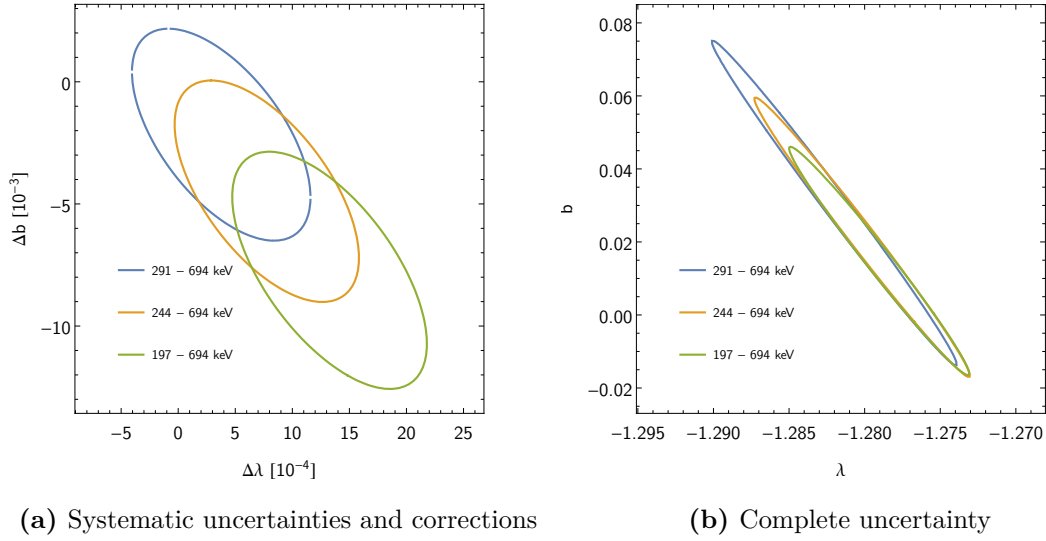
(a) Systematic uncertainties and corrections

(b) Complete uncertainty

Fig. 9.7: Comparison of the results obtained for different fit ranges. The correlated systematic uncertainties slightly decrease when including energies down to 200 keV due a reduced correlation between the parameters. The total uncertainty which is dominated by statistics also decreases.

9.2.2 Comparison with the Beta Asymmetry

The two-parameter result for λ and b given above can be projected to a λ result with the assumption $b = 0$ which yields:

$$\lambda = -1.27607(68). \tag{9.18}$$

This is in good agreement with the result obtained from the beta asymmetry analysis. Slight deviations are expected since a different fit range and less data is used in this analysis. This also increases the statistical uncertainty.

9.2.3 Limits on scalar- and tensor-interactions

Using the limit on the Fierz interference term, allows to place direct constraints on the allowed parameter space for scalar- and tensor coupling constants. Figure 9.8 shows the resulting error band. Combining this measurement with the measurement of the neutrino asymmetry B performed with PERKEO II [Sch+07] allows to place limits on C_S and C_T from neutrons only. The limit obtained for C_S is on the 10^{-2} level whereas previous neutron limits on C_S without considering the energy dependence of the experimental beta asymmetry restrict C_S on the 10^{-1} level [Kon+12b].

Better limits are obtained when also including the world average of the neutron lifetime [PDG16] and superallowed Fermi decays [HT15], which are used to constrain $\overline{\mathcal{F}t}$ in the neutron lifetime and to limit C_S. The single parameter limits obtained for this combination
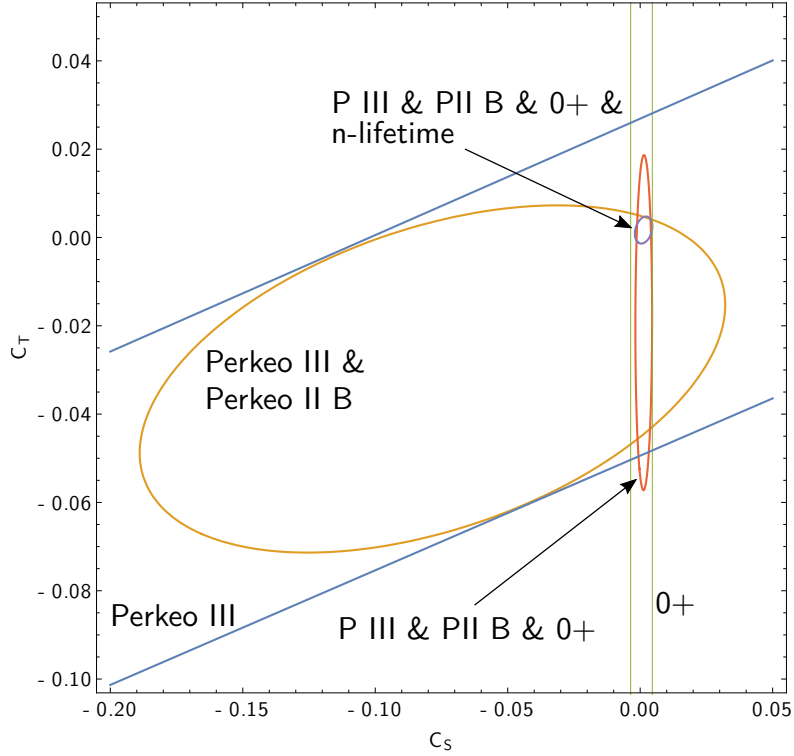
Fig. 9.8: 95% confidence regions obtained when combining the result of the λ-b analysis with other measurements. A combination with the measurement of the B correlation coefficient yields limits from neutrons only. The best limit is obtained by a combination with superallowed nuclear decays (0^+) and the neutron lifetime.

are

$$
\begin{aligned}
C_S &= 1.3(1.4) \cdot 10^{-3} \quad (68\% \text{ C.L.}) \\
C_T &= 1.7(1.3) \cdot 10^{-3} \quad (68\% \text{ C.L.}).
\end{aligned}
\tag{9.19}
$$

where the limit on C_S is dominated by superallowed Fermi decays and C_T is dominated by neutron data. Note that similar limits could be achieved by using the result of A as obtained from the beta asymmetry analysis, as the combination with the neutron lifetime allows to disentangle λ and b (see e.g. [PHY13]). Besides placing a direct limit on b, using the two-parameter analysis also allows to check for consistency of the results and provides much higher sensitivity on b without sacrificing on λ when using neutron decay data only. The detailed study of systematic uncertainties including parameter correlations will become more important for future measurements where the statistics will be increased and likely not be the limiting factor.

9.3 Outlook

The measurement of the beta asymmetry will remain one of the most important topics in neutron decay measurements. It provides the most precise determination of λ which is an essential ingredient when describing semileptonic charged current interactions. As shown in the previous section, the energy-dependent analysis of λ and b allows to set limits on scalar and tensor-couplings from neutron decay data alone. This is useful especially since current measurements of the Fierz interference term from the unpolarised neutron decay spectrum are systematically limited. In combination with the neutron lifetime and super allowed decays the measurement of the beta asymmetry allows to place competitive bounds on scalar and tensor interactions.

Future measurements of the Electron-Neutrino Correlation Coefficient a may provide a similar precision in λ. Such measurements are planned by the Nab spectrometer which also aims to measure the Fierz interference term with a precision of $|b| < 3 \cdot 10^{-3}$ [Bae+13].

9.3.1 PERC

The new neutron decay facility PERC will allow to measure several correlation coefficients with increased precision, including the beta asymmetry A [Kon+12a; Dub+08]. PERC will be set up at the new beam facility MEPHISTO at the FRMII, Garching, which will provide a similar neutron flux as the PF1B beamline at the ILL and is expected to start operation by the end of 2020.
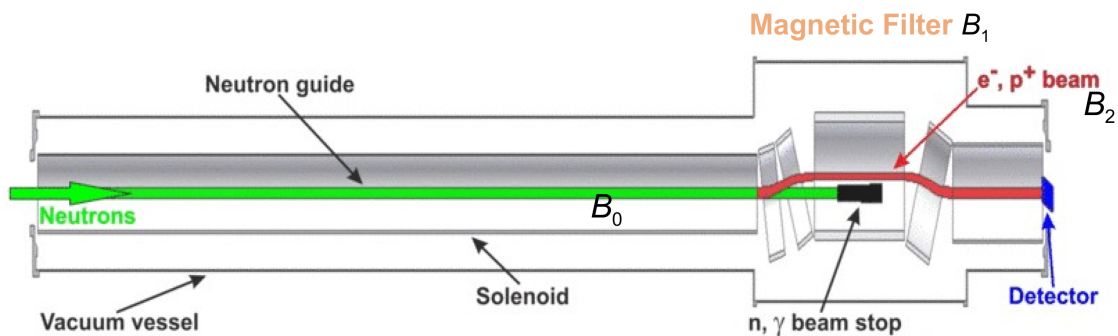
Fig. 9.9: Schematic of the PERC intrument.

Figure 9.9 shows a schematic view of PERC. The main component of PERC is a 12m superconducting magnet which contains the 7m long decay volume. Here the neutrons decay inside a non-depolarizing neutron guide, which allows to transport the diverging neutron beam through the setup with only little losses. This strongly increases the number of neutrons transported through the decay volume and thus the number of decay events expected.

The charged decay products are guided along the magnetic field passing a high field magnetic filter region that allows to limit the emission angle of decay products that are transported to the end of PERC. The charged decay products are then delivered to the exit of PERC, where different detector systems (secondary spectrometers) can be set up dedicated to the measurement of a single or several observables.

Fig. 9.10: PERC setup at the MEPHISTO beam facility in the Neutron Guide Hall East of the research reactor FRM-II.

While the detector characteristics depend on the secondardy spectrometer, the design of PERC allows to limit important systematics related to the magnetic field,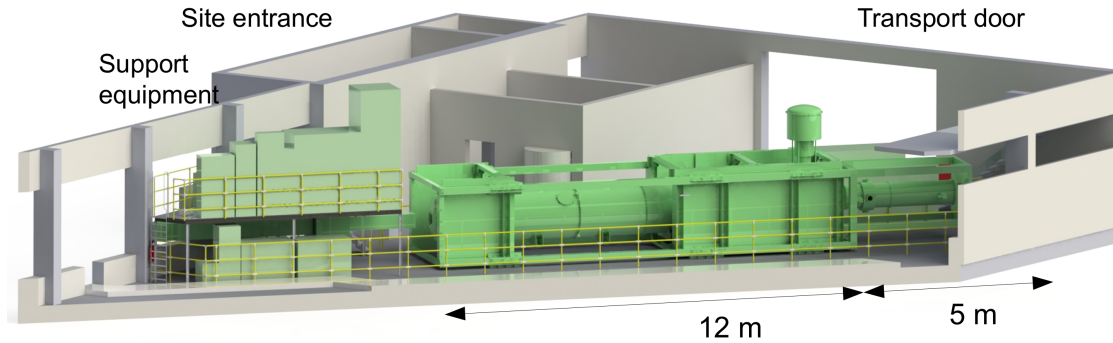 background and the neutron beam polarisation on the lower 10^{-4} level [Kon+12a]. Paired with the increase in statistics this will allow to improve the precision of several correlation coefficients on the 10^{-4} level.

Among the planned measurements are the beta asymmetry A, the proton asymmetry C and a direct measurement of the Fierz interference term b. For the latter a new spectrometer, *NoMoS*, is currently developed at the Stefan-Meyer Institut, Wien. This spectrometer uses the drift of charged particles inside a curved magnetic field and a spatial resolution detector to measure the momentum of the particles [WKA13]. The aim is to provide a direct limit on the Fierz interference term with a precision of $|b| < 10^{-3}$.

The measurement of the proton asymmetry C has a similar impact as the measurement of the neutrino asymmetry B, with slightly reduced sensitivity on C_S and C_T, though. The advantage of the proton asymmetry, however, is the fact that it can be extracted without requiring the coincident detection of electrons and protons and thus will allow to fully utilise the increased statistics of PERC.

A recent measurement of C performed with PERKEO III is currently being analysed and will provide a relative precision of $\delta C/C \simeq 0.01$ [Roi18; Raf16]. In this experiment proton detection is achieved by accelerating protons by a high voltage system to a thin conversion foil made of carbon where electrons are released and measured with a scintillator based electron detector. During the measurement a high contribution of background related to this proton conversion setup was found. An improved setup for PERC will allow a measurement with a precision in the lower 10^{-3} region [Roi18].

The first measurement performed with PERC will likely be the measurement of the beta asymmetry using a detector setup similar to that used for the beta asymmetry measurement. Based on the studies performed in this thesis several improvements related to the detector setup and monitoring can be made. In the following some of these aspects are addressed.

Detector non-linearity and calibration

In order to improve systematic limitations due to the detector non-linearity dedicated characterisation of the used electronics will be performed in advance (compare section 7.2). An update of the anaolgue electronics or the use of sampling ADCs are currently investigated and should allow to severely reduce the non-linearity contributions of the electronics.

The monitoring of the detector calibration performed with electron conversion sources already provides sufficient precision to be applied for an improved measurement with PERC for energy regions of about 200 - 700 keV. Another method using the time-of-flight of electrons inside PERC can provide complementary information as it is sensitive especially at lower electron energies. A prototype system has recently been tested showing promising result [Roi+18].

Temperature drift of the detector

In both analysis performed within this thesis the detector drift provides one of the major detector systematics. In the PERKEO III setup the drift is the result of the varying coil temperature of the normal conducting magnet system which is not temperature stabilised. The superconducting magnet system of PERC on the other hand is temperature stabilized which will result in a largely reduced detector drift. Additionally, temperature stabilisation of the photomultipliers is planned. Such a stabilisation is already included in an updated detector design used for the measurement of the proton asymmetry [Raf16]. Dedicated drift measurements to monitor the overall detector amplitude, can be complemented with LED pulser monitoring of individual photomultipliers to monitor the stability of individual photomultipliers and thus the spatial detector response. A first study of the feasibility for electron beta spectroscopy has been performed in [Sac16]. A stable LED pulser which allows the simultaneous distribution of pulses from the same LED to different PMTs is currently under development [Ber18].

Spatial response of the detector

Although currently not providing a major systematic uncertainty the uniformity of the detector becomes more important when decreasing the lower bound of the fit range.

The light transport simulations performed within this thesis (see section 5.2.2) can be easily adopted to other detector configurations. The uniformity of the detector is given by the light transport profile and the individual gain factors of individual photomultipliers. Utilising the results of these simulations combined with mapping of the spatial detector response will allow to extract these gain factors and either adjust the high voltage or the simulation accordingly to have a reliable description of the detector uniformity.

These improvements should allow to reduce the contribution of the detector systematics for the beta asymmetry by a factor of two to $\delta A/A = < 3 \cdot 10^{-4}$. Replacing the Mesh-Photomultipliers with a readout based on Silicon-Photomultipliers might give additional advantage if the capability of detecting single photoelectrons can be utilized. This would eliminate the drift of the photomultipliers and any non-linearity from the electronics completely.

Combined with the increase in statistics provided by PERC a reasonable goal for such a measurement is

$$\Delta A/A = 5 \cdot 10^{-4}. \tag{9.20}$$

The analysis of the Fierz interference term b is currently limited by statistics and can be improved with PERC immediately. The contribution of detector systematics currently is $\delta b \simeq 5 \cdot 10^{-3}$ (68.27% two-parameter uncertainty). Assuming the same improvement for the detector systematics and statistics, the limits on the Fierz interference term can be improved to

$$\delta b = 7 \cdot 10^{-3} \tag{9.21}$$

for an extraction from the beta asymmetry.

Summary

Neutron decay studies play an important role for studying the nature of the weak interaction. They allow the precise determination of the ratio of axialvector and vector couplings $\lambda = g_A/g_V$, as well as the measurement of the first element of the CKM-matrix V_{ud}. The measurement of the beta asymmetry provides the currently most precise method to determine λ. The spectral shape of the experimental beta asymmetry, however, contains further information about hypothetical scalar and tensor couplings, via the Fierz interference term b, which are not predicted by the standard model.

Within this thesis the data analysis as well as the analysis of detector and background systematics of the experimental beta asymmetry measured with PERKEO III at the Institut Laue-Langevin are 2009 is presented. The analysis of the neutron beam polarisation and the magnetic mirror effect have been performed seperately in order to achieve a blinded analysis.

Using a pulsed beam allows to measure the background and neutron decay electrons simultaneously. This allows to reduce the systematic corrections and uncertainties related to the ambient background significantly. Background contributions induced by the neutron beam itself are quantified and on the same order.

The electron detectors have been calibrated and monitored using electron conversion sources placed inside the spectrometer. The small meshed monitoring of the temperature drift allows to correct for this drift directly in the data reduction. A more fundamental understanding and modelling of the detector response allows to describe the measured calibration spectra and finally applying the extracted calibration to the beta asymmetry. This is the first PERKEO measurement which uses a detector calibration performed with electron conversion sources, solely. This is important in particular when searching for physics beyond the standard model, as the calibration using neutron decay spectra is not independent of the assumptions of the standard model.

A major fraction of the necessary enhancement in the detector modelling is achieved through improving the description of the detector non-linearity. The potential origins are identified by analysing the calibration spectra as well as offline measurements. However, a small model uncertainty remains. The calculation of the detector non-linearity also takes the multi-electron structure of the calibration spectral into account which is important when applying the calibration to the beta asymmetry. Further, the gain process of photomultipliers is modelled. Although the spectral effect is negligible for the experimental beta asymmetry, it improves the description of the calibration measurements. A detailed investigation of systematic effects related to undetected backscattering of electrons and the spatial uniformity of the detector are investigated [Roi18]. These effects are included as systemtic corrections.

All systematic uncertainties considered in the final error budget of the measuremnt are well balanced and on the order of 10^{-4}. The result of the measurement is the most precise

measurement of the beta asymmetry and λ:

$$A = -0.11985(12)_{sys}(17)_{stat} = -0.11985(21)$$
$$\lambda = -1.27641(56) \ (68.27\% \ \text{C.L.}). \tag{9.22}$$

All systematic effects and theoretical corrections to the experimental beta asymmetry are analysed in an energy-dependent fashion. This allows to perform a correlated λ-b analysis of the experimental beta asymmetry including the full correlation of statistics and systematics. The resulting single parameter limit on b is

$$b = 0.017(21) \ \ (68.27\% \ \text{C.L.}), \tag{9.23}$$

which is the most precise measurement of the Fierz interference term in neutron decay and compatible with the standard model assumption $b = 0$.

Bibliography

[Abe+02]   H. Abele, M. Astruc Hoffmann, S. Baeßler, D. Dubbers, F. Glück, U. Müller, V. Nesvizhevsky, J. Reich, and O. Zimmer. "Is the Unitarity of the Quark-Mixing CKM Matrix Violated in Neutron β-Decay?" In: *Phys. Rev. Lett.* 88 (21 May 2002), p. 211801. DOI: 10.1103/PhysRevLett.88.211801.

[Abe+97]   H. Abele, S. Baeßler, D. Dubbers, et al. "A measurement of the beta asymmetry A in the decay of free neutrons". In: *Physics Letters B* 407.3 (1997), pp. 212–218. ISSN: 0370-2693. DOI: 10.1016/S0370-2693(97)00739-9.

[Abe+06]   H. Abele, D. Dubbers, H. Häse, et al. "Characterization of a ballistic supermirror neutron guide". In: *Nuclear Instruments and Methods in Physics Research Section A: Accelerators, Spectrometers, Detectors and Associated Equipment* 562.1 (2006), pp. 407–417. ISSN: 0168-9002. DOI: http://dx.doi.org/10.1016/j.nima.2006.03.020.

[Abe+11]   C. Aberle, C. Buck, F. X. Hartmann, S. Schönert, and S. Wagner. "Light output of Double Chooz scintillators for low energy electrons". In: *Journal of Instrumentation* 6.11 (2011), P11006. DOI: 10.1088/1748-0221.

[Ago+03]   S. Agostinelli et al. "GEANT4: A Simulation toolkit". In: *Nucl. Instrum. Meth.* A506 (2003), pp. 250–303. DOI: 10.1016/S0168-9002(03)01368-8.

[Ant+13]   A. Antognini, F. Nez, K. Schuhmann, et al. "Proton Structure from the Measurement of 2S-2P Transition Frequencies of Muonic Hydrogen". In: *Science* 339.6118 (2013), pp. 417–420. ISSN: 0036-8075. DOI: 10.1126/science.1230016.

[Bae+13]   S. Baeßler, R. Alarcon, L. P. Alonzi, et al. "Neutron beta decay studies with Nab". In: *AIP Conference Proceedings* 1560.1 (2013), pp. 114–116. DOI: 10.1063/1.4826731.

[Baz+93]   A. Bazhenov, V. Lobashev, A. Pirozhkov, and V. Slusar. "An adiabatic resonance spin-flipper for thermal and cold neutrons". In: *Nuclear Instruments and Methods in Physics Research Section A: Accelerators, Spectrometers, Detectors and Associated Equipment* 332.3 (1993), pp. 534–536. ISSN: 0168-9002. DOI: 10.1016/0168-9002(93)90311-5.

[Ber+05]   M. Berger, J. Coursey, M. Zucker, and J. Chang. "ESTAR, PSTAR, and ASTAR: Computer Programs for Calculating Stopping-Power and Range Tables for Electrons, Protons, and Helium Ions (version 1.2.3)". In: Originally published as: Berger, M.J., NISTIR 4999, National Institute of Standards and Technology, Gaithersburg, MD (1993). National Institute of Standards and Technology, Gaithersburg, MD., 2005. DOI: 10.18434/T4NC7P.

[Ber18]   K. Bernert. MA thesis. Technische Universität München, Oct. 2018.

[Bha+12]   T. Bhattacharya, V. Cirigliano, S. D. Cohen, A. Filipuzzi, M. González-
           Alonso, M. L. Graesser, R. Gupta, and H.-W. Lin. "Probing novel scalar and
           tensor interactions from (ultra)cold neutrons to the LHC". In: *Phys. Rev. D*
           85 (5 Mar. 2012), p. 054512. DOI: 10.1103/PhysRevD.85.054512.

[Bic]   Bicron. *BC-400 / BC-404 / BC-408 / BC-412 / BC-416 Premium Plastic
           Scintillators, General Description.*

[Bir51]   J. B. Birks. "Scintillations from Organic Crystals: Specific Fluorescence and
           Relative Response to Different Radiations". In: *Proceedings of the Physical
           Society. Section A* 64.10 (1951), p. 874. DOI: 10.1088/0370-1298.

[Bir52]   J. B. Birks. "Theory of the Response of Organic Scintillation Crystals to
           Short-Range Particles". In: *Phys. Rev.* 86 (4 May 1952), pp. 569–569. DOI:
           10.1103/PhysRev.86.569.

[Bro+18]   M. A.-P. Brown, E. B. Dees, E. Adamek, et al. "New result for the neutron
           β-asymmetry parameter A_0 from UCNA". In: *Phys. Rev. C* 97 (3 Mar.
           2018), p. 035505. DOI: 10.1103/PhysRevC.97.035505.

[Cab63]   N. Cabibbo. "Unitary Symmetry and Leptonic Decays". In: *Phys. Rev. Lett.*
           10 (12 June 1963), pp. 531–533. DOI: 10.1103/PhysRevLett.10.531.

[Cha+18]   C. C. Chang, E. Rinaldi, A. N. Nicholson, et al. "A percent-level determination
           of the nucleon axial coupling from Quantum Chromodynamics". In: *Nature*
           558 (May 2018). DOI: 10.1038/s41586-018-0161-8.

[Chu+12]   T. E. Chupp et al. "Search for a T-odd, P-even Triple Correlation in Neu-
           tron Decay". In: *Phys. Rev.* C86.3 (Sept. 2012), p. 035505. DOI: 10.1103/
           physrevc.86.035505. arXiv: 1205.6588 [nucl-ex].

[CGH13]   V. Cirigliano, S. Gardner, and B. Holstein. "Beta Decays and Non-Standard
           Interactions in the LHC Era". In: *Prog. Part. Nucl. Phys.* 71 (2013), pp. 93–
           118. DOI: 10.1016/j.ppnp.2013.03.005. arXiv: 1303.6953 [hep-ph].

[CGG13]   V. Cirigliano, M. González-Alonso, and M. L. Graesser. "Non-standard
           charged current interactions: beta decays versus the LHC". In: *Journal of
           High Energy Physics* 2013.2 (2013), pp. 1–18. ISSN: 1029-8479. DOI: 10.1007/
           JHEP02(2013)046.

[CB83]   E. D. Commins and P. H. Bucksbaum. *Weak interactions of leptons and
           quarks.* Cambridge University Press, 1983.

[Dar+17]   G. Darius, W. A. Byron, C. R. DeAngelis, et al. "Measurement of the Electron-
           Antineutrino Angular Correlation in Neutron β Decay". In: *Phys. Rev. Lett.*
           119 (4 July 2017), p. 042502. DOI: 10.1103/PhysRevLett.119.042502.

[Dub+08]   D. Dubbers, H. Abele, S. Baeßler, B. Märkisch, M. Schumann, T. Soldner,
           and O. Zimmer. "A clean, bright, and versatile source of neutron decay
           products". In: *Nuclear Instruments and Methods in Physics Research Section
           A: Accelerators, Spectrometers, Detectors and Associated Equipment* 596.2
           (2008), pp. 238–247. ISSN: 0168-9002. DOI: 10.1016/j.nima.2008.07.157.

[Dub15]   D. Dubbers. "Magnetic guidance of charged particles". In: *Physics Letters B* 748.Supplement C (2015), pp. 306–310. ISSN: 0370-2693. DOI: `10.1016/j.physletb.2015.07.004`.

[Fel51]   W. Feller. "Diffusion Processes in Genetics". In: *Proceedings of the Second Berkeley Symposium on Mathematical Statistics and Probability.* Berkeley, California: University of California Press, 1951, pp. 227–246.

[FG58]   R. P. Feynman and M. Gell-Mann. "Theory of the Fermi Interaction". In: *Phys. Rev.* 109 (1 Jan. 1958), pp. 193–198. DOI: `10.1103/PhysRev.109.193`.

[Fri08]   F. Friedl. "Einfluss der Detektorfunktion auf die Messung des schwachen Magnetismus im Neutronenzerfall". Diploma Thesis. Ruprecht-Karls-Universität, Heidelberg, 2008. `http://www.physi.uni-heidelberg.de//Publications/dipl_friedl.pdf`.

[GJL95]   F. Glück, I. Joó, and J. Last. "Measurable parameters of neutron decay". In: *Nuclear Physics A* 593.2 (1995), pp. 125–150. ISSN: 0375-9474. DOI: `10.1016/0375-9474(95)00354-4`.

[GT92]   F. Glück and K. Toth. "Oder-α radiative corrections for semileptonic decays of polarized baryons". In: *Physical Review D* 46.5 (1992), pp. 2090–2101. DOI: `10.1103/PhysRevD.46.2090`.

[GGS58]   M. Goldhaber, L. Grodzins, and A. W. Sunyar. "Helicity of Neutrinos". In: *Phys. Rev.* 109 (3 Feb. 1958), pp. 1015–1017. DOI: `10.1103/PhysRev.109.1015`.

[GNS18]   M. González-Alonso, O. Naviliat-Cuncic, and N. Severijns. "New physics searches in nuclear and neutron β decay". In: (2018). arXiv: `1803.08732` `[hep-ph]`.

[Ham96]   Hamamtsu Photonics. *Photomultiplier Tube R5924, Datasheet.* 1996.

[HT15]   J. C. Hardy and I. S. Towner. "Superallowed $0^+ \to 0^+$ nuclear β decays: 2014 critical survey, with precise results for V_{ud} and CKM unitarity". In: *Phys. Rev. C* 91 (2 Feb. 2015), p. 025501. DOI: `10.1103/PhysRevC.91.025501`.

[Har89]   T. E. Harris. *The theory of branching processes.* Dover, 1989.

[Häs+02]   H. Häse, A. Knöpfler, K. Fiederer, U. Schmidt, D. Dubbers, and W. Kaiser. "A long ballistic supermirror guide for cold neutrons at ILL". In: *Nuclear Instruments and Methods in Physics Research Section A: Accelerators, Spectrometers, Detectors and Associated Equipment* 485.3 (2002), pp. 453–457. ISSN: 0168-9002. DOI: `10.1016/S0168-9002(01)02105-2`.

[Hic+17]   K. P. Hickerson, X. Sun, Y. Bagdasarova, et al. "First direct constraints on Fierz interference in free-neutron β decay". In: *Phys. Rev. C* 96 (4 Oct. 2017), p. 042501. DOI: `10.1103/PhysRevC.96.042501`.

[Hol74]   B. R. Holstein. "Recoil effects in allowed beta decay: The elementary particle approach". In: *Rev. Mod. Phys.* 46 (4 Oct. 1974), pp. 789–814. DOI: `10.1103/RevModPhys.46.789`.

[IPT13]   A. N. Ivanov, M. Pitschmann, and N. I. Troitskaya. "Neutron β^- decay as a laboratory for testing the standard model". In: *Phys. Rev. D* 88 (7 Oct. 2013), p. 073002. DOI: 10.1103/PhysRevD.88.073002.

[JTW57]   J. D. Jackson, S. B. Treiman, and H. W. Wyld. "Possible Tests of Time Reversal Invariance in Beta Decay". In: *Phys. Rev.* 106 (3 May 1957), pp. 517–521. DOI: 10.1103/PhysRev.106.517.

[Jac75]   J. D. Jackson. *Classical electrodynamics.* Wiley, 1975.

[KM18]   M. Klopf and B. Märkisch. PERKEO III *magnetic mirror effect analysis.* internal report. Apr. 2018.

[KM73]   M. Kobayashi and T. Maskawa. "CP-Violation in the Renormalizable Theory of Weak Interaction". In: *Progress of Theoretical Physics* 49.2 (1973), pp. 652–657. DOI: 10.1143/PTP.49.652.

[Kon+12a]   G. Konrad, H. Abele, M. Beck, et al. "Neutron Decay with PERC: a Progress Report". In: *Journal of Physics: Conference Series* 340.1 (2012), p. 012048. DOI: 10.1088/1742-6596/340/1/012048.

[Kon+12b]   G. Konrad, W. Heil, S. Baeßler, D. Počanić, and F. Glück. "Impact of neutron decay experiments on non-standard model physics". In: *Physics Beyond the Standard Models of Particles, Cosmology and Astrophysics.* 2012, pp. 660–672. DOI: 10.1142/9789814340861_0061. arXiv: 1007.3027 [nucl-ex].

[LY56]   T. D. Lee and C. N. Yang. "Question of Parity Conservation in Weak Interactions". In: *Phys. Rev.* 104 (1 Oct. 1956), pp. 254–258. DOI: 10.1103/PhysRev.104.254.

[Leo87]   W. R. Leo. *Techniques for nuclear and particle physics experiments.* Springer, 1987.

[LT84]   V. Luschikov and Y. Taran. "On the calculation of the neutron adiabatic spin-flipper". In: *Nuclear Instruments and Methods in Physics Research Section A: Accelerators, Spectrometers, Detectors and Associated Equipment* 228.1 (1984), pp. 159–160. ISSN: 0168-9002. DOI: 10.1016/0168-9002(84)90025-1.

[MB16]   W. J. Marciano and E. Blucher. "V_{ud}, V_{us}, The Cabibbo Angle and the CKM Unitarity". In: *Chin. Phys.* C40.10 (2016). in [PDG16], p. 100001. DOI: 10.1088/1674-1137/40/10/100001.

[MS06]   W. J. Marciano and A. Sirlin. "Improved Calculation of Electroweak Radiative Corrections and the Value of V_{ud}". In: 96 (3 Jan. 2006), p. 032002. DOI: 10.1103/PhysRevLett.96.032002.

[Mär+09]   B. Märkisch, H. Abele, D. Dubbers, F. Friedl, A. Kaplan, H. Mest, M. Schumann, T. Soldner, and D. Wilkin. "The new neutron decay spectrometer Perkeo III". In: *Nuclear Instruments and Methods in Physics Research Section A: Accelerators, Spectrometers, Detectors and Associated Equipment* 611.2 (2009). Particle Physics with Slow Neutrons, pp. 216–218. ISSN: 0168-9002. DOI: 10.1016/j.nima.2009.07.066.

[Mär06]   B. M. Märkisch. "Das Spektrometer PERKEO III und der Zerfall des freien Neutrons". PhD thesis. Ruprecht-Karls-Universität, Heidelberg, Oct. 2006. `http://www.physi.uni-heidelberg.de//Publications/phd_maerkisch.pdf`.

[Mes11]   H. F. Mest. "Measurement of the Beta-Asymmetry in the Decay of Free Polarized Neutrons with the Spectrometer PERKEO III". PhD thesis. Ruprecht-Karls-Universität, Heidelberg, June 2011. `http://www.physi.uni-heidelberg.de//Publications/dissertation_mest.pdf`.

[Mun+13]   D. Mund, B. Maerkisch, M. Deissenroth, J. Krempel, M. Schumann, H. Abele, A. Petoukhov, and T. Soldner. "Determination of the Weak Axial Vector Coupling from a Measurement of the Beta-Asymmetry Parameter A in Neutron Beta Decay". In: *Phys. Rev. Lett.* 110 (2013), p. 172502. DOI: `10.1103/PhysRevLett.110.172502`. arXiv: `1204.0013` `[hep-ex]`.

[Mun06]   D. Mund. "Messung der Betaasymmetrie A im Neutronenzerfall". PhD thesis. Ruprecht-Karls-Universität, Heidelberg, May 2006. `http://www.physi.uni-heidelberg.de//Publications/phd_mund.pdf`.

[NG13]   O. Naviliat-Cuncic and M. González-Alonso. "Prospects for precision measurements in nuclear β decay at the LHC era". In: *Annalen Phys.* 525 (2013), pp. 600–619. DOI: `10.1002/andp.201300072`. arXiv: `1304.1759` `[hep-ph]`.

[Opp16]   C. Oppenheimer. "Development, production and characterization of high-purity $CaWO_4$ crystals for the CRESST-Experiment". MA thesis. Technische Universität München, Dec. 2016.

[PDG16]   C. Patrignani et al. "Review of Particle Physics". In: *Chin. Phys.* C40.10 (2016), p. 100001. DOI: `10.1088/1674-1137/40/10/100001`.

[Pat+18]   R. W. Pattie, N. B. Callahan, C. Cude-Woods, et al. "Measurement of the neutron lifetime using a magneto-gravitational trap and in situ detection". In: *Science* (2018). ISSN: 0036-8075. DOI: `10.1126/science.aan8895`.

[PHY13]   R. W. Pattie, K. P. Hickerson, and A. R. Young. "Limits on Tensor Coupling from Neutron β-Decay". In: *Phys. Rev.* C88 (2013). [Erratum: Phys. Rev.C92,no.6,069902(2015)], p. 048501. DOI: `10.1103/PhysRevC.92.069902`, `10.1103/PhysRevC.88.048501`. arXiv: `1309.2499` `[nucl-th]`.

[Plo00]   C. Plonka. "Verbesserung der Lichtausopplung zur Messung der Neutrinoasymmetry mit PERKEO II". Diploma Thesis. Ruprecht-Karls-Universität, Heidelberg, Jan. 2000. `http://www.physi.uni-heidelberg.de//Publications/dipl_plonka.pdf`.

[Poh+10]   R. Pohl, A. Antognini, F. Nez, et al. "The size of the proton". In: *Nature* 466 (7303 Aug. 2010), pp. 213–216. ISSN: 0028-0836. DOI: `10.1038/nature09250`.

[Raf16]   L. Raffelt. "Measurement of the Proton Asymmetry (C) in free neutron β-decay with Perkeo III". PhD thesis. Ruprecht-Karls-Universität, Heidelberg, Aug. 2016. `https://www.ene.ph.tum.de/fileadmin/w00buw/www/theses/diss_raffelt.pdf`.

[Rei99]   J. C. Reich. "Angular Correlations in Polarized Neutron Decay". PhD thesis. Ruprecht-Karls-Universität, Heidelberg, Nov. 1999. `http://www.physi.uni-heidelberg.de//Publications/phd_reich.pdf`.

[Roi+18]   C. Roick, D. Dubbers, B. Märkisch, H. Saul, and U. Schmidt. "Electron time-of-flight: A new tool in β-decay spectroscopy". In: *Phys. Rev. C* 97 (3 Mar. 2018), p. 035502. DOI: `10.1103/PhysRevC.97.035502`.

[Roi18]   C. Roick. "Particle Detection and Proton Asymmetry in Neutron Decay". PhD thesis. Technische Universität München, Sept. 2018.

[Sac16]   R. Sachsenhauser. "Detektorkalibration für Präzisionsbetaspektroskopie". B. S. Thesis. Technische Universität München, July 2016.

[SFS11]   F. Salvat, J. M. Fernández-Varea, and J. Sempau. "PENELOPE-2011: A Code System for Monte Carlo Simulation of Electron and Photon Transport". In: *OECD NEA Data Bank/NSC DOC(2011)/5*. OECD Nuclear Energy Agency, Issy-les-Moulineaux, 2011.

[Sch+08]   M. Schumann, M. Kreuz, M. Deissenroth, F. Gluck, J. Krempel, B. Märkisch, D. Mund, A. Petoukhov, T. Soldner, and H. Abele. "Measurement of the Proton Asymmetry Parameter C in Neutron Beta Decay". In: *Phys. Rev. Lett.* 100 (2008), p. 151801. DOI: `10.1103/PhysRevLett.100.151801`. arXiv: `0712.2442 [hep-ph]`.

[Sch+07]   M. Schumann, T. Soldner, M. Deissenroth, F. Gluck, J. Krempel, M. Kreuz, B. Märkisch, D. Mund, A. Petoukhov, and H. Abele. "Measurement of the neutrino asymmetry parameter B in neutron decay". In: *Phys. Rev. Lett.* 99 (2007), p. 191803. DOI: `10.1103/PhysRevLett.99.191803`. arXiv: `0706.3788 [hep-ph]`.

[SA08]   M. Schumann and H. Abele. "Unrecognized backscattering in low energy beta spectroscopy". In: *Nuclear Instruments and Methods in Physics Research Section A: Accelerators, Spectrometers, Detectors and Associated Equipment* 585.1 (2008), pp. 88–92. ISSN: 0168-9002. DOI: `10.1016/j.nima.2007.11.016`.

[SBN06]   N. Severijns, M. Beck, and O. Naviliat-Cuncic. "Tests of the standard electroweak model in nuclear beta decay". In: *Rev. Mod. Phys.* 78 (3 Sept. 2006), pp. 991–1040. DOI: `10.1103/RevModPhys.78.991`.

[Sha71]   R. T. Shann. "Electromagnetic effects in the decay of polarized neutrons". In: *Il Nuovo Cimento A (1965-1970)* 5.4 (1971), pp. 591–596. ISSN: 1826-9869. DOI: `10.1007/BF02734566`.

[Sir67]   A. Sirlin. "General Properties of the Electromagnetic Corrections to the Beta Decay of a Physical Nucleon". In: *Phys. Rev.* 164 (5 Dec. 1967), pp. 1767–1775. DOI: `10.1103/PhysRev.164.1767`.

[Sol+02]   T. Soldner et al. *Installation and first tests of the new PF1b polariser*. Tech. rep. ILL03SO10T. Institut Laue-Langevin, Grenoble, France, 2002.

[Sol18]   T. Soldner. PERKEO III *polarisation analysis*. internal report. Apr. 2018.

[Tan82]   H. H. Tan. "A Statistical Model of the Photomultiplier Gain Process with applications to Optical Pulse Detection". In: *International Telemetering Conference Proceedings*. International Foundation for Telemetering, Sept. 1982.

[PDG18]   M. Tanabashi et al. "Review of Particle Physics". In: *Phys. Rev. D* 98 (3 Aug. 2018), p. 030001. DOI: `10.1103/PhysRevD.98.030001`.

[WKA13]   X. Wang, G. Konrad, and H. Abele. "RxB drift momentum spectrometer with high resolution and large phase space acceptance". In: *Nuclear Instruments and Methods in Physics Research Section A: Accelerators, Spectrometers, Detectors and Associated Equipment* 701.Supplement C (2013), pp. 254–261. ISSN: 0168-9002. DOI: `10.1016/j.nima.2012.10.071`.

[Wan13]   X. Wang. "The Free Neutron β-Decay: A Powerful Tool for the Investigation in Particle Physics". PhD thesis. Technische Universität München, Mar. 2013. `https://mediatum.ub.tum.de/node?id=1121297`.

[WGH14]   F. Wauters, A. García, and R. Hong. "Limits on tensor-type weak currents from nuclear and neutron β decays". In: *Phys. Rev. C* 89 (2 Feb. 2014), p. 025501. DOI: `10.1103/PhysRevC.89.025501`.

[Wer09]   D. Werder. "Development and Characterization of a Pulsed Beam for Neutron Decay Experiments". Diploma Thesis. Ruprecht-Karls-Universität, Heidelberg, Aug. 2009. `http://www.physi.uni-heidelberg.de//Publications/dipl_werder.pdf`.

[Wil07]   D. Wilkin. "Aufbau eines Kollimationssystems und Entwicklung eines Scanners für das Spektrometer PERKEO III". Diploma Thesis. Ruprecht-Karls-Universität, Heidelberg, Mar. 2007. `http://www.physi.uni-heidelberg.de//Publications/dipl_wilkin.pdf`.

[Wil82]   D. Wilkinson. "Analysis of neutron β-decay". In: *Nuclear Physics A* 377.2 (1982), pp. 474–504. ISSN: 0375-9474. DOI: `10.1016/0375-9474(82)90051-3`.

[Wu+57]   C. S. Wu, E. Ambler, R. W. Hayward, D. D. Hoppes, and R. P. Hudson. "Experimental Test of Parity Conservation in Beta Decay". In: *Phys. Rev.* 105 (4 Feb. 1957), pp. 1413–1415. DOI: `10.1103/PhysRev.105.1413`.

Acknowledgements

First and foremost I like to thank Eva Stark for her support, understanding and for helping me to put things into perspective, which certainly helped me through the tougher times of this work.

I like to thank my parents and family for their absolute support. It is the reason that I have been able to start and finally finish this project.

I like to thank my supervisors Hartmut Abele and Bastian Märkisch for entrusting me with this work, giving me the opportunity to participate in the field of neutron decay and for the support throughout my thesis.

Werner Heil, Jochen Schieck and Lothar Oberauer I like to thank for reviewing this thesis.

Jens Klenke I like to thank for getting me on board with neutron decay and experimental physics in general as a student and for his support over the last years.

Thanks to Kathrin Lehmann for helping me out a lot with construction work and to stand my disordered desk.

I thank Christoph Roick for his enthusiasm, especially when problems became complex.

Dirk Dubbers, Gertrud Konrad, Ulrich Schmidt and Torsten Soldner I like to thank for the many interesting and challenging discussions. I learned a lot working with them.

Also I like to thank Michael Klopf, Lukas Raffelt, Willi Mach, Daniel Moser, Max Lamparth and Benjamin Daiber for a great beamtime in Grenoble.

Thanks to Karina Bernert for proofreading this thesis.

Finally, I like to thank all the colleagues in Munich, Vienna, Heidelberg, Grenoble and anywhere else, which I got to know throughout the years and with whom I had a great time at and outside of work.